Title
Nanostructured Metal Oxide enabled Silicon based Solar Fuel Cell

Author
Sun, Ke

Publication Date
2013

UNIVERSITY OF CALIFORNIA, SAN DIEGO

Nanostructured Metal Oxide enabled Silicon based Solar Fuel Cell

A dissertation submitted in partial satisfaction of the
requirements for the degree Doctor of Philosophy

in

Electrical Engineering (Nanoscale Device and System)

by

Ke Sun

Committee in charge:

Professor Deli Wang, Chair
Professor Peter M. Asbeck
Professor Sungho Jin
Professor Clifford P. Kubiak
Professor Paul K. L. Yu

2013

The Dissertation of Ke Sun is approved, and it is acceptable in quality and form for publication on microfilm and electronically:

Chair

University of California, San Diego

2013

DEDICATION

For Mingke, Luke,

Mom and Dad

TABLE OF CONTENTS

LIST OF FIGURES

Chapter 1

Chapter 2

Chapter 3

LIST OF TABLES

Chapter 1

Chapter 3

ACKNOWLEDGEMENTS

I would like to acknowledge Professor Deli Wang for the opportunity to work in his group and his continuous support as the chair of my committee for the past 4 years. I specially thank him for spending valuable time day and night on multiple manuscripts whenever I needed him to review. I would like to thank him for sharing his envision and thoughts which are really encouraging.

I appreciate kind support I received from all the committee members and participating faculties. Professor Yu has provided me valuable guidance and encouragement on my career. Professor Jin generously supported me with every available time he may have for every short meeting and update, provided me with the suggestions on missing points. I also thank Professor Kubiak for reviewing my review article and insights that he shared. I also thank Professor Asbeck for stimulating questions and discussions.

I also would like to thank my colleagues at UCSD who have been really helpful. Cesare, Wei, Yi and Winnie helped me a lot on MOCVD, monochromator, Hall and XRD measurement. Group members Namseok, Sonia, Alireza, Muchuan, Conor, Siarhei and Brain have provided me lots of technical support. I am also so grateful to the talented undergrad and graduate students that I have been working with, Kristian, Pål, Justin, Weining, and Qiang. I also thank Jigang, Jian and Yongfeng at Canadian Light Source for their generous assistance on the X-ray absorption measurement and development of an in-situ measurement setup for catalyst studies.

I have to thank friends back in China who have been really supportive on my dissertation work. Shaohua, Xiaolu and Yongqi were always there when I need to do some XPS, XRD, and Raman measurement or maybe just an enjoyable conversation and a stimulus discussion.

Finally, I want to dedicate last few sentences to my wife, Mingke. I thank her so much for being there for me during the hard time for the last 4 years; thank her for all the encouragement, understanding, and patience she has provided me, and happiest time we shared together. I shall have no more words, but Mingke - thank you and I love you so much.

Chapter 1, in full, has been submitted for publication of the material as it may appear in Chemical Reviews 2013, Ke Sun, Shaohua Shen, Yongqi Liang, Samuel S. Mao, Deli Wang 2013. Reproduced with permission from Chemical Reviews, submitted for publication. Unpublished work copyright 2013 American Chemical Society. The dissertation author was the primary investigator and the first author of this paper.

Chapter 2, in full, is a reprint of the materials as it appears in Journal of American Chemical Society communication 2010, Nanoscale 2012, and Nanotechnology 2012. Reproduced with permission from Journal of American Chemical Society, vol.132, pp.15465 (2010) Copyright 2010 American Chemical Society. Nanoscale, vol. 4, pp. 1515 (2012) - Reproduced by permission of The Royal Society of Chemistry. Nanotechnology, vol.23, no.19, pp.194013 (2012) - Reproduced by permission of Institute of Physics Publishing. The dissertation author was the primary investigator and the first author of these papers.

Chapter 3, in full, is a reprint of the materials as it appears in Energy and Environmental Science 2012 and Nano Letters 2013; also in part is currently being prepared for submission for publication of the material. Reproduced with permission from Nano Letters, DOI: 10.1021/nl400343a Copyright 2013 American Chemical Society. Energy and Environmental Science, vol.5, pp.7872 (2012) - Reproduced by permission of The Royal Society of Chemistry. The dissertation author was the primary investigator and the first author of these papers.

VITA

2003	Bachelor of Science, Beijing Institute of Technology, Beijing, China
2006	Master of Science, University of Puerto Rico, Mayaguez, Puerto Rico, USA
2009	Master of Engineering, University of South Florida, Tampa, FL, USA
2013	Doctor of Philosophy, University of California, San Diego, La Jolla, CA, USA

PUBLICATIONS

1) “Ultrathin NiO_x on Si p^+n-Junction Photoanode for Efficient Solar Water Oxidation”, under preparation, 2013.

2) "Enabling Si for solar fuel production: history and prospects", under review Chemical Reviews, submitted on 11/15/2012.

3) "Metal Oxide Composite Enabled Nanotextured Si Photoanode for Efficient Solar Driven Water Oxidation", Nano Letters, DOI: 10.1021/nl400343a.

4) "Branched TiO2/Si Nanostructures for Enhanced Photoelectrochemical Water Splitting", online Nano Energy, 2012.

5) "Zinc Oxide Nanowire as an Electron-Extraction Layer for Broadband Polymer Photodetectors with an Inverted Device Structure", Journal of Physical Chemistry C, vol.116, pp.13650 (2012).

6) "Nickel oxide functionalized silicon for efficient photo-oxidation of water", Energy and Environmental Science, vol.5, pp.7872 (2012).

7) "Metal Catalyst on Metal Oxide Nanowire Coated Si Photocathode for Solar Water Splitting", Nanotechnology, vol.23, no.19, pp.194013 (2012).

8) "3D Branched Nanowire Heterojunction Photoelectrodes for High-Efficiency Solar Water-Splitting", Nanoscale, vol. 4, pp. 1515 (2012).

9) “Crystalline ZnO Thin Film from Hydrothermal Growth", ChemComm, vol.47, pp.7776 (2011).

10) "Compound Semiconductor Nanowire Solar Cells", IEEE Journal of Selected Topics in Quantum Electronics, vol.17, no.4, pp.1044 (2011).

11) “Solution Synthesis of Large-Scale, High-Sensitivity ZnO/Si Hierarchical Nanoheterostructure Photodetectors”, Journal of American Chemical Society, vol.132, pp.15465 (2010).

FIELD OF STUDY

Major Field: Electrical Engineering (Nanoscale Device and System)

ABSTRACT OF THE DISSERTATION

Nanostructured Metal Oxides Enabled Silicon based Solar Fuel Cell

by

Ke Sun

Doctor of Philosophy in Electrical Engineering (Nanoscale Device and System)

University of California, San Diego, 2013

Professor Deli Wang, Chair

Intrinsic drawbacks of Si, a well adapted material in photovoltaics, including the high valence band position compared to the proton reduction level, the unfavorable self-oxidation level compared to the one of water oxidation, and indirect energy band, prevent Si as a good candidate for applications in photoelectrochemical water splitting, despite its small band gap which matches the solar irradiance spectrum. Strategies need to be developed to overcome these problems. This dissertation presents a study of metal oxides integrated Si photoelectrode for solar driven water splitting. Different metal oxides including zinc oxide, titanium dioxide, indium tin oxide, and nickel oxide are coated on polished and nanotextured p-type and n-type Si from various methods. This heterogeneous uniform coating effectively replaces the problematic water|Si interface which can be corrosive and oxidative to Si. The Schottky junction formed either using an n-type coating (ZnO and TiO_2) on p-type Si or a p-type coating (NiO) on n-type Si is able to effectively separate the photo-generated charges in Si. In addition, nanotextured Si is able to dramatically improve light absorption and provide enlarged surface chemical reaction sites. In this case, integration of metal oxides in the form of nanoscale structures on the nanostructured Si, a so-called branched nanowire structure or a "nanotree" array, is able to enhance the light absorption and reduce the radius of curvature to ease the gas evolution. Earth abundant transition metal, primarily Ni, was used to catalyze the water reduction and oxidation reaction. Solution-casted NiO from a cost-effective approach provides higher activity compared to the one prepared from gas phase sputtering. Surfactant and thermal treatment effect are studied to achieve an optimized catalytic activity. This catalyst is then successfully demonstrated on a surface inverted n-Si photoanode protected with a novel semitransparent conducting oxide. Considerable contributions have been made through this dissertation study. Suggestions on future improvements are provided.

CHAPTER 1

1.1 Introduction

After about 150 years' exploitation and utilization of fossil fuels, nowadays the human have been encountering two great global problems of expected depletion of fossil fuels and increasingly serious environmental pollution. To maintain our sustainable living and development, it is imperative to discover a viable alternative to reduce the excessive use earth's natural energy resources - fossil fuels. Importantly, this alternative energy should be in principle environmental friendly with minimum or zero greenhouse gas emission, renewable, storable, and economical. Sunlight and seawater are the ultimate sustainable energy sources on earth among the clean energy resources. Together they constitute a potential solution to the global energy and environmental crisis. Low-cost harvesting, conversion and storage of solar energy as chemical fuels, an artificial photosynthesis process, are believed to be of great economic and environmental interests.

Since the pioneer work by Fujishima and Honda in 1972[1], the technology of solar-fuel production from water, mainly H_2 production and CO_2 reduction, via a semiconductor photocatalytic or photoelectrochemical process, becomes to be one of the hottest research topics in multi-disciplinary fields related to energy, material science, chemistry and physical sciences[2]. In the past few decades, tremendous research efforts on photocatalysis and photoelectrocatalysis have yielded better understanding of the processes involved in solar driven H_2 production and CO_2 reduction in water, along with exploration and development of efficient and stable catalytic materials, including oxides, sulfides and (oxy)nitrides, and others[3]. Some significant progresses have been achieved, for example, $Rh_{2-x}Cr_xO_3$/GaN-ZnO (pure water splitting, quantum yield at 420-440 nm: 5.9%) as a photocatalyst[4], np-junction GaAs/p-$GaInP_2$ (solar-hydrogen conversion efficiency: 12.4%)[5], and Cu_2O (incident photon-to-current conversion efficiency: 40 % at 0 V vs. RHE in the wavelength range of 350-480 nm)[6] as photoelectrodes, to name a few. Regarding the energy conversion efficiency, material cost and durability, none of the so-far developed materials is capable for practical application with the goal of high-performance and long-term solar fuel production.

Silicon (Si), as the second most abundant element in the earth's crust, is widely used for photovoltaic applications, due to its superior advantages of low cost and narrow band gap (E_g = ~1.1 eV) which matches to the solar spectrum. This property equally renders Si as a promising material for photoelectrodes in a photoelectrochemical system for solar fuel production. Si, in fact, is one of the most examined materials in the early evolution of the semiconductor photoelectrochemistry field for various reasons, such as high level of technological infrastructures that already exists, rich chemical/physical properties, etc.

Solar fuel production using Si can be realized in two approaches. The first one is a technical approach, in which one can connect a Si solar panel to an electrolyzer. This method requires high-cost photovoltaic panels and electrolyzer typically composed of precious noble metal catalysts. This approach does not meet the requirement as a major energy production in a cost-effective mannar. Meanwhile, energy conversion efficiency using this method for H_2 generation compared to other renewable sources remains the lowest based on a recent reported exengy analysis[7]. The other one is a much under-developed scientific approach through Si based photoelectrodes. This method, on the other hand, relies on the fundamental understanding on Si photoelectrochemistry particularly in aqueous solution for proton/carbon dioxide reduction and/or water oxidation. The goal of the second approach is to replace the two expensive components from the first one by a significantly cheaper photoelectrolysis cell (or solar fuel cell)[8]. Enabling Si as photoelectrodes for a practical solar fuel production from water is nature mimicking, where light absorption and catalytic reaction does not happen on the same material. Different from other widely studied oxide photoactive materials, practical Si-based solar fuel production should be consisting of a photoabsorber - Si, rectified linked to an electrocatalyst, on which the aforementioned reactions take place. Toward this, there have been tremendous research efforts spanning from fundamental science to system design and engineering to overcome intrinsic problems of Si, and from screening and synthesis outperforming cost-effective electrocatalysts in order to realize artificial photosynthesis for distributed energy production[9].

This review covers most of the literatures about silicon photoelectrochemistry since 1976[10]. To differentiate from many recent review articles[9], the emphasis of this work is on fundamental problems of silicon electrolyte interface, materials/strategies developed to modify interfacial energetics, and finally Si-based solar fuel conversion devices from spontaneous water splitting and artificial photosynthesis. Rather than attempting to provide specific technical details, the goal of this review is to educate readers with the development of solar-fuel production primarily water and CO_2 reduction in aqueous electrolyte using Si photoelectrochemistry, to review innovative ideas, and most importantly to trigger research effort for practical photoelectrochemical cells/panels for artificial photosynthesis.

1.2 Properties of Si and Si/electrolyte interface

We start with fundamental Si electrochemistry with an introduction of important properties of Si and Si electrolyte interface (S/E) relevant to the solar fuel conversion process, including topics such as light absorption, thermodynamic limitations, Fermi level pinning due to surface states, S/E energetics[11], barrier height between Si and electrolyte[12] and etc. To gain background in broader semiconductor electrochemistry, readers are recommended to refer books by Memming[13] and Morrison[14]. The interfacial energetics for a p- and n-Si in an electrolyte solution under equilibrium, flat band position (Fig.1a) and anodic bias are as indicated in the Figure 1 below. E_g is the energy band gap, E_f is the Fermi level or electrochemical potential, E_{VB} is the potential of the top of the valence band at the interface, E_{CB} is the potential of the bottom of the conduction band, and H^+/H_2 and H_2O/O_2 is the electrochemical potentials for proton reduction and water oxidation. For a given solution, positions of E_{CB} and E_{VB} are generally fixed. For p-Si interfacing H^+/H_2 (Fig.1b) the majority holes are effectively blocked by the energy barrier, but photogenerated electrons in the depletion region in Si can be driven by the electric field to the S/E interface to reduce proton to get H_2 spontaneously if additional electron donors are present. Similarly, for n-Si interfacing with H_2O/O_2 (Fig.1c) typically operating under anodic bias, electrons are blocked, but photogenerated holes rise to the E_{VB} and are ideally capable of oxidizing water to obtain O_2 under certain conditions that we are going to discuss in this section. Electron excited to the conduction band are driven to the bulk of the semiconductor away from the interface, which can further drive electrons with sufficient energy to the counter electrode for the water reduction reaction.

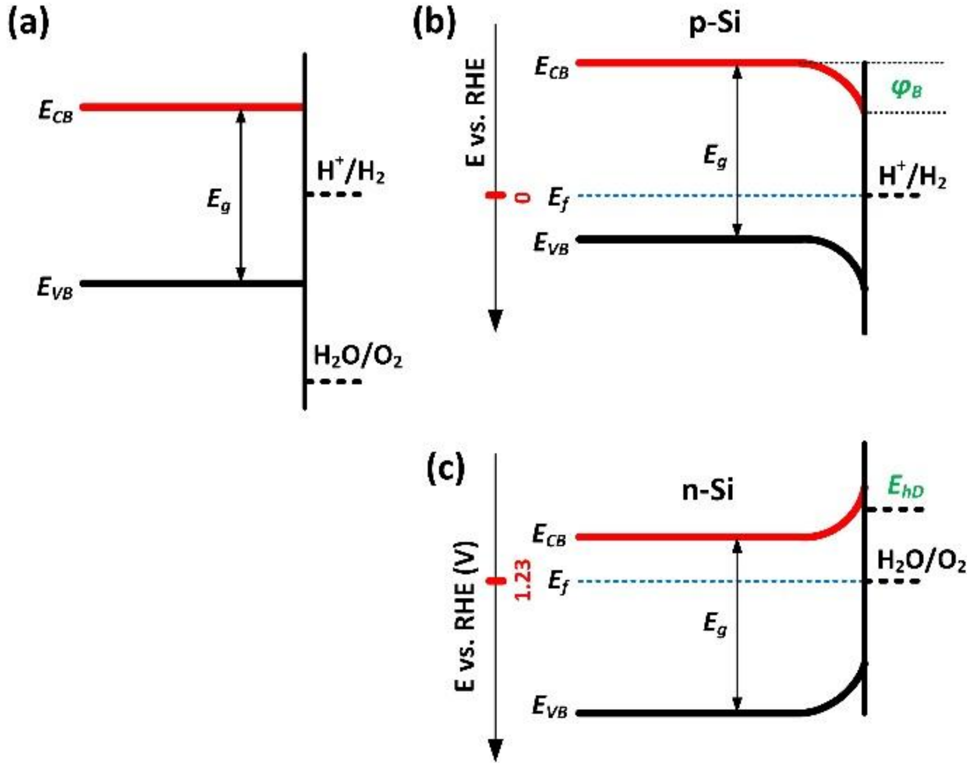

Figure 1. Si band edge positions with respect to water redox level at flat band condition (a), and energy band diagram of p-Si at equilibrium (b), and n-Si under anodic bias (c).

1.2.1 Optical absorption

Electronic band structure of single crystal Si (sc-Si) shows the band edge absorption is indirect, in which the conduction minimum and valence band maximum are located at different position in the wave vector space (first Brillouin zone). The indirect band gap affects the absorption of incident photons, which complicates the light absorption process and makes the absorption less effective than direct band gap materials[15]. This unique optical property of Si leads to a poor absorption coefficient resulting in a requirement for a long optical pathway for effective light absorption.

GaN, ZnO and TiO_2 exhibit wide band gaps due to low valence band position from filled N 2p or O 2p states limiting their absorption in the UV region, which is only about 5% in the whole solar spectrum (Fig.2 purple area). Some other commonly seen photoactive semiconductors, such as GaP, Cu_2O, Fe_2O_3, CdSe etc, could absorb visible light (Fig.2 purple+blue area). Nonetheless, the 1.1-eV band gap of sc-Si which effectively absorbs light spectrum from UV to near IR (Fig.2 purple+blue+gray area) leads to a higher maximum theoretical photocurrent (Fig.2 blue curve, assume 100% above energy band gap photon-to-electron conversion) than that from other aforementioned direct band gap semiconductors. Acceptable electron mobility leads to a wide application of Si in photoactive material for solar energy conversions.

To further justify the use of small band gap materials photoactive material in water, it is important to confirm the water absorption spectrum. It was reported by Hale et al.[16] that - water showed near perfect transmittance to visible and UV light, but stronger near IR absorption. One can see from Fig.2 (red curve) that absorption peaks of water are consistent with the dips in solar spectrum due to the water vapor in atmosphere. Considerable IR loss occurs at wavelength above 1500 nm where absorption coefficient reaches above 1 cm^{-1}, meaning within the useful wavelength range that Si can effectively absorb water absorption effect can be reasonably neglected.

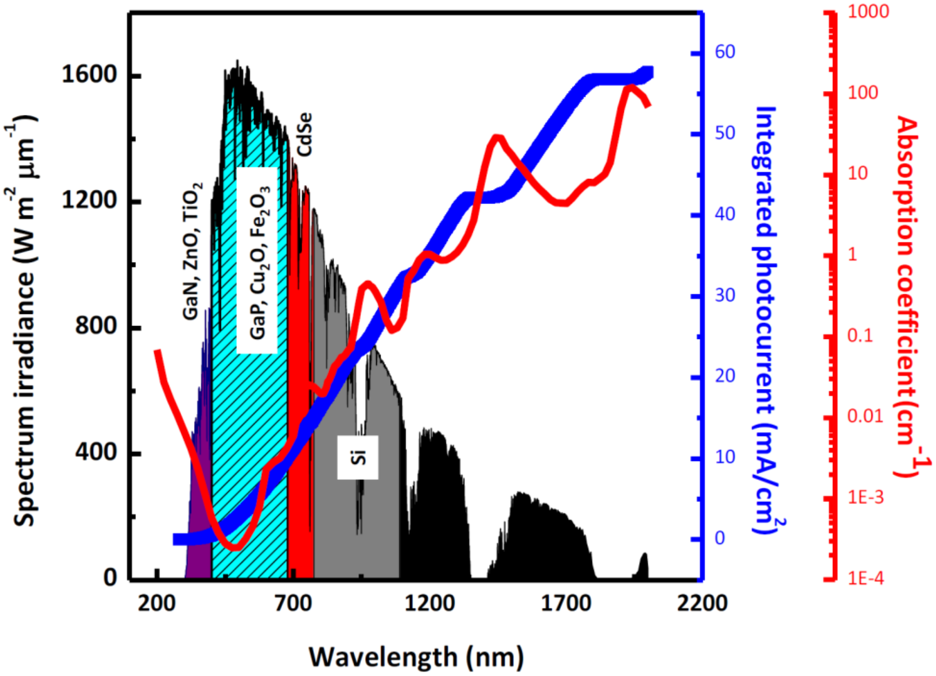

Figure 2. Solar AM1.5G solar spectrum (black curve, data from National Renewable Energy Laboratory), calculated maximum photocurrent density (blue curve), and absorption coefficient of water (red curve) data from ref [16]. Band absorptions of solar spectrum of several commonly studied photoactive semiconductors are highlighted by the shaded areas.

1.2.2 Thermodynamics

Fundamental thermodynamic energy required for spontaneous water splitting is 1.229 eV[17]. Considering all the losses including reaction overpotentials, ohmic and transportation loss, this minimum requirement lands in a more realistic range of 1.5-1.6 eV, meaning the minimum band gap of semiconductor should be in this range in order to be capable to provide 1.229-eV free energy for water splitting without an external power assistance[18]. Si, apparently, does not have enough band gap energy for spontaneous water splitting (1.1 eV for single junction crystal, which can theoretically provide a maximum photovoltage of 0.8 eV). Although a single crystal Si is not able to split water spontaneously, Si is good for proton reduction spontaneously since E_{CB} of Si is well above water reduction level (Fig.1a). H2 generation can be realized in this case if one can add an electron donor that has a lower redox potential than H_2O/O_2 (less redox potential means higher in the energy band diagram, for example I^-/I_2 redox couple). The conduction band, on the other hand, is too high, which limits the electron energy need to reduce water for H_2 production due to low photovoltage and low surface band bending. Moreover, although Si is an attractive semiconductor with a broad spectrum utilization, thus high photocurrent density in comparison with some other typical photoelectrochemical materials as discussed in section 2.1, it rapidly forms an insulating oxide under irradiation or under anodic bias in aqueous solution and gradually passivates[19]. Technically, oxidation of Si occurs when a Si surface atom meets holes from the valence band that are potential induced on p-Si where accumulation of majority carriers is formed upon anodic polarization. The oxidation can also occur on n-Si where minority carriers are excited by incident energetic photons[20]. This deleterious effect can substantially suppress the photo conversion process due to the thick insulating oxide layer formed effectively blocking the charges from reaching electrolyte. This photo/anodic oxidation of Si photoelectrodes in aqueous solution is more feasible than oxidation of water (equation 1), while reductive degradation of Si is kinetically difficult at normal condition. Stability against anodic decomposition is widely studied during the early development of Si photoelectrochemistry. Research focus to enable Si for solar fuel production from water is to alter kinetics to reduce the current efficiency for the growth of insulating SiO_2 at the interface and improve the current efficiency for the net interfacial reduction or oxidation of water[21].

Photo/anodic oxidation reaction (E_{hD}) on Si with the presence of water can be expressed in the equation (1) as below:

$$Si + 2H_2O + 4h_{VB}^{+}(h\nu/V_a) \rightarrow SiO_2 + 4H_{aq}^{+} \qquad (1)$$

This passivation reaction occurs at a potential range of -0.887 ~ -0.889 V vs. reversible hydrogen electrode (RHE) depending on the form of SiO_2[17], where $h\nu$ and V_a are incident photon and anodic polarization, respectively. The rate of passivation in a given solution depends on anodic bias level, light intensity, stirring rate, previous history of electrodes, and etc[19]. p-Si passivation under idle conditions (under dark and at zero bias) is also possible and observed. Proper protection to block hole transfer to the S/E surface across the barrier through surface defects is also essential for practical p-Si photocathodes.

Taking into consideration of the water oxidation reaction level,

$$2H_2O + 2h^+ \rightarrow O_2 + 4H^+ \qquad (2)$$

which theoretically occurs at 1.229 V (vs. RHE) without considering the overpotential losses, Si self-oxidation (E_{hD}) is much more thermodynamically viable, which is competing with the water oxidation process. This competing reaction needs to be well suppressed for efficient and practical water oxidation. Thus, a fast, irreversible oxidation of water for O_2 generation is highly desired in order to preclude photoanodic surface decomposition. On the cathode side, unfavorable reduction processes reproducing water instead limits the H_2 fuel evolution, including oxygen and carbon dioxide reduction reactions:

$$O_2 + 4H^+ + 4e^- \rightarrow 2H_2O \qquad (3a)$$

$$CO_2 + 8H^+ + 8e^- \rightarrow CH_4 + 2H_2O \qquad (3b)$$

Therefore, research experiments on photoelectrochemical water splitting for H_2 production normally utilize purged solution with inert gas (N_2 or Ar) to suppress rates of these reactions and finally ignore these competing processes. In addition, separating H_2 and O_2 products from each other to prevent back reactions is essential. In section 5.2, CO_2 reduction for hydrocarbon or CO production is the main reaction on the cathode in artificial photosynthesis, in which water/proton reduction needs to be suppressed for better selectivity. Nevertheless, most of the discussions here focus on the water reduction and oxidation reaction for H_2 and O_2 formation unless specified.

1.2.3 Kinetics:

At an ideal S/E interface, change of potential between the bulk semiconductor and bulk solution mainly results in the change of potential in the space charge region in the semiconductor instead of Helmholtz layer or diffusion double layer in the liquid[22]. It is estimated that when a surface states density becomes larger than 10^{12} cm^{-2}, charge density from surface states becomes larger than the charge density in depletion region for moderately doped nondegenerate semiconductor. Roughly, since the number of atoms on the surface is around 10^{15} cm^{-2}, surface states representing ~1% surface coverage will bring about Fermi level pinning. High surface states density increases surface recombination velocity and this large number of energy states "pinned" the Fermi level at the surface, which leads to a fixed energy barrier independent from redox level or electrolyte pH. In other words, the pinned Fermi level effectively shift the band edge position with the redox level or pH level. With the Fermi level pinning at the surface states, the change of potential mainly occurs in the Helmholtz layer rather than in the space charge region as in the case of ideal S/E interface. Therefore, charge-transfer kinetics is profoundly affected by the surface states induced change in surface chemistry and electrochemistry[23]. Surface state level plays a role as an electron transfer mediator. It is worth noticing that the nature of the surface states energy distribution typically including uniformly distributed surface states density over a range of energy and localized surface states density at a single energy levels also affects the potential distribution[24]. Detailed calculations on an surface-states free interface as well as practical SC surface with surface states can be found in Green's work[25]. Surface chemistry will be useful in changing the nature of the surface states. For example, Lieber et al. pointed out that surface state is not a limiting factor compared to the bulk electrode properties and solution overpotential losses, through which one can provide rational control and design of semiconductor–liquid interface[26].

Therefore, Fermi level at the surface can be un-pinned from surface states level by chemical treatment. Inversion layer developed when the surface states becomes too high at the interface can also effectively un-pin the surface Fermi level[27]. Surface treatment to regain the control of energy barrier at S/E was considered as one of the key focuses to alter the surface kinetics of Si before. Various techniques have been developed such as surface functionalization using monolayer molecules[28], converting the surface to highly doped inversion layer[29], heterogeneous p-n junction[30], and etc. Similar strategies of surface modification to improve light utilization and surface kinetics were also important to other oxides photo(electro)catalysts[31].

Competing thermodynamic reactions and slow charge transfer kinetics of Si in contact with an aqueous solution are critical issues to solve, besides poor light absorption. Surface alteration techniques are desired to overcome these intrinsic disadvantages of Si for solar fuel production from water. Surface treatment affects cell performance in several ways. Controlling the gross topography modifies the ratio of absorbed to reflected light and the local current density. It can also modify the surface states density and distribution (which, in turn, influence the open-circuit voltage and the fill factor), the population of surface traps (which increase surface recombination rates and thus decrease the photocurrent), the electrochemical reaction rate (which contributes to the apparent internal resistance)[32], and interfacial charge transfer kinetics (which improves the long-term stability)[33].

1.3 Surface texture

Similar to solid-state photovoltaic cell, surface textures can be preferably introduced to Si photoelectrochemical cells to solve the problem of low light absorption. Efficient light management from surface textures is physically due to the suppressed Fresnel reflection from a smooth refractive index transition from that of the electrolyte to that of Si[34], the enhanced internal reflection, and intensity multiplication[35]. Surface textures could further suppresses the incident angle effect and minimize the polarization sensitivity[36]. Therefore, the light absorption can be enhanced and hence the energy conversion efficiency in energy conversion devices and sensitivity/limit of detection in photon detectors can be enhanced. Because of the efficient light utilization, surface texture is believed to offer possibility to reduce cost by cutting down material usage with a comparable performance to that of bulk substrates[37]. In addition to the light management, surface texture provides large junction area and shorter collection length of photogenerated minority carriers than the optical penetration depth, which significantly decouple the light absorption and charge separation process for improved charge collection efficiency[38]. In addition, surface texture fabricated from bottom-up or top-down method provides defects-free crystal with reduced charge recombination. However, increased surface area (or roughness factor, defined as the ratio of the surface area of the surface textures and polished surface) by introducing surface textures reduces the open circuit voltage because of the reduced splitting of quasi-Fermi levels at the S/E interface[38]. Surface texture of <100> Si for photoelectrochemical cell was first proposed by Lewis and co-workers[26,39]. In this section, we will review the studies on the surface textured Si with improved light utilization. Typical sub-wavelength nanostructures of Si and related techniques developed for nanostructure design, as well as microscale Si wires will be discussed.

1.3.1 Light absorption and anti-reflection

To enhance the absorption of sc-Si without sacrificing charge carrier collection efficiency over a thick absorption layer, orthogonalizing the processes of light absorption and charge carrier collection were proposed using wire array structures. In this structure, light is effectively absorbed due to smoothed transition of refractive indices from media to substrate, enhanced internal reflection, broadened absorption wavelength range, and minimized sensitivity to incident angle and polarization. Light trapping feature provides significant improvement on the generation of free carriers which results in increased photocurrent. Light trapping effect greatly depends on the physical profile and geometry of the wire array disregarding the substrate absorption[34]. Various attractive profiles were introduced and experimental/computational analysis were conducted[34,40], such as, random array, cylindrical wire array with uniform diameter[41] (Fig.3a and c), multi-size cylindrical wire array[42], pyramid array[43], cone array with sharp tips[44] (Fig.3b), sphere array[45], hole array[47], inverted pyramid[46] (Fig.3d), and wire array with other controlled sidewall profiles[47]. Technologies for patterning wire geometries on Si include photolithography, electron-beam lithography, focused ion beam, and nano-lithography using scanning tunneling microscope tips or atomic force microscope tips. Application of these technologies is a trade-off between design flexibility and productivity.

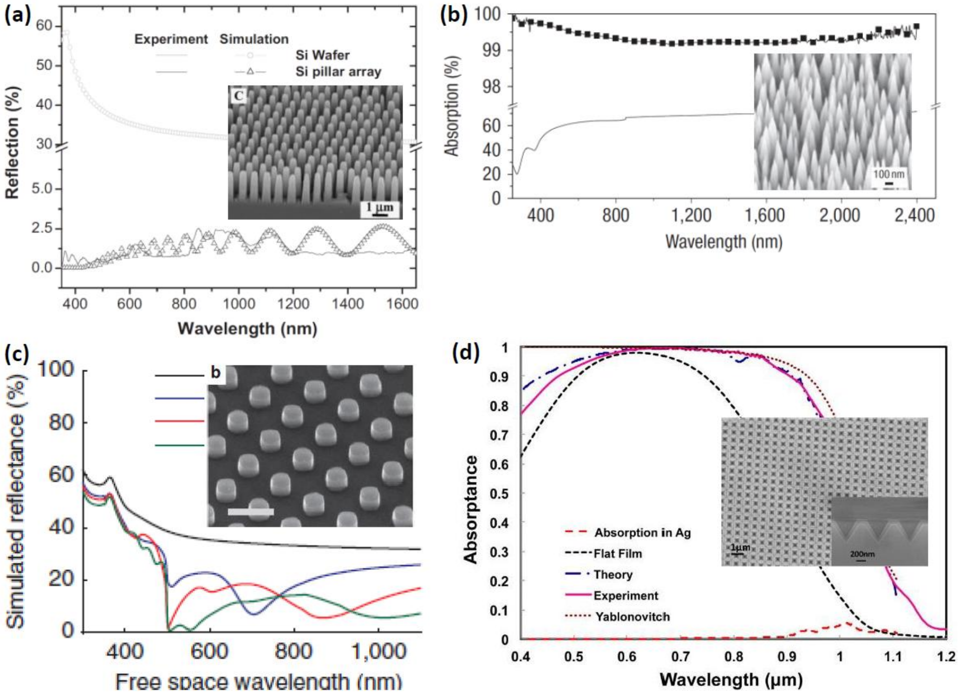

Figure 3. Surface textures on single crystal Si for reduced reflection and enhanced absorption. (a) nanopillar from dry-etching through a self-organized silica sphere masks[41] (copy right Wiley), (b) nanotip from plasma etching[44] (copy right AAA Science), (c) nanopillar from sphere nanoimprinting and RIE-etching[48] (black curve: plain Si, colored curves: nanopillar array with different diameters, copy right Nature), and (d) inverted nano-pyramid from interference lithography and KOH wet etching[46] (copy right American Chemical Society). Insets show scanning electron microscopic images of the surface structure.

To demonstrate a direct comparison of the profile dependent absorption, we did a simulation based on effective refractive media theory using the transfer matrix method on textured Si substrates. Si wire arrays with two profiles of refractive index transition were compared, including a step profile typically from a cylindrical wire array and a parabolic profile from a cone-shape array (Fig.3a insets i and ii). The effective refractive index transition profile from water media (n_m=1.33) to Si substrate (n_{Si}=4.015) of these two structures at a wavelength of 570 nm are shown in Fig.4a. The effective refractive index of the cylindrical wire array (n_w) remains constant of 1.5985 with sharp transitions at the water/wire and wire/substrate interfaces (red curve in Fig.4a). However, cone-shape wire array with a parabolic profile shows (n_c)

smoothed transition at both interfaces (green curve in Fig.4b), which is recognized as the main reason of light trapping[49]. The mathematical model of n_w and n_c can be described by the two equations as below,

$$n_w = ff \times n_m + (1 - ff) \times n_{Si} \quad (4a)$$

$$n_c = n_m + (n_{Si} - n_m) \times (10t^3 - 15t^4 + 6t^5) \quad (4b)$$

where t = [0, L] and L is the wire length.

It is assumed that Si is immersed in aqueous electrolyte, all the spaces between the wires are filled with water, and n_m of water is wavelength independent. Real and imaginary of the refractive index of Si are wavelength dependent and data used in this simulation were based on a refractive index database from Filmetrics[50]. In this set of simulation, wavelength-dependent absorptions coefficient of Si as well as distinction coefficient of water (Fig.2 red curve) were not considered. Wire length and incident angle vs. wavelength of arrays with step and parabolic profile are shown in Fig.4b/c and 4d/e, respectively. It can be seen that with the increase of wire length in the cylindrical wire array, reflectance does not show much difference particularly at the wavelength below 400 nm, primarily due to the retarded absorption of Si in the UV region (Fig.4b). Resonance peaks are shifted with the increase of the wire length. The incident angle effect for the cylindrical wire array with wire length of 1 μm and fill factor of 0.5 is shown in Fig.4d. One can see that with the increase incident angle from parallel (0 degree) to near perpendicular to the wire axis (80 degree), the reflection increases over the entire spectrum. Due to the vertical orientation and considerable area of the flat tip, the reflectance is significant at the normal incident (0 degree). Similar effect was reported before on microwire arrays[42]. For the cone-shape wire array, a broadband suppression of reflectance and minimized resonance over a wide wavelength region can be reached. Reflectance can be reduced using longer wires. It can be seen that with a wire length around 1 μm, the reflectance spectrum does not change with the increase of length, indicating a minimum length requirement for effective light trapping using this cone-shape wire array structure (Fig.4c). The incident angle effect on the cone wire array with a length of 1 μm is also shown in Fig.4e. Under normal incidence (0 degree), reflectance is effectively suppressed due to the strong coupling of the light at the wire tip. Although the reflectance increases with the increasing incident angle similar to that observed on the cylindrical wire array, the broadband reduction of reflectance is realized using the cone array with a parabolic sidewall profile of n_c, which is consistent with previous results[52].

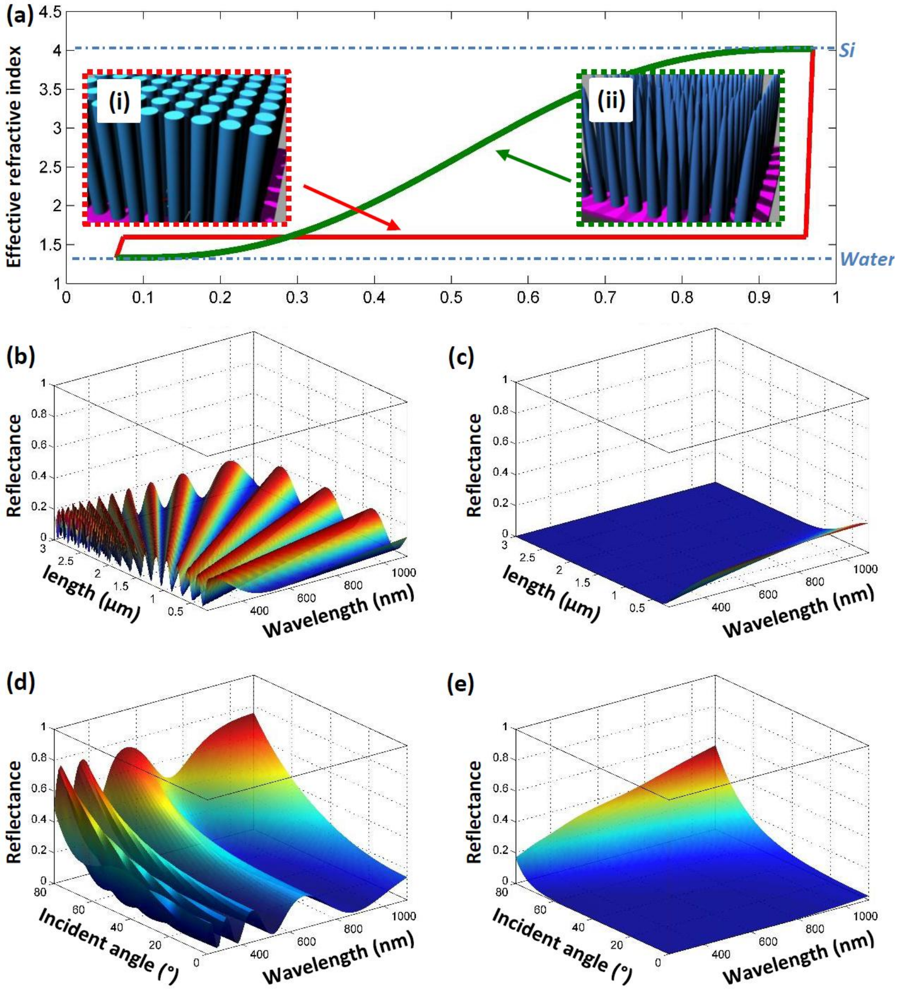

Figure 4. Comparison of cylindrical wire array (with a fill factor of 0.5) and cone array, reflectance verses wire length and incident angle. (a) Transition profiles of refractive index from water to Si substrate on wire array with step shape (ii-red) and parabolic profile (i-green) at wavelength of 570 nm. Insets show schematics of these two wire arrays. Length dependent (b and c) and incident angle dependent (d and e) reflectance spectrum over a wavelength range of 250 nm to 1100 nm.

1.3.2 Si wet etching and sub-wavelength structure:

To create textured surface on a crystal Si, a standard chemical method adopted by PV industry for surface texturing has been well established since 1960 by using a mixture of sodium/potassium hydroxide (NaOH or KOH) with water or isopropyl alcohol (IPA). This technology was well-investigated and typical surface morphology was realized from this orientation dependent etching (Fig.5a)[51]. However, KOH/NaOH-IPA solutions have some limitations[52]. Potassium and sodium are believed to contaminate the dielectrics in microelectronics as well as in optoelectronic devices which could potentially degrade the performance and stability[53]. Moreover, IPA is flammable, not cost-effective and hard for disposal, which requires searching for IPA-free alternatives. For example, the KOH/NaOH-IPA system could be replaced with TMAH water solution (tetramethyl ammonium hydroxide)[52], Na_3PO_4 water solution[54], $Na_2CO_3/NaHCO_3$ water solution[55], or hydrazine (N_2H_4) water solution[56]. Laboratory bulk Si processing to create holes and pillars are also developed based on the gas phase etching, which is known as dry etching[57], such as reactive ion etching[41] and ultrafast laser texturing[59]. Both wet etching and dry etching techniques can be controlled anisotropically as well as isotropically to create surface textures on Si. Although dry etching has been proposed and investigated, wet etching using chemical solutions remains as a cost-effective method for mass-productions. It should be noted that the success of wet chemical texturing depends on orientation dependent etch rate, which indicates a limited application to poly-crystal or amorphous Si. Surface textures on these materials normally relies on the drying etching (Fig.5d) or directly using textured conductive substrates (ZnO:Al or stainless steel) particularly for tandem/multijunction amorphous Si solar cells.

As discussed in the section 2.2, Si photoelectrochemical oxidation is one of the most critical issues to overcome in photoelectrochemical devices to ensure a durable lifetime.

However, when this instability-related phenomenon is in a good control, it can be of extreme potential to produce highly ordered surface textures. Porous Si fabricated from photoelectrochemical etching was first introduced in the 50's when an electrochemical polishing experiment was carried out at Bell labs[59]. Electrochemical etching of p-Si in the dark and n-Si under light illumination in fluoride-contained electrolyte is typically used to dissolve the oxidized Si from the energetic holes and porous Si can be formed with anodic current less than the critical current density. In addition, morphology of pores can be further controlled by adjustable parameters such as HF concentration, pH value, electrolyte temperature, Si dopant concentration, Si crystal orientation, and illumination density[58]. Photoelectrochemical method is recognized to be most cost-effective for porous Si fabrication with a high controllability for various applications such as reflector, waveguide, photonic crystals, antireflection coating, and sensors. An important early review paper about the porous Si forming mechanism was reported by Smith and Collins in 1992 providing a close-look at the formation models[59].

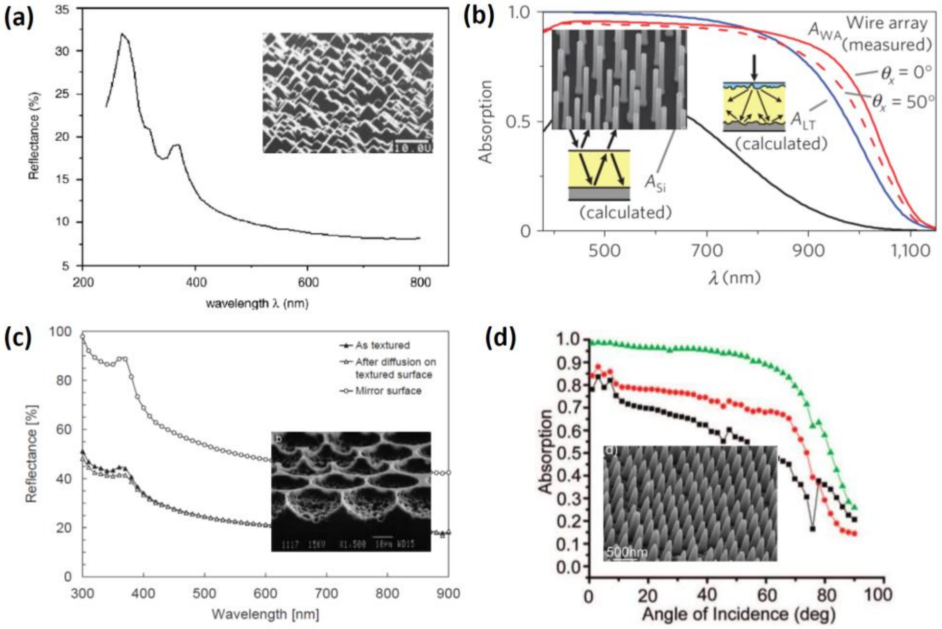

Figure 5. (a) Micro pyramid from alkaline wet etching of (100) Si[54] (copy right Elsevier), (b) randomized Si microwire array fabricated from chemical vapor deposition[42] (copy right Nature), (c) hierarchical microhole array from patterned dry etching using ClF_3 gas[60] (copy right Elsevier), and (d) nanosphere patterned and RIE-etched textures on amorphous Si[61] (copy right American Chemical Society). Insets show scanning electron microscopic images of structures.

Metal assisted chemical etching or so called electroless etching was proposed by Zhu's group[62]. Large area textured Si can be fabricated from ionic metal HF solution containing Ag, Fe, Ni and etc[63] without external anodic bias or light illumination. This mechanism fully relies on the localized micro-electrochemical redox reaction process. Later, to investigate the fundamental mechanism, researchers from the same group used two-step etching. Metal nanoparticles (NPs) were first electrodeposited by dipping Si substrate in metal ion-contained HF solution. Then, metal NPs coated Si substrates were continuously etched in Fe^{3+}-HF solution[65]. In this etching scheme, Fe^{3+} works as an oxidizing agent for Si. Metal ions in the etchant can be substituted by H_2O_2[65] and other oxidants[64]. A recent review covering different aspects in metal assisted etching of Si can be found in ref [64]. To reach a better anti-reflection effect, post alkaline etching in diluted KOH was proposed to generate tapered Si nanowires tips following the two-step electroless etching method as described above[65].

All the techniques briefly mentioned above are applicable for lithography-free, maskless and low-cost surface texturing of Si. In these cases, exact position of Ag nanoparticles where Si is etched catalytically, is self-oriented and spontaneous. Therefore, textures directly patterned from these methods are random. To define a regular array of either holes or pillars on the Si surface with spatial ordering and diameter uniformity, one can use patterning techniques such as lithography and nano-imprinting to define metal masks either by electrochemical or gas phase deposition. In addition, one can also use self-assembled polystyrene beads lithography (Fig.4a and c)[66], anodic aluminium oxide (AAO) film as a mask[68], interferometric lithography (Fig.3d)[46], block co-polymer lithography[67], and stamping/nano-imprinting[68].

Anodically etched n- and p-Si have been studied for photoanode and photocathode applications by Koshida et al[69]. With the increased thickness of the porous layer from 8 to 57 μm, photo-sensitivity (defined as the ratio between saturation current and light intensity) and the quantum efficiency (obtained at 632nm laser 1W power) were both decreased (Fig.6b). Further spectral response study revealed that the reduced sensitivity in the short (<600 nm) and long (>800 nm) wavelength region with the increased thickness of porous layer was due to the enhanced surface recombination rate of photogenerated carriers (Fig.6a). Interestingly, porous structure in p-Si demonstrated suppressed dark current when compared to the polished Si electrode. However, stability study revealed a certain degree of dissolution of porous layer, which resulted in increased dark current after long-term operation. Mechanism for this dissolution was related to the out-diffusion of holes under illumination. Similar nanoporous structure was recently studied and similar results were reported[70]. It was shown that onset potential for H_2 evolution was anodic shifted on the black Si photocathode (Fig. 6c). This surface area-induced anodic shift was presumably due to the catalytic activity of metal impurities in porous Si and the increased number of reaction sites for H_2 production. Poor spectral response of the nanoporous black Si at short wavelengths was likely due to the high surface recombination originating from increased surface area and/or recombination at Au impurities. This loss of blue response suggests that the maximum H_2 production rate might actually decrease even further if effective surface area of the nanostructured electrode is increased. This observation drew a conclusion similar to Koshida's studies[69]. Increased surface area induced by nanoporous structure also increased the bubble nucleation density and led to an increase in the hydrophilicity of the nanostructured surface[69], which could maximize the gas evolution and minimize the current fluctuation. Oh et al. used really long Si nanowires of 20 um in length also from chemical etching process and then decorated with Pt nanoparticles[71]. They demonstrated an anodic turn on voltage at -0.42 V vs. RHE and 17 mA/cm^2 at 0 V vs. RHE in H_2SO_4 and 0.5 M K_2SO_4 solution (pH=1). Author also noticed degradation of photocathode when biased at positive bias in dark, suggesting a protective coating on this photocathode when in idle conditions.

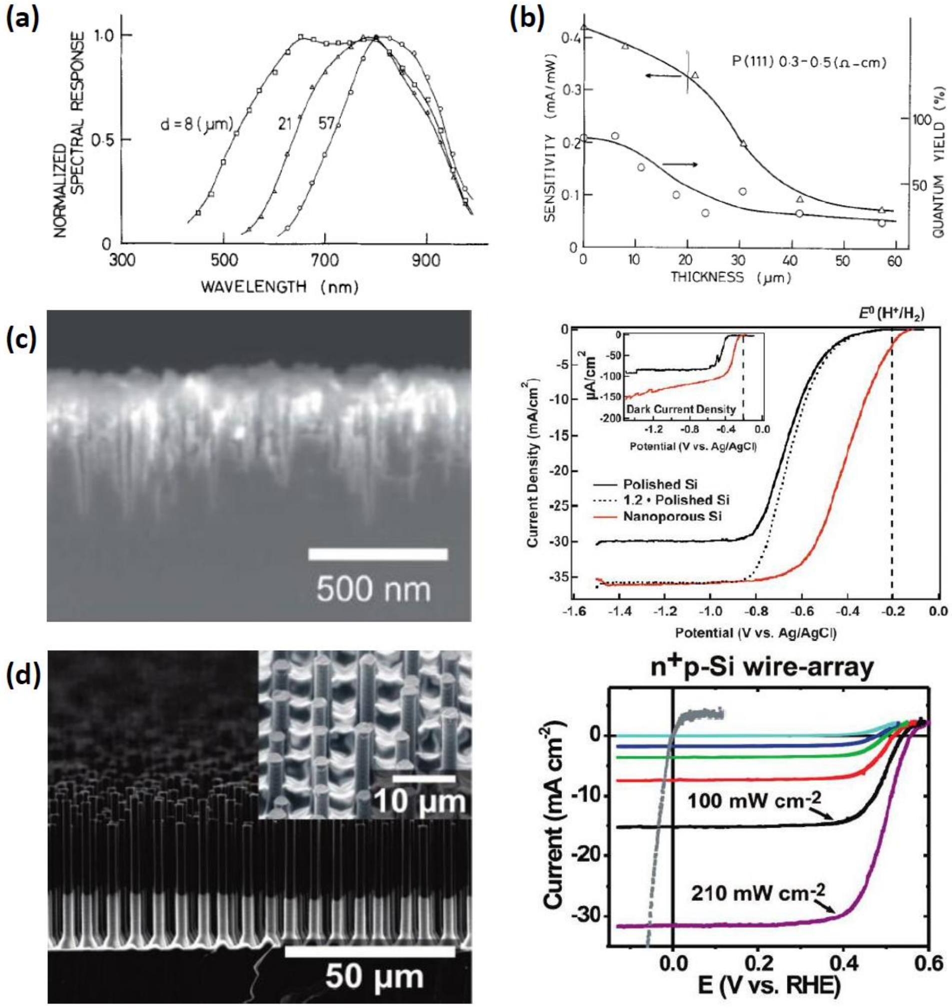

Figure 6. Bare p-Si photocathode with sub-wavelength and microwire surface structures. (a) decreased spectral response in short as well as long wavelength on samples with thicker porous layer, (b) reduced quantum yield with the increased porous Si thickness[69] (a and b, copy right Electrochemical Society), (c) electrochemically etched black Si (left) and its photocathodic behavior (right)[70] (copy right Royal Society of Chemistry), and (d) p-core/n$^+$-shell Si microwire photocathode (left) and its polarization curves under different light intensity (right)[72] (copy right American Chemical Society).

On the other hand, it has been pointed out that using porous n-Si as a photoanode can improve the long term stability operation with no significant irreversible reaction noticed[73] and can also improve the efficiency[74]. Prolonged lifetime of nanoporous n-Si photoanode was realized without additional protective coating or catalytic treatment in aqueous electrolyte containing 0.01 M Na_2HPO_4. It was also shown that the onset potential was cathodic shifted for the porous Si which led to an improved water oxidation efficiency. Although the photoanode remained alive over a longer period, the stability is still far from that required for practical use. As the goal of photoelectrode lifetime by the Department of Energy (DOE) is 1000 hrs by 2015, further improvement is in great need.

The capacitance and impedance analysis can be used to reveal the importance of the surface states density to photoelectrode performance. A recent study compared the difference of the surface states density on chemically etched and gas-phase grown Si nanowires[75]. The capacitance of surface states with nearly 2 orders of magnitude higher was noticed on Si nanowires from gas phase growth, leading to the inferior energy conversion efficiency in comparison with the chemical etched ones. This extremely high surface state density was actually recognized as the major reason for the loss of photovoltage and photocurrent in nanostructure compared to their planar counterpart. Meanwhile, finite element study revealed pathways for carrier recombination, providing a guidance to the advanced nanostructured design of photoelectrodes for solar fuel conversion[76].

1.3.3 Microwire array

Microscale Si wires are developed to avoid complete depletion as commonly noticed in sub-wavelength nanostructures and to achieve efficient carrier collection,[77] with wire diameter similar to the minority carrier diffusion length. Light trapping in Si microwire array was studied experimentally (Fig.5d)[42] and computationally[78] based on Ray optics, for the significantly larger size of wires compared to wavelength. This is quite different from the sub-wavelength nanoscale structures, in which wave optics dominates. Fabrication of Si microwire array relies on the vapor-liquid-solid (VLS) mechanism[79], and Si microwire can be also obtained through top-down wet etching or dry etching from proper masked planar Si substrates. For example, metal Cu islands were patterned and confined in a thermal Si oxide film (300-nm thickness), which acted as the guidance for vertical wire growth. P-type doping in Si wire was realized by controlling the BCl_3 concentration in the reactive gas on p^+-Si substrate, which did not contribute to the photoresponse due to lack of photo-activity. Majority carrier concentration *ca,* 7×10^{17} cm^{-3} showed optimum photoelectrochemical energy conversion performance, presumably due to the wire geometry, redox chemical potential, and thus the optimized junction energetics. As-grown wires were then chemically treated to remove Cu, Cu contaminants near Si wire surface, and native oxides developed during growth. Later on, modified system using a cold-wall process and rectangular quartz tube (holding 6 inch wafer) provided predictable growth over large area[80], showing a potentially commercializable technique.

This microwire structure has successfully demonstrated outstanding photovoltaics performance than nanostructure based devices with similar core-shell geometry[38,81]. Radial solid-state p-n junction can be formed by thermal diffusion of a solid source, which results in a shallow diffusion profile in Si microwire. 200-nm junction depth was realized on a planar control sample with a background concentration (N_D) of 2.2×10^{16} cm^{-3}, which was more than 1 order of magnitude lower than that of the wire configuration (7×10^{17} cm^{-3}). Theoretically, because of the higher N_D, the junction depth should be shallower on the microwire considering the identical processing temperature and drive-in time, assuming the microwire structure does not cause disturbance and difference in diffusion process. Nonetheless, p-base in microwire was still more than 7 times larger in length than the n^+-emitter. Wire diameter (2.8 μm) was much smaller than the minority diffusion length (>30 μm). Therefore, this structure can be considered as a narrow base emitter. As-grown Si microwire arrays were tested and reduced V_{OC} and significantly lower J_{SC} compared to the planar control were noticed (Fig.6d). However, this J_{SC} value was larger considering the low filling factor (~12.6%) of the wire array with respect to the optical plane. This was primarily owed to the efficient light management in wire geometry and large surface area[72].

Photoelectrochemical cells using p- and n-Si microwires in organic electrolyte have been demonstrated[29,80,82]. Si microwire decorated with high performance electrocatalysts and heterostructures using Si microwire array as a platform for solar fuel production have been reported. All these, together with effects of surface inversion and metal catalyst coating will be discussed in later sections.

Besides aforementioned gas phase growth of Si to eliminate the use of high cost crystal Si, researches are continued by searching for other cost-effective alternatives to produce Si photoelectrodes. Very recently, Cho et al. explored the electrodeposition of Si for photoelectrodes applications[83]. The electrodeposition of Si was realized from a direct electroreduction of SiO_2 in a $CaCl_2$ melt under a constant bias at high temperature. The p-type photoresponse of the Si was believed due to the incorporation of catalyst Ag during the electrodeposition. A comparable photoresponse to crystal p-Si was realized. However, a sharp drop of photocurrent was noticed due to the surface recombination at the Ag.

1.4 Modification of interfacial energetics

The focus on Si based materials for photoelectrochemical solar fuel conversion is to alter surface kinetics to reduce the current efficiency for the growth of insulating SiO_2[33] and to improve the current efficiency for the net interfacial decomposition of water[21]. In addition to the surface texturing as discussed in the previous section where considerable success has been achieved in terms of improved photoelectrode efficiency and stability, one can also introduce a heterogeneous coating on the Si surface for these purposes. General criteria for selecting surface coating to modify the interfacial energetics include, (1) this coating should be a pin-hole free film, particularly important for n-Si; (2) this film should offer minimum light reflection and absorption resulting in a majority light absorption at the Si; and (3) this film should be also capable of driving photo-induced charges efficiently to the electrolyte for water oxidation or reduction with minimum self-reduction or -oxidation.

In a Si|coating|electrolyte (S/C/E) system, **photo-electro-chemistry** involves a number of different processes: light absorption in Si (**photo**), charge separation/transport in Si photoelectrode, charge transfer across the Si/coating (S/C) interface, charge transport through the coating (**electro**), charge transfer at the coating/electrolyte (C/E) interface, mass transport and reaction in the electrolyte solution (**chemistry**)[19]. To simplify the analysis, the following assumptions are normally considered valid. For example, work function, position of conduction and valence band edges of semiconductors are not changed during interaction with redox and aqueous electrolyte. Also the possibility for the formation of intermediate compounds at the junction creating additional barriers or the surface states is small[84]. However, study on such a heterogeneous system is not an easy task even with all the valid assumptions. One still needs to consider consequential changes and practical issues involved in this multiphysics process, for example, potential distribution across the multiple junctions, interfacial states at S/C, doping modification between coating and underneath Si during preparation, electrical/optical loss in the coating and interfaces, photoresponse and band bending at the C/E interface, and chemical stability. Last but not the least, one may also consider the morphology and inherent properties of the film, such as ionic/covalent (non-uniqueness of surface atoms in ionic solid was pointed out before[85]) and hydrophobic/hydrophilic nature.

It is worth to point out that the S/C interface is very critical, as spontaneous oxidation of Si occurs at room temperature resulting in the formation of a native oxide on the Si surface. Removing native oxide using HF or buffered oxide etching (BOE) prior to coating process leads to a formation of stable hydride-terminated Si (H-Si), which is known as one of the best surfaces with low recombination velocity[86]. However, it was suggested that the native oxide at the S/C interface is not necessarily to prevent[86, 87], considering some advantages that this intermediate native oxide layer between heterogeneous coating and underneath Si provides:

1) the native oxide provides a smooth transition from the semiconductor substrate to the overlying coating and minimizes problems related to high interface state densities caused by mismatch in lattice constants, expansion coefficients, and other geometric factors;

2) the native oxide reduces the leakage (diode) current generated by the flow of majority carriers in the opposite direction and thus improves the V_{oc} relative to an abrupt S/C junction; and most importantly,

3) e^-/h^+ direct tunneling (normally ~3 nm in thickness) is effective[87].

In this section, we will review important research efforts on surface coating and several related techniques to enable Si for solar fuel production.

1.4.1 Metal, metal alloy, silicide and 1D/2D carbon

It is believed that metal coating, particularly noble metals, provides the most complicated modification to semiconductor properties due to unique shape-, size-, cyrstallanity-, chemical position-, and environment-dependent optical (Fig. 7a), physical (Fig. 7b), and chemical (Fig. 7c) characteristics, such as surface plasmon resonance, scattering/anti-reflection, hot carrier injection, energy band bending, electrocatalytic effect, modification of substrate doping, and more. Although some of these effects have not been demonstrated on Si and even photoelectrochemistry yet, these scientific findings certainly will develop new understandings and trigger innovative ideas for efficient artificial photosynthesis and solar fuel production in the foreseen future.

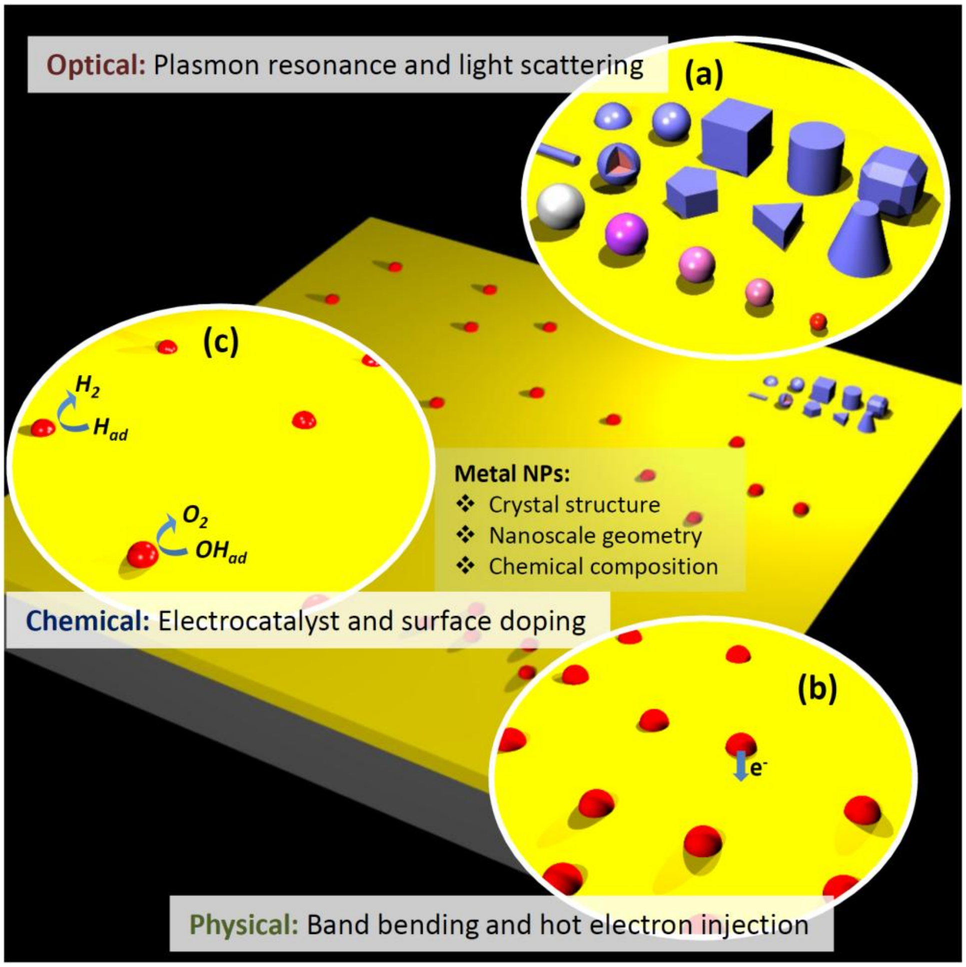

Figure 7. Modulation of metal nanoparticles on a photoactive substrate: (a) optical effect of plasmon resonance and nanoparticle light scattering, (b) physical effect of surface recombination and hot electron injection, and (c) chemical effect of catalytic effect and surface doping modulation. All these effects depend greatly on crystal orientation, nanostructure geometry, and chemical composition of nanoparticles.

Noble metal: Several noble metals including Pd[85], and Pt[88] are used to coat Si in the early development stage of Si photoelectrodes, as well as other photocatalysts[86]. Regarding the thermodynmic and kinetic problems of Si, metal coating is initially proposed to suppress the photocorrosion of n-Si and to catalyze H_2 evolution on p-Si. A thin layer of metal and the formed Schottky junction are desired to isolate Si from direct contact to oxidizing electrolyte, meanwhile to allow minimum optical loss at the reflecting/absorbing metal layer, and to provide sufficient driving force for photo-induced carriers[89]. The barrier height of metal/Si junction is ideally controlled by the difference between the Fermi level of Si and the work function of the metal.

Therefore, in addition to the excellent catalytic activity, the barrier height is also important in the selection of metal coating while considering the semiconductor Fermi level. Surface recombination becomes significant on metal coated Si, resulting in reduced quasi-Fermi level separation, reduced carrier concentration at the surface, and thus low photovoltage. This surface recombination is believed to occur due to the metal-induced gap states[88]. Therefore, in order to reach the most effective potential barrier for charge generation and separation at the S/E interface, sparse nanoparticles with in-between spaces filled with thick passivation SiO_2 could be introduced to replace uniform metal film[90]. In this case, the loss of photovoltage and the loss of light intensity reaching Si depletion region could be minimized, thus photocurrent could be effectively enhanced. Therefore, metal decoration in forms of nanoparticles is necessary to maximize light absorption and photovoltage in Si, while to provide large surface area for catalytic reactions. Actually, the catalytic performance is also very sensitive to the size, orientation and density of nanoparticle coating[91].

Ru, Ir and their oxides are known as the best OER catalysts[89]. Ru metal and oxides from electron beam evaporation and spray method were applied on Si photoanode before by Tsubomura et al[92]. Ru electrocatalysts minimized the high resistance loss at the S/E interface with a reduced Tafel slope at the onset potential region. Ir metal with a thickness of only 3 nm from physical vapor deposition was coated on n-Si photoanode to catalyze OER reaction[93]. Recently, a study on the intrinsic catalytic activity of Ru, Ir, and Pt nanoparticles was presented by Reier et al[94]. In this study, the catalytic activity and stability of carbon supported nanoparticles and bulk materials were studied and compared. Pt showed the lowest OER activity and complete deactivation and Ru showed the highest activity, but strong corrosion and deactivation. Ir nanoparticles showed high OER activity comparable to Ru, and extended lifetime. This study provided insights on the selection of durable nanoscale OER catalysts that could significantly reduce the use of expensive bulk materials.

To lower the amount of precious metal usage using Pt as an example, while maintaining the outstanding electrocatalytic activity[95], monolayer of alloy[96] (Fig.8a), mesoporous film[97] (Fig.8b), controlled surface orientation/cyrstallanity (Fig.8c), and low cost material supported structure (Fig.8d)[98] with large surface area are of potential interest towards developing of highly active, stable, and cheap electrocatalysts. Major concern on nanoparticle or other types of high surface area metal coating is the potential failure of underneath Si photoelectrode in the working/idle condition due to the porosity in the metal layer and (photo)anodic attack at the surface of Si through the pores[90]. Thus, strategies to satisfy both requirements for both durability of both underneath Si and metal coating, large surface area and thus reaction sites are highly desired.

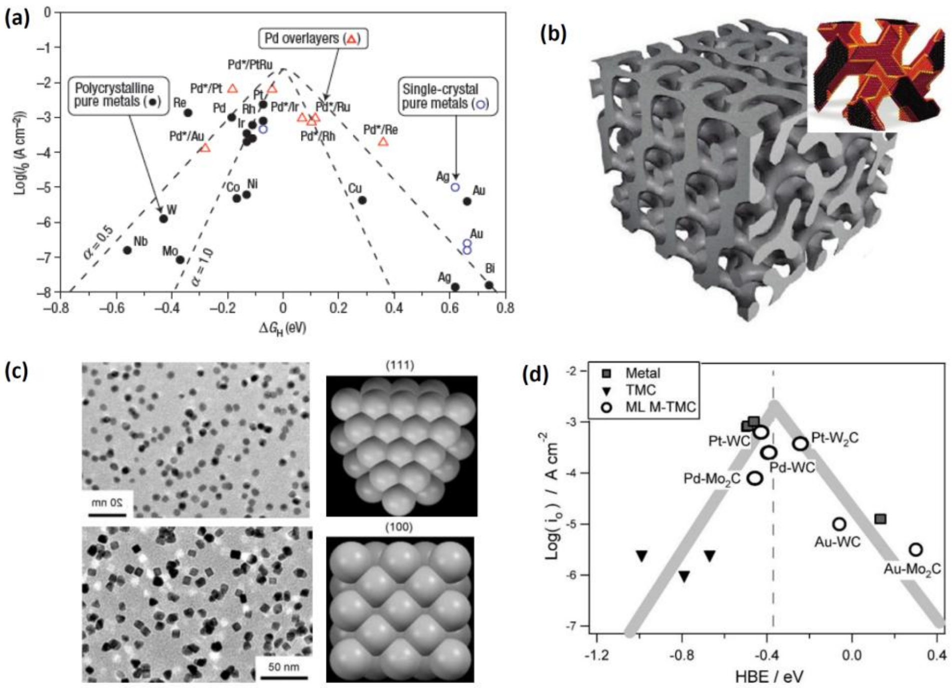

Figure 8. (a) monolayer of Pt[96] (copy right AAA Science), (b) mesoporous Pt[97a] (copy right American Chemical Society), (c) Pt nanoparticles with different size and shape[99] (copy right Wiley), and (d) transition metal carbide supported Pt[98a] (copy right American Chemical Society)

Besides surface band bending and catalytic effects, noble metal nanoparticles are known to provide optical modulations, such as plasmon resonance, light scattering[100], and etc. Surface plasmon resonance of metal nanoparticles, particularly Ag and Au, for improved light absorption was introduced for photovoltaics and photodetectors[101]. For photoelectrochemical devices, this effect is firstly introduced in TiO_2 photocatalyst to enhance visible light absorption[102]. Later study also demonstrated plasmon enhanced photocatalytic effect on Fe_2O_3[103] and WO_3[104] using Au or Ag nanoparticles. A review on this research topic was reported recently, which provides a thorough survey of the plasmonic photoelectrochemical cell[105]. The first application of core-shell metal nanoparticles (Au particles coated with Pt shell) and investigation of plasmon enhanced Si photocathode based on this core-shell particle were demonstrated recently by Lublow et al[106]. The authors found that this configuration, depending on the Pt shell thickness, could provide enhanced light absorption up to 20% in the wavelength above 600 nm with slight loss of absorption below 600 nm.

Besides effects discussed above, hot electron/hole injection[107] and light scattering[108] from noble metal nanoparticles could also provide additional enhancement to photoelectrochemical devices. However, to the best of our knowledge, there is no demonstration of hot carrier effect from metal nanoparticles on small band gap materials based photoelectrochemical devices like Si yet. Identification of contributions from each of these effects listed above is controversial and certainly is not an easy task[109], which still requires a continuous development of fundamental studies in respected areas.

Non-noble metal, alloy and doping: The fundamental reason of superior catalytic behavior from transition metals over non-transition metal is mainly due to the vacant d-orbital which acts as both the bonding and adsorptive orbitals for intermediates. Additional effect from electronic density defines the overall kinetics and reaction rates[110]. Normally, earth abundant materials containing elements from the first row of group 8, 9 and 10 are earth abundant materials, which are widely used in industry-scale electrolysis. Ni or Ni coated metal is wide used in commercial electrolyzer as a cathode due to its chemical stability. Its kinetics in the HER catalytic reaction were also studied[111]. Raney-Ni, a Ni alloy with porous structure, has showed a low HER overpotential than Ni. Nickel nanoparticles normally come from the reduction of metal salt in solution[112] or gas phase[113]. Nanoparticle dimension and crystal orientation have to be controlled for optimized activity. Nanoparticles with high active surface areas have been extensively demonstrated as effective HER catalysts with activities comparable to Pt. For example, Yamada et al. reported that Ni nanoparticles with different size and crystal structure have been synthesized and studied as a HER catalyst[112]. It was observed that Ni nanoparticles with hexagonal close-packed structure and smaller sizes were more active than those with face-centered cubic structure and greater size. Ni nanoparticles showed significant higher catalytic activity than other metals including Fe, Co, and Cu. Based on a theoretical study, Ni metal showed the highest exchange current compared to other first row transition metals[110a], similar trends for exchange current density and potential were also observed on the other two group 10 elements among other elements in the same row (Fig.9).

Ni-contained metal alloys have also been developed to obtain improved catalytic activity. Majority researches are focused on alloying Ni with other low-cost transition metals, such as Mo, Fe, Co, Cu and Zn, as well as adding small amount of platinum group metals, like Rh, Pt, and Pd. These alloys are typically formed on conductive substrates through electrodeposition in a mixture bath containing Ni and other metal salts at low temperature, in which the composition is simply controlled by the ratio between the metals in the mixed solution. For example, NiMo alloy can be electrochemically deposited on Si surface in an acidic bath[114] to avoid instability of Si and improve adhesion between NiMo and Si. Ni/Mo ratio is controlled by the concentration of Mo-contained salt in Ni plating solution. Results showed that the increased Mo concentration caused poor adhesion and lower HER catalytic activity than the pure Ni metal catalyst, which was similar to previously observed results[115]. Importantly, proper cathodic current density during electrochemical deposition is essential to obtain more active NiMo catalysts with high surface area. However, large surface area of NiMo does not necessarily enhance the energy conversion efficiency of Si photocathode due to the lower photovoltage between NiMo and Si compared to that between Ni and Si. Fe can be another additive to Ni for enhanced HER activity. For example, Carvalho et al. has demonstrated that NiFe electrocatalyst in the form of micron size clusters co-deposited from electrochemical method exhibited high activity and maintained operational for more than 1000 hrs[116]. Meanwhile, Co, Fe and their metal mixtures were also used as HER catalyst alternatives. For example, CoMo has been fabricated through electrodeposition[117] and sputtering[118]. As a HER catalyst, CoMo showed the lowest overpotential compared to other binary metal alloys, such as NiMo, NiW and CoW[117]. Co metal also showed higher OER[119] activity than other noble metal such as Au and Pt[120].

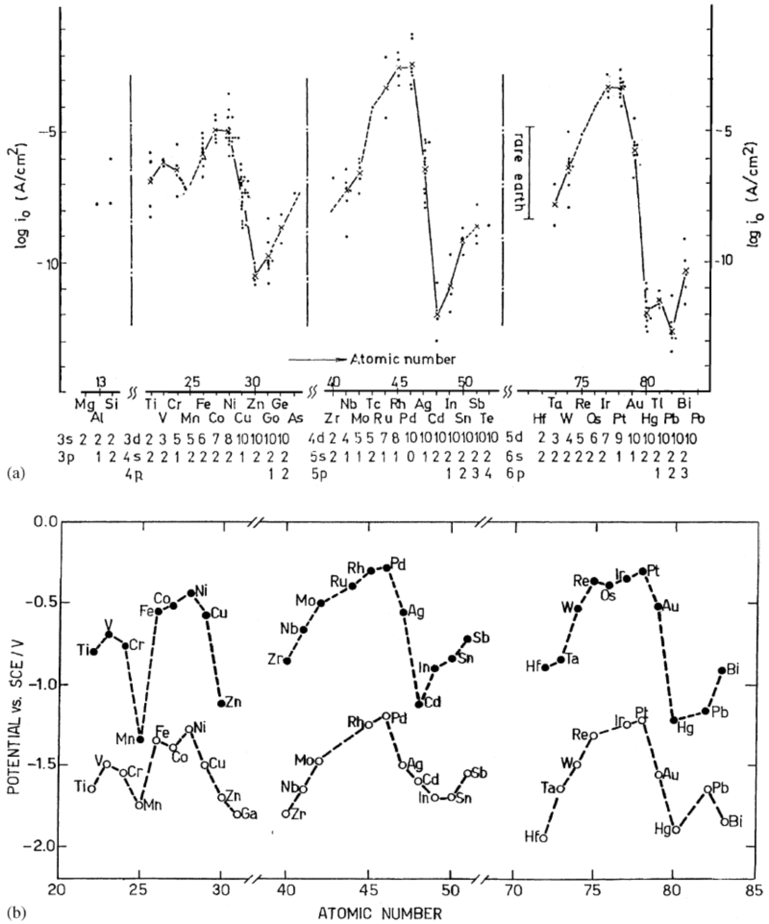

Figure 9. (a) exchange current density and (b) potential verses atomic numbers (copy right)[110b]

Techniques have been developed to combine superior catalytic activity with enhanced surface area by introducing a third metal, which can be (partially) etched, resulting in a porous structure with beneficial catalytic activity. Zn and Cu, as sacrificial components, are typically used. Giz et al., for example, fabricated ternary NiZnFe from electrochemical deposition and subsequently removed Zn partially in concentrated alkaline solution to obtain porous NiFe alloy[121]. Recently, He et al. synthesized mesoporous Si/SiO_2 nanorods array by selectively etching Cu in the Cu-Si/SiO_2 composite[122]. Silica or alumina can be used as a template for fabricating mesoporous or freestanding wire array structure. The oxide template can be simply etched by acid and provide enhanced active surface area[123]. As a third component, carbon is also widely used in alloy HER metal catalyst to enhance charge transfer between metal ions. For example, carbon has been introduced to NiFe[124], CoFe[125], NiCoFe[126] alloy and more. In these work, effects of additive carbon on the activity and durability have been investigated. Results showed that carbon can effectively prevent the corrosion and dissolution of Fe and thus can maintain the activity.

Electrochemical activation is generally used to treat the coated electrode for improved catalytic activity through the modification of active sites under a constant bias[127] or cyclic sweep in a bias range[128]. Additives can be introduced during this post activation process. For example, a small amount of Pd was added during the post activation of Ni nanoparticles to form $Ni_{99}Pd_1$, which successfully showed enhanced activity over non-activated sample[129]. Finally, it should be noted that anodic bias applied on the metal-coated photoanode could introduce competition between metal and water oxidation, due to the typically lower oxidation potentials of metal than the oxygen evolution level. In this case, one should consider the oxidation current of metal together with water oxidation current. This is important when reporting the ultimate water oxidation efficiency based on current density values.

Moreover, novel structure using graphene as a supporting material for electrocatalysts has demonstrated enhanced activity in OER and ORR. Particularly for HER, Agegnehu et al. recently demonstrated that Ni nanoparticles/graphene composite showed improved H_2 evolution activity due to the facile electron transfer from graphene to Ni catalyst[130].

Surface inversion: Surface inversion of Si at the S/E interface was introduced in our previous sections. This approach can effectively unpin the Si surface and regain the control of the Si band edge position and most importantly the energy barrier height. This idea has been demonstrated on n-Si photoanode[131] and on p-Si photocathode[29,132], through a doping of group III (B, Al, and In) and V (P) elements, respectively. It was realized by solid source diffusion at high temperature in inert environment. This modification of surface doping could elongate lifetime of n-Si at certain level due to the downward band bending at the S/E interface, which is effective to confine energetic holes away from S/E interface. Further conversion of the p-type surface to p^+ could thinner the barrier and enhance the hole tunneling. PtSi coated surface inverted n-Si showed stable photoresponse for over 4500 hrs in electrolyte containing I_2/I^- redox couples[131b]. Enhanced photovoltage could be also realized utilizing this simple surface inversion strategy[29].

Transition metal silicide: Transition metals could form silicides that are metallic and chemically resistive. Noble metal silicide such as PtSi[33,133] and IrSi[134] are formed on Si through metal deposition (4 nm in thickness) and subsequent thermal annealing in vacuum. Silicide coated n-Si showed extensively improved stability than naked n-Si, and no significant reduction of photocurrent in aqueous solution over 20 days discontinuous measurement was noticed[33]. IrSi showed improved photoanodic response. However, slow degradation was also noticed over long time study. It was shown that adding RuO_2 on IrSi could further improve the long-term stability. However, RuO_2 coating did not change the voltammetric behavior of the n-Si|IrSi electrodes, presumably due to the outstanding OER catalytic behavior from Ir metal. In this study, it was shown that over 7 days test, electrode showed no significant degradation of photocurrent from n-

Si|SiIr|RuO$_2$, while the photocurrent dropped below half of the initial value in 3 hrs without RuO$_2$ coating.

Metallic CNT and graphene: Graphene and carbon nanotubes (CNT) have received a lot of attention in various fields[135]. Researchers also demonstrated application of these materials on Si photoelectrode to enhance its photoelectrochemical performances. Particularly, graphene with extremely high optical transmittance and electron mobility could be applied to Si surface to suppress reflection and enhance the surface charge transfer kinetics[136]. Investigations on graphene decorated ITO glass showed improved cathodic current and negatively shifted on-set potential, indicating the HER catalytic effect of graphene. However, since graphene was applied to substrate through electrophoresis, the graphene multilayer (4-6 layers) coated porous p-Si photocathode showed instable performance due to the mechanical adhesion. Carbon based materials, like black carbon, carbon nanotube (CNT), and graphene, provide potentials for scalability and low-cost to replace precious-metal ORR electrocatalysts in fuel cells. However, previous research showed insufficient activity and low stability of CNT ORR catalyst. Fe and N doped CNT/graphene complexes proposed by Li and co-workers have demonstrated good ORR catalytic activity[137]. Recent work also showed great potential of doping of group III and V elements to enhance the activity of carbon based ORR catalyst[138]. Although this structure has not been demonstrated as a HER catalyst yet, this is of great potential in the future. Similar to metal coating, this carbon-based approach requires a Schottky junction between graphene or CNT and Si. Later research actually showed excellent energy barriers. For example, Miao et al. showed a barrier height of 0.89 eV between single layer graphene and n-Si[139]. Recently Li et al. showed chemical modulation on the graphene work function to tune the barrier height between graphene and n-Si[140]. Tune and co-workers measured a 0.4 eV barrier height between CNT and n-Si[141]. Yang et al. showed that a single layer doped graphene from chemical vapor deposition (CVD) formed a Schottky junction on p- and n-Si with a barrier height of 0.45 eV[142]. Therefore, tuning the dopant into graphene and CNT, as well as the interface between graphene/CNT to Si could be a potentially attractive surface modification approach in addition to metal coatings. Moreover, unlike metal Schottky junction to Si, light arriving at the graphene (CNT)/Si interface in this strategy is improved.

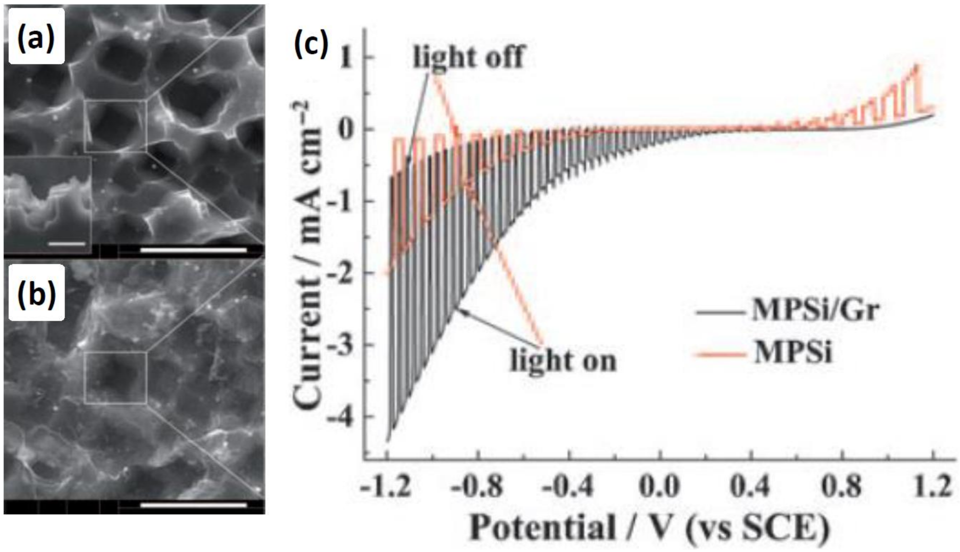

Figure 10. Multilayer graphene enabled porous p-Si photocathode before (a) and after (b) graphene coating, and (c) polarization study in 0.01 M Na_2SO_4[136] (copy right of Wiley)

1.4.2 Compound semiconductor

This section is focused on heterogeneous coatings on Si using semiconductors. Based on the properties of the coating, this section is categorized into three parts, including coatings a) that are stable non-degenerately doped semiconductors with photocatalytic properties, b) that are degenerately doped semiconductors with no significant photosensitivity or electrocatalytic activity, and c) that are compound semiconductors containing first-row d-band transition metals, normally recognized as cost-effective electrocatalysts. One of the most important differences between type a) and b) coatings is the resistivity of the coating film. An intrinsically doped coating usually shows a moderate resistivity. When a potential is applied to an S/C electrode, a large portion of the potential drop is across the coating film considering the mildly doped Si (doping concentration 10^{15}-10^{16} cm^{-3}). This reduces the band bending and the thickness of depletion layer of Si and thus decreases the photoresponse[19]. In the low-biasing potential region, the resistance of the coating limits the charge transport through the S/C system. High resistance film also assists the accumulation of holes at the interface and slow oxidation of n-Si could present when water penetration occurs through the cracks or grain boundaries. On the other hand, the highly conductive coating film can remove photogenerated holes more rapidly from the Si surface. In this case, only a small potential drop in the low-resistance film occurs, which increases the band bending in the Si and suppresses the recombination, as compared to the highly resistive film. Finally, type c) coating, acting as a mediator or electrocatalyst, completely alters the charge transfer and reaction pathways, similar to effects offered from noble metals, but with lower material costs. Several preliminary demonstrations using this type coating on Si photoelectrode are discussed. Many other developed materials of this type with outstanding performances have not been applied to photoelectrode yet. Integration considerations and strategies will be also discussed in this section.

1.4.2.1 Non-degenerate photocatalytic semiconductor: oxide and III-V compound

Wide band gap semiconductors are normally stable and for this reason, they are selected to protect n-type photoelectrode that are unstable in aqueous solution. Non-degenerate semiconductors are also typically photoactive. The band bending in this case occurs in n-type substrates as well as in the non-degenerate photocatalyst coating at both S/C and C/E interfaces.

The first semiconductors applied to Si is TiO_2, reported by Kohl in 1977[84], a high quality n-type rutile TiO_2 thin film from chemical vapor deposition (CVD) method was deposited on p-GaAs and n-InP as well as n/p-Si. The small band gap photoelectrodes were stabilized by the stable TiO_2 with completely reproducible results and with no passivation or change in behavior for days (Fig.11a). When cracks were present, photocurrents caused by substrate dissolution at absorption wavelengths of the Si at a typically lower bias were observed. Initial demonstration of TiO_2 protected photoelectrode used a coating with a thickness of above 1 μm[143]. The results for n-type photoanode with TiO_2 on the surface showed the photo-oxidation of water could only be accomplished by the UV excitation of an electron-hole pair in this thick TiO_2 (Fig.11a inset). This was because holes excited in the n-type substrate were effectively blocked from transferring through the TiO_2 to the solution even the TiO_2 coating was partially reduced by H_2 to enhance conductivity. It was further observed that TiO_2 coating annealed at higher temperature (curve c in Fig.11b) showed improved onset behavior compared to the one deposited (curve a in Fig.11b) or annealed at lower temperature (curve b in Fig.9b). Incorporation of Ru-catalyst showed enhanced photoanodic behavior (curve d in Fig.9b). This pioneer demonstration of photoanode protection was successful and promising. However, with such a thick protection coating, photoanode exhibited a minimum utilization of solar spectrum due to the unfavorable energy band alignment and charge transfer. The same protection concept can be applied to nanostructured Si photoanode. Yang's group, for example, examined TiO_2 protected Si photoanode (Fig.11c)[144]. The charge transportation process was further clarified by the energy band analysis under filtered incident light. It is important to note that the current depended upon not only the band bending of the TiO_2 at the solution interface, but also the band bending of the substrate and TiO_2 at the heterojunctions interface. A given current corresponded to a unique band-bending situation at both junctions under a particular condition. So far, saturated photocurrent from Si photoanode protected by thick TiO_2 coating of <0.3 mA/cm^2 at ~1.23 V vs. RHE) was around 10 times smaller than that from the best TiO_2 photoanode, which is presumably due to the unfavorable interfacial recombination and two photon-to one charge process[145]. Thus, a thinner but high quality protection layer is desired. For example, Tsubomura et al. demonstrated a more promising TiO_2 coating with a thickness of 5-20 nm to protect surface inverted n-Si[92]. Different from the direct interface between TiO_2 and n-Si, the surface inversion p^+ layer eased the charge recombination. It should be noted that Nb doping in TiO_2 and heat treatment made the $TiO_2|p^+Si$ junction ohmic. Different from early results, visible light response from underneath Si in this case was maintained with a photocurrent of 26.6 mA/cm^2 (AM1 condition). TiO_2 was also used to effectively protect photocathode from cathodic reduction. For example, in the initial attempt from Kohl et al., TiO_2 coated p-Si and p-GaAs showed improved cathodic photocurrent and durability[84]. Recently, Paracchino et al, demonstrated application of this stable material with a thickness of 11 nm to stablize p-Cu_2O photocathode for elongated operation lifetime[6]. Highly doped ZnO:Al prepared using atomic layer deposition (ALD) was used as an n^+ coating before deposition of TiO_2 protection layer. In this work, photocurrent at 0 V vs. RHE reached about 5.7 mA/cm^2. Compared to bare Cu_2O photocathode which deactives in 5 mins in aqueous solution, multilayer structure protected Cu_2O showed operational lifetime of more than 20 mins in their initial attempt.

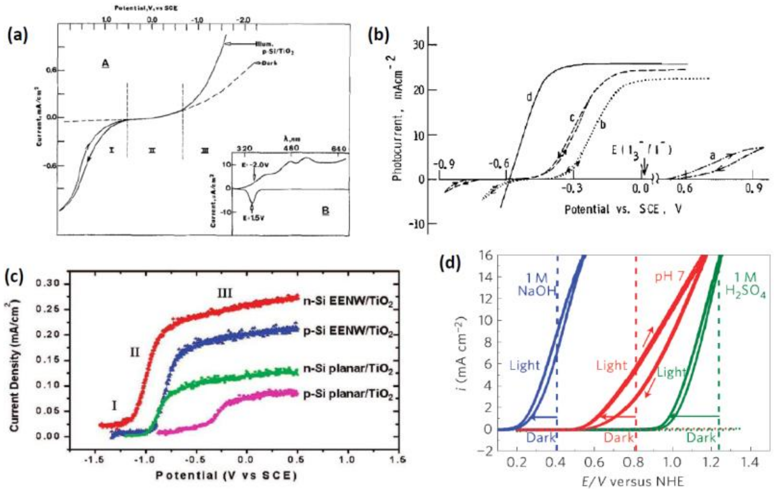

Figure 11. TiO_2 coated Si photoelectrode: a) CVD TiO_2 coated p-Si photocathode[84] (measurement was taken in 0.5 M Na_2SO_4. Inset shows the photocurrent vs. wavelength at anodic as well as cathodic bias. Copy right Journal of Electrochemical Society), b) np^+-Si photoanode[92] (measurement was taken in 7.6 M HI and 0.05 M I_2 aqueous solution. Curves shown are from samples with different TiO_2 treatment. Copy right Canadian Journal of Chemistry), c) ALD TiO_2 on n-Si and p-Si nanowire array[144] (measurement was taken 1 M KOH electrolyte, copy right American Chemical Society), and d) ALD TiO_2 coated n-Si photoanode[93] (measurement was taken in various electrolyte, copy right Nature Publishing Group)

To further overcome charge transfer problem, an ultrathin TiO_2 with a thickness around 2 nm was deposited on n-Si photoanode using ALD without removing the native oxide[93]. Similar to Tsubomura early work[92], major light absorption and carrier generation were confined in the Si photoelectrode. Majority carriers were effectively blocked by the Schottky junction, while minority carriers can still tunnel through. Extended lifetime of more than 24 hrs for protected Si photoanode compared to less than 0.5 hr for unprotected ones under working condition was demonstrated. Finally, Ir metal was deposted on the protected Si photoanode which showed the highest catalytic activity and photocurrent (>5 mA/cm^2 at 1.23 V vs. RHE, Fig.11d) compared to previously discussed results using a TiO_2 based coating.

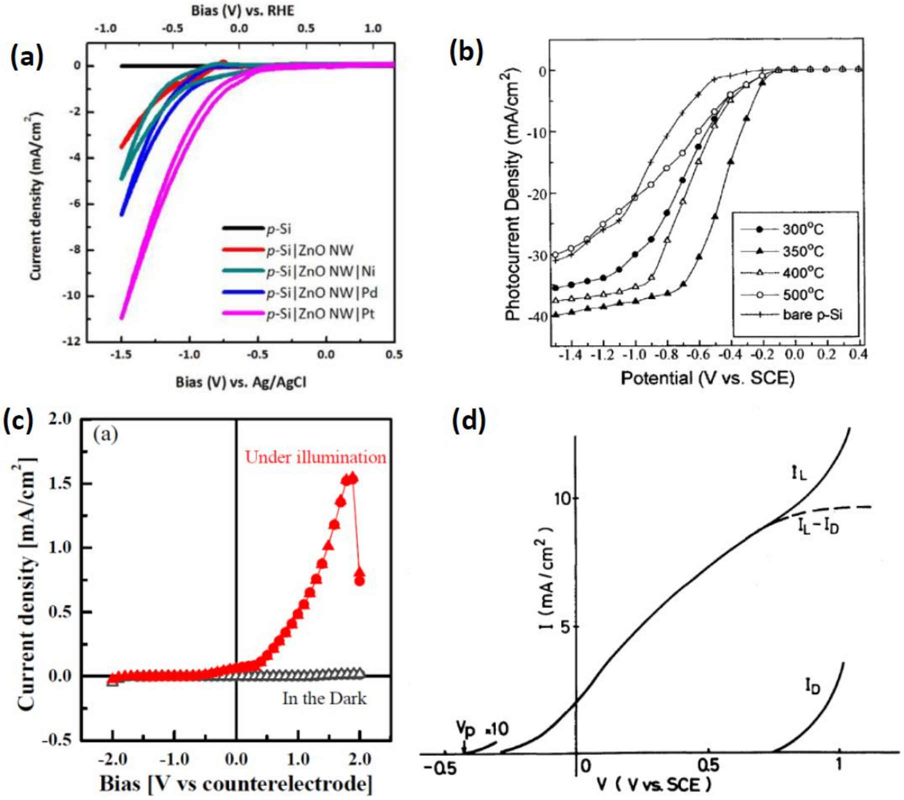

Figure 12. Other non-degenerate semiconductor coated Si photoelectrode p-Si (a and b) and n-Si (c and d)performances: a) ZnO nanowire[30] (measurement was taken in buffered 0.25 M Na_2SO_4, copy right American Institute of Physics), b) WO_3[146] (measurement was taken in 0.1 M H_2SO_4. Copy right American Institute of Physics), c) GaN nanodots[147] (measurement was taken in 1 M HCl electrolyte, copy right John Wiley and Sons), and d) Fe_2O_3[148] (measurement was taken in 0.1 M NaOH, copy right The Japan Society of Applied Physics).

ZnO (~3.1 eV), a very similar metal oxide to TiO_2, has also been studied on Si. A thin coating of ZnO from sputtering on p-Si photocathode replaced the retarded S/E interface and effectively improved the charge transfer kinetics, similar to reported work using surface inverted p-Si photocathode. Optimization of the heterojunction was conducted by altering the thickness, doping, and morphology of the ZnO coating[30,149]. Based on these results, it was concluded that despite the inferior chemical stability of ZnO, photocurrent of p-Si photocathode measured in near neutral electrolyte was enhanced due to the improved surface kinetics (Fig.12b). Similar conclusions can be found using an n-type WO_3 (~2.7 eV) to anodically shift the flat band potential and to improve the photocurrent density (~7 mA/cm^2 at 0 V vs. RHE in 0.1 M H_2SO_4 solution)of p-Si photocathode as reported by Yoon et al.[146,150]. Effects of electrical resistivity, carrier concentration, and surface band bending of WO_3 coating were investigated. Annealing temperature dependent polarization characteristics of p-Si|WO_3 is shown in Fig.12a, where further increased annealing temperature showed degraded photocurrent.

Another stable wide-band gap semiconductor is GaN. Demonstration of nanostructured n-GaN coating on n-Si was reported by Fujii et al[147]. Slightly higher photocurrent (~0.4 mA/cm^2 at 1.23 V vs. RHE) compared to thick TiO_2 coated Si was achieved (Fig.12c). Stable device performance was realized using acidic electrolyte and lower anodic bias (< 1.3 V vs. RHE). However, surface morphology of the coating was not reported in this paper, which might be the key reason of the electrode failure due to the possible non-uniform nanodot coating and exposed Si to the oxidizing aqueous solution. Moreover, electrochemical dissolution of GaN nanodots was noticed after test, which could contribute to further accelerate the anodic passivation process of the exposed Si photoanode.

Compositional modification leads to the band gap engineering of GaN, which can be realized by incorporating In doping results in GaN[151]. Nanostructured n-type InGaN with an energy band gap of 2 eV was grown on highly doped n^+-Si wire and used as a photoanode for water splitting recently (Fig.13a)[152]. Stability of InGaN in extremely acidic and basic electrolytes is a concern and could be effectively improved through a thin and robust TiO_2 coating. Photoelectrochemical performance of GaP (~2.2 eV) from metal organic chemical vapor deposition (MOCVD) coated on n^+-Si microwire was recently demonstrated by Strandwitz et al (Fig.13b)[153]. Further optimization was suggested by maximizing absorption, optimizing charge transportation and shunting resistance through controlling experimental conditions. Another example that uses heterogeneous coating on highly doped n^+-Si was presented by Shi et al. using TiO_2 nanowire (Fig.13c)[154]. In these examples, degenerately doped Si was not active for the light absorption and free carrier generation, but acted as a high surface area and freestanding template. Meanwhile, n^+-Si with electrons as majority carriers in these cases acted as a conducting channel for electrons injected from respective n-type photoactive coatings on the its surface.

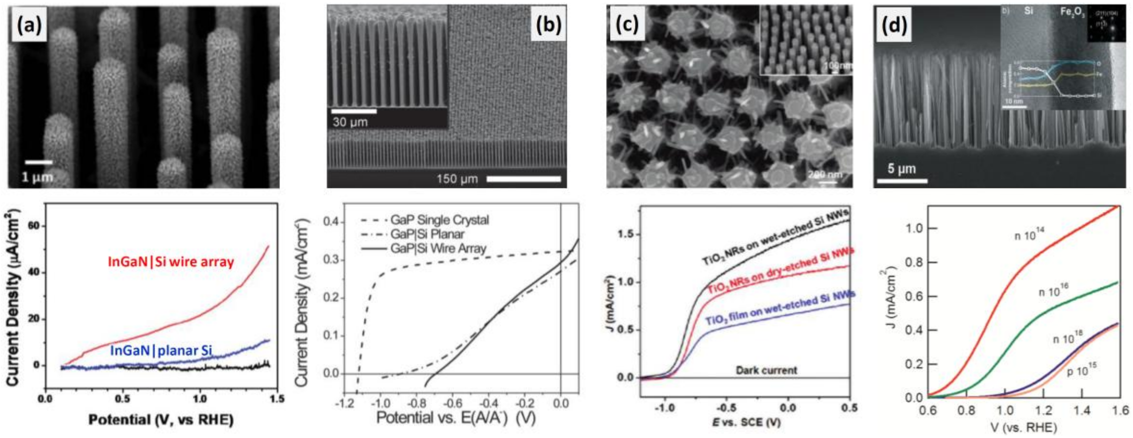

Figure 13. Heterogeneous n^+-Si wire array based photoanode coated with: a) InGaN nanowires[152] (copy right of American Chemical Society), b) GaP thin film[153] (copy right of Wiley), c) TiO_2 nanowires[154] (copy right of American Chemical Society), and Fe_2O_3 thin film[155] (copy right of American Chemical Society). Second row shows polarization curves of corresponding structures in the first row measured in: (a) pH 3 H_2SO_4 solution with 0.5 M of Na_2SO_4, (b) 0.50 mM ferrocenium tetrafluoroborate, 20 mM ferrocene, and 1.0 M lithium perchlorate, (c) 1 M KOH, and d) 1 M NaOH (curves correspond to different Si doping levels).

Besides wide band gap materials such as TiO_2, ZnO, WO_3 and GaN as discussed above, photoelectrochemical properties of n-Si coated with smaller band gap materials have been studied. For example, Yazawa and co-workers used stoichiometric α-Fe_2O_3 to coat n-type Si as an efficient heterogeneous photoanode in 1980[156]. Thickness of the Fe_2O_3 layer affected the performance of the heterostructure photoanode in terms of spectral response and stability. Thicker Fe_2O_3 film blue-shifted the spectral response and improved stability, while thinner Fe_2O_3 film maintained Si spectrum response up to 1140 nm[157]. These conclusions were consistent with the case using TiO_2 coating. It was further shown in the study that film thickness < 20 nm showed notable degradation of photocurrent during continuous operation presumably due to the Si passivation from the failed protection. Most importantly, although heterostructure improved the hole injection from n-Si to the solution, spontaneous photodecomposition of water was still not realized using this structure due to the positive flatband potential of the heterostructure photoanode (on-set potential 1.35 V vs. RHE). In Yazawa's follow-up research[148], a negative on-set potential of 0.603 V vs. RHE was reported using the same heterostructure with Fe_2O_3 film fabricated from a different method, which led to improved conversion efficiency (Fig.12d). Interestingly, saturation current at higher anodic potential was not noticed in this study, but a decreased photocurrent after reaching maximum. It was proposed that a more significant mechanism dominated the current at higher anodic potential. Electrons could tunnel through the barrier to the conduction band creating dark current and recombine with valence holes contributing to the decreased photocurrent, when electron potential was high enough to reach the surface states on Fe_2O_3. Although this design exhibited negatively shifted onset potential, the photoanode suffered from the limited spectrum response primarily below 600 nm. As discussed in previous sections, sub-wavelength nanostructure provides significantly enhanced light absorption and surface area. Applying a photoactive n-Fe_2O_3 conformal coating (20 nm in thickness) from ALD on n-Si nanowire array with various background doping levels (carrier concentration of 10^{14}-10^{18} cm^{-3}) as a photoanode was demonstrated by Mayer et al[155]. Successful protection of n-Si was realized. Filtered light measurement confirmed a two photon-to charge conversion process in the proposed structure. Spectrum response measurement showed photocurrent response up to 600 nm, which also confirmed the dual absorber mechanism. In addition, this heterostructure lowered the on-set of anodic photocurrent, potentially from the catalytic effect of Fe-based electrocatalyst. These studies on Fe based OER catalysts indicates that if one can significantly lower the thickness while maintain the uniformity of the catalyst coating to maximize the light absorption in Si, one may reduce the overpotential to drive water oxidation using n-Si. This has been demonstrated already by Jun et al[158], which will be discussed in the next section.

Another photosensitive compound semiconductor used for Si coating is the intrinsically p-type Cu_2O[159], different from previously discussed n-type semiconductors. To reach an efficient hole-injection, higher valence band edge than that of Si is desired. An enhancement of photoanodic current and spectra response over unprotected n-Si was noticed. However, high overpotential was still needed to drive the reaction and small photocurrent at zero overpotential was observed on n-Si|p-Cu_2O photoanode. Moreover, competitive processes between Cu_2O anodic decomposition and H_2O oxidation could be potentially troublesome with such an unstable coating.

Finally, besides electrical modifications on Si, semiconductors could also provide optical modulations like metal particles. Dielectric nanoparticles made of semiconducting materials can provide efficient scattering[160] as well as absorption at the surface plasmon resonances for some highly doped semiconductors, such as metal nitride, oxides, silicides and etc[161]. Importantly, optical loss can be minimized in semiconducting materials compared to typical metals such as Au or Ag[161d]. Actually, results simulated by Akimov et al. showed dielectric nanoparticles can provide more effective photocurrent enhancement owing to the larger permittivity (abs(Re[ε])) and smaller light dissipation (abs(Im[ε])) in dielectric materials. Besides scattering, recently simulation studies by Grandidier et al. showed when an array of SiO_2 nanospheres are placed on an amorphous Si surface, light absorption can be enhanced through a guided whispering gallery mode(WGM)[162]. Close coupling between adjacent spheres were very important to reach strong optical dispersion, and the enhancement of photocurrent can be up to 15% in an optimized structure. When the size and arrangement of the nanospheres are well-controlled, light absorption can be further optimized. Simulation results showed higher improvement than the typical backside nanodome textured amorphous Si solar cells[163].

1.4.2.2 Degenerate non-electrocatalytic semiconductor

Most of the aforementioned thick photocatalytic semiconductors coated Si photoelectrodes suffer from limited spectrum photoresponse primarily because of the photoresponse from the coating materials. Degenerate semiconductor oxides, known as transparent conducting oxides (TCO), such as mixture of SnO_2 and In_2O_3 (ITO, 90:10 mole ratio composition), can be effective coatings to Si for the following reasons: (1) the wider band gap (3.6 eV) results in minimal spectrum loss in the coating and thus allows for efficient light absorption by Si, (2) the lower optical loss admits a thicker protection coating which reduces chances of electrode failure; (3) the lower refractive index (~2.0 for ITO) makes it a partial antireflection coating on Si; (4) the higher electron conductivity reduces ohmic loss in the system; and (5) the minimized interdiffusion between Si and TCO coating due to the low deposition temperature, which in turn improves short-wavelength response.

The first successful demonstration of TCO coated Si photoelectrodes using 3-100 nm ITO film was reported by Thompson et al[164]. However, ITO coating on p-Si showed instability in prolonged experiments under acidic conditions at a negative bias. In fact, chemical or electrochemical stability of ITO highly depends on the deposition and operation conditions[165], including deposition temperature, oxygen concentration in chamber, film thickness, and electrolyte pH. The most stable ITO was observed on a thick film deposited under substrate heating and without addition of O_2 in the sputtering chamber, and importantly measured in basic electrolyte. Although thicker ITO became more stable, the thickness of the ITO layer had to be optimized, so that photogenerated carriers arriving at the Si/ITO interface could traverse the ITO layer without experiencing too much ohmic loss within the ITO layer. Moreover, researchers pointed out that the major loss mechanism in S/C/E structures was the overpotential at the C/E interface. Charge transfer across this interface will have to be optimized (either by choice of a couple with fast kinetics or by suitable electrocatalytic modification of the surface layer), so that the useful photovoltage gained at the Si/ITO interface could be reflected in the ultimate performance of the overall photoelectrochemical system[165]. To solve the dilemma of having stable and effective TCO coating, FTO (fluorine doped tin oxide) glass was further used to protect ITO layer through a conductive epoxy[165]. Other degenerate TCO such as SnO_2[166] and Sb/Ru-SnO_2[167] were reported for Si photoanode. Sb and Ru dopants introduced in the SnO_2 significantly reduced the Tafel slope and onset potential due to the improved conductivity and catalytic activity.

Note that additional metallic doping would generally reduce the transmittance of the coating, thus reduce the amount of light arriving at the S/C interface. Therefore, optical loss should be considered while optimizing the electrical and catalytic properties of the coating to reach an optimum photoelectrochemical performance. Moreover, the energy band dispersion suggests that the upper valance band are relatively flat, which means a large effective mass of holes are present in typical n-type TCOs (n-TCOs). This property normally results in a fact that n-TCOs are typically effective for conducting electrons but not holes. For n-Si as well as other n-type photoanode materials, it could be important to look into wide band gap TCOs with p-type conductivity[168]. Cu_2O based p-type hole conductors have been already developed. However, Cu(I) is not able to survive in the competition reaction of self-oxidation to Cu(II) and water oxidation[169]. Meanwhile, Cu oxides exhibit strong light absorption with direct energy band gaps with reported values ranging in 1.2-1.5 eV for CuO[170] and 2.0-2.2 eV for Cu_2O[171]. Other transparent and stable p-type materials should be developed. For example, In doped MoO_3[172], Mn/N doped Cr_2O_3[173], $ZnIr_2O_4$[174], and more transition metal oxides that are typically p-type will be discussed in the next section.

1.4.2.3 Electrocatalytic late d-band transition metal containing compound

Conduction band of Si is well above the H_2/H^+ redox potential (Fig.1a), which results in a small band bending leading to slow charge transfer kinetics (Fig.1b). Moreover, due to the lack of oxidation energy of holes, Si is not capable of spontaneous water splitting without external bias (Fig.2c). Therefore, heterogeneous hydrogen and oxygen evolution reaction (OER/HER) catalysts to reduce the overpotential needed to drive the reactions are highly required for Si as well as for other materials to reach efficient electrochemical fuel production[175], energy storage devices[176], and fuel cells[177]. Pt group metals (PGMs) are recognized as the best electrocatalysts for water electrolysis. For example, Pt and Pd are the best HER catalysts, and Ru and Ir are considered the best OER catalysts[178]. In fact, electrocatalytic activity is largely determined by the binding energy of the reaction intermediates to the electrode surface[179]. DFT (density function theory) study provides an approach to estimate this energy accurately. Progress in DFT studies on HER and OER catalysts could be found in ref[180] and ref[181]. Recently an experimental in-situ study also provided evidence to support numerical studies on the relationship between surface binding energy and the catalytic activity[182]. Strategies to synthesis of nanostructured[183] or supported[184] catalysts based on precious metals or metal alloys which dominate at the top of the pyramid in the famous "volcano plot" (Fig.8a and 8d) should be developed to reduce the extensive use of expensive noble metals without sacrificing their catalytic activity. On the other hand, cost-effective and PGM-like catalysts (left curves in Fig.9a and 9b) that are typically located at the shoulder or lower part of the "volcano plot" attract research attentions. These catalysts normally consist of first row or late transition metals in forms of inorganics, such as oxide, hydroxide, nitride, carbide, chalcogenide, and complex organic compound. These cheap materials with comparable or outperforming activity compared to PGMs are recognized as the ultimate solution to large scale solar fuel production. Successful demonstrations on the development of HER and OER catalysts based on earth-abundant metals, namely Mo, Mn, Ni, Fe and Co, have been realized[185], which contribute continuous expending of the "volcano plot" (Fig.14a and 17). To differentiate from previously published review work, we will focus on inorganic catalysts developed for solar fuel production from water using Si photoelectrodes. Also, we will review very recent published/conference-reported milestones of low cost transition metal-based catalysts with improved performance, as well as novel strategies using 1D or 2D carbon (CNT and graphene), which have not yet demonstrated applications to photoactive substrates. At the end, we will briefly discuss the molecular complex based biochemical water splitting through hetero/homo-geneous catalyzed semiconductors or organic photosensitizers[186].

1.4.2.3.1 HER catalysts

Mo HER: MoS_2 is widely used in industry as a hydrodesulphurization (HDS) catalyst[187]. Recently, its nanocrystal form exhibited promising catalytic activities for electrochemical water splitting as an inexpensive alternative to expensive Pt metal[188]. First demonstration of MoS_2 as a catalyst on photocatalytic CdS substrate can be found in ref [189].

It was experimentally recognized that MoS_2 showed high activity at the edges of S-Mo-S single trilayers instead of the basal plane in desulfurization reactions through a scanning tunneling microscopic (STM) study[190]. It was also suggested by Lauritsen et al. in their study that the catalytic property was dependent on the MoS_2 nanocrystals size. Lately, Jaramillo et al. used STM and identified the edges of S-Mo-S single trilayers as the activation site in the H_2 evolution reaction[191]. Experimental verification was conducted through a study of the nanoparticle size dependent catalytic activity. MoS_2 nanoparticles in this report were deposited from gas phase and the controlled edge length was obtained by varying sintering temperature. Results showed the highest TOF of around 0.02 s^{-1} and a j_0 of 8×10^{-3} mA/cm^2 (Fig.14a). The low atomic H coverage at the edge was recognized as the reason of inferior activity. Recently, researchers from the same group demonstrated a synthesize of mesoporous MoS_2 using a mesoporous silica template[192] through a Mo electrodepostion and subsequent sulphidization at 200 C in H_2S/H_2 (1:9) environment. This mesoporous MoS_2 film showed comparable catalytic activity with a j_0= 6.7×10^{-4} mA/cm^2 and Tafel slope of 50 mV/dec to the amorphous MoS_x that we are going to discuss in later text. This work demonstrated a versatile technique using the powerful mesoporous substrates as a template.

To further utilize the large basal plane potentially having a larger H coverage, rational control of the crystal orientation in order to activate the basal plane for improved HER activity was demonstrated. Chhowalla's group recently showed that the basal plane of the 1T metallic phase of MoS_2[193] from solution processing was actually more active than the edges, due to an additional strain in this phase. By optimizing the strain in the basal plane, one can tune the Gibbs free energy for atomic hydrogen adsorption (ΔG_{H*})[194]. It was found that 2.7% strain could result in a nearly zero ΔG_{H*} suggesting an improved activity than edge active MoS_2 nanoparticles.

Another class of Mo-S cluster-based catalysts composed of incomplete cubane-like MoS_x was synthesized and characterized by Jaramillo et al[195]. The MoS_x showed similar behavior compared to MoS_2 (Fig. 13b). Application of this MoS_x on p-Si photocathode was presented by Hou et al. in 2011 (Fig. 18a and b)[196]. MoS_x cluster was adsorbed on Si through a ligand bonding. Photocurrent can be as high as 8 mA/cm^2 from MoS_x decorated planar Si and 9 mA/cm^2 on p-Si microwire substrate at 0 V vs. RHE under red light illumination (>620 nm, 28.3 mW/cm^2). Decreased limiting current was noticed at high cathodic bias, presumably due to the hydrophobicity of the modified Si surface resulting in bubble accumulation. Moreover, MoS_x modified p-Si microwire showed reduced turnover frequency (TOF, 65 s^{-1}) than the planar counterpart (960 s^{-1}) based on the assumption of comparable surface coverage of catalyst at identical condition. In this study, MoS_x centred molecules demonstrated comparable catalytic activity to noble Pt catalyst and no deactivation was noticed within 24 hrs operation. However, degradation was actually noticed on the Si part that was not decorated with MoS_x electrocatalysts. This is primarily due to the passivation of Si by forming oxides at dark under idle condition. To prevent oxidation of Si during the cycling deposition of MoS_x catalysts, researchers from the same group further sputtered a robust Ti metal coating (9 nm) on the surface inverted p-Si prior to the MoS_x catalysts formation[197]. This $MoS_x|Ti|n^+p$-Si photocathode showed onset potential of 0.33 V vs. RHE comparable to that of Pt electrode (0.44 V vs. RHE). This Ti protection layer has to be optimized to minimize the light loss while maintaining the effective lifetime. Further improvement using cubane-like heterobimetallic sulfide compounds was also achieved[198]. It was found that Cu contained MoS_x showed reduced Tafel slope and improved photocurrent density, while Co contained MoS_x showed instable performances[199]. Similar finding was also reported by Tran et al[200].

Amorphous MoS_3 nanoparticle and partially reduced MoS_3 are also alternatives of molybdenum sulfide catalysts. Recently, Tang et al. demonstrated the application of an amorphous MoS_3 film on CdSe/CdS photosensitizer through a low temperature one-step solution based coating process. The MoS_3 was partially reduced to form an under-coordinated species which showed HER catalytic activity[201]. Vrubel et al. synthesized amorphous MoS_3 particles from acidification of a mixture of MoO_3 and Na_2S[202]. A superior catalytic activity was realized on this amorphous MoS_3 (Fig. 13c) due to the larger number of unsaturated S atoms at the surface than that on crystal MoS_2 and sintered MoS_3. For another example, Benck et al. recently showed a study of amorphous MoS_3 prepared by mixing a molybdenum and sulphur precursor solution at room temperature[203]. This method is capable of large-scale synthesis of low-cost transition metal HER catalyst with high activity (10 mA/cm^2 at ~200 mV overpotential). The amorphous nanoparticles prepared using this method showed prolonged lifetime in the 10000 cycles study.

Merki et al. recently reported that addition of first row transition metals (Fe, Co and Ni) to MoS_3 significantly enhanced the HER activity in both acidic and neutral condition (Fig.14d)[199]. Other interesting structures based on supported MoS_x can be also found like graphene supported MoS_2 nanoparticles[204], MoO_3 supported MoS_2 thin film coating[205], and etc. A recent perspective on MoS_x HER catalyst was presented to point out a further enhancement on catalytic activity can be realized using MoS_x/CNT nanocomposites and controlled alignment with maximized exposure of actives sites[206].

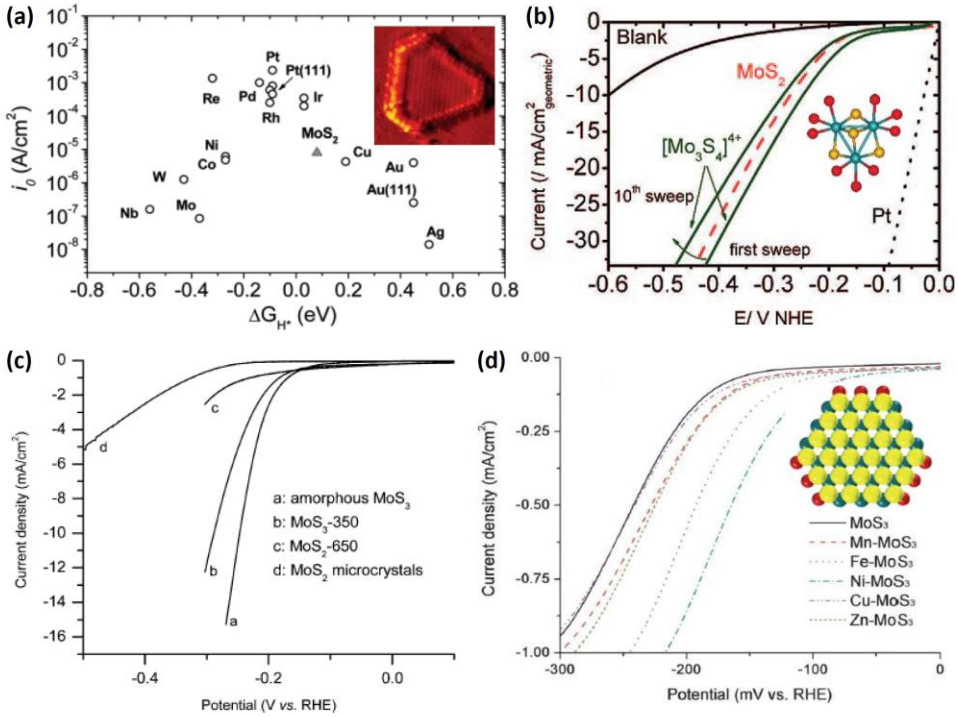

Figure 14. Molybdenum sulfide based HER catalysts and their performances. (a) single crystal MoS_2 showed similar trend as the pure metals in the "volcano plot" of exchange current density as a function of calculated Gibbs free energy of adsorbed atomic hydrogen[191] (inset: atomically resolved MoS_2 particle showing the predominance of the sulfided Mo-edge) (copy right AAA science), (b) polarization curves of incomplete cubane-like MoS_x in 0.5 M H_2SO_4[195] (inset: molecular structure of incomplete cubane-like MoS_x Blue (Mo), yellow (S), and red (O).) (copy right American Chemical Society), (c) polarization curve of amorphous MoS_3 compared to reduced MoS_3 and crystal MoS_2 at 1 M H_2SO_4 solution[202] (copy right Royal Society of Chemistry), and (d) polarization curve of other transition metal promoted a-MoS_3 in a standard phosphate buffer solution (pH=7)[207] (inset: molecular structure of promoted MoS_2 nanocrystals. (yellow) S, (dark cyan) Mo and (red) Co/Ni.) (copy right Royal Society of Chemistry).

Another low-cost HER electrocatalyst is based on transition metal nitride. Similar to previously mentioned MoS_x, properties of MoN_x is also governed by the surface structure and stoichiometry[208]. Comparable catalytic activity to that of Pt noticed on MoN_x makes this non-noble metal nitride a good candidate to replace Pt as a new cost-effective counter electrode[209]. $NiMoN_x$ nanosheet with Ni/Mo ratio around 0.21 was synthesized by reducing Ni and Mo containing salt and substantially further transformed to nitride by annealing in ammonia gas. Compared to MoN_x catalyst, $NiMoN_x$ showed reduced onset potential (80 mV shift), reduced Tafel slope (18.6 mV/dec shift) and dramatically increased exchange current density (6.7 times higher). Compared to its alloy counterpart (NiMo) as a HER catalyst, nitride form showed dramatically enhanced catalytic activity and improved stability (Fig.15a). Ni-rich surface or edge was noticed and was believed as the primary formation force of the nanosheet geometry. Furthermore, Ni-rich surface/edge also resulted in reduced Mo-H bond strength and increased density of states near the Fermi level due to d-band modification. Further optimization was suggested by controlling the surface distribution and ratio of Ni.

Other forms of Mo based compound materials as HER catalysts were reported before. For example, Chen et al. recently used carbon supported Mo_2C for H_2 generation from water (Fig.15b)[210]. Carbon supported Mo_2C prepared from solid-state carburization method showed higher activity compared to bulk Mo_2C as well as the metal Mo due to enhanced surface area. Similarly Wirth et al. showed WC, Mo_2C and WB exhibited the lowest onset potential and lowest overpotential for a certain current density among 18 other early transition metals IVB-VIB transition metal carbides, nitrides, sulfides, silicides and borides[211]. Moreover, very recently Vrubel and Hu demonstrated tha Mo_2C showed superior HER catalytic activity than MoB in both acidic and basic environment after activation[212].

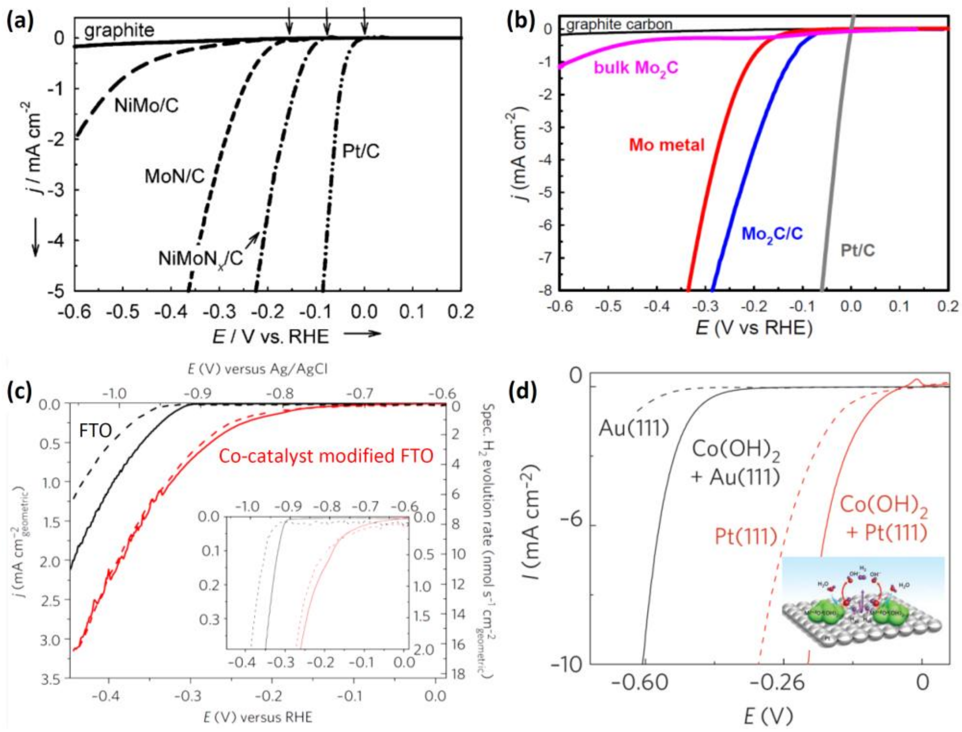

Figure 15. Polarization characteristics of some HER catalysts. (a) NiMoN$_x$ measured in 0.1 M $HClO_4$ solution[208] (copy right Wiley), (b) Mo_2C measured in H_2-saturated 0.1 M $HClO_4$ solution[210] (copy right American Electrochemical Society), (c) Co-Cat measured at 0.5 M KPi (pH=7)[213] (solid line: current density, dotted line: H_2 evolution rate) (modified copy right Nature), and (d) hydroxide of Ni, Co, Fe and Mn measured in 0.1M KOH/LiOH electrolyte[214] (copy right Nature)

Co HER: a cobalt based HER catalyst was recently electrochemically synthesized through a Co-contained salt in phosphate buffered aqueous solution[213]. The H_2-CoCat electrocatalyst consisting of a metallic Co coated with a cobalt-oxo/hydroxo-phosphate showed significantly improved HER catalytic activity (overpotential 50 mV and exchange current of $10^{-5.5}$ A cm^{-2}) compared to Co metal (exchange current of 10^{-6} A cm^{-2}) and previously reported NiMo, as well as MoS_2 catalysts (Fig.15c). Recent demonstration of $CoSe_x$ as a replacement of Pt counter electrode in dye sensitized solar cell (DSSC) was reported to show a comparable activity[215].

Oxyhydroxide of Ni and Co island decorated Pt also showed higher activity than pure Pt metal. Subbaraman et al. showed in their experimental study that Pt electrode needed nearly 200 mV overpotential to drive 5 mA/cm^2 cathodic current[214]. However, for electrodes that were covered by $Co(OH)_2$ and $Ni(OH)_2$ showed lower overpotentials of ~125 mV and ~30 mV at 5 mA/cm^2, respectively (Fig.15d).

Ni HER: Nickel metal and alloys, were also developed as low-cost HER catalysts and showed considerable activity to replace precious Pt in industrial electrolysis. Ni compounds, such as Ni-S[216] and Ni-Se[217], have also been studied for HER catalysts. Major concern of using later group V and VI non-metal elements is the toxicity and chemical stability in aqueous solution. Gao et al. showed a electrochemical measurement of NiSe based HER catalyst and noticed that the loss of catalytic activity was significant in 0.5 M H_2SO_4 presumably due to the NiSe oxidation at high potentials[217]. Successful demonstration of some sulfide and selenide can be found with the presence of sacrificial agents[218]. Surface attached species are recognized as effectively promoters to the catalytic reactions[219]. Recently, Danilovic et al. demonstrated a utilization of $Ni(OH)_2$ nano-island to tailor the HER activity of the noble metal in alkaline environment[220]. HER activies remains low in alkaline conditions due to the limited proton availability. This study applied $Ni(OH)_2$ on metal surface which locally enhanced the dissociation of H_2O and thus proton ions for hydrogen generation. The structure effectively reduced the overpotential of metal for H_2 generation and a comparable activity to the acidic condition.

1.4.2.3.2 OER catalysts

Mn-OER: Inspired by nature's Mn centered (Mn_4Ca) molecular complex which is considered as the most efficient and stable catalyst with TOF up to 400 s^{-1}, biomimicing Mn-complex catalysts were developed for efficient water oxidation[221].

Mn oxide, a well-received inorganic Mn contained compound, can be simply electrodeposited at low temperature. For example, Jaramillo et al. presented a MnO_x based electrocatalyst deposited from a constant potential. This bi-functional material was active in both oxygen reduction and evolution reaction (ORR/OER) directions[222]. Current density of ~0.5

mA/cm^2 at 1.23 V vs. RHE was reached, approaching to those from Ru and Ir metal catalysts. For another example, Zaharieva et al. recently reported that MnO_x electrochemically deposited through a simply controlled voltage-sweeping technique (MnCat) could improve OER catalytic activity[223]. For comparison, the authors reproduced some representative electrodeposition techniques for Mn oxide synthesis, including constant potential used in ref [222], cycling from two constant potentials, and various buffer solutions. At overpotential of 565 mV, Faradaic efficiency was quite close to 100% and TOF is about 0.01 s^{-1}, which was comparable to Co (0.017 s^{-1}) and Ni-based (0.01 s^{-1}) electrocatalysts from electrodeposition. At overpotential of 590 mV, current density reached at 1 mA/cm^2. Identification of oxidation states was conducted using electrochemical measurement and x-ray absorption spectroscopy (XAS). It was revealed that the activated MnCat from the controlled voltage-sweeping technique contained a mixture of Mn(III) and Mn(IV) while inactive MnCat contained mainly Mn(IV). Detailed structural studies also revealed that di-μ-oxo bridging existing in synthesized MnCat was recognized crucial to OER catalysts, similar to nature's Mn_4Ca complex and other first-row transition metal catalysts containing Co and Ni. The high activity of MnCat was attributed to the high concentration of mono-μ-oxo bonds, relatively low concentration of saturated μ_{3-5}-oxo bonds, and high availability of coordination sites for water binding. However, the reason for catalytic activity loss in stability test was still unclear, although authors claimed it might result from the dissolution of the catalyst. Very recently, Takashima et al. provided insights on reaction mechanism targeting on providing guidance on developing strategies to further lower the overpotential on MnO_2 based OER catalysts[224]. They have found that effectively suppress the formation of Mn^{2+} and Mn^{4+} from Mn^{3+} is important to maintain the activity. Surface functionalization using N-Mn bonds through surface bonded amine groups stabilize the surface Mn^{3+} species and further reduced the overpotential.

Addition of other cations in the Mn oxides was studied, which could be potentially a facile approach for improved OER catalytic activity. For example, hydrate $CaMn_2O_4$ synthesized from precipitation of a mixed aqueous solvent was introduced by Najafpour et al[225]. Incorporation of Ca greatly enhanced the catalytic performance. Interestingly, it was also observed that the hydrate catalysts showed better activity than anhydrous ones in their study. Other transition metals were also introduced to MnO_x. For example, Ghany et al presented a Mn-Mo-Fe oxides system using anodic deposition[226], which was able to electrolyze seawater with enhanced OER efficiency and long term stability. Matsui et al. presented a ternary Mn-Mo-W oxide from anodic deposition[227]. They noticed the deposition condition-dependent activity, selectivity and durability on their OER catalysts.

MnO_x coating on n-Si was demonstrated by Kainthla et al. using electrochemical deposition in a bath containing 3 mM $MnCl_2$, 0.25 m NH_4Cl and 1.4 M NH_4OH aqueous solution[228]. Mn_2O_3 in a thickness of 20 nm was formed by removing water from $Mn(OH)_2$ precipitated on the Pd monolayer coated Si surface at 250℃ in vacuum for 15 min, in which Mn was mainly in 3+ oxidation states,. From the polarization study shown in Fig.16a, the Mn_2O_3|Pd|n-Si demonstrated onset potential of 1.285 V vs. RHE in 0.2 M NaOH (pH=13.3) (Fig.16a) and Mn_2O_3|Ti showed an overpotential of 800 mV at 1 mA/cm^2. This Mn_2O_3|Pd|n-Si showed stable photocurrent response of around 1 mA/cm^{2}for more than 650 hrs operation which did not show any mechanical or chemical degradation. Recently Strandwitz et al. (unpublished data presented in IPS-19 meeting at Caltech 2012) reported MnOx from ALD on p +/n-Si microwire array. A thin MnO_x of 10-20 nm was conformally coated on an n-Si microwire array substrate with surface inverted to p^+ emitter. Catalyzed photooxidation of water was successfully realized using this structure, while photodecomposition of n-Si was substantially suppressed.

Fe-OER: In the previous section, we reviewed the investigation of Fe_2O_3 coating on a Si photoanode. Here, we will make a further discussion on catalytic effect offered by Fe containing oxides as OER catalysts. Recently, Jun et al. demonstrated an application of high-quality hematite (α-Fe_2O_3) thin film coating from chemical vapor deposition (CVD) on n-Si photoanodes for efficient water oxidation[158]. Photocurrent of 1 mA/cm^2 at 1.23 V vs. RHE was achieved by coating a 10-nm Fe_2O_3 layer on polished n-Si. Such a thin coating maintained the Si photoresponse without strong electronic or optical modification introduced to S/E interface. Optimized system by converting backside to highly doped n$^+$-Si and by utilizing Si microwire array eventually gave a record-breaking photocurrent of 20 mA/cm^2 at 1.23 V vs. RHE (Fig.16b).

Dopants can be also introduced in Fe_2O_3. For example, Singh et al. introduced a mixture of Mo and Fe oxides through a co-precipitation of a mixed aqueous solution[229]. It was found that OER electrocatalyst with a Mo/Fe ratio of 1.0 was able to provide the best activity with the lowest Tafel slope (35 mV). To guide an efficient search for dopants in Fe_2O_3, Liao et al. recently used periodic density function theory +U calculations to screen the cation doping effect in Fe_2O_3 (including Ti, Si, Mn, Co, Ni, and F)[230]. A predicted "volcano plot" was obtained (Fig.17d), where Ni and Co were considered as the best dopants for favorable OER catalytic reaction on Fe_2O_3 surface, inviting further experimental verification on their findings.

Co-OER: Theoretical calculation suggested that Co- and Ni-oxide are among the OER catalysts with comparable overpotential to the best PGM-oxides such as RuO_2 and IrO_2[181] (Fig.17a). Nanostructured Co_3O_4 based OER catalysts containing Co(II) and Co(III) have also been studied extensively[231]. For example, Cong et al. showed that Co_3O_4 nanoparticles decorated Ta_3N_5 nanotube array photoanode showed comparable OER activity to IrO_2 decorated nanotubes, particularly at high anodic bias with three times higher than bare Ta_3N_5[232]. However, Co_3O_4 showed less activity at zero or small anodic bias region compared to Co-Pi (a cobalt phosphate OER catalyst, which will be further reviewed in later text). Improvement on the Co_3O_4 catalytic activity can be realized by manipulation of surface orientation, nanoparticle size and shape. Recently Xiao et al. presented a facile method to control the shape and surface orientation of Co_3O_4 and its effect on electrochemical performances[233]. The control on the morphology of the nanoparticles were realized by varying the concentration of NaOH and $Co(NO_3)_2 \cdot 6H_2O$. The phase dependent activity was noticed which could be helpful to understand and achieve higher OER catalytic activity using such materials. Koza et al. reported a electrodeposited spinel Co_3O_4 from Co(II)tartrate in alkaline solution without additional heat treatment[234]. This Co_3O_4 showed a Tafel slope of 49 mV/dec and a j_0 of 2.0×10^{-7} mA/cm^2, which exhibited an outperformed activity to the Co-Pi catalyst. This film was crack-free and provided stable current for more than 50 hrs, which showed great potential to protect and catalyze n-Si photoanode.

Supported Co_3O_4 nanoclusters using mesoporous silica (SBA-15) synthesized from thermal annealing method was reported by Jiao and Frei[235]. The synthesized Co_3O_4 nanorod clusters with average diameter of ~7.6 nm showed spinel structure in SBA-15 scaffold. The estimated TOF of samples with SBA-15/4% Co_3O_4 at mild conditions (pH=5.8) was about 1140 s^{-1}, which is the highest among Co oxide based catalysts reported.

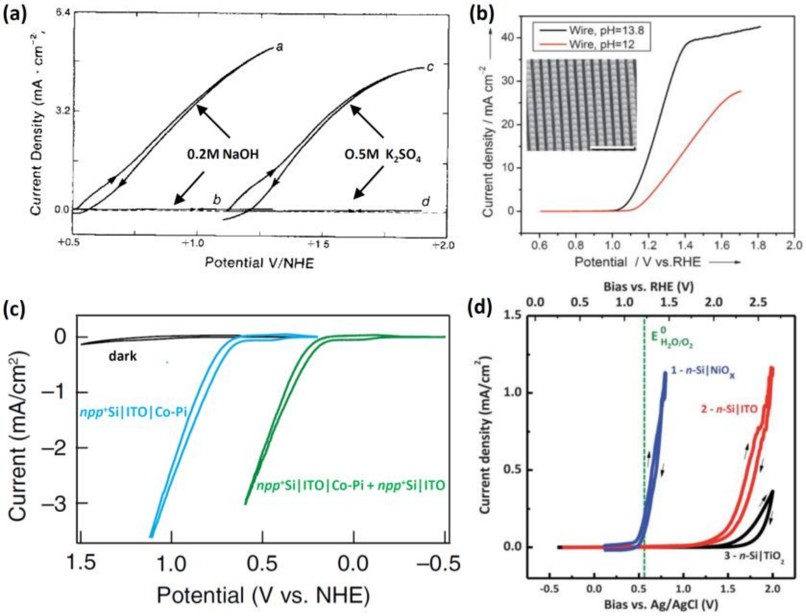

Figure 16. First row transition metal-based electrocatalysts decorated n-Si photoanodes for water oxidation. (a) MnO_2 from ALD coated p^+/n-Si microwire measured in 0.2 M NaOH and 0.5 M K_2SO_4[228] (copy right American Electrochemical Society), (b) Fe_2O_3 from CVD grown on n-Si microwire with backside converted to n^+ to minimize ohmic loss measured in Na_2HPO_4/NaOH adjusted electrolyte[158] (copy right Wiley), (c) CoPi from electrochemical deposition on surface inverted n-Si measured in Pi electrolyte[236] (copy right National Academy of Science), and (d) NiO_x coated n-Si from sol-gel method measured in PBS buffered Na_2SO_4 electrolyte[237] (copy right Royal Society of Chemistry).

Introduction of other cations can also improve the OER catalytic activity. For example, Li et al. presented Ni doped Co_3O_4 nanowire array was synthesized from solution based method showed considerable OER catalytic activity[238]. Mixed valence state of Co(II/III) and Ni(II/III) were discovered in the doped nanowire. Additional Ni in Co_3O_4 nanowire enhanced the conductivity, surface roughness, and increased surface active sites, compared to pure Co_3O_4 nanowire. For another example, Lu et al. investigated the OER properties of Ni substituted Co_3O_4 nanowire array ($Ni_xCo_{3-x}O_4$)[239]. It was found that the optimum OER activity and stability was realized at the 1:1 ratio of Ni:Co. To further obtain a high specific surface area, mixed Ni-Co oxide in the form of aerogel was prepared[240]. The aerogel was synthesized from a Co and Ni chloride gel and dried in a supercritical dryer. $NiCo_2O_4$ aerogel with a specific surface area of the about 134 m^2/g, which was 10 times larger than typical $NiCo_2O_4$ nanoparticles, showed the lowest overpotential of 184 mV at 100 mA/cm^2. This superior OER activity was due to the high porosity and low charge transfer resistance associated with the OER process.

Recently, Liang et al. introduced Mn into Co_3O_4 together with nitrogen doped graphene ($MnCo_2O_4$/N-rmGO, 5 nm particle size)[241]. This nanocomposite was synthesized by low-temperature solution based method. The Mn substituted Co_3O_4 showed lower Co^{3+} concentration, while Mn in the hybrid was mainly of 3+ state. Co^{3+} and Mn^{3+} were considered as OER and ORR active sites, respectively. Therefore, Mn doping showed reduced OER activity[242]. However, the $MnCo_2O_4$/N-rmGO exhibited much higher OER activity than $MnCo_2O_4$, suggesting an excellent strategy for developing novel OER electrocatalysts using [135c] from the reduced charge transfer resistance offered by the hybrid structure with the presence of nitrogen doped-graphene. For another example, Koninck et al. synthesized $Cu_xCo_{3-x}O_4$ (x=0 and 1) nanoparticles from a sol-gel based method[243]. Addition of Cu reduced the resistivity of Co_3O_4 and most importantly the metal-OH bond strength, both of which led to an enhanced catalytic activity in $CuCo_2O_4$ composites.

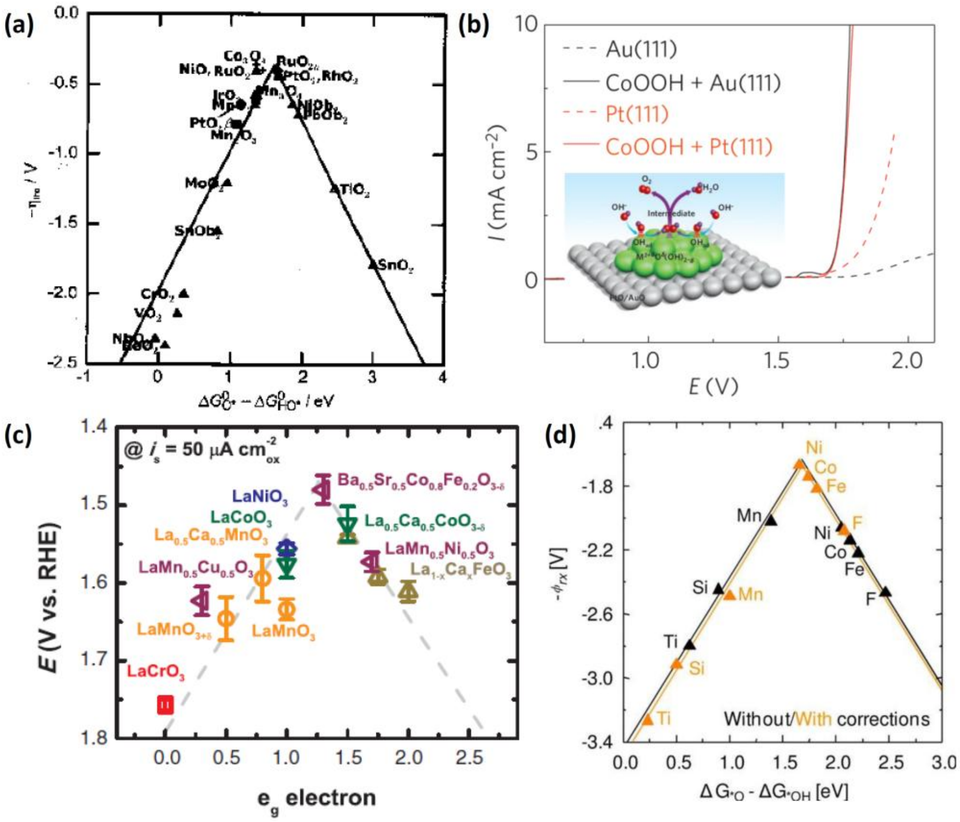

Figure 17. (a) Negative theoretical overpotential verses the binding energy difference (ΔG_{O*}-ΔG_{OH*}) showing a volcano-shape activity trend of several transition metal oxides[181] (copy right Wiley), (b) overpotential needed to drive 5 mA/cm^2 anodic current between oxyhydroxide of Mn, Fe, Co and Ni on Pt substrates measured in 0.1M KOH/LiOH electrolyte[214] (copy right Nature), (c) overpotential to drive 50 μA/cm^2 verses the occupancy of the e_g-symmetry electron of several perovskites[244] (copy right AAA Science), and (d) negative theoretical overpotential verses the binding energy difference (ΔG_{O*}-ΔG_{OH*}) showing a volcano-shape activity trend of several transition metals doped Fe_2O_3 (0001) surface[230].

Research effort on optimizing the first row transition metal based electrocatalysts has been continuing with the hope of outperformance relative to noble metals or their oxides in order to replace expensive elements in scaled-up systems. Ternary metal oxides such as Co-Fe-Cr oxide[245] and Co-Fe-Ni/Mn oxides[246] were also investigated. Recently, Suntivich et al. reported that a quaternary perovskite oxide $Ba_{0.5}Sr_{0.5}Co_{0.8}Fe_{0.2}O_{3-\delta}$ (BSCF) showed much higher OER activity than state-of-the-art IrO_2 catalysts in alkaline media (Fig.17c)[244]. Different from previously proposed surface binding energy between metal and OH ions[181,247], this newly developed strategy suggested that the near unity occupancy of 3d electrons and the high covalency of transition metal-oxygen bonds would enhance the OER activity[248]. The successful discovery of the new compound materials for OER electrocatalyst relies on the new strategies and principles developed.

Besides oxides, the most well-studied Co based inorganic OER catalysts is certainly Co-Pi (cobalt phosphate) initially proposed by Nocera in 2008[249]. Afterwards, this catalysts has been extensively applied and studied on various photocatalysts, such as Ta_3N_5[232], $BiVO_4$[250], Fe_2O_3[251], ZnO[252], TiO_2[253], as well as Si[236,254] (Fig. 15c), to enhance OER activity and efficiency. Co-Pi OER catalyst can be (photo)electrodeposited on the surface of conductive substrates or photoelectrodes in a mixture of phosphate and Co salt in aqueous electrolyte. The electrolyte played an important role in chemical composition, activity, as well as the selectivity of Co based catalysts[255]. Further insights on nucleation and growth of Co catalysts during electrodeposition were revealed through an electronkinetic study[256]. Co-Pi OER catalyst on Si photoanode was demonstrated for efficient water oxidation[254b]. Optimization of Si photoanode led to an improved Tafel slope, minimized ohmic loss[236], and eventually capability of spontaneous water splitting with the assistance of multijunction Si cell[254a].

Ahn and Tilley recently reported another cobalt based electrocatalysts synthesized from thermal processing of molecular precursors[257]. The prepared metaphosphate, $Co(PO_3)_2$ exhibited improved catalytic activity compared to Co_3O_4 as well as Co-Pi. The TOF of 0.1-0.21 s^{-1} remained the highest among the first row metal heterogeneous catalysts, showing its great potential as one of the promising catalysts for water oxidation.

The other Co-based catalyst recently developed by Gao et al. was $CoSe_2$ nanobelt[258]. The $CoSe_2$ was synthesized from a hydrothermal based method by mixing $Co(Ac)_2$ and Na_2SeO_3 with diethylenetriamine (DETA) and water. Pure $CoSe_2$ was realized by removing amine from DETA at elevated temperature. The synthesized nanobelt showed layered nanostructure of $CoSe_2$

assisted by the amine groups during the formation. Recently, a hybrid nanocomposite system of Mn_3O_4 and $CoSe_2$ were developed and showed superior OER catalytic activity[259]. Mn_3O_4 nanopartilces decorated $CoSe_2$ nanobelt realized via a heterogeneous nucleation process showed improved OER activity and stability than pure $CoSe_2$ nanobelt or Mn_3O_4 nanorods in 0.1 M KOH electrolyte. The fundamental of the improved activity was confirmed by x-ray absorption spectroscopic study. The measurement confirmed a positive shift of the binding of Co 2p due to the electron donation from Mn_3O_4. This transferred electrons increased the acidicity of Mn_3O_4, which leads to the enhanced OER activity through the Lewis acid-base interaction.

Ni-OER: Ni in forms of (oxy)hydroxides, compared to Mn, Fe and Co is believed to give the lowest overpotential for a fixed current density which was experimentally verified by Subbaraman recently (Fig.17b)[214]. This was consistent with the observation in the study by Brockis et al. on transition metal terminated perovskites[247], in which Ni-terminated perovskite showed highest current density level at a fixed overpotential. All these results triggered further utilization of Ni based OER catalysts.

Ni oxide has been widely used as a co-catalyst on transition metal oxides based photocatalysts for oxygen evolution[260]. The first demonstration of NiO coating on Si photoelectrode was reported by Li et al[261]. Ni metal with a thickness of 10-30 nm was first sputtered on n^+/p-Si substrate and further anodically treated to form NiO(OH). This catalyzed photoanode showed much higher OER activity than Pt. Further improvement was realized by incorporation of W in the Ni film. This structure showed extended lifetime compared to NiO(OH) directly decorated Si photoanode. Recently, Sun et al. synthesized a high quality nonstoichiometric NiO_x thin film from cost-effective low temperature solution based sol-gel method on n-Si photoanode which showed significantly higher catalytic activity than near stoichiometric sputtered NiO[262]. This film served as a protection layer to elongate the lifetime of Si photoanode, an electrocatalyst to reduce the external bias, and a p-type coating for rectifying junction formation to further provide junction voltage. Compared to results presented in ref [158], inferior water oxidation performance from this preliminary study (photocurrent density of 0.2 mA/cm^2 at 1.23 V vs. RHE, Tafel slope of 129 mV/dec in Fig. 15d) was presumably due to the high back-contact resistance, high ohmic loss from NiO_x coating, interfacial loss between NiO_x and Si, and low surface active sites. The demonstrated NiO_x coated n-Si photoanode also suffered with low stability primarily due to developed substantial porosity and subsequent Si corrosion. Combinatorial method by adding alkaline metals or other transition metals in the uniform and pin-hole free NiO_x film to further enhance the catalytic activity and conductivity[263] hopefully with the maintaining photovoltage is current under investigation. Further performance improvement approaches are also under investigation, for example enhancing surface activation sites by introducing mesoporous layer, using passivated "black Si" to replace the polished one, and introducing post-activation processing such as electrochemical or heat treatment.

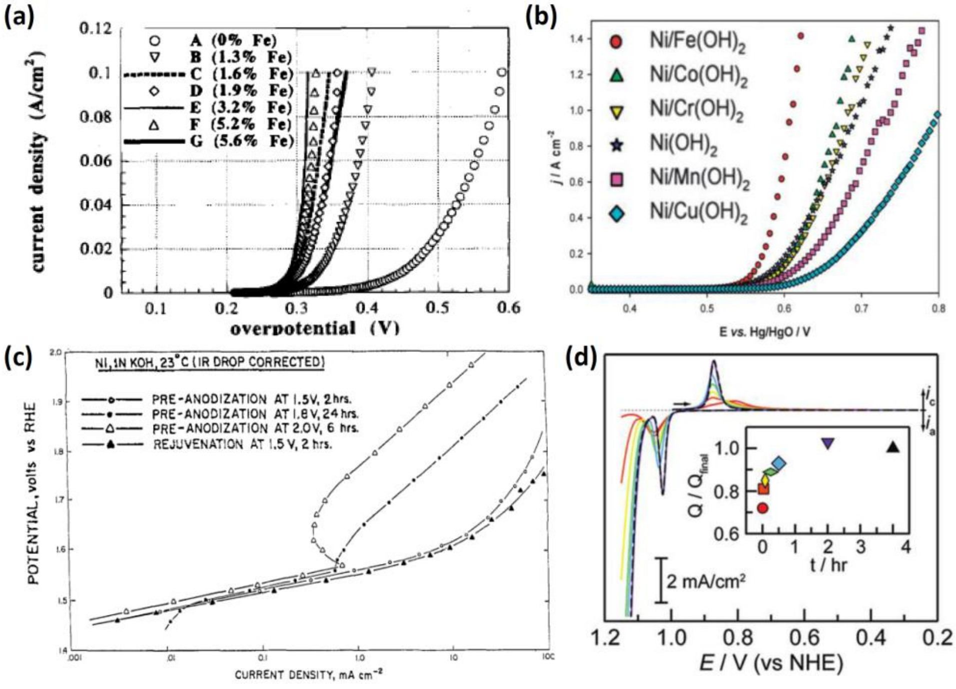

Figure 18. Polarization characteristics of several Ni based OER catalysts. (a) electrochemically deposited Fe-NiO[264] measured in 5.5 M KOH showing reduced Tafel slope with incorporated Fe in the NiO and elongated lifetime after 100 cycle scan (copy right Electrochemical Society), (b) co-sputtered Fe-NiO measured in 1 M KOH showing reduced onset oxygen evolution potential with increased Fe concentration, further increasing Fe concentration reduced the activity[263a] (copy right Electrochemical Society), (c) anodization activation and rejuvenation of Ni catalysts on Ni rod under anodic bias for hours effectively reduced the Tafel slope measured in 1 M KOH[265] (copy right Electrochemical Society), and (d) time of anodization activation effect on NiBi catalyst measured in 1 M KBi (pH=9.2), showing anodization dependent OER activity[127] (copy right American Chemical Society).

Doping NiO using other transition metals (Fe, Co) could improve its activity. Miller et al, for example, showed that adding Fe into NiO film improved the catalytic activity by reducing the anodic on-set potential (Fig.18a)[263]. They demonstrated the improved stability using reactive sputtering. Fe doping showed reduced Tafel slope (95 to 35 mV/dec) and overpotential (447 to 285 mV at 8 mA/cm^2) compared to bare NiO, but exchange current density was dropped significantly ($10^{-6.8}$ to $10^{-10.10}$ A/cm^2). Similar observations were also noticed by Corrigan[264]. However, the Tafel slope and overpotential to reach the same current density reported by Miller et al. were much worse than the electrodeposited film presented by Corrigan[264]. It was also noticed that addition of Fe in the NiO effectively elongated the operation lifetime. However, Miller et al. demonstrated a low temperature processing of electrocatalysts, which showed non-degradation during 7000 hrs of operation, while Corrigan observed the porosity developed in the electrodeposited counterpart. Recently, Landon et al. presented a detailed spectroscopic study on Ni/Fe mixed oxides and revealed that 10 mol% Fe should give the best OER activity with a Tafel slope as low as 40 mV/dec[266]. X-ray absorption study revealed the oxidation state of Fe mainly in 3+, which indicated the improved activity was not due to the Fe active sites but the introduced $NiFe_2O_4$ phase. To the best of our knowledge, the most active NiFe-oxide OER catalyst was presented by Merrill et al[267] using cathodic electrodeposition, in which NiFe-oxide exhibited j_0 of 9.4×10^{-3} mA/cm^2 and Tafel slope of 33.7 mV/dec. Another example of study of transition metals, including Fe, Co, and Cu, doped NiO from cathodic deposition and thermal decomposition was presented by Li et al[268]. Similarly conclusions that Fe doping led to an improved catalytic activity of NiO compared to other metal dopants were drawn (Fig.18b). Lena et al. presented a study of several typical transition metal oxide based OER catalysts including NiO_x, CoO_x, Co-NiO_x, Fe-NiO_x, MnO_x, FeO_x and IrO_x from solution based method[269]. Films with ultrathin thickness of 2-3 nm were studied. The NiOx based catalyst doped with Fe also showed the best OER catalytic activity with a Tafel slope of 30 mV/dec and current density of 10 mA/cm^2 at overpotential of 336 mV.

In addition to foreign dopants using other transition metals, the activity of Ni based OER catalysts can be improved by electrochemical treatment. Activation and rejuvenation of aged oxides film can be realized by applying anodic bias for a period of time, which was attributed to the recovery of active sites on the surface[265]. The film rejuvenated at a lower anodic bias (1.5 V vs. Hg/HgO) compared to the operation bias (1.8 V vs. Hg/HgO) at room temperature for 2 hrs showed comparable performance, compared to fresh activated samples (Fig.18c curve 3 and 4).

Another Ni based OER catalyst electrodeposited from borate or phosphate buffer (NiCat) showed similar structure to Co based catalysts prepared using similar methods[270]. Most importantly, NiCat and CoCat prepared using this method shared some common features with the well-known natural Mn_4Ca catalysts. The detailed structure study was recently elaborated by Bediako et al[271]. Ni Borate (Ni-B_i) with a formula of $Ni^{III}O(OH)_{2/3}(H_2BO_3)_{1/3} \cdot 1.5H_2O)$ synthesized from electrochemical deposition was demonstrated by Nocera's group as a good alternative to previously proposed Co-OERs. Initial study on non-optimized coating on ITO glass showed catalytic activity of 1 mA/cm^2 at overpotential of 425 mV. Recently researchers demonstrated improved performance (2 orders of magnitude increased in OER activity) by introducing anodic activation on the electrodeposited film (Fig.18d)[127]. X-ray absorption studies revealed increased oxidation state (average from +3.16 to +3.6) and local structure change in the activated Ni-Bi catalyst. Important experimental evidences brought to conclusions that Ni(IV) oxidation state was more active and γ-NiOOH phase was more efficient than β-NiOOH phase, which was against well-accepted theories.

OER catalytic activities of other transition metal compounds were also investigated. For example, Osaka et al. prepared the transition metal borides including Ni_xB, Co_xB and Fe_xB were prepared through solid state reaction by annealing metal and boron powder[272]. They found metal borides showed higher Tafel slope than that of the metals and Tafel slope reduced with the increasing metal concentration. Transition metal boride showed higher OER activity than pure metals in the order of $Ni_xB \approx Co_xB >> Fe_xB > LaB_6 > Co \approx Fe > Ni$.

Others: A small band gap degenerate Tl_2O_3 film was coated on n-Si using photoelectrochemical deposition. A band bending of 1 eV through the junction of n-Si and degenerate Tl_2O_3 with an energy band gap of 1.4 eV and first direct transition of 2.2 eV was reported[273]. This semi-transparent film also showed antireflection, but significant absorption with increased thickness. Interestingly, this coating showed enhanced catalytic activity similar to Pt and good stability in alkaline solution under anodic bias.

Outperforming and cost-effective catalysts containing earth abundant elements are essential for high efficiency and large-scale production of solar fuel. There is a great demand on engineering new transition metal electrocatalysts with high activity and stability, through compositional and local structural manipulation. To understand the local structure of transition metal based compound and active sites, oxidation states, reaction intermediates/kinetic, as well as degradation pathways are extremely important in order to design and engineer optimized electrocatalyst meeting all the required criteria. Well accepted techniques for obtaining these insights through in-situ measurements include ellipsometry[265], x-ray absorption near edge spectroscopy (XANES)[214], x-ray absorption fine structure (EXAFS)[274], Raman spectroscopy[275], X-band electron paramagnetic resonance (EPR) spectroscopy[276], and FT-IR spectroscopy[277]. Recently, it was reported to use high energy x-ray scattering and pair distribution function analysis for structural information that are not able to be obtained directly from other previously used methods, such as full range of atom-atom distances[278]. To obtain improved surface area or to expose edge/face active sites for high-current density applications, electrocatalysts with mesoporous or nanoscale structures are desired. However, porous/nano-structure does not provide integrity of Si protection, which could result in photopassivation of Si over long time reaction. Not only is this true for semiconductors that have anodic decomposition potential more negative than water oxidation level[279], but also for semiconductors that have cathodic reduction level more positive than water reduction level[6,280]. In this case, additional interfacial layer between electrocatalyst and underneath photoactive material should be considered for protection purpose, which has to be stable and meanwhile maintains the facile carrier transportation to oxidant or reductant in electrolyte. Rectifying interfaces between electrocatalysts and underneath photoactive materials are also critical in system design to prevent back flow of electrons. When examining the developed catalysts, materials are typically coated on TCO substrates and undergo high temperature thermal treatment. Thus, one should be aware of the interdiffusion of elements from TCO to the catalysts and loss of conductivity of substrates when conducting temperature dependent activity studies. Therefore, there is a continuous need for catalysts that can be processed at low temperature that is compatible with the processing of temperature sensitive substrates like multijunction amorphous Si[203]. Finally, fundamental understanding of the degradation process with great effort on developing nanoscale electrocatalysts is critical to design stable electrocatalysts with long-term stability. Meier et al. recently reported an aging study using transmission electron microscope (TEM)[281]. Processes of stability loss were revealed including detachment, dissolution, Ostward ripening, agglomeration, and support corrosion. Understanding these fundamental issues will assist on designing and optimizing electrocatalyst coating on photoelectrodes in solar fuel production applications.

1.4.3 Hybrid system

Physically, a qualified organic modification should effectively unpin the surface Fermi level and regain the control of energy barriers, meanwhile isolate Si from aqueous solution, and separate/conduct photo-induced charge carriers. These requirements are similar to the previous discussed inorganic approach. Most concerns of the organic system include its stability under illumination in aqueous solution with harsh environment (basic/acidic or even neutral), adhesion strength to underneath substrates, and efficiency of charge transfer. However, organic approach does have some advantages. For example, typical organic coating does not require high temperature or high vacuum, and thus does not need high profile equipments for deposition, which could make this approach relatively cheap and affordable. Moreover, hybrid system utilizing redox couples as a sacrificial agent enables the use of single junction Si photoelectrode for H_2 fuel production. Hybrid systems are typically realized in several different ways. We will first review methods including organic polymer coatings, molecular approach to modify Si surface termination, and electroactive polymer containing redox couples. In the second sub-section, we will brief summarize the development of heterogeneous and homogeneous molecular HER and OER catalysts.

1.4.3.1 Polymer, surface derivatization, and redox couples

Polymer: Specifically, bare n-Si passivates completely in a few seconds under illumination with light intensity close to 100 mW/cm^2. Besides inorganic materials discussed in previous sections, organic polymers were proposed and used to protect photoelectrode from this undesirable passivation[282]. Advantages include convenience of preparation and facile characterization of the polymer, rapid deposition of films onto a variety of surfaces, and stability of the electrostatically bound ion systems. Apparently, conductive polymer has superior advantages over non-conductive one due to the lower ohmic loss in the coating. Skotheim et al. demonstrated an addition of conductive polypyrrole film on n-Si using electrochemical deposition which showed a low resistance resulting in an improved fill factor due to the rapid electron transfer kinetics, and improved photovoltage due to a lower degree of surface pinning[283]. Further improvement on conversion efficiency was realized by integrating with a thin Pt film[284].

Another hole conductive polymer for n-type photoelectrode protection is polyacetylene $(CH)_x$, the simplest conjugate polymer. The n-Si|$(CH)_x$ photoanode was able to maintain structure integrity and current density up to 23 hrs operation at low light intensity[285]. The formed Schottky junction and conductive nature of the polymer helped the photogenerated holes transfer to the electrolyte.

Unlike polypyrrole or polyacetylene, polyaniline film shows good conductivity for both holes and electrons, meaning its potential application for both photocathode and photoanode. Polyaniline coated n-Si showed significantly improved stability up to 72 hrs, while polyaniline coated p-Si showed cathodic shifted onset potential which assisted on the improvement of charge transfer kinetics[286]. The photopassivation of Si was greatly suppressed by polymer coating on n-Si, due to the improved kinetics of charge transfer to electrolyte[286]. Limited long-term stability in previous studies was believed due to the non-uniform coating of a thick film with weak adhesion strength. Moreover, optical properties of the polymer in the early development of photoelectrode coating are not considered, such as the dielectric constant, refractive index and absorption coefficient[287].

Application of phthalocyanine (Pc, a covalently bonded mediators) as a dye to sensitize wide band gap materials, such as TiO_2[288], WO_3, and SnO_2 has been demonstrated, because of its visible light sensitivity[289]. P-type semiconducting nature has enabled metal phthalocyanines (M-Pc) to be broadly applied in organic optoelectronics devices[290]. Pc films are potentially useful for photoelectrochemical cells because of their hydrophobicity and catalytic properties[19,291]. Applications of metal-free phthalocyanine (H_2Pc)[291] and metal-Pc like Cu-Pc[19] and Fe-Pc[292] coating on n-Si have been conducted. These formed heterojunctions showed rectifying current-voltage behavior, indicating a formed Schottky barrier which was essential to provide driving force for charge separation[293]. The photocorrosion process was remarkably decreased on the Pc coated Si photoelectrode, but the rate of formation of the insulating layer was greatly dependent upon the nature of the redox couple in the measurement electrolyte. Addition of iodine, which is a dopant for the Pc layer, led to larger photo effects and a lower rate of photopassivation. However, the electrode was still unstable after long time irradiation. Bard et al. reported that Pc coated n-Si never showed long term stability at high light intensities (135 mW/cm^2)[19]. Moreover, light absorption could be significant in the Pc coating, which would limit the Si response and also lead to photoresponse and significant surface band bending at the Pc coating/electrolyte interface[294]. Toshiyuki et al. demonstrated that H_2Pc outperformed metal-Pcs with higher surface kinetics and activity as a photoanode coating[295]. Recently, Yang et al. extended this Pc on n-Si nanowire array coated with iodine doped PEDOT polymer. The nanowire array was etched using a metal assisted chemical etching[296]. Only H_2 gas was generated due to introduced redox shuttles with a solar fuel conversion efficiency of 3%.

Surface functionalization: Hydride-terminated Si shows lowest density states and recombination velocity[86], but it is not stable in aqueous solution as discussed above. Different from polymer coated Si, surface functionalization of Si through molecular monolayer treatment by forming alkyl-group[297], methyl-group (C_2H_5), ethyl-group (CH_3), allyl-group (CH_2CHCH_2), and mixed functional groups terminated surface could maintain the electrical properties of Si. For example, H-Si, through a facile tunneling barrier, provided improved stability in aqueous solution[28,298]. Meanwhile, this surface functionalization could also manipulate S/E energetics to allow the surface band edge position independent from pH change, while energy barrier depends on the pH value. Moreover, the surface functionalization could minimize the surface defects and thus recombination velocities. Moreover, functionalized Si surface can be further derivatized by attaching some redox couples, such as Fc[299], to modify the charge transfer kinetics.

Redox couples: Organic or nonaqueous solvents were used to effectively limit the photopassivation of Si, in which dissolved redox couples were the electron donor instead of water[300], and to provide more options on selecting efficient intermediate redox couples with different redox potentials between the band edge of Si for Si photoelectrodes[301]. Moreover, electrolyte containing redox couples can avoid hassles in fabricating conformal metal contact particularly when dealing with nanostructured photoelectrodes in liquid junction solar cell. For example, Legg et al. used ferrocene/ferricenium couple on n-Si[301]. Yuan et al. used a methanolic electrolyte solution consisted of dimethylferrocene (Me_2Fc) and Me_2FcBF_4 to study the photoanodic behavior[75]. Similarly, Santori et al. investigated lightly doped n-Si microwire in contact with a 1-1’-dimethylferrocene ($Me_2Fc^{+/0}$). Heller et al. presented p-Si photocathode with vanadium[302], and Warren et al. used N,N'-dimethyl-4,4'-bipyridiniumredox ($MV^{2+/+}$) on p/n^+-Si microwire[29].

Concept of water splitting using this strategy relies on the mediated redox reaction (A/A^+, B/B^+) by manipulating charge transfer kinetics[303], which can be described using the equations below:

$$A^+ + e^- \xrightarrow{p-Si,h\nu} A \qquad (5a)$$

$$2A + 2H_2O \xrightarrow{Catalyst} 2A^+ + 2OH^- + H_2 \uparrow \qquad (5b)$$

$$B^+ + h^+ \xrightarrow{n-Si,h\nu} B \qquad (6a)$$

$$2B + 2H_2O \xrightarrow{Catalyst} 2B^+ + 4H^+ + O_2 \uparrow \quad (6b)$$

Based on these studies, a wide selection of electroactive redox couples either covalently bonded to surface or confined in supporting polymers close to the electrode surface, has also been studied and applied to Si surface[18]. For example, Wrighton et al. proposed a new structure containing a photoelectrochemical active ferrocene (Fc) covalently attached to the surface derivatized n-Si to stabilize the electrode from photocorrosion[21,304]. This derivatized n-Si exhibited acceptable durability in acidic condition, while corrosion of Fc coating happened in alkaline solution[21]. This surface-attached Fc species can be repetitively cycled between its oxidized and reduced form by linearly sweeping the illuminated electrode cyclically. Results using this derivatized surface showed that this structure did protect the n-Si to a substantial extent from SiO_2 formation up to over 30 min, and the surface attached species were photoelectrochemically active. Mediation reaction of Fc in this system was further investigated by Bocarsly et al. using a two-electron reductant-N,N,N',N'-tetramethyl-p-phenylenediamine (TMPD),which showed separated one-electron transfer on a Fc derived n-Si[305]. In this study, Fc was first attached on cleaned and NaOH treated Si surface through Si-O-Si bond[304a]. It was observed that n-Si without surface derivatization gave a very irreproducible behavior at low

TMPD concentrations presumably because the Si oxidation was competitive with the TMPD oxidation, while the derivatized n-Si showed mediated TMPD oxidation through the regeneration of surface ferricenium. This surface derivatization method successfully inhibited the Si photopassivation. However, energetically the Fc derivatized Si was not able to oxidize water spontaneously.

Besides covalent attachment of redox mediators onto Si surface, redox couples can be also incorporated in a polymer. For example, the polymer incorporated with Fc redox ions was electroactive and applied to the n-Si photoanode surface[306]. Because of the positive charges on the backbone, negatively charged ions were attracted to the polymer. Increased negatively charged ions on the polymer surface helped to increase the capability to capture holes generated from the n-Si. Improved photocurrent stability of p-Si with surface decorated with a N,N'-dialkyl-4,4'-bipyridiniumredox ($PQ^{2+/+}$) contained polymer was reported by Bookbinder et al[307] based on a previous research on the liquid junction containing a $PQ^{2+/+}$ redox couple[303]. The coating significantly lowered the cathodic photocurrent onset potential by 0.3 V compared to naked p-Si. However, this structure did not exhibit a significantly improved HER efficiency without addition of catalyst. Pt was then introduced into the polymer through ion exchange followed by photoreduction of $PtCl_6^{2-}$, which resulted in a uniform Pt distribution in the PQ contained polymer[308].

Another electroactive polymer layer containing polybenzylviologen (PBV) with a thickness of 50 nm ~ 2 μm, presented by Abruña and Bard, was deposited on p-Si[309]. PBV electroactive polymer dramatically catalyzed the water reduction reaction by shifting the onset potential anodically and improving photocurrent. Incorporating a HER catalyst of photoreduced Pt into the polymer coating could further enhance the H_2 evolution, which would successfully regenerate the reduced PBV. For this system, the loss of photocurrent was mainly due to the decomposition of viologen even at low light intensity.

Others: Early development on Si electrochemistry/photoelectrochemistry was involved in the use of HF containing electrolyte to in-situ etch away the insulating oxides during Si operation in aqueous solution. Examples electrolytes include HF/HNO_3[310], HF buffered by HCl, fluoride/HF[311]. It was also reported to have a greater improvement in stability when a concentrated electrolyte was used[312]. This can be attributed to a decrease in water activity and a concomitant decrease in the rate of water penetration through the film[19]. However, these methods require harsh acidic/toxic electrolytes, which could not be a low-cost environmental friendly approach for solar fuel production.

1.4.3.2 Molecular complex

Inspired by hydrogenases for water reduction and Mn-centered complex catalyst for water oxidation existing in nature[313], engineers can certainly apply highly active enzymes on inorganic light absorber for a hybrid system. The first breakthrough of the hybrid system using molecular complex on inorganic photoactive material was demonstrated by Nann et al. using Fe-Fe hydrogenase linked onto a layered nanocrystal InP photocatalyst[314] to realize electrocatalyzed proton reduction for H_2 generation. The catalytic reaction was recognized through the Fe-H and/or S-H bond. The system demonstrated no-deactivation for 1 hr operation at low overpotential in neutral electrolyte. Recently, homogeneous Fe-Fe hydrogenase catalyst demonstrated robust H_2 generation from proton reduction together with p-Si photocathode (Fig.19c and d)[315]. All these pioneer work paved promising future for efficient solar fuel production using such a hybrid system, like DS-PEC (dye sensitized photoelectrochemical cell) by attaching molecular electrocatalysts on molecular dyes in DSSC[316]. There is lots of research focusing on this area[317]. Organic complexes surface functionalized Sican be realized by effectively binding the enzyme to the substrate through active binding sites. However, research should focus on the intra- and inter-molecular charge transfers to reach high activity by lowering the overpotential, minimizing back charge transfer/reaction, and increasing exchange current. Light sensitivity of molecules and its photo-stability are also important. Interfacial protection layer between complex catalysts and Si substrate is highly required to prevent Si photoabsorber from passivation.

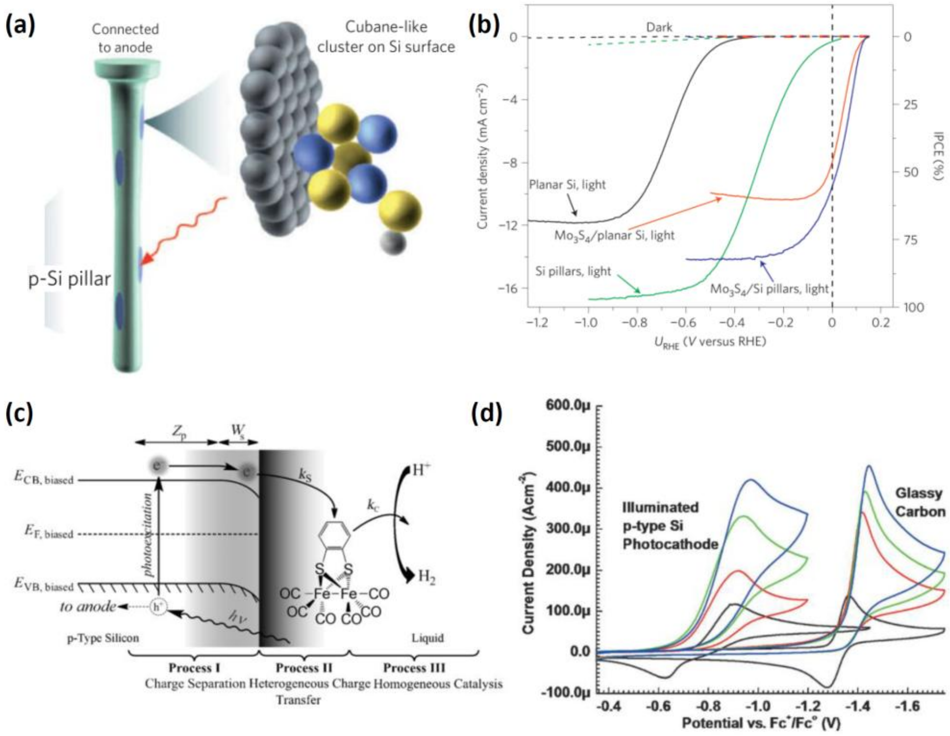

Figure 19. Hybrid photocathode based heterogeneous and homogeneous catalyst modified p-Si. (a) schematic of Si microwire decorated with MoS_x molecular catalyst, (b) polarization characteristics of catalyzed planar Si and microwire array measured in 1 M $HClO_4$ solution showing improved HER activity[196] (copy right Nature), and (c) energy band diagram and illustration of charge transfer process on [Fe-Fe] homogeneous catalyzed Si for proton reduction, and (d) cyclic voltammetric study measured in 0.2 mM $[Fe_2(\mu\text{-bdt})(CO)_6]$ (bdt=benzene-1,2-dithiolate) in 0.5 M TBAH/acetonitrile with varying $HClO_4$ concentrations[315] (copy right Royal Society of Chemistry).

Thermodynamic and kinetic issues of Si photoelectrode in aqueous solution are considered as the major problems for Si as practical photoelectrodes. In this section, we have reviewed research efforts aiming to solve these issues through a heterogeneous alternation at the S/E interface using metal, compound semiconductors, organics etc. An ideal method should provide a coating, that 1) is robust with minimum corrosion in the operation window and high quality to lower the chance of electrode degradation both in dark and under operation, 2) provides large photovoltage to lower the bias needed to drive the reaction, 3) enhances light scattering or at least does not absorb too much light, and 4) offers electrocatalytic activity to further lower the externally applied electrical energy input. Some developed approaches have successfully demonstrated improved efficiency and lifetime of Si photoelectrodes. The high quality Schottky junction between the coating and Si is essential to replace the direct junction between Si and electrolyte and isolate Si from photoanodic passivation. The solar conversion efficiency of surface modified Si photoelectrode greatly relies on the new Schottky junction formed between the coating materials and underneath Si[318], as well as the charge transfer between coating material and redox couple in aqueous electrolyte, though there are limited examples of different approaches that have been successfully demonstrated to be applied to Si photoelectrode yet.

1.5 Spontaneous water splitting and artificial photosynthesis

1.5.1 Spontaneous water splitting

Regarding the intrinsic limitations of Si, spontaneous water splitting using Si was proposed, which can be realized through two typical configurations: a photochemical diode (Fig. 19a) and a tandem junction photoelectrochemical cell (Fig. 20a).

Photoanode and photocathode configuration (Fig.20a) or so called photochemical diode was firstly proposed by Nozik[319]. This system is represents an inorganic analogy of biological photosynthesis (z-scheme), where two photons are absorbed to generate one electron[320]. Design strategies considering the material band gap and overpotential loss were presented by Weber[321]. Generally, overlapping of the photoanodic and photocathodic current is necessary to obtain a spontaneous water splitting device. Ideally, the two photoelectrodes with high fill factor cross at high current density level (curve a and d in Fig.20b) exhibits high efficiency. On the other hand, if two photocurrents cross at low current density (curve b and e in Fig.20b) or even do not cross, external bias will be needed.

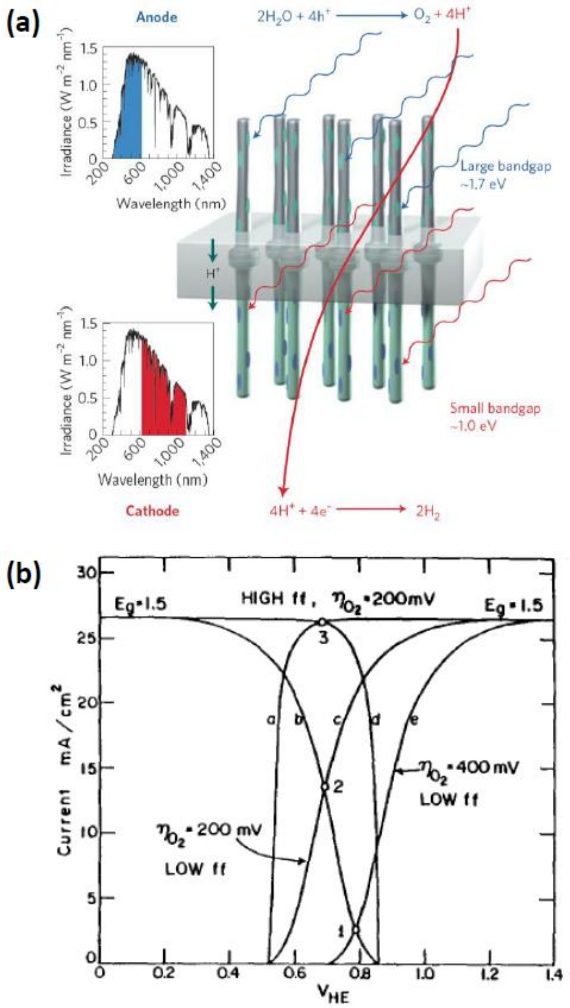

Figure 20. (a)Photoelectrochemical diode configuration using microwire arrays[8] (copy right Nature) (b) Efficiency analysis[321] in which curve a, c, and e are photoanodic current, curve b and d are photocathodic current (copy right Elsevier).

As illustrated in Fig. 19a, this design consists of 4 important components: n-type photoanode material which has E_{VB} lower than the water oxidation level, p-type photocathode material which has E_{CB} higher than the water reduction level, an ohmic contact between cathode and anode, and finally a proton exchange membrane (PEM) for proton transfer and pH balancing.

Using Si for spontaneous water splitting and artificial photosynthesis can be simply realized by incorporation a p-Si photocathode with a photoanode, which can effectively handle the water oxidation half reaction (Fig.22 Scheme 1). In this scheme, a minimum required photovoltage from the photoanode is 1 V assuming that the amorphous Si photocathode with HER provides an onset potential of 0.3 V vs. RHE. This photovoltage can be translated to an anodic photocurrent onset potential at around 0.2 V vs. RHE. Several wide band gap photoanode materials can be selected. For example, n-type WO_3 and InGaN could be candidates as the photoanode materials that can be used to couple with p-type Si in a spontaneous water splitting device. Considering the solar spectrum and absorption coefficient, the theoretical maximum photocurrent from anode and cathode should match (Fig.20a shaded spectrum on the left), otherwise total photocurrent and thus conversion efficiency are limited by the low current end. Transparent ohmic contact to both photoanode and photocathode is important to provide charge conducting channels and to allow maximized light with longer wavelength arriving at the Si photocathode side.

Ohmic contact and PEM that are electrically and ionically conductive are required to allow charge transfer between photoelectrodes and protons transport from one side to the other side of photoelectrodes. Widely used PEM provides transportation of protons; meanwhile separate the reactants and products. PEM is a critical component, actually, in both of the spontaneous water splitting devices as illustrated in Fig.20a and Fig.21a, to minimize the ionic loss and electronic loss[322]. Typically, metal junction to connect anode and cathode has to be avoided to maximize the light arriving at the cathode through the membrane (Fig.20 incident light comes from the anode side and longer wavelength light arrives at the cathode side). Therefore, this PEM also serves as the transparent ohmic contact between the photoanode and photocathode to minimize the optical loss through this membrane. In addition to the capability of transporting charge carriers and ions with minimal ohmic losses, this membrane should be chemically/mechanically stable.

A demonstration of this membrane was realized through a simple mixture of PEDOT-PSS (poly(3,4-ethylenedioxythiophene)–poly(styrene sulfonate)) and Nafion. The electrical and ionic conductivity of the composite, as well as the transmittance, mechanical stability was characterized as a function of the PEDOT-PSS weight concentration in the composite. Suitability studies on this composite material for this technique are currently under investigation. For example, investigation on the electrical conductivity particularly at the composite membrane and single Si microwire interface was demonstrated by Yahyaid et al[323]. The polymer composite of PEDOT-PSS/Nafion with 12 wt% PEDOT/PSS was drop casted on the p-Si microwire or on both p- and n-Si microwire. The total resistance of the microwire/polymer and microwire/polymer/microwire system, in which the ohmic junction were formed by applying smaller amount of pressure (12 $mN/\mu m^2$) on both p- and n-Si microwire, was measured using a force-assisted probing method. The resistance measured at low bias region was larger (1040 $k\Omega$) than the desired resistance (480 $k\Omega$) needed in the proposed system. This additional loss can be minimized by applying a highly doped region between the polymer and Si, as well as by effectively removing the native oxides. Two membranes of Si microwire embedded in Nafion were assembled through an intermediate PEDOT-PSS film by Spurgeon et al[324]. Addition of PEDOT-PSS offered minimum reduction of ionic conductivity of Nafion membrane. This hybrid system showed impermeability of produced H_2 comparable to the commercial Nafion. Although the assembly showed acceptable ionic and electrical resistance, further improvement was suggested. For example, metallic ohmic metal contact can be applied to semiconductor before embedding in membrane to reduce the contact resistance.

Interestingly, in the report by Spurgeon et al[324], the anion exchange membrane (AEM) consisting anion exchange ionomer poly(arylene ether sulfone) functionalized with quaternary ammonium groups (QAPSF) was also proposed and for the alkaline electrolysis. Needs for alkaline electrolysis over traditional acid electrolysis increase for various reasons: 1) oxygen evolution reaction is inherently easier at alkaline condition, 2) eliminate the use of expensive Pt usage as HER catalyst and enable to use of non-noble transition metal catalysts which show alkaline activity and extended stability in alkaline environment[325] (see Table. 1), and 3) enable the use of cheaper materials with controllable corrosions[326]. Recently Xiao et al. demonstrated the first alkaline solid electrolyte which allowed the device to work in pure water environment[327].

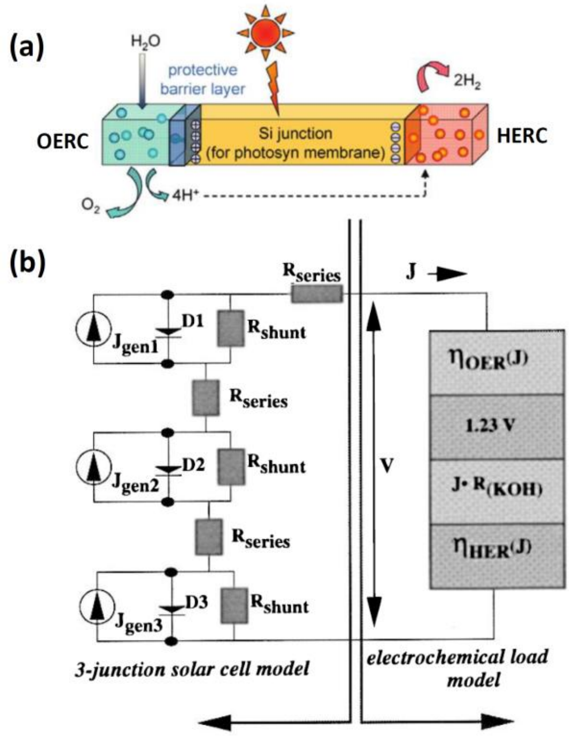

Figure 21. (a) Si multijunction solar cell based solar fuel cell (modified from ref [9]), and (b) Analytical model for photoelectrolysis based on a solid-state photogenerator (shown for a triple-junction device) driving an electrochemical load[118] (copy right American Chemical Society).

So far we have discussed the photochemical diode configuration for spontaneous water splitting and fundamental consideration in the system design in the material and device level. The other format of device capable of spontaneous water splitting is based on tandem junction solar cell with two sides decorated with property electrocatalysts (Fig.21a). First demonstration of practical solar water splitting was realized by utilizing a tandem junction amorphous Si photoelectrode built on stainless steel (SS)[328]. Thin Pt film was evaporated on the n-Si side to catalyze water reduction and heat-treatment of deposited Pt could slow down the photocurrent decay. H_2 evolution was noticed at the bias that was 0.8 V more positive to Pt electrode, due to the high photovoltage generated by the SS|p-i-n|Pt junction. The solar fuel conversion efficiency (SCE) was calculated to be 2.3% in 0.5 M H_2SO_4 electrolyte and later optimized to be as high as 3.56% under assistance of an external bias[329]. The double junction SS|2×[p-i-n]|Pt tandem cell showed onset of photocurrent and H_2 evolution at 1.6 V more positive to Pt electrode. This photovoltage was higher than the thermodynamic required for water splitting 1.23 V, indicating the spontaneous decomposition of water in this double junction tandem cell. In this case, the conversion efficiency was as low as 0.25% under standard condition. Improved energy conversion efficiency of 1.98% was achieved on RuO_2|SS|2×[p-i-n]|Pt tandem cell, due to the utilization of Ru-OER catalyst[329]. H_2 evolution and photocurrent onset potential could further reach as high as 2.08 V and dark current was suppressed based on a new tandem structure, GaIn|crystal p-Si|microcrystal n-Si|2×[p-i-n]|Pt. The net SCE was improved to be 2.93% on RuO_2|GaIn|crystal p-Si|microcrystal n-Si|2×[p-i-n]|Pt tandem cell with a short circuit current (J_{SC}) of 2.38 mA/cm^2.

The first wireless demonstration of spontaneous water splitting using triple junction amorphous Si and low-cost electrocatalysts in a system of NiFeO|SnO_2|3×[p-i-n]|ZnO|MoNi showed a SCE efficiency of 2.5%[330] with J_{SC} of 3.9 mA/cm^2. An improved SCE as high as 5-6% and a photocurrent of 4 mA/cm^2 were achieved utilizing an inverted structure Ni/Pt|SS|3×[n-i-p]|ITO|FTO working in alkaline electrolyte[165]. ITO was recognized as the main cause of photoelectrode deactivation. Success in protection of ITO resulted in extended lifetime up to 50 hrs. Pt|SS|3×[n-i-p]|Pt showed J_{SC}=6.6 mA/cm^2 and SEC efficiency of 7.8%[331]. By replacing Pt with cost effective CoMo alloy as HER catalyst and Fe doped NiO as more effective OER catalyst, a higher photocurrent of J_{SC}=6.48 mA/cm^{2}and an improved SCE of 7.45% could be obtained on a system of CoMo|SS|3×[n-i-p]|TCO|NiFeO$_x$[118]. Recently, another amorphous Si-based triple junction tandem cell with a structure of NiMoZn|SS|3×[n-i-p]|ITO|Co-Pi was demonstrated by Reece et al. as a water splitting device[254a]. The wireless configuration of this device could operate stably for over 30 hrs in KBi supported electrolyte, and demonstrated a SCE efficiency of 1.7% with J_{SC}=5.9 mA/cm^2, while the wired configuration gave 4.7% for the SCE efficiency with J_{SC}=6.5 mA/cm^2. The reduced efficiency from the wireless configuration was presumably due to the ohmic loss through longer transfer pathway and low ionic conductivity of the electrolyte. Again, authors argued the instability of the photoelectrode was primarily due to the ITO. Replacing ITO with a more stable TCO that is compatible with the low temperature processing of amorphous Si could potentially elongate the operation lifetime. Actually, the records held for spontaneous water splitting were from group III-V based tandem junction cell with a J_{SC}=120 mA/cm^2 and SCE of 12.4%[5]. Licht et al. demonstrated a hybrid III-V/Si with efficient RuO_2 OER catalyst which showed a J_{SC}=20.5 mA/cm^2 and SCE of 18.3%[332]. Overall, SCE greatly depends on the tandem cell design and performance of electrocatalysts. Generally, it is concluded that PV cells with low V_{OC} should be matched well to the catalysts with higher catalytic activity, while PV cells with high V_{OC} is less sensitive to the catalytic activity[333]. A detailed discussion on the tandem solar cell method and system-level comparisons of various milestone electrocatalysts developed in literatures can be found in section 5.3.

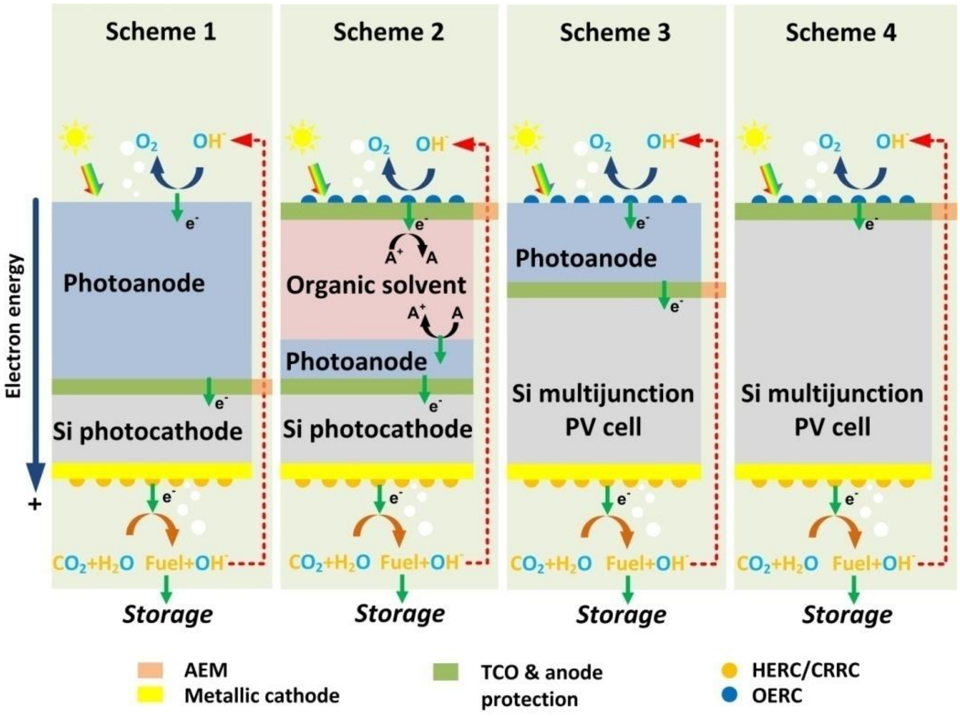

Figure 22. Si based solar fuel production schemes based on alkaline electrolysis: (scheme 1) photoelectrochemical diode using Si photocathode and a semiconductor photoanode, (scheme 2) hybrid solar fuel cell using Si photocathode and a DSSC, (scheme 3) multijunction Si cell and photoanode, and (scheme 4) multijunction amorphous Si.

Besides the two aforementioned strategies for Si based spontaneous water splitting and artificial photosynthesis (scheme 1 and 4 in Fig.22), two other schemes for these purposes are also promising. All the viable schemes for spontaneous water splitting and artificial photosynthesis are summarized in Fig.22. Note that light management, such as light trapping or guiding features, on photoactive components is not shown in the schemes proposed in Fig.22 for simplicity. All the physical geometries are not to scale.

In scheme 1, besides selections of photoanode discussed by Weber[321], additional features developed in the literatures can be incorporated. For example, light comes in from the large band gap material side - the photoanode side. TCO between the anode and cathode maximizes the light arriving at the Si, provides minimum electrical ohmic loss. Metallic cathode decorated with HER or CRR catalysts also works as a back metal mirror to reflect light, and provides protection of the photocathode particularly at idle conditions. Between the p-Si and metallic cathode layer, a n^+ layer can be incorporated between the metallic cathode and p-Si photocathode to enhance the photovoltage. Anode and cathode are effectively isolated by an anion exchange membrane to conduct OH^- ions, because most low-cost transition metal-based catalysts are active and stable in alkaline environment. Red broken line shows the movement direction of OH^- ions. The principle is balancing the ionic current and electric current while minimizing the distance (d) that OH^- ions have to travel from the cathode to the anode. Therefore, geometrical arrangement of photoactive electrodes and the AEM membrane similar to "zero-gap electrolysis cell" has to be optimized considering the complex mass transfer problem under certain hydrodynamic conditions with evolving bubbles at the electrode surface[334]. The ohmic loss in the electrolyte is proportional to the distance and invert proportional to the specific conductivity, which is expressed below,

$$\xi_{jR} = j \cdot \kappa^{-1} \cdot d \qquad (7)$$

where k is the specific ionic conductivity and d is the distance between electrodes[335]. All these engineering approaches to optimize the mass transfer in the photoelectrolysis process ensure the maximized energy conversion efficiency.

Two other schemes, which can be future promising research directions are presented in Fig.22 scheme 2 and 3. In order to gain additional photovoltage to drive the Si photocathode (scheme 2) or the photoanode (scheme 3), one can integrate with a photovoltaic cell. Scheme 2 relies on the high photovoltage from a dye-sensitized solar cell (DSSC). Yum et al. presented a Co based redox for DSSC with high V_{OC} of 1 V[336], which is still not able to split water by itself. Coupling with a Si photocathode could further pump up the electron energy for spontaneous artificial photosynthesis. Considering the absorption spectrum of the dye (Y123) up to 650 nm allowing the rest of the light (700-1100 nm) to reach Si which could potentially generate a J_{SC} of 6.52 mA/cm^2 at a light intensity of 51 mW/cm^2 based on the result reported by Boettcher et al[72]. Similarly, the DS-PEC proposed by Meyer[337] relies also on the DSSC where organic sensitizers are linked to organic catalysts for water splitting. In order to reach a minimum energy of 1.23 V for water splitting and 1.28 V for CO_2 reduction to CH_4. Researchers are right now focusing on the molecular dye and electrocatalysts, interconnection and bonding. Another practical question is what performance one can get from the DSSC. Therefore, future research direction include replacing TiO_2 with other nanostructured semiconductors (such as Nb_2O_5[338]), tandem DSSC by coupling a traditional n-DSSC with p-DSSC using p-type semiconductors such as NiO[339], $CuGaO_2$[340], and $CuCrO_2$[341] to further improve the V_{OC}, and a new redox couple for example $[Co(bpy\text{-}pz)_2]3^+/2^+$ with lower redox potential, hydroquinone/benzoquinone[342], or Fc/Fc^+[343] to replace inferior two electron redox couples I_3^-/I^-.

Scheme 3, on the other hand, relies on a photovoltage from a single[101b] or double junction Si cell (Fig.22). In this case, the battle from having wide band gap requirement for the photoanode in scheme 1, while maintaining high photocurrent density is eased. In this case, front side of the photoanode can be coated with low cost alkaline catalysts, which is not critical for the photoanode in scheme 1 with a wider energy band gap. Importantly, the OER catalyst coating should be transparent to light with minimum absorption to maximize the light arriving at photoactive substrates underneath. Actually, those catalysts that effectively absorb light are not favorable and cannot be directly applied to any other schemes that have photoactive materials underneath.

Besides design criteria in management of light, electron, and ion, researches on practical photoelectrochemical panel modeling are currently conducted in the Joint Center of Artificial Photosynthesis (JCAP)[334], Imperial College London[344] and more others through multiphysics modeling, also for water, gas, and heat management in a practical scaling-up photoelectrochemical reactor. Ideally, what desired are bubbles with small size and short departure time in order to avoid formation of a bubble shield on the electrode surface, which results in a fluctuation of current density, a reduced current density at a fixed bias or an increased overpotential for a fixed current density. So far, researchers from photoelectrochemical field mainly focus on the materials properties of catalysts. Certainly, bubble behavior is a material-related behavior. In industrial electrolysis, it is well-known that the bubble evolution depends greatly on the electrode geometry[335]. In fact, strategies developed in commercial electrolysis could be adopted directly here in the solar fuel devices, for example, at a fixed current density, one may increase the flow-rate of feed-in water, and increase the concentration/temperature of electrolyte[345]. One may also, increase the hydrophilicity of the electrode surface by applying nano-textures.

1.5.2 Artificial photosynthesis

Artificial photosynthesis can be described in the equation below

$$CO_2 + H_2O \overset{h\nu}{\rightarrow} O_2 + hydrocarbon/(CO + H_2) \quad (8)$$

Thermodynamically compared to water splitting, CO_2 reduction (equation 3b as an example) potentials are slightly positive to proton reduction potentials, meaning theoretically if electrons are able to reduce proton, these electrons can be used for CO_2 reduction. Bond strength of carbon oxide and hydrocarbon bond on catalysts surface, similar to OH and H bond on OER and HER catalysts is the key controlling parameter and design guidance for new class of catalysts[346]. Possible pathways of CO_2 reduction reaction are enormous. Selectivity on CO_2 reduction reaction in terms of reaction products with undesired side reaction prevented is crucial. The selectivity is normally a function of catalyst materials, surface morphology/orientation, and interestingly on external bias.

Noble metals, such as Pt[347] and Au[348] showed improved CO_2 reduction catalytic activity by controlling the surface morphology and size. Late transition metal, Cu, is one of the most well studied CO_2 reduction catalysts[349]. Cu, together with Au and Ag decorated on p-Si showed CO_2 reduction capability under illumination[350]. Surface morphology and cyrstallanity can be controlled for improved selectivity[351]. Cotineau et al. demonstrated Cu nanoparticle decorated p-Si photocathode for CO_2 reduction[350b]. Cu particles were deposited from electrochemical deposition and the size of Cu particles was controlled by the deposition conditions. It was found that pulsed deposition assisted the formation of nanometer size particles with an optimized Cu coverage. However, this electrode showed severe degradation from unstablized Si substrates due to significant oxidation at exposed area. Further modification can be realized by replacing Cu with oxidized Cu(I) and Cu alloy nanoparticles[352] for better catalytic activity[353]. CO_2 reduction on other low-cost 3d transition metals has been theoretically and experimentally studied before. For example, Liu et al. recently presented a computational study of intrinsic catalytic activity of 3d transition metals (Fe, Co, Ni and Cu) by investigating the CO_2 reduction on the (100) surface of FCC (face centered cubic) lattice structure[354]. Based on their plane-wave density functional theory (PW-DFT) calculation, Cu showed minimum interaction with CO_2, while Fe is the most favorable surface for CO_2 adsorption. Both Co and Ni showed favorable thermodynamics and low CO_2 decomposition energy barriers.

Besides inorganic CRR catalysts, application of metal organic complexes for CO_2 reduction are developed. For example, Arai et al. demonstrated a heterogeneous Ru complex or complex containing polymers as a heterogeneous catalysts on a small band gap material CZTS (Cu_2ZnSnS_4) or p-InP for CO_2 reduction to generate organic compound such as $HCOO^-$[355]. Kumar at al. demonstrated Re-complexes in electrolyte and Si as an electron source when illuminated by sun light for CO_2 reduction was reported using p-Si[356]. Free electrons excited in p-Si by photons are able to transfer to the S/E interface to generate H_2 with p-Si operated in aqueous electrolyte. Meanwhile, excited electrons are able to work with the homogeneous Re complex based catalysts with TOF > 200 s^{-1} in the electrolyte for CO_2 reduction to generate CO as another kind of fuels. The competition of reduction of CO_2 and water could be tuned by varying the concentration of the Re complex and water content. The Re complex catalyst exhibited selectivity of CO_2 over water reduction. The origins of the selectivity and deactivation were investigated and reported recently[357], to understand the basic principles for the improved performance. Surface functionalized Si using phenylethyl-group showed improved catalytic current behavior over H-Si, suggesting a scientific importance to understand the charge transfer from Si to electrocatalyst for designing future artificial photosynthesis system[358]. Innovative ideas to avoid struggling on poor selectivity for direct reduction of CO_2 on various catalysts were demonstrated on p-Si nanowire by mimicking the CO_2 fixation reaction in Calvin Cycle[359]. Si nanowire in this experiment was treated by metal assisted electroless etching. CO_2, instead of directly reduced with free electrons, was first fixed through surface attached benzophenone on Si nanowires. Electrochemical carboxylation reaction was then driven by the free electrons excited at the rectifying junction with energy barrier height of 0.86 V between benzophenone and illuminated p-Si in organic solvent. This system showed Faradic efficiency of over 94% and TOF of up to 25.8 s^{-1} under AM 1.5 illuminations and at low overpotential.

1.5.3 Electrocatalyst evaluation and system efficiency analysis

Among all the aforementioned spontaneous water splitting schemes based on Si, scheme 4 is the only one that has demonstrated practical prototypes together with advanced electrocatalysts. In this section, we will extend the discussions in ref [333] and compare the system using different combination of some outperforming electrocatalysts summarized in section 4.2.3. The analytical model of tandem junction driven electrolysis was first proposed by Miller et al (Fig.21b)[118]. The total conversion efficiency can be expressed by equation below.

$$\eta = \eta_{opt} \cdot \eta_{ele} \qquad (9)$$

Where η is the ultimate SCE, η_{opt} and η_{ele} are the multifunction solar cell and electrolysis efficiency, respectively. η_{opt} can be expressed by standard solar cell I-V curve.

$$\eta_{opt} = \frac{\mathrm{FF} \cdot \mathrm{V_{OC}} \cdot \mathrm{J_{SC}}}{\mathrm{P}} \quad (10)$$

where FF is the fill factor, V_{OC} is the open circuit voltage, J_{SC} is the short circuit current and P is the incident solar energy.

η_{opt} of solar energy conversion can be expressed by the equation below.

$$\eta_{opt} = \eta_a \cdot \eta_g \cdot \eta_s \cdot \eta_c \quad (11)$$

where η_a, η_g, η_s, and η_c, are light absorption, charge generation, separation and collection efficiency, respectively. One can introduce surface texture, antireflection, or plasmonics to enhance the η_a, optimize the solar cell design such as graded band gap, multijunction, intrinsic layer and etc, to enhance the η_g and η_s, and finally minimize the bulk and contact loss to enhance η_c.

Practical solar cell IV curve can be modeled using the equation below

$$j_{ph} = J_{SC} - J_0 \left(e^{\frac{q\left(V - j_{ph} \cdot R_S\right)}{nkT}} - 1 \right) - \frac{V - j_{ph} \cdot R_S}{R_{SH}} \quad (12)$$

where j_{ph} is the photocurrent density under illumination, J_0 is the dark saturation current density, R_S and R_{SH} are the series resistance and shunt resistant, respectively, J_{SC} is the short circuit current, k, q are constants and T is temperature. J_0 can be calculated

$$J_0 = J_{SC} \cdot \left(e^{\frac{qV_{oc}}{nkT}} - 1 \right) \quad (13)$$

The electrolysis efficiency can be described (Fig.21b left right half) as

$$\eta_{ele} = \frac{1.229}{1.229 + \xi_{\mathrm{HER}}\left(\xi_{\mathrm{CRR}}\right) + \xi_{\mathrm{OER}} + \xi_{jR}} \quad (14)$$

where ξ_{HER} and ξ_{OER} are the overpotentials for HER and OER half reaction in V, respectively, ξ_{CRR} is the carbon dioxide reduction reaction (CRR) overpotential in V, when current reaches j, j is the electrolysis current density in mA/cm^2, and R in ohm sums all the ohmic loss from cell[360], electrocatalyst and ion transfer in bulk solution. Based on Butler-Volmer model, one can reconstruct the kinetic I-V behavior of electrocatalysts from the equation below,

$$\xi_{\mathrm{HER/CRR/OER}} = b \cdot \log_{10} \frac{j}{j_0} \qquad (15)$$

where b is the Tafel slope in mV/dec and j_0 is the exchange current density in mA/cm^2. The kinetic data (b and j_0) of some milestone electrocatalysts reviewed in previous sections compared to state-of-the-art novel metal-based electrocatalysts are summarized in Table 1. The Tafel behavior describes the overpotential needed to overcome the activation barrier and to force the current to flow for the reaction to happen. This model typically works for higher bias where reverse reaction rate is negligible. In fact, a typical catalytic kinetic behavior switches from Butler-Volmer kinetics to resistive kinetics when working bias is switched to higher values, which can be expressed using the equation below.

$$\xi_{\mathrm{HER/CRR/OER}} = (\mathrm{j} - \mathrm{j}_b) \cdot \mathrm{R}_{lim} \qquad (16)$$

where j_b and R_{lim} are the resistive kinetic parameters at high working biases. As we can see, smaller R_{lim} and greater j_b correspond to lower overpotential and thus better catalytic kinetics. Typically the resistance loss becomes significant and cannot be neglected when the current density exceed 100 mA/cm^2. Therefore, for the PV-electrolysis water splitting device with an efficiency of 10%, it is reasonable to ignore the high resistive kinetics and assume the electrocatalysts are still governed by the Butler-Volmer model which is not limited by the transportation. Other important assumption one may think about is that gas bubbles are released from the electrode surface immediately up on formation, meaning bubbles do not increase the overpotential need to drive the same amount of current density. The last but not the least, we assume that there is no additional efficiency loss when connect optical system (left half) and electrical system (right half) of Miller's model in Fig 20b. In practical cases, this additional loss is significant and strategies have to be considered, which will be discussed later.

On the other hand, looking at the efficiency from thermodynamic point of view, one can simply have the efficiency of the whole system using the equation below

$$\eta = \frac{1.229 \cdot \mathrm{j}}{\mathrm{P}} \tag{17}$$

from which, assuming a "holy grail" of solar fuel production efficiency of 10%, one can get current density j is around 8.13 mA/cm^2.

Furthermore, having

$$\eta = \frac{1.229 \cdot \mathrm{j}}{\mathrm{P}} = \frac{\mathrm{FF} \cdot \mathrm{V_{OC}} \cdot \mathrm{J_{SC}}}{\mathrm{P}} \cdot \frac{1.229}{1.229 + \xi_{\mathrm{HER}}(\xi_{\mathrm{CRR}}) + \xi_{\mathrm{OER}} + \xi_{jR}} \tag{18}$$

we can get a general guidance on the design of a such a system

$$\mathrm{j} \cdot (1.229 + \xi_a) = \mathrm{J_{SC}} \cdot \mathrm{FF} \cdot \mathrm{V_{OC}} \tag{19}$$

where ξ_a represents the summation of all the overpotential of OER and HER half reactions and ohmic loss.

Table 1. Kinetic parameters for some HER and OER catalysts reported

Catalysts	**b (mV/dec)**	**j_0 (mA/cm^2)**	**ξ(mV@8.13 mA/cm^2)**	**Condition**	**Ref**
HER					
Pt	30	1.0	27		361
PtRuIr	30	3.6×10^{-4}	131	0.5M H_2SO_4	362
PtBi		0.56		pH=0.4 H_2SO_4	363
NiMoCd	26	$10^{-2.2}$	75	1M NaOH	364
MoS_2	55	5.0×10^{-4}	232	pH=0.23 H_2SO_4	187
MoS2	50	6.7×10^{-4}	225	0.5 M H_2SO_4	192
MoS_3	39	1.2×10^{-4}	188	pH=7 PBS solution	207
a-MoS_3	41	$10^{-4.7}$	230	1M H_2SO_4	202
$NiMoN_x$	35.9	0.24	55	0.1M $HClO_4$	208
Co-MoS_3	43	5.0×10^{-4}	181	pH=7 PBS solution	207
CoCat	140	$10^{-2.5}$	547	0.5M KPi	213
$Co(OH)_2$	-	-	186*	0.1M KOH/LiOH	214
Cu_2MoS_4	95	0.04	219	0.5M H_2SO_4	200

Table 1. Kinetic parameters for some HER and OER catalysts reported continued

Catalysts	**b (mV/dec)**	**j_0 (mA/cm^2)**	**ξ(mV@8.13 mA/cm^2)**	**Condition**	**Ref**
HER					
FeMo	78	0.67	85	30 W/O KOH	365
NiVO	33.8	2.7×10^{-3}	118	1M KOH	267
OER					
RuO_2	42	11.7×10^{-5}	203	5M KOH	366
IrO_2	33	9.5×10^{-5}	163	5M KOH	366
Mn-Cat	59	10^{-9}	585	0.1M KH_2PO_4/ K_2HPO_4	223
Ni-Bi	29	5×10^{-15}	441	1M KBi	333
NiFeO	33.7	9.4×10^{-3}	99	1M KOH	267
Co-Bi	52	2×10^{-9}	499	1M KBi	333
Co-oxide	69	3.0×10^{-8}	582	0.1M NaH_2PO_4/Na_2HPO_4	367
Co-Pi	59	-		0.1 M KPi	236
Co_3O_4	49	2×10^{-7}	373	1 M KOH	234
$Ni_{0.9}Fe_{0.1}O_x$	30	-	>310	1 M KOH	269

*186 mV at 8.13 mA/cm^2 is extracted from ref [214] at $Co(OH)_2$ coated Pt (111) surface with a coverage of 40%

Theoretically, V_{OC} has to be equal or bigger than the $1.229+\xi_a$, and then electrolysis current j cannot be bigger than $J_{SC}\cdot FF$. Therefore, j will be higher if multijunction solar cell has a better fill factor. On the other hand, maximum electrolysis current j equals to J_{SC}. Therefore, with the same overpotential loss, better fill factor lowers the requirement for high V_{OC}. That is to say at a fixed fill factor, increased overpotential loss requires a larger V_{OC}. Based on reported data of some typical electrocatalysts and milestones (Table.1), one can extract the exchange current and Tafel slope, typically given at the onset potential region defined by researchers. It is possible to extend the PV-electrolysis plot (presented by Surendranath et al.[333]) in a PV-electrolysis system by compared different combination of low-cost HER and OER catalysts (Fig.23).

Based on an ideal Si triple junction PV, the maximum efficiency of this spontaneous water splitting devices can be estimated. One can see that state-of-the-art system with RuO_2 and Pt, as OER and HER, respectively, gives the best efficiency of 10%, disregarding their high cost. Similarly, Ni based alkaline catalysts (NiFeO-OER/NiVO-HER) contained system showed comparable maximum efficiency of 10%. NiBi was demonstrated as a very effective neutral water OER catalyst recently. The system consisting of NiBi combined with some breakthrough HER catalysts, such as $NiMoN_x$, NiMoCd and $CoMoS_3$ presenting noble metal-like behavior, could theoretically give efficiency of 9.94%, 9.88% and 7.50%, respectively. System utilizing a combination of MnCat and $CoMoS_3$ gives the maximum efficiency of 1.79%. Using both cobalt based catalysts, CoBi-OER and CoCat-HER, one can reach efficiency as low as 0.17%. Moreover, the efficiency of the system drops when considering a practical solar cell with a finite shunt resistance (R_{SH}) and a series resistance (R_S). The polarization curve of a practical solar cell is shown as the dotted line in Fig.23. As one can see, cross points of Tafel curves of electrocatalysts and the solar cell IV curve drop significantly indicating a loss of conversion efficiency.

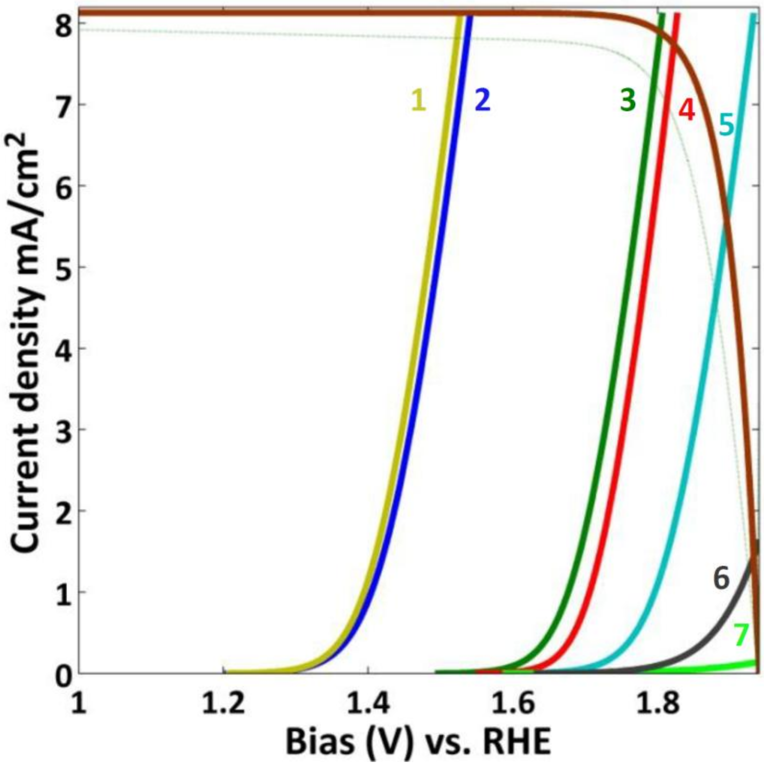

Figure 23. Theoretical efficiency analysis of PV-electrolysis system based on some state of the art cheap transition metals electrocatalysts. NiFeO-OER/NiVO-HER(1), RuO_2-OER/Pt-HER (2), NiBi-OER/NiMoNx-HER (3), NiBi-OER/NiMoCd-HER (4), NiBi-OER/$CoMoS_3$-HER (5), MnCat-OER/$CoMoS_3$-HER(6), CoBi-OER/CoCat-HER(7). PV cell is based on a triple junction amorphous Si solar cell with typical parameters, J_{SC}=8.13 mA/cm^2, V_{OC}=1.94 V, ideal factor=1,. Kinetics behaviors of electrocatalysts are reconstructed from Table 1. Dotted line shows the practical solar cell IV curve with R_{SH}=5 ohm-cm^2 and R_S=0.005 ohm-cm^2.

Fabrication and characterization conditions for these electrocatalysts may need harsh environment namely high temperature sintering or extremely basic/acidic electrolyte. The synthesis condition could worsen the Si PV/electrocatalyst interface, which gives reduced charge kinetics, and thus the Tafel behavior may not be retained over long-term operation. Moreover, it is also possible that the charge recombination channels at this interface can be facilitated during the catalyst deposition or the catalyst treatment, such as conditioning procedures like high temperature or leaching in highly concentrated alkaline for long time. In this case, a correction factor is needed in equation 6, representing an additional loss when these two systems are integrated[368], primarily from deconstructive processes, which could lead to degraded or compromised performances from each system. The correction factor should also include the optical modulation from the integration of these two systems including positive and negative from each component and process, which are discussed primarily in section 4.

Screening and searching for excellent photoactive materials as well as electrocatalysts are currently world-widely recognized through combinatory experimental. High throughput screening methods to identify new materials through an identical synthesis conditions and a single experiment are developed[369], which can be realized either from direct electrochemical polarization measurement or from indirect measurement through a gas product induced optical modulation. For example, Parkinson's group from the University of Wyoming presented fast screening method using ink-jet printed precursors on conductive substrates[370]. Materials screened in this study were then activated through a thermal annealing process. Electrochemical monitoring and mapping of the photocurrent under a laser excitation were recorded. Jordan et al. presented a similar study of high through-put screening of photoactive materials by monitoring photocurrent and polarity/magnitude of photovoltage[371]. Recently Liu et al. reported an ultrafast photocatalysts characterization with a rate of 1000000-fomulations/hour with up to 8-component compositions[372]. Fast identification of cost-effective and efficient photocatalysts for H_2 generation was achieved through a multidimensional group testing strategy. McFarland's group from the University of California, Santa Barbara, also presented a fast screening through monitoring the photocurrent[373]. McFarland's group presented in 2001 a screening of HER metal catalysts made from electron beam evaporation[374]. The fast screening was realized by monitoring the reduce of reflectance from the WO_3:Pd film H_2 sensor. Similarly, Gerken et al. recently presented a work on screening non-noble metal based electrocatalysts for photooxidation of water through an optical approach with a potentially high through-put[375]. Commercially available dual-chromophore paint is placed above the metal oxides in a three-electrode measurement setup. The activity of the OER catalyst containing Ni and Co with non-redox active Lewis-acidic metal ions was investigated. Oxygen evolution was monitored by the color change of the paint using a digital camera.

In addition to the extensive development in experimental screening, new computational screening plays an important role on predicting and identifying new materials[376]. Based on surface electronic structures which in turn determines the adsorption free energy and thus catalytic activity, DFT-based kinetic models are used and have showed great accuracy and consistency to experimental results[377]. Computational models could also consider the stability based on evaluation of free-energies needed for the change of surface morphology, oxygen adsorption, and dissolution[96]. Greeley et al. presented a computational screening based on density function theory on the activity study of over 700 binary surface alloys for HER catalysts[363]. It was found that BiPt is found to have improved HER catalytic activity than pure Pt, which was proved experimentally (Fig.9a). On the other hand for OER catalysts, Castelli et al. presented a computational screening of 19000 compound semiconductors with cubic perovskite structures[378]. Several combinations were selected through this recent study, which could provide guidance for experimental verifications.

However, the reported experimental screening of photocatalytic or electrocatalytic materials for better catalysts are only judged by activity. We believe a more considerable criterion on the performance judgment should include the stability. Selectivity should be also evaluated through the modeling of each possible competing reaction pathways[377]. Therefore, future research focused on developing new criteria and respective high throughput screening experiments should be conducted searching for cheap, outperforming, specific, and stable electrocatalyst and photocatalyst materials. A larger database including electrocatalysts behavior under standard synthesis (compatible to amorphous Si processing) and measurement conditions (current range, pH of electrolyte, etc) is essential during the screening study towards an optimized system design for future practical devices. This kind of tandem junction configuration can be eventually applied to the development of Si based artificial photosynthesis system by simply replacing the water reduction catalyst with an CO_2 reduction catalyst (as shown in Fig.22)[358a].

1.6 Conclusion and prospects

Over the past few decades, human has dedicated tremendous efforts to solve the energy problem and to deal with the consequences from excessive use of fossil fuels. Solar energy is recognized as the ultimate solution to all the energy and environmental crisis due to its unlimited power. Mimicking the natural photosynthesis to synthesize chemical fuels from light for conventional energy consumption devices in a clean and cheap fashion is one of the promising approaches. Exploration of this approach using organic molecular photochemistry or inorganic semiconductor photoelectrochemistry has been enormously successful. Si is widely used for photovoltaic applications, due to its superior advantages of low cost and narrow band gap (E_g = ~1.1 eV) matched to the solar spectrum. Thermodynamics and kinetics of Si photoelectrode in aqueous solution are considered as the major issues to solve in order to enable Si for photoelectrochemical solar fuel production. Surface alteration techniques are desired for overcoming intrinsic disadvantages of Si for solar fuel production from water. An ideal heterogeneous coating should 1) be robust and high quality to lower the chance of electrode degradation both in dark and under illumination operation, 2) provide large photovoltage to lower the bias needed to drive the reaction, 3) enhance light scattering or at least does not absorb too much light, and also 4) offer electrocatalytic activity to further lower the externally applied electrical energy input. Strategies to enable Si for solar fuel production are broadly reviewed in this article, including surface textures, inorganic metallic and semiconductive coating, as well as organic polymers and briefly discussed molecular complexes. Significant successes obtained from these studies provide fundamental design guidance for developing unassisted solar fuel production. To develop practical spontaneous water splitting and artificial photosynthesis based on Si photoelectrodes, prototypes based on configurations such as a photoelectrical diode and a triple junction amorphous Si solar cell were proposed and studied. Hybrid configurations by integrating molecular sensitized solar cell and Si photocathode could be another alternative approach and a future research direction to realize practical fuel production from solar energy. Research are focus on rational management of efficiencies of each steps in this complex multiphysics and chemistry process, such as light absorption, free carrier collection/transportation, ion conduction, gas evolution, as well as material stability, catalyst activity, heat/water flow control and etc. In addition, cost-effective fabrication process like inkjet printing and solution processing, as well as abundant and cheap materials such as late first row transition metal based nanoscale electrocatalyst through compositional and structural modifications are developed. Computational screening together with combinatorial experimental verification provides an effective way to successful identification of novel, extremely durable and selective photocatalysts/electrocatalysts with high activity.

1.7 References:

(1) Fujishima, A.; Honda, K. *Nature* **1972**, *238*, 37.

(2) Dresselhaus, M. S.; Thomas, I. L. *Nature* **2001**, *414*, 332.

(3) Inoue, Y. *Energy Environ. Sci.* **2009**, *2*, 364.

(4) Maeda, K.; Takata, T.; Hara, M.; Saito, N.; Inoue, Y.; Kobayashi, H.; Domen, K. *J. Am. Chem. Soc.* **2005**, *127*, 8286.

(5) Khaselev, O.; Turner, J. A. *Science* **1998**, *280*, 425.

(6) Paracchino, A.; Laporte, V.; Sivula, K.; Grätzel, M.; Thimsen, E. *Nat. Mater.* **2011**, *10*, 456.

(7) Christopher, K.; Dimitrios, R. *Energy Environ. Sci.* **2012**, *5*, 6640.

(8) Dahl, S.; Chorkendorff, I. *Nat. Mater.* **2012**, *11*, 100.

(9) Nocera, D. G. *Acc. Chem. Res.* **2012**, *45*, 767.

(10) Candea, R. M.; Kastner, M.; Goodman, R.; Hickok, N. *J. Appl. Phys.* **1976**, *47*, 2724.

(11) Koval, C. A.; Howard, J. N. *Chem. Rev.* **1992**, *92*, 411.

(12) Chazalviel, J. N. *Surf. Sci.* **1979**, *88*, 204.

(13) Memming, R. *Semiconductor Electrochemistry*; Wiley-VCH, 2001.

(14) Morrison, S. R. *Electrochemistry at Semiconductor and Oxidized Metal Electrodes*; Plenum Press, New York, 1980.

(15) (a) Iyer, S. S.; Xie, Y.-H. *Science* **1993**, *260*, 40 (b) Liang, D.; Bowers, J. E. *Nat. Photonics* **2010**, *4*, 511.

(16) Hale, G. M.; Querry, M. R. *Appl. Opt.* **1973**, *12*, 555.

(17) Bard, A. J.; Parsons, R.; Jordan, J. *Standard Potentials in Aqueous Solution*; International Union of Pure and Applied Chemistry, 1985.

(18) Wrighton, M. S. *Acc. Chem. Res.* **1979**, *12*, 303.

(19) Leempoel, P.; Castro-Acuna, M.; Fan, F.-R. F.; Bard, A. J. *J. Phys. Chem.* **1982**, *86*, 1396.

(20) *Photoelectrochemical Materials and Energy Conversion Processes*; Alkire, R. C.; Kolb, D. M.; Lipkowski, J.; ROss, P. N., Eds.; Wiley-VCH 2010; Vol. 12.

(21) Bolts, J. M.; Bocarsly, A. B.; Palazzotto, M. C.; Walton, E. G.; Lewis, N. S.; Wrighton, M. S. *J. Am. Chem. Soc.* **1979**, *101*, 1378.

(22) Bard, A. J.; Bocarsly, A. B.; Fan, F. R. F.; Walton, E. G.; Wrighton, M. S. *J. Am. Chem. Soc.* **1980**, *102*, 3671.

(23) Bocarsly, A. B.; Bookbinder, D. C.; Dominey, R. N.; Lewis, N. S.; Wrighton, M. S. *J. Am. Chem. Soc.* **1980**, *102*, 3683.

(24) (a) Meyerhof, W. E. *Phys. Rev.* **1947**, *71*, 727 (b) Bardeen, J. *Phys. Rev.* **1947**, *71*, 717.

(25) Green, M. *J. Chem. Phys.* **1959**, *31*, 200.

(26) Lieber, C. M.; Gronet, C. M.; Lewis, N. S. *Nature* **1984**, *307*, 533.

(27) Turner, J. A.; Manassen, J.; Nozik, A. J. *Appl. Phys. Lett.* **1980**, *37*, 488.

(28) Johansson, E.; Boettcher, S. W.; O'Leary, L. E.; Poletayev, A. D.; Maldonado, S.; Brunschwig, B. S.; Lewis, N. S. *J. Phys. Chem. C* **2011**, *115*, 8594.

(29) Warren, E. L.; Boettcher, S. W.; Walter, M. G.; Atwater, H. A.; Lewis, N. S. *J. Phys. Chem. C* **2010**, *115*, 594.

(30) Sun, K.; Madsen, K.; Andersen, P.; Bao, W.; Sun, Z.; Wang, D. *Nanotechnol.* **2012**, *23*, 194013.

(31) Kronawitter, C. X.; Vayssieres, L.; Shen, S.; Guo, L.; Wheeler, D. A.; Zhang, J. Z.; Antoun, B. R.; Mao, S. S. *Energy Environ. Sci.* **2011**, *4*, 3889.

(32) Parkinson, B. A.; Heller, A.; Miller, B. *Appl. Phys. Lett.* **1978**, *33*, 521.

(33) Fan, F. R. F.; Hope, G. A.; Bard, A. J. *J. Electrochem. Soc.* **1982**, *129*, 1647.

(34) Raut, H. K.; Ganesh, V. A.; Nair, A. S.; Ramakrishna, S. *Energy Environ. Sci.* **2011**, *4*, 3779.

(35) Saeta, P. N.; Ferry, V. E.; Pacifici, D.; Munday, J. N.; Atwater, H. A. *Opt. Express* **2009**, *17*, 20975.

(36) Sun, K.; Kargar, A.; Park, N.; Madsen, K. N.; Naughton, P. W.; Bright, T.; Jing, Y.; Wang, D. *Selected Topics in Quantum Electronics, IEEE Journal of* **2011**, *17*, 1033

(37) Zhu, J.; Cui, Y. *Nat. Mater.* **2010**, *9*, 183.

(38) Boettcher, S. W.; Spurgeon, J. M.; Putnam, M. C.; Warren, E. L.; Turner-Evans, D. B.; Kelzenberg, M. D.; Maiolo, J. R.; Atwater, H. A.; Lewis, N. S. *Science* **2010**, *327*, 185.

(39) Gronet, C. M.; Lewis, N. S.; Cogan, G.; Gibbons, J. *Proc. Natl. Acad. Sci. USA* **1983**, *80*, 1152.

(40) (a) Li, Y.; Zhang, J.; Yang, B. *Nano Today* **2010**, *5*, 117 (b) Lou, S.; Guo, X.; Fan, T.; Zhang, D. *Energy Environ. Sci.* **2012** (c) Zhu, J.; Yu, Z.; Fan, S.; Cui, Y. *Mater. Sci. Eng., R* **2010**, *70*, 330.

(41) Wei-Lun, M.; Bin, J.; Peng, J. *Adv. Mater.* **2008**, *20*, 3914.

(42) Kelzenberg, M. D.; Boettcher, S. W.; Petykiewicz, J. A.; Turner-Evans, D. B.; Putnam, M. C.; Warren, E. L.; Spurgeon, J. M.; Briggs, R. M.; Lewis, N. S.; Atwater, H. A. *Nat. Mater.* **2010**, *9*, 239.

(43) Vazsonyi, E.; De Clercq, K.; Einhaus, R.; Van Kerschaver, E.; Said, K.; Poortmans, J.; Szlufcik, J.; Nijs, J. *Sol. Energy Mater. Sol. Cells* **1999**, *57*, 179.

(44) Huang, Y.-F.; Chattopadhyay, S.; Jen, Y.-J.; Peng, C.-Y.; Liu, T.-A.; Hsu, Y.-K.; Pan, C.-L.; Lo, H.-C.; Hsu, C.-H.; Chang, Y.-H.; Lee, C.-S.; Chen, K.-H.; Chen, L.-C. *Nat. Nanotechnol.* **2007**, *2*, 770.

(45) Li, Y.; Yu, H.; Li, J.; Wong, S.-M.; Sun, X. W.; Li, X.; Cheng, C.; Fan, H. J.; Wang, J.; Singh, N.; Lo, P. G.-Q.; Kwong, D.-L. *Small* **2011**, *7*, 3138.

(46) Mavrokefalos, A.; Han, S. E.; Yerci, S.; Branham, M. S.; Chen, G. *Nano Lett.* **2012**, *12*, 2792.

(47) Stavenga, D. G.; Foletti, S.; Palasantzas, G.; Arikawa, K. *Proc. R. Soc. Lond., Ser. B: Biol. Sci.* **2006**, *273*, 661.

(48) Spinelli, P.; Verschuuren, M. A.; Polman, A. *Nat. Commun.* **2012**, *3*, 692.

(49) (a) Rayleigh, L. *Proc. London Math. Soc.* **1879**, *s1-11*, 51 (b) Yablonovitch, E. *J. Opt. Soc. Am.* **1982**, *72*, 899.

(50) http://www.filmetrics.com/refractive-index-database/Si/Silicon

(51) Seidel, H.; Csepregi, L.; Heuberger, A.; Baumgärtel, H. *J. Electrochem. Soc.* **1990**, *137*, 3612.

(52) Iencinella, D.; Centurioni, E.; Rizzoli, R.; Zignani, F. *Sol. Energy Mater. Sol. Cells* **2005**, *87*, 725.

(53) Clemens, J. T. *Bell Labs Tech. J.* **1997**, *2*, 76.

(54) Xi, Z.; Yang, D.; Que, D. *Sol. Energy Mater. Sol. Cells* **2003**, *77*, 255.

(55) Nishimoto, Y.; Namba, K. *Sol. Energy Mater. Sol. Cells* **2000**, *61*, 393.

(56) Declercq, M. J.; Gerzberg, L.; Meindl, J. D. *J. Electrochem. Soc.* **1975**, *122*, 545.

(57) Kovacs, G. T. A.; Maluf, N. I.; Petersen, K. E. *Proc. IEEE* **1998**, *86*, 1536.

(58) Levy-Clement, C.; Lagoubi, A.; Tenne, R.; Neumann-Spallart, M. *Electrochim. Acta* **1992**, *37*, 877.

(59) Smith, R. L.; Collins, S. D. *J. Appl. Phys.* **1992**, *71*, R1.

(60) Saito, Y.; Kosuge, T. *Sol. Energy Mater. Sol. Cells* **2007**, *91*, 1800.

(61) Zhu, J.; Yu, Z.; Burkhard, G. F.; Hsu, C.-M.; Connor, S. T.; Xu, Y.; Wang, Q.; McGehee, M.; Fan, S.; Cui, Y. *Nano Lett.* **2008**, *9*, 279.

(62) Peng, K.-Q.; Yan, Y. J.; Gao, S. P.; Zhu, J. *Adv. Mater.* **2002**, *14*, 1164.

(63) Peng, K.; Yan, Y.; Gao, S.; Zhu, J. *Adv. Funct. Mater.* **2003**, *13*, 127.

(64) Huang, Z.; Geyer, N.; Werner, P.; de Boor, J.; Gösele, U. *Adv. Mater.* **2011**, *23*, 285.

(65) Jung, J.-Y.; Guo, Z.; Jee, S.-W.; Um, H.-D.; Park, K.-T.; Lee, J.-H. *Opt. Express* **2010**, *18*, A286.

(66) Huang, Z.; Fang, H.; Zhu, J. *Adv. Mater.* **2007**, *19*, 744.

(67) Chang, S.-W.; Chuang, V. P.; Boles, S. T.; Ross, C. A.; Thompson, C. V. *Adv. Funct. Mater.* **2009**, *19*, 2495.

(68) Chern, W.; Hsu, K.; Chun, I. S.; Azeredo, B. P. d.; Ahmed, N.; Kim, K.-H.; Zuo, J.-m.; Fang, N.; Ferreira, P.; Li, X. *Nano Lett.* **2010**, *10*, 1582.

(69) Koshida, N.; Nagasu, M.; Sakusabe, T.; Kiuchi, Y. *J. Electrochem. Soc.* **1985**, *132*, 346.

(70) Oh, J.; Deutsch, T. G.; Yuan, H.-C.; Branz, H. M. *Energy Environ. Sci.* **2011**, *4*, 1690.

(71) Oh, I.; Kye, J.; Hwang, S. *Nano Lett.* **2011**, *12*, 298.

(72) Boettcher, S. W.; Warren, E. L.; Putnam, M. C.; Santori, E. A.; Turner-Evans, D.; Kelzenberg, M. D.; Walter, M. G.; McKone, J. R.; Brunschwig, B. S.; Atwater, H. A.; Lewis, N. S. *J. Am. Chem. Soc.* **2011**, *133*, 1216.

(73) (a) Koshida, N.; Kiuchi, Y. *Jpn. J. Appl. Phys.* **1985**, *24*, L166 (b) Koshida, N.; Koyama, H.; Kiuchi, Y. *Jpn. J. Appl. Phys.* **1986**, *25*, 1069.

(74) Levy-Clement, C.; Lagoubi, A.; Neumann-Spallart, M.; Rodot, M.; Tenne, R. *J. Electrochem. Soc.* **1991**, *138*, L69.

(75) Yuan, G.; Aruda, K.; Zhou, S.; Levine, A.; Xie, J.; Wang, D. *Angew. Chem. Int. Ed.* **2011**, *50*, 2334.

(76) Foley, J. M.; Price, M. J.; Feldblyum, J. I.; Maldonado, S. *Energy Environ. Sci.* **2012**, *5*, 5203.

(77) Kayes, B. M.; Atwater, H. A.; Lewis, N. S. *J. Appl. Phys.* **2005**, *97*, 114302.

(78) Kosten, E. D.; Warren, E. L.; Atwater, H. A. *Opt. Express* **2011**, *19*, 3316.

(79) Ganapati, V.; Fenning, D. P.; Bertoni, M. I.; Kendrick, C. E.; Fecych, A. E.; Redwing, J. M.; Buonassisi, T. *Small* **2011**, *7*, 563.

(80) Tamboli, A. C.; Chen, C. T.; Warren, E. L.; Turner-Evans, D. B.; Kelzenberg, M. D.; Lewis, N. S.; Atwater, H. A. *IEEE J. Photovoltaics* **2012**, *PP*, 1.

(81) (a) Kelzenberg, M. D.; Turner-Evans, D. B.; Putnam, M. C.; Boettcher, S. W.; Briggs, R. M.; Baek, J. Y.; Lewis, N. S.; Atwater, H. A. *Energy Environ. Sci.* **2011**, *4*, 866 (b) Cho, C. J.; O'Leary, L.; Lewis, N. S.; Greer, J. R. *Nano Lett.* **2012**, *12*, 3296 (c) Putnam, M. C.; Boettcher, S. W.; Kelzenberg, M. D.; Turner-Evans, D. B.; Spurgeon, J. M.; Warren, E. L.; Briggs, R. M.; Lewis, N. S.; Atwater, H. A. *Energy Environ. Sci.* **2010**, *3*, 1037.

(82) (a) Maiolo, J. R.; Kayes, B. M.; Filler, M. A.; Putnam, M. C.; Kelzenberg, M. D.; Atwater, H. A.; Lewis, N. S. *J. Am. Chem. Soc.* **2007**, *129*, 12346 (b) Santori, E. A.; Maiolo Iii, J. R.; Bierman, M. J.; Strandwitz, N. C.; Kelzenberg, M. D.; Brunschwig, B. S.; Atwater, H. A.; Lewis, N. S. *Energy Environ. Sci.* **2012**, *5*, 6867.

(83) Cho, S. K.; Fan, F.-R. F.; Bard, A. J. *Angew. Chem. Int. Ed.* **2012**, n/a.

(84) Kohl, P. A.; Frank, S. N.; Bard, A. J. *J. Electrochem. Soc.* **1977**, *124*, 225.

(85) Kurtin, S.; McGill, T. C.; Mead, C. A. *Phys. Rev. Lett.* **1969**, *22*, 1433.

(86) Higashi, G. S.; Chabal, Y. J.; Trucks, G. W.; Raghavachari, K. *Appl. Phys. Lett.* **1990**, *56*, 656.

(87) Jimenez-Molinos, F.; Gamiz, F.; Palma, A.; Cartujo, P.; Lopez-Villanueva, J. A. *J. Appl. Phys.* **2002**, *91*, 5116.

(88) Nakato, Y.; Tsubomura, H. *Electrochim. Acta* **1992**, *37*, 897.

(89) Harris, L. A.; Gerstner, M. E.; Wilson, R. H. *J. Electrochem. Soc.* **1977**, *124*, 1511.

(90) Menezes, S.; Heller, A.; Miller, B. *J. Electrochem. Soc.* **1980**, *127*, 1268.

(91) Lombardi, I.; Marchionna, S.; Zangari, G.; Pizzini, S. *Langmuir* **2007**, *23*, 12413.

(92) Tsubomura, H.; Nakato, Y.; Hiramoto, M.; Yano, H. *Can. J. Chem.* **1985**, *63*, 1759.

(93) Chen, Y. W.; Prange, J. D.; Dühnen, S.; Park, Y.; Gunji, M.; Chidsey, C. E. D.; McIntyre, P. C. *Nat. Mater.* **2011**, *10*, 539.

(94) Reier, T.; Oezaslan, M.; Strasser, P. *ACS Catalysis* **2012**, *2*, 1765.

(95) Stephens, I. E. L.; Chorkendorff, I. *Angew. Chem. Int. Ed.* **2011**, *50*, 1476.

(96) Greeley, J.; Jaramillo, T. F.; Bonde, J.; Chorkendorff, I.; Norskov, J. K. *Nat. Mater.* **2006**, *5*, 909.

(97) (a) Kibsgaard, J.; Gorlin, Y.; Chen, Z.; Jaramillo, T. F. *J. Am. Chem. Soc.* **2012**, *134*, 7758 (b) Fujita, T.; Guan, P.; McKenna, K.; Lang, X.; Hirata, A.; Zhang, L.; Tokunaga, T.; Arai, S.; Yamamoto, Y.; Tanaka, N.; Ishikawa, Y.; Asao, N.; Yamamoto, Y.; Erlebacher, J.; Chen, M. *Nat. Mater.* **2012**, *11*, 775.

(98) (a) Esposito, D. V.; Hunt, S. T.; Kimmel, Y. C.; Chen, J. G. *J. Am. Chem. Soc.* **2012**, *134*, 3025 (b) Yamada, Y.; Tsung, C.-K.; Huang, W.; Huo, Z.; Habas, S. E.; Soejima, T.; Aliaga, C. E.; Somorjai, G. A.; Yang, P. *Nat. Chem.* **2011**, *3*, 372.

(99) Kotani, H.; Hanazaki, R.; Ohkubo, K.; Yamada, Y.; Fukuzumi, S. *Chem. Eur. J.* **2011**, *17*, 2777.

(100) Wan, D.; Chen, H. L.; Tseng, T. C.; Fang, C. Y.; Lai, Y. S.; Yeh, F. Y. *Adv. Funct. Mater.* **2010**, *20*, 3064.

(101) (a) Schaadt, D. M.; Feng, B.; Yu, E. T. *Appl. Phys. Lett.* **2005**, *86*, 063106 (b) Derkacs, D.; Lim, S. H.; Matheu, P.; Mar, W.; Yu, E. T. *Appl. Phys. Lett.* **2006**, *89*, 093103.

(102) (a) Liu, Z.; Hou, W.; Pavaskar, P.; Aykol, M.; Cronin, S. B. *Nano Lett.* **2011**, *11*, 1111 (b) Hou, W.; Liu, Z.; Pavaskar, P.; Hung, W. H.; Cronin, S. B. *J. Catal.* **2011**, *277*, 149 (c) Awazu, K.; Fujimaki, M.; Rockstuhl, C.; Tominaga, J.; Murakami, H.; Ohki, Y.; Yoshida, N.; Watanabe, T. *J. Am. Chem. Soc.* **2008**, *130*, 1676 (d) Tian, Y.; Tatsuma, T. *J. Am. Chem. Soc.* **2005**, *127*,

7632 (e) Murdoch, M.; Waterhouse, G. I. N.; Nadeem, M. A.; Metson, J. B.; Keane, M. A.; Howe, R. F.; Llorca, J.; Idriss, H. *Nat. Chem.* **2011**, *3*, 489.

(103) Thomann, I.; Pinaud, B. A.; Chen, Z.; Clemens, B. M.; Jaramillo, T. F.; Brongersma, M. L. *Nano Lett.* **2011**, *11*, 3440.

(104) Solarska, R.; Królikowska, A.; Augustyński, J. *Angew. Chem. Int. Ed.* **2010**, *49*, 7980.

(105) (a) Warren, S. C.; Thimsen, E. *Energy Environ. Sci.* **2012**, *5*, 5133 (b) Hou, W.; Cronin, S. B. *Adv. Funct. Mater.* **2012**, n/a.

(106) Lublow, M.; Bouabadi, B.; Kubala, S. *Sol. Energy Mater. Sol. Cells* **2012**, *107*, 56.

(107) (a) Knight, M. W.; Sobhani, H.; Nordlander, P.; Halas, N. J. *Science* **2011**, *332*, 702 (b) Furube, A.; Du, L.; Hara, K.; Katoh, R.; Tachiya, M. *J. Am. Chem. Soc.* **2007**, *129*, 14852.

(108) Atwater, H. A.; Polman, A. *Nat. Mater.* **2010**, *9*, 205.

(109) Cushing, S. K.; Li, J.; Meng, F.; Senty, T. R.; Suri, S.; Zhi, M.; Li, M.; Bristow, A. D.; Wu, N. *J. Am. Chem. Soc.* **2012**, *134*, 15033.

(110) (a) Jaksic, J. M.; Ristic, N. M.; Krstajic, N. V.; Jaksic, M. M. *Int. J. Hydrogen Energy* **1998**, *23*, 1121 (b) Jaksic, M. M. *Int. J. Hydrogen Energy* **2001**, *26*, 559.

(111) Lasia, A.; Rami, A. *J. Electroanal. Chem. Interfac. Electrochem.* **1990**, *294*, 123.

(112) Yamada, Y.; Miyahigashi, T.; Kotani, H.; Ohkubo, K.; Fukuzumi, S. *Energy Environ. Sci.* **2012**, *5*, 6111.

(113) Li, P.-Z.; Aijaz, A.; Xu, Q. *Angew. Chem. Int. Ed.* **2012**, *51*, 6753.

(114) (a) McKone, J. R.; Warren, E. L.; Bierman, M. J.; Boettcher, S. W.; Brunschwig, B. S.; Lewis, N. S.; Gray, H. B. *Energy Environ. Sci.* **2011**, *4*, 3573 (b) Warren, E. L.; McKone, J. R.; Atwater, H. A.; Gray, H. B.; Lewis, N. S. *Energy Environ. Sci.* **2012**, *5*, , 9653.

(115) Sato, T.; Takahashi, H.; Matsubara, E.; Muramatsu, A. *Mater. Trans.* **2002**, *43*, 1525.

(116) De Carvalho, J.; Tremiliosi Filho, G.; Avaca, L. A.; Gonzalez, E. R. *Int. J. Hydrogen Energy* **1989**, *14*, 161.

(117) Fan, C.; Piron, D. L.; Sleb, A.; Paradis, P. *J. Electrochem. Soc.* **1994**, *141*, 382.

(118) Rocheleau, R. E.; Miller, E. L.; Misra, A. *Energy & Fuels* **1998**, *12*, 3.

(119) Sasaki, Y.; Nemoto, H.; Saito, K.; Kudo, A. *J. Phys. Chem. C* **2009**, *113*, 17536.

(120) Yeo, B. S.; Bell, A. T. *J. Am. Chem. Soc.* **2011**, *133*, 5587.

(121) Giz, M. J.; Bento, S. C.; Gonzalez, E. R. *Int. J. Hydrogen Energy* **2000**, *25*, 621.

(122) He, Y.; Brown, C.; He, Y.; Fan, J.; Lundgren, C.; Zhao, Y. P. *Chem. Commun.* **2012**, *48*, 7741.

(123) (a) Hoffmann, F.; Cornelius, M.; Morell, J.; Fröba, M. *Angew. Chem. Int. Ed.* **2006**, *45*, 3216 (b) Joshi, R. K.; Schneider, J. J. *Chem. Soc. Rev.* **2012**, *41*, 5285.

(124) Meguro, S.; Sasaki, T.; Katagiri, H.; Habazaki, H.; Kawashima, A.; Sakaki, T.; Asami, K.; Hashimoto, K. *J. Electrochem. Soc.* **2000**, *147*, 3003.

(125) Zabinski, P. R.; Meguro, S.; Asami, K.; Hashimoto, K. *Mater. Trans.* **2003**, *44*, 2350.

(126) Zabinski, P. R.; Meguro, S.; Asami, K.; Hashimoto, K. *Mater. Trans.* **2006**, *47*, 2860.

(127) Bediako, D. K.; Lassalle-Kaiser, B.; Surendranath, Y.; Yano, J.; Yachandra, V. K.; Nocera, D. G. *J. Am. Chem. Soc.* **2012**, *134*, 6801.

(128) (a) Tench, D.; Warren, L. F. *J. Electrochem. Soc.* **1983**, *130*, 869 (b) Lyons, M. E. G.; Brandon, M. P. *PCCP* **2009**, *11*, 2203.

(129) Baranova, E. A.; Cally, A.; Allagui, A.; Ntais, S.; Wüthrich, R. *Comptes Rendus Chimie* **2012**.

(130) Agegnehu, A. K.; Pan, C.-J.; Rick, J.; Lee, J.-F.; Su, W.-N.; Hwang, B.-J. *J. Mater. Chem.* **2012**, *22*, 13849.

(131) (a) Nakato, Y.; Tsumura, A.; Tsubomura, H. *Chem. Lett.* **1982**, *11*, 1071 (b) Nakato, Y.; Hiramoto, M.; Iwakabe, Y.; Tsubomura, H. *J. Electrochem. Soc.* **1985**, *132*, 330.

(132) Nakato, Y.; Egi, Y.; Hiramoto, M.; Tsubomura, H. *J. Phys. Chem.* **1984**, *88*, 4218.

(133) Pham, D.; Hope, G. *Aust. J. Chem.* **1985**, *38*, 1719.

(134) Fan, F. R. F.; Keil, R. G.; Bard, A. J. *J. Am. Chem. Soc.* **1983**, *105*, 220.

(135) (a) Brownson, D. A. C.; Kampouris, D. K.; Banks, C. E. *Chem. Soc. Rev.* **2012** (b) Chen, D.; Feng, H.; Li, J. *Chem. Rev.* **2012** (c) Dai, L. *Acc. Chem. Res.* **2012**.

(136) Yu, H.; Chen, S.; Fan, X.; Quan, X.; Zhao, H.; Li, X.; Zhang, Y. *Angew. Chem.* **2010**, *122*, 5232.

(137) Li, Y.; Zhou, W.; Wang, H.; Xie, L.; Liang, Y.; Wei, F.; Idrobo, J.-C.; Pennycook, S. J.; Dai, H. *Nat. Nanotechnol.* **2012**, *7*, 394.

(138) Choi, C. H.; Park, S. H.; Woo, S. I. *ACS Nano* **2012**.

(139) Miao, X.; Tongay, S.; Petterson, M. K.; Berke, K.; Rinzler, A. G.; Appleton, B. R.; Hebard, A. F. *Nano Lett.* **2012**, *12*, 2745.

(140) Lin, Y.; Li, X.; Xie, D.; Feng, T.; Tian, H.; Wang, K.; Zhu, H. *Energy Environ. Sci.* **2012**.

(141) Tune, D. D.; Flavel, B. S.; Krupke, R.; Shapter, J. G. *Adv. Energy Mater.* **2012**, *2*, 1043.

(142) Yang, H.; Heo, J.; Park, S.; Song, H. J.; Seo, D. H.; Byun, K.-E.; Kim, P.; Yoo, I.; Chung, H.-J.; Kim, K. *Science* **2012**, *336*, 1140.

(143) Hardee, K. L.; Bard, A. J. *J. Electrochem. Soc.* **1975**, *122*, 739.

(144) Hwang, Y. J.; Boukai, A.; Yang, P. *Nano Lett.* **2008**, *9*, 410.

(145) Noh, S. Y.; Sun, K.; Choi, C.; Niu, M.; Xu, K.; Yang, M.; Jin, S.; Wang, D. *Submitted to Nanoenergy* **2012**.

(146) Yoon, K. H.; Shin, C. W.; Kang, D. H. *J. Appl. Phys.* **1997**, *81*, 7024.

(147) Fujii, K.; Kato, T.; Sato, K.; Im, I.; Chang, J.; Yao, T. *Phys. Status Solidi C* **2010**, *7*, 2218.

(148) Ono, H.; Morisaki, H.; Yazawa, K. *Jpn. J. Appl. Phys.* **1982**, *21*, 1075.

(149) Sun, K.; Jing, Y.; Li, C.; Zhang, X.; Aguinaldo, R.; Kargar, A.; Madsen, K.; Banu, K.; Zhou, Y.; Bando, Y.; Liu, Z.; Wang, D. *Nanoscale* **2012**, *4*, 1515.

(150) Yoon, K. H.; Seo, D. K.; Cho, Y. S.; Kang, D. H. *J. Appl. Phys.* **1998**, *84*, 3954.

(151) Kuykendall, T.; Ulrich, P.; Aloni, S.; Yang, P. *Nat. Mater.* **2007**, *6*, 951.

(152) Hwang, Y. J.; Wu, C. H.; Hahn, C.; Jeong, H. E.; Yang, P. *Nano Lett.* **2012**, *12*, 1678.

(153) Strandwitz, N. C.; Turner-Evans, D. B.; Tamboli, A. C.; Chen, C. T.; Atwater, H. A.; Lewis, N. S. *Adv. Energy Mater.* **2012**, *2*, 1109.

(154) (a) Shi, J.; Hara, Y.; Sun, C.; Anderson, M. A.; Wang, X. *Nano Lett.* **2011**, *11*, 3413 (b) Shi, J.; Wang, X. *Energy Environ. Sci.* **2012**, *5*, 7918.

(155) Mayer, M. T.; Du, C.; Wang, D. *J. Am. Chem. Soc.* **2012**, *134*, 12406.

(156) Morisaki, H.; Ono, H.; Dohkoshi, H.; Yazawa, K. *Jpn. J. Appl. Phys.* **1980**, *19*, L148.

(157) Morisaki, H.; Baba, T.; Yazawa, K. *Phys. Rev. B: Condens. Matter* **1980**, *21*, 837.

(158) Jun, K.; Lee, Y. S.; Buonassisi, T.; Jacobson, J. M. *Angew. Chem. Int. Ed.* **2012**, *51*, 423.

(159) Yoon, K. H.; Choi, W. J.; Kang, D. H. *Thin Solid Films* **2000**, *372*, 250.

(160) Yu, A. A.; Koh, W. S.; Sian, S. Y.; Ren, S. *Appl. Phys. Lett.* **2010**, *96*, 073111.

(161) (a) Naik, G. V.; Schroeder, J. L.; Ni, X.; Kildishev, A. V.; Sands, T. D.; Boltasseva, A. *Opt. Mater. Express* **2012**, *2*, 478 (b) Naik, G. V.; Liu, J.; Kildishev, A. V.; Shalaev, V. M.; Boltasseva, A. *Proc. Natl. Acad. Sci. USA* **2012**, *109*, 8834 (c) Naik, G. V.; Kim, J.; Boltasseva, A. *Opt. Mater. Express* **2011**, *1*, 1090 (d) Boltasseva, A.; Atwater, H. A. *Science* **2011**, *331*, 290.

(162) Grandidier, J.; Callahan, D. M.; Munday, J. N.; Atwater, H. A. *Adv. Mater.* **2011**, *23*, 1272.

(163) Grandidier, J.; Deceglie, M. G.; Callahan, D. M.; Atwater, H. A. *J. Photonics Energy* **2012**, *2*, 024502.

(164) (a) Thompson, L.; DuBow, J.; Rajeshwar, K. *J. Electrochem. Soc.* **1982**, *129*, 1934 (b) Hodes, G.; Thompson, L.; DuBow, J.; Rajeshwar, K. *J. Am. Chem. Soc.* **1983**, *105*, 324.

(165) Kelly, N. A.; Gibson, T. L. *Int. J. Hydrogen Energy* **2006**, *31*, 1658.

(166) Bélanger, D.; Dodelet, J. P.; Lombos, B. A. *J. Electrochem. Soc.* **1986**, *133*, 1113.

(167) (a) Decker, F.; Fracastoro-Decker, M.; Badawy, W.; Doblhofer, K.; Gerischer, H. *J. Electrochem. Soc.* **1983**, *130*, 2173 (b) Badawy, W. A. *Sol. Energy Mater. Sol. Cells* **2002**, *71*, 281.

(168) (a) Kawazoe, H.; Yasukawa, M.; Hyodo, H.; Kurita, M.; Yanagi, H.; Hosono, H. *Nature* **1997**, *389*, 939 (b) Hosono, H. *Thin Solid Films* **2007**, *515*, 6000 (c) Cui, J.; Wang, A.; Edleman, N. L.; Ni, J.; Lee, P.; Armstrong, N. R.; Marks, T. J. *Adv. Mater.* **2001**, *13*, 1476.

(169) Patrick, V. Ph.D Thesis, California Institute of Technology, 1989.

(170) Yin, M.; Wu, C.-K.; Lou, Y.; Burda, C.; Koberstein, J. T.; Zhu, Y.; O'Brien, S. *J. Am. Chem. Soc.* **2005**, *127*, 9506.

(171) Hara, M.; Kondo, T.; Komoda, M.; Ikeda, S.; N. Kondo, J.; Domen, K.; Shinohara, K.; Tanaka, A. *Chem. Commun.* **1998**, 357.

(172) Chen, H.-Y.; Su, H.-C.; Chen, C.-H.; Liu, K.-L.; Tsai, C.-M.; Yen, S.-J.; Yew, T.-R. *J. Mater. Chem.* **2011**, *21*, 5745.

(173) Arca, E.; Fleischer, K.; Shvets, I. V. *Appl. Phys. Lett.* **2011**, *99*, 111910.

(174) Dekkers, M.; Rijnders, G.; Blank, D. H. A. *Appl. Phys. Lett.* **2007**, *90*, 021903.

(175) Cook, T. R.; Dogutan, D. K.; Reece, S. Y.; Surendranath, Y.; Teets, T. S.; Nocera, D. G. *Chem. Rev.* **2010**, *110*, 6474.

(176) Simon, P.; Gogotsi, Y. *Nat. Mater.* **2008**, *7*, 845.

(177) Debe, M. K. *Nature* **2012**, *486*, 43.

(178) (a) Koji, H.; Zenta, K.; Naokazu, K.; Koichi, I. *J. Phys. Conf. Ser.* **2009**, *144*, 012009 (b) Lee, Y.; Suntivich, J.; May, K. J.; Perry, E. E.; Shao-Horn, Y. *J. Phys. Chem. Lett.* **2012**, *3*, 399.

(179) Nørskov, J. K.; Bligaard, T.; Logadottir, A.; Kitchin, J. R.; Chen, J. G.; Pandelov, S.; Stimming, U. *J. Electrochem. Soc.* **2005**, *152*, J23.

(180) Nørskov, J. K.; Abild-Pedersen, F.; Studt, F.; Bligaard, T. *Proc. Natl. Acad. Sci. USA* **2011**, *108*, 937.

(181) Man, I. C.; Su, H.-Y.; Calle-Vallejo, F.; Hansen, H. A.; Martínez, J. I.; Inoglu, N. G.; Kitchin, J.; Jaramillo, T. F.; Nørskov, J. K.; Rossmeisl, J. *ChemCatChem* **2011**, *3*, 1159.

(182) Subbaraman, R.; Tripkovic, D.; Chang, K.-C.; Strmcnik, D.; Paulikas, A. P.; Hirunsit, P.; Chan, M.; Greeley, J.; Stamenkovic, V.; Markovic, N. M. *Nat. Mater.* **2012**, *advance online publication*.

(183) Chen, A.; Holt-Hindle, P. *Chem. Rev.* **2010**, *110*, 3767.

(184) Esposito, D. V.; Hunt, S. T.; Stottlemyer, A. L.; Dobson, K. D.; McCandless, B. E.; Birkmire, R. W.; Chen, J. G. *Angew. Chem. Int. Ed.* **2010**, *49*, 9859.

(185) (a) Du, P.; Eisenberg, R. *Energy Environ. Sci.* **2012**, *5*, 6012 (b) Wang, M.; Chen, L.; Sun, L. *Energy Environ. Sci.* **2012** (c) Merki, D.; Hu, X. *Energy Environ. Sci.* **2011**, *4*, 3878.

(186) Young, K. J.; Martini, L. A.; Milot, R. L.; Snoeberger Iii, R. C.; Batista, V. S.; Schmuttenmaer, C. A.; Crabtree, R. H.; Brudvig, G. W. *Coord. Chem. Rev.* **2012**, *256*, 2503.

(187) Jaramillo, T. F.; Jørgensen, K. P.; Bonde, J.; Nielsen, J. H.; Horch, S.; Chorkendorff, I. *Science* **2007**, *317*, 100.

(188) (a) Karunadasa, H. I.; Montalvo, E.; Sun, Y.; Majda, M.; Long, J. R.; Chang, C. J. *Science* **2012**, *335*, 698 (b) Hinnemann, B.; Moses, P. G.; Bonde, J.; Jørgensen, K. P.; Nielsen, J. H.; Horch, S.; Chorkendorff, I.; Nørskov, J. K. *J. Am. Chem. Soc.* **2005**, *127*, 5308.

(189) Zong, X.; Yan, H.; Wu, G.; Ma, G.; Wen, F.; Wang, L.; Li, C. *J. Am. Chem. Soc.* **2008**, *130*, 7176.

(190) Helveg, S.; Lauritsen, J. V.; Lægsgaard, E.; Stensgaard, I.; Nørskov, J. K.; Clausen, B. S.; Topsøe, H.; Besenbacher, F. *Phys. Rev. Lett.* **2000**, *84*, 951.

(191) Jaramillo, T. F.; Jorgensen, K. P.; Bonde, J.; Nielsen, J. H.; Horch, S.; Chorkendorff, I. *Science* **2007**, *317*, 100.

(192) Kibsgaard, J.; Chen, Z.; Reinecke, B. N.; Jaramillo, T. F. *Nat. Mater.* **2012**, *advance online publication*.

(193) Eda, G.; Fujita, T.; Yamaguchi, H.; Voiry, D.; Chen, M.; Chhowalla, M. *ACS Nano* **2012**, *6*, 7311.

(194) Chhowalla, M. *Nature under revision* **2012**.

(195) Jaramillo, T. F.; Bonde, J.; Zhang, J.; Ooi, B.-L.; Andersson, K.; Ulstrup, J.; Chorkendorff, I. *J. Phys. Chem. C* **2008**, *112*, 17492.

(196) Hou, Y.; Abrams, B. L.; Vesborg, P. C. K.; Björketun, M. E.; Herbst, K.; Bech, L.; Setti, A. M.; Damsgaard, C. D.; Pedersen, T.; Hansen, O.; Rossmeisl, J.; Dahl, S.; Nørskov, J. K.; Chorkendorff, I. *Nat. Mater.* **2011**, *10*, 434.

(197) Seger, B.; Laursen, A. B.; Vesborg, P. C. K.; Pedersen, T.; Hansen, O.; Dahl, S.; Chorkendorff, I. *Angew. Chem. Int. Ed.* **2012**, *51*, 9128.

(198) Hou, Y.; Abrams, B. L.; Vesborg, P. C. K.; Bjorketun, M. E.; Herbst, K.; Bech, L.; Seger, B.; Pedersen, T.; Hansen, O.; Rossmeisl, J.; Dahl, S.; Norskov, J. K.; Chorkendorff, I. *J. Photonics Energy* **2012**, *2*, 026001.

(199) Merki, D.; Vrubel, H.; Rovelli, L.; Fierro, S.; Hu, X. *Chemical Science* **2012**, *3*, 2515.

(200) Tran, P. D.; Nguyen, M.; Pramana, S. S.; Bhattacharjee, A.; Chiam, S. Y.; Fize, J.; Field, M. J.; Artero, V.; Wong, L. H.; Loo, J.; Barber, J. *Energy Environ. Sci.* **2012**, *5*, 8912.

(201) Tang, M. L.; Grauer, D. C.; Lassalle-Kaiser, B.; Yachandra, V. K.; Amirav, L.; Long, J. R.; Yano, J.; Alivisatos, A. P. *Angew. Chem. Int. Ed.* **2011**, *50*, 10203.

(202) Vrubel, H.; Merki, D.; Hu, X. *Energy Environ. Sci.* **2012**, *5*, 6136.

(203) Benck, J. D.; Chen, Z.; Kuritzky, L. Y.; Forman, A. J.; Jaramillo, T. F. *ACS Catalysis* **2012**, 1916.

(204) Li, Y.; Wang, H.; Xie, L.; Liang, Y.; Hong, G.; Dai, H. *J. Am. Chem. Soc.* **2011**, *133*, 7296.

(205) Chen, Z.; Cummins, D.; Reinecke, B. N.; Clark, E.; Sunkara, M. K.; Jaramillo, T. F. *Nano Lett.* **2011**, *11*, 4168.

(206) Laursen, A. B.; Kegnaes, S.; Dahl, S.; Chorkendorff, I. *Energy Environ. Sci.* **2012**, *5*, 5577.

(207) Merki, D.; Vrubel, H.; Rovelli, L.; Fierro, S.; Hu, X. *Chem. Sci.* **2012**, *3*, 2515.

(208) Chen, W.-F.; Sasaki, K.; Ma, C.; Frenkel, A. I.; Marinkovic, N.; Muckerman, J. T.; Zhu, Y.; Adzic, R. R. *Angew. Chem. Int. Ed.* **2012**, *51*, 6131.

(209) Li, G. R.; Song, J.; Pan, G. L.; Gao, X. P. *Energy Environ. Sci.* **2011**, *4*, 1680.

(210) Chen, W.-F.; Wang, C.-H.; Sasaki, K.; Marinkovic, N.; Xu, W.; Muckerman, J.; Zhu, Y.; Adzic, R. R. *Meeting Abstracts* **2012**, *MA2012-02*, 1817.

(211) Wirth, S.; Harnisch, F.; Weinmann, M.; Schröder, U. *Appl. Catal., B* **2012**, *126*, 225.

(212) Vrubel, H.; Hu, X. *Angew. Chem. Int. Ed.* **2012**, n/a.

(213) Cobo, S.; Heidkamp, J.; Jacques, P.-A.; Fize, J.; Fourmond, V.; Guetaz, L.; Jousselme, B.; Ivanova, V.; Dau, H.; Palacin, S.; Fontecave, M.; Artero, V. *Nat. Mater.* **2012**, *11*, 802.

(214) Subbaraman, R.; Tripkovic, D.; Chang, K.-C.; Strmcnik, D.; Paulikas, A. P.; Hirunsit, P.; Chan, M.; Greeley, J.; Stamenkovic, V.; Markovic, N. M. *Nat. Mater.* **2012**, *11*, 550.

(215) Gong, F.; Wang, H.; Xu, X.; Zhou, G.; Wang, Z.-S. *J. Am. Chem. Soc.* **2012**, *134*, 10953.

(216) (a) Vandenborre, H.; Vermeiren, P.; Leysen, R. *Electrochim. Acta* **1984**, *29*, 297 (b) Han, Q.; Liu, K.; Chen, J.; Wei, X. *Int. J. Hydrogen Energy* **2003**, *28*, 1207.

(217) Gao, M.-R.; Lin, Z.-Y.; Zhuang, T.-T.; Jiang, J.; Xu, Y.-F.; Zheng, Y.-R.; Yu, S.-H. *J. Mater. Chem.* **2012**, *22*, 13662.

(218) (a) Hensel, J.; Wang, G.; Li, Y.; Zhang, J. Z. *Nano Lett.* **2010**, *10*, 478 (b) Levy-Clement, C.; Heller, A.; Bonner, W. A.; Parkinson, B. A. *J. Electrochem. Soc.* **1982**, *129*, 1701.

(219) Tong, Y. J. *Chem. Soc. Rev.* **2012**.

(220) Danilovic, N.; Subbaraman, R.; Strmcnik, D.; Chang, K.-C.; Paulikas, A. P.; Stamenkovic, V. R.; Markovic, N. M. *Angew. Chem. Int. Ed.* **2012**, n/a.

(221) (a) Kanady, J. S.; Tsui, E. Y.; Day, M. W.; Agapie, T. *Science* **2011**, *333*, 733 (b) Hocking, R. K.; Brimblecombe, R.; Chang, L.-Y.; Singh, A.; Cheah, M. H.; Glover, C.; Casey, W. H.; Spiccia, L. *Nat. Chem.* **2011**, *3*, 461.

(222) Gorlin, Y.; Jaramillo, T. F. *J. Am. Chem. Soc.* **2010**, *132*, 13612.

(223) Zaharieva, I.; Chernev, P.; Risch, M.; Klingan, K.; Kohlhoff, M.; Fischerb, A.; Dau, H. *Energy Environ. Sci.* **2012**, *5*, 7081.

(224) Takashima, T.; Hashimoto, K.; Nakamura, R. *J. Am. Chem. Soc.* **2012**.

(225) Najafpour, M. M.; Ehrenberg, T.; Wiechen, M.; Kurz, P. *Angew. Chem. Int. Ed.* **2010**, *49*, 2233.

(226) Abdel Ghany, N. A.; Kumagai, N.; Meguro, S.; Asami, K.; Hashimoto, K. *Electrochim. Acta* **2002**, *48*, 21.

(227) Matsui, T.; Habazaki, H.; Kawashima, A.; Asami, K.; Kumagai, N.; Hashimoto, K. *J. Appl. Electrochem.* **2002**, *32*, 993.

(228) Kainthla, R. C.; Zelenay, B.; Bockris, J. O. M. *J. Electrochem. Soc.* **1986**, *133*, 248.

(229) Singh, R. N.; Madhu; Awasthi, R.; Tiwari, S. K. *Int. J. Hydrogen Energy* **2009**, *34*, 4693.

(230) Liao, P.; Keith, J. A.; Carter, E. A. *J. Am. Chem. Soc.* **2012**, *134*, 13296.

(231) (a) Hamdani, M.; Singh, R. N.; Chartier, P. *Int. J. Electrochem. Sci.,* **2010**, *5*, 556 (b) Jiao, F.; Frei, H. *Energy Environ. Sci.* **2010**, *3*, 1018.

(232) Cong, Y.; Park, H. S.; Wang, S.; Dang, H. X.; Fan, F.-R. F.; Mullins, C. B.; Bard, A. J. *J. Phys. Chem. C* **2012**, *116*, 14541.

(233) Xiao, X.; Liu, X.; Zhao, H.; Chen, D.; Liu, F.; Xiang, J.; Hu, Z.; Li, Y. *Adv. Mater.* **2012**, n/a.

(234) Koza, J. A.; He, Z.; Miller, A. S.; Switzer, J. A. *Chem. Mater.* **2012**.

(235) Jiao, F.; Frei, H. *Angew. Chem. Int. Ed.* **2009**, *48*, 1841.

(236) Pijpers, J. J. H.; Winkler, M. T.; Surendranath, Y.; Buonassisi, T.; Nocera, D. G. *Proc. Natl. Acad. Sci. USA* **2011**, *108*, 10056.

(237) Sun, K.; Park, N.; Sun, Z.; Zhou, J.; Wang, J.; Pang, X.; Shen, S.; Noh, S. Y.; Jing, Y.; Jin, S.; Yu, P.; Wang, D. *Energy Environ. Sci.* **2012**, *5*, 7872.

(238) Li, Y.; Hasin, P.; Wu, Y. *Adv. Mater.* **2010**, *22*, 1926.

(239) Lu, B.; Cao, D.; Wang, P.; Wang, G.; Gao, Y. *Int. J. Hydrogen Energy* **2011**, *36*, 72.

(240) Chien, H.-C.; Cheng, W.-Y.; Wang, Y.-H.; Wei, T.-Y.; Lu, S.-Y. *J. Mater. Chem.* **2011**, *21*, 18180.

(241) Liang, Y.; Wang, H.; Zhou, J.; Li, Y.; Wang, J.; Regier, T.; Dai, H. *J. Am. Chem. Soc.* **2012**, *134*, 3517.

(242) Liang, Y.; Li, Y.; Wang, H.; Zhou, J.; Wang, J.; Regier, T.; Dai, H. *Nat. Mater.* **2011**, *10*, 780.

(243) De Koninck, M.; Poirier, S.-C.; Marsan, B. *J. Electrochem. Soc.* **2006**, *153*, A2103.

(244) Suntivich, J.; May, K. J.; Gasteiger, H. A.; Goodenough, J. B.; Shao-Horn, Y. *Science* **2011**, *334*, 1383.

(245) Singh, R. N.; Singh, N. K.; Singh, J. P. *Electrochim. Acta* **2002**, *47*, 3873.

(246) Godinho, M. I.; Catarino, M. A.; da Silva Pereira, M. I.; Mendonça, M. H.; Costa, F. M. *Electrochim. Acta* **2002**, *47*, 4307.

(247) Bockris, J. O.; Otagawa, T. *J. Phys. Chem.* **1983**, *87*, 2960.

(248) Vojvodic, A.; Nørskov, J. K. *Science* **2011**, *334*, 1355.

(249) Kanan, M. W.; Nocera, D. G. *Science* **2008**, *321*, 1072.

(250) (a) Jeon, T. H.; Choi, W.; Park, H. *PCCP* **2011**, *13*, 21392 (b) Zhong, D. K.; Choi, S.; Gamelin, D. R. *J. Am. Chem. Soc.* **2011** (c) Abdi, F. F.; Krol, R. v. d. *J. Phys. Chem. C* **2012**, *116*, 9398.

(251) (a) Zhong, D. K.; Cornuz, M.; Sivula, K.; Gratzel, M.; Gamelin, D. R. *Energy Environ. Sci.* **2011**, *4*, 1759 (b) Barroso, M.; Cowan, A. J.; Pendlebury, S. R.; Grätzel, M.; Klug, D. R.; Durrant, J. R. *J. Am. Chem. Soc.* **2011**, *133*, 14868 (c) Klahr, B.; Gimenez, S.; Fabregat-Santiago, F.; Bisquert, J.; Hamann, T. W. *J. Am. Chem. Soc.* **2012**.

(252) Steinmiller, E. M. P.; Choi, K.-S. *Proc. Natl. Acad. Sci. USA* **2009**, *106*, 20633.

(253) Khnayzer, R. S.; Mara, M. W.; Huang, J.; Shelby, M. L.; Chen, L. X.; Castellano, F. N. *ACS Catalysis* **2012**, 2150.

(254) (a) Reece, S. Y.; Hamel, J. A.; Sung, K.; Jarvi, T. D.; Esswein, A. J.; Pijpers, J. J. H.; Nocera, D. G. *Science* **2011**, *334*, 645 (b) Young, E. R.; Costi, R.; Paydavosi, S.; Nocera, D. G.; Bulovic, V. *Energy Environ. Sci.* **2011**, *4*, 2058.

(255) Surendranath, Y.; Dincă, M.; Nocera, D. G. *J. Am. Chem. Soc.* **2009**, *131*, 2615.

(256) Surendranath, Y.; Lutterman, D. A.; Liu, Y.; Nocera, D. G. *J. Am. Chem. Soc.* **2012**, *134*, 6326.

(257) Ahn, H. S.; Tilley, T. D. *Adv. Funct. Mater.* **2012**, n/a.

(258) Gao, M.-R.; Yao, W.-T.; Yao, H.-B.; Yu, S.-H. *J. Am. Chem. Soc.* **2009**, *131*, 7486.

(259) Gao, M.-R.; Xu, Y.-F.; Jiang, J.; Zheng, Y.-R.; Yu, S.-H. *J. Am. Chem. Soc.* **2012**, *134*, 2930.

(260) Osterloh, F. E. *Chem. Mater.* **2007**, *20*, 35.

(261) Li, G.; Wang, S. *J. Electroanal. Chem. Interfac. Electrochem.* **1987**, *227*, 213.

(262) Sun, K.; Park, N.; Sun, Z.; Zhou, J.; Wang, J.; Pang, X.; Shen, S.; Noh, S. Y.; Jing, Y.; Jin, S.; Yu, P. K. L.; Wang, D. *Energy Environ. Sci.* **2012**, *5*, 7872.

(263) (a) Miller, E. L.; Rocheleau, R. E. *J. Electrochem. Soc.* **1997**, *144*, 3072 (b) Miller, E. L.; Rocheleau, R. E. *J. Electrochem. Soc.* **1997**, *144*, 1995.

(264) Corrigan, D. A. *J. Electrochem. Soc.*, **1987**, *134*, 377.

(265) Lu, P. W. T.; Srinivasan, S. *J. Electrochem. Soc.* **1978**, *125*, 1416.

(266) Landon, J.; Demeter, E.; İnoğlu, N.; Keturakis, C.; Wachs, I. E.; Vasić, R.; Frenkel, A. I.; Kitchin, J. R. *ACS Catalysis* **2012**, *2*, 1793.

(267) Merrill, M. D. Ph.D Thesis, The Florida State University, 2007.

(268) Li, X.; Walsh, F. C.; Pletcher, D. *PCCP* **2011**, *13*, 1162.

(269) Trotochaud, L.; Ranney, J. K.; Williams, K. N.; Boettcher, S. W. *J. Am. Chem. Soc.* **2012**.

(270) Risch, M.; Klingan, K.; Heidkamp, J.; Ehrenberg, D.; Chernev, P.; Zaharieva, I.; Dau, H. *Chem. Commun.* **2011**, *47*, 11912.

(271) Dincă, M.; Surendranath, Y.; Nocera, D. G. *Proc. Natl. Acad. Sci. USA* **2010**, *107*, 10337.

(272) Osaka, T.; Ishibashi, H.; Endo, T.; Yoshida, T. *Electrochim. Acta* **1981**, *26*, 339.

(273) Switzer, J. A. *J. Electrochem. Soc.* **1986**, *133*, 722.

(274) Friebel, D.; Viswanathan, V.; Miller, D. J.; Anniyev, T.; Ogasawara, H.; Larsen, A. H.; O'Grady, C. P.; Nørskov, J. K.; Nilsson, A. *J. Am. Chem. Soc.* **2012**, *134*, 9664.

(275) Yeo, B. S.; Bell, A. T. *J. Phys. Chem. C* **2012**, *116*, 8394.

(276) Han, H.; Frei, H. *J. Phys. Chem. C* **2008**, *112*, 16156.

(277) Sivasankar, N.; Weare, W. W.; Frei, H. *J. Am. Chem. Soc.* **2011**, *133*, 12976.

(278) Du, P.; Kokhan, O.; Chapman, K. W.; Chupas, P. J.; Tiede, D. M. *J. Am. Chem. Soc.* **2012**, *134*, 11096.

(279) (a) Bard, A. J.; Wrighton, M. S. *J. Electrochem. Soc.* **1977**, *124*, 1706 (b) Gerischer, H. *J. Electroanal. Chem. Interfac. Electrochem.* **1977**, *82*, 133.

(280) Paracchino, A.; Mathews, N.; Hisatomi, T.; Stefik, M.; Tilley, D.; Gratzel, M. *Energy Environ. Sci.* **2012**, *5*, 8673.

(281) Meier, J. C.; Katsounaros, I.; Galeano, C.; Bongard, H.; Topalov, A. A.; Kostka, A.; Karschin, A.; Schuth, F.; Mayrhofer, K. J. J. *Energy Environ. Sci.* **2012**.

(282) (a) Noufi, R.; Frank, A. J.; Nozik, A. J. *J. Am. Chem. Soc.* **1981**, *103*, 1849 (b) Frank, A. J.; Honda, K. *J. Photochem.* **1985**, *29*, 195 (c) Cooper, G.; Noufi, R.; Frank, A. J.; Nozik, A. J. *Nature* **1982**, *295*, 578 (d) Noufi, R.; Tench, D.; Warren, L. F. *J. Electrochem. Soc.* **1980**, *127*, 2310.

(283) Skotheim, T.; Lundstrom, I.; Prejza, J. *J. Electrochem. Soc.* **1981**, *128*, 1625.

(284) Skotheim, T.; Petersson, L. G.; Inganas, O.; Lundstrom, I. *J. Electrochem. Soc.* **1982**, *129*, 1737.

(285) Simon, R. A.; Wrighton, M. S. *Appl. Phys. Lett.* **1984**, *44*, 930.

(286) Noufi, R.; Nozik, A. J.; White, J.; Warren, L. F. *J. Electrochem. Soc.* **1982**, *129*, 2261.

(287) Leising, G. *Synth. Met.* **1989**, *28*, D215.

(288) Zhang, M.; Shao, C.; Guo, Z.; Zhang, Z.; Mu, J.; Cao, T.; Liu, Y. *ACS Appl. Mater. Interfaces* **2011**, null.

(289) Giraudeau, A.; Fan, F.-R. F.; Bard, A. J. *J. Am. Chem. Soc.* **1980**, *102*, 5137.

(290) (a) Loutfy, R. O.; Sharp, J. H.; Hsiao, C. K.; Ho, R. *J. Appl. Phys.* **1981**, *52*, 5218 (b) Liu, Z. T.; Kwok, H. S.; Djurišić, A. B. *J. Phys. D: Appl. Phys.* **2004**, *37*, 678.

(291) Nakato, Y.; Shioji, M.; Tsubomura, H. *J. Phys. Chem.* **1981**, *85*, 1670.

(292) Zhao, S.; Li, X.; Yang, M.; Sun, C. *J. Mater. Chem.* **2004**, *14*, 840.

(293) PARK, C.; NAM, H. W.; OVCHINNIKOV, A. A.; PARK, Y. W. *Synthetic. Metals* **1993**, *55-57*, 4065.

(294) (a) Meshitsuka, S.; Tamaru, K. *J. Chem. Soc., Faraday Trans. 1 F* **1977**, *73*, 236 (b) Rieke, P. C.; Armstrong, N. R. *J. Am. Chem. Soc.* **1984**, *106*, 47.

(295) Abe, T.; Miyakushi, S.; Nagai, K.; Norimatsu, T. *PCCP* **2008**, *10*, 1562.

(296) Yang, T.; Wang, H.; Ou, X.-M.; Lee, C.-S.; Zhang, X.-H. *Adv. Mater.* **2012**, n/a.

(297) Haran, A.; Waldeck, D. H.; Naaman, R.; Moons, E.; Cahen, D. *Science* **1994**, *263*, 948.

(298) O'Leary, L. E.; Johansson, E.; Brunschwig, B. S.; Lewis, N. S. *J. Phys. Chem. B* **2010**, *114*, 14298.

(299) Ciampi, S.; Le Saux, G.; Harper, J. B.; Gooding, J. J. *Electroanalysis* **2008**, *20*, 1513.

(300) Taniguchi, Y.; Yoneyama, H.; Tamura, H. *Chem. Lett.* **1983**, *12*, 269.

(301) Legg, K. D.; Ellis, A. B.; Bolts, J. M.; Wrighton, M. S. *Proc. Natl. Acad. Sci. USA* **1977**, *74*, 4116.

(302) Heller, A.; Lewerenz, H. J.; Miller, B. *J. Am. Chem. Soc.* **1981**, *103*, 200.

(303) Bookbinder, D. C.; Lewis, N. S.; Bradley, M. G.; Bocarsly, A. B.; Wrighton, M. S. *J. Am. Chem. Soc.* **1979**, *101*, 7721.

(304) (a) Wrighton, M. S.; Austin, R. G.; Bocarsly, A. B.; Bolts, J. M.; Haas, O.; Legg, K. D.; Nadjo, L.; Palazzoto, M. C. *J. Am. Chem. Soc.* **1978**, *100*, 1602 (b) Bocarsly, A. B.; Walton, E. G.; Wrighton, M. S. *J. Am. Chem. Soc.* **1980**, *102*, 3390.

(305) Bocarsly, A. B.; Walton, E. G.; Bradley, M. G.; Wrighton, M. S. *J. Electroanal. Chem. Interfac. Electrochem.* **1979**, *100*, 283.

(306) (a) Malpas, R. E.; Rushby, B. *J. Electroanal. Chem. Interfac. Electrochem.* **1983**, *157*, 387 (b) Rosenblum, M. D.; Lewis, N. S. *J. Phys. Chem.* **1984**, *88*, 3103.

(307) Bookbinder, D. C.; Bruce, J. A.; Dominey, R. N.; Lewis, N. S.; Wrighton, M. S. *Proc. Natl. Acad. Sci. USA* **1980**, *77*, 6280.

(308) Dominey, R. N.; Lewis, N. S.; Bruce, J. A.; Bookbinder, D. C.; Wrighton, M. S. *J. Am. Chem. Soc.* **1982**, *104*, 467.

(309) Abruna, H. D.; Bard, A. J. *J. Am. Chem. Soc.* **1981**, *103*, 6898.

(310) Turner, D. R. *J. Electrochem. Soc.* **1960**, *107*, 810.

(311) (a) Matsumura, M.; Morrison, S. R. *J. Electroanal. Chem. Interfac. Electrochem.* **1983**, *144*, 113 (b) Matsumura, M.; Roy Morrison, S. *J. Electroanal. Chem. Interfac. Electrochem.* **1983**, *147*, 157.

(312) Kubiak, C. P.; Schneemeyer, L. F.; Wrighton, M. S. *J. Am. Chem. Soc.* **1980**, *102*, 6898.

(313) Lewis, N. S. *Nature* **2001**, *414*, 589.

(314) Nann, T.; Ibrahim, S. K.; Woi, P.-M.; Xu, S.; Ziegler, J.; Pickett, C. J. *Angew. Chem. Int. Ed.* **2010**, *49*, 1574.

(315) Kumar, B.; Beyler, M.; Kubiak, C. P.; Ott, S. *Chem. Eur. J.* **2012**, *18*, 1295.

(316) Frischmann, P. D.; Mahata, K.; Wurthner, F. *Chem. Soc. Rev.* **2012**.

(317) (a) Gloaguen, F.; Rauchfuss, T. B. *Chem. Soc. Rev.* **2009**, *38*, 100 (b) Boghossian, A. A.; Ham, M.-H.; Choi, J. H.; Strano, M. S. *Energy Environ. Sci.* **2011**, *4*, 3834 (c) Armstrong, F. A.; Hirst, J. *Proc. Natl. Acad. Sci. USA* **2011**, *108*, 14049 (d) Artero, V.; Fontecave, M. *Comptes Rendus Chimie* **2011**, *14*, 799 (e) Artero, V.; Chavarot-Kerlidou, M.; Fontecave, M. *Angew. Chem. Int. Ed.* **2011**, *50*, 7238 (f) Andreiadis, E. S.; Chavarot-Kerlidou, M.; Fontecave, M.; Artero, V. *Photochem. Photobiol.* **2011**, *87*, 946 (g) Tran, P. D.; Artero, V.; Fontecave, M. *Energy Environ. Sci.* **2010**, *3*, 727 (h) Jacques, P.-A.; Artero, V.; Pecaut, J.; Fontecave, M. *Proc. Natl. Acad. Sci. USA* **2009**, *106*, 20627 (i) Kilgore, U. J.; Roberts, J. A. S.; Pool, D. H.; Appel, A. M.; Stewart, M. P.; DuBois, M. R.; Dougherty, W. G.; Kassel, W. S.; Bullock, R. M.; DuBois, D. L. *J. Am. Chem. Soc.* **2011**, *133*, 5861 (j) Helm, M. L.; Stewart, M. P.; Bullock, R. M.; DuBois, M. R.; DuBois, D. L. *Science* **2011**, *333*, 863 (k) Rakowski Dubois, M.; Dubois, D. L. *Acc. Chem. Res.* **2009**, *42*, 1974 (l) Duan, L.; Bozoglian, F.; Mandal, S.; Stewart, B.; Privalov, T.; Llobet, A.; Sun, L. *Nat. Chem.* **2012**, *4*, 418 (m) Cao, R.; Lai, W.; Du, P. *Energy Environ. Sci.* **2012**, *5*, 8134.

(318) Zhang, Z.; Yates, J. T. *Chem. Rev.* **2012**.

(319) (a) Nozik, A. J. *Appl. Phys. Lett.* **1976**, *29*, 150 (b) Nozik, A. J. *Appl. Phys. Lett.* **1977**, *30*, 567.

(320) Tachibana, Y.; Vayssieres, L.; Durrant, J. R. *Nat. Photonics* **2012**, *6*, 511.

(321) Weber, M. F.; Dignam, M. J. *Int. J. Hydrogen Energy* **1986**, *11*, 225.

(322) McFarlane, S. L.; Day, B. A.; McEleney, K.; Freund, M. S.; Lewis, N. S. *Energy Environ. Sci.* **2011**, *4*, 1700.

(323) (a) Yahyaie, I.; McEleney, K.; Walter, M. G.; Oliver, D. R.; Thomson, D. J.; Freund, M. S.; Lewis, N. S. *J. Phys. Chem. C* **2011**, *115*, 24945 (b) Yahyaie, I.; McEleney, K.; Walter, M.; Oliver, D. R.; Thomson, D. J.; Freund, M. S.; Lewis, N. S. *J. Phys. Chem. Lett.* **2011**, *2*, 675.

(324) Spurgeon, J. M.; Walter, M. G.; Zhou, J.; Kohl, P. A.; Lewis, N. S. *Energy Environ. Sci.* **2011**, *4*, 1772.

(325) Leng, Y.; Chen, G.; Mendoza, A. J.; Tighe, T. B.; Hickner, M. A.; Wang, C.-Y. *J. Am. Chem. Soc.* **2012**, *134*, 9054.

(326) (a) Miles, M. H. *J. Electroanal. Chem. Interfac. Electrochem.* **1975**, *60*, 89 (b) Miles, M. H.; Thomason, M. A. *J. Electrochem. Soc.* **1976**, *123*, 1459.

(327) Xiao, L.; Zhang, S.; Pan, J.; Yang, C.; He, M.; Zhuang, L.; Lu, J. *Energy Environ. Sci.* **2012**, *5*, 7869.

(328) Matsumura, M.; Sakai, Y.; Sugahara, S.; Nakato, Y.; Tsubomura, H. *Sol. Energy Mater.* **1986**, *13*, 57.

(329) Sakai, Y.; Sugahara, S.; Matsumura, M.; Nakato, Y.; Tsubomura, H. *Can. J. Chem.* **1988**, *66*, 1853.

(330) Yamada, Y.; Matsuki, N.; Ohmori, T.; Mametsuka, H.; Kondo, M.; Matsuda, A.; Suzuki, E. *Int. J. Hydrogen Energy* **2003**, *28*, 1167.

(331) Khaselev, O.; Bansal, A.; Turner, J. A. *Int. J. Hydrogen Energy* **2001**, *26*, 127.

(332) Licht, S.; Wang, B.; Mukerji, S.; Soga, T.; Umeno, M.; Tributsch, H. *J. Phys. Chem. B* **2000**, *104*, 8920.

(333) Surendranath, Y.; Bediako, D. K.; Nocera, D. G. *Proc. Natl. Acad. Sci. USA* **2012**, *109*, 15560.

(334) Haussener, S.; Xiang, C.; Spurgeon, J.; Ardo, S.; Lewis, N.; Weber, A. Z. *Energy Environ. Sci.* **2012**.

(335) Fischer, J.; Hofmann, H.; Luft, G.; Wendt, H. *AICHE J.* **1980**, *26*, 794.

(336) Yum, J.-H.; Baranoff, E.; Kessler, F.; Moehl, T.; Ahmad, S.; Bessho, T.; Marchioro, A.; Ghadiri, E.; Moser, J.-E.; Yi, C.; Nazeeruddin, M. K.; Grätzel, M. *Nat. Commun.* **2012**, *3*, 631.

(337) Song, W.; Chen, Z.; Brennaman, M. K.; Concepcion, J. J.; Patrocinio, A. O. T.; Iha, N. Y. M.; Meyer, T. J. *Pure Appl. Chem.* **2011**, *83*, 749.

(338) (a) Ou, J. Z.; Rani, R. A.; Ham, M.-H.; Field, M. R.; Zhang, Y.; Zheng, H.; Reece, P.; Zhuiykov, S.; Sriram, S.; Bhaskaran, M.; Kaner, R. B.; Kalantar-zadeh, K. *ACS Nano* **2012**, *6*, 4045 (b) Ghosh, R.; Brennaman, M. K.; Uher, T.; Ok, M.-R.; Samulski, E. T.; McNeil, L. E.; Meyer, T. J.; Lopez, R. *ACS Appl. Mater. Interfaces* **2011**, *3*, 3929.

(339) Gibson, E. A.; Smeigh, A. L.; Le Pleux, L.; Fortage, J.; Boschloo, G.; Blart, E.; Pellegrin, Y.; Odobel, F.; Hagfeldt, A.; Hammarström, L. *Angew. Chem. Int. Ed.* **2009**, *48*, 4402.

(340) Yu, M.; Natu, G.; Ji, Z.; Wu, Y. *J. Phys. Chem. Lett.* **2012**, *3*, 1074.

(341) Xiong, D.; Xu, Z.; Zeng, X.; Zhang, W.; Chen, W.; Xu, X.; Wang, M.; Cheng, Y.-B. *J. Mater. Chem.* **2012**.

(342) Cheng, M.; Yang, X.; Zhang, F.; Zhao, J.; Sun, L. *Angew. Chem. Int. Ed.* **2012**, n/a.

(343) Daeneke, T.; Kwon, T.-H.; Holmes, A. B.; Duffy, N. W.; Bach, U.; Spiccia, L. *Nat. Chem.* **2011**, *3*, 211.

(344) Carver, C.; Ulissi, Z.; Hellgardt, K.; Ong, C. K.; Dennison, S.; Kelsall, G. The American Institute of Chemical Engineers annual meeting, Salt lake city, UT, 2010.

(345) Sillen, C. W. M. P.; Barendrecht, E.; Janssen, L. J. J.; van Stralen, S. J. D. *Int. J. Hydrogen Energy* **1982**, *7*, 577.

(346) Kuhl, K. P.; Cave, E. R.; Abram, D. N.; Jaramillo, T. F. *Energy Environ. Sci.* **2012**, *5*, 7050.

(347) Wang, W.-N.; An, W.-J.; Ramalingam, B.; Mukherjee, S.; Niedzwiedzki, D. M.; Gangopadhyay, S.; Biswas, P. *J. Am. Chem. Soc.* **2012**, *134*, 11276.

(348) Kauffman, D. R.; Alfonso, D.; Matranga, C.; Qian, H.; Jin, R. *J. Am. Chem. Soc.* **2012**, *134*, 10237.

(349) Peterson, A. A.; Abild-Pedersen, F.; Studt, F.; Rossmeisl, J.; Norskov, J. K. *Energy Environ. Sci.* **2010**, *3*, 1311.

(350) (a) Hinogami, R.; Nakamura, Y.; Yae, S.; Nakato, Y. *J. Phys. Chem. B* **1998**, *102*, 974 (b) Cottineau, T.; Morin, M.; Belanger, D. *ECS Transactions* **2009**, *19*, 1.

(351) Tang, W.; Peterson, A. A.; Varela, A. S.; Jovanov, Z. P.; Bech, L.; Durand, W. J.; Dahl, S.; Norskov, J. K.; Chorkendorff, I. *PCCP* **2012**, *14*, 76.

(352) Xu, Z.; Lai, E.; Shao-Horn, Y.; Hamad-Schifferli, K. *Chem. Commun.* **2012**, *48*, 5626.

(353) Li, C. W.; Kanan, M. W. *J. Am. Chem. Soc.* **2012**, *134*, 7231.

(354) Liu, C.; Cundari, T. R.; Wilson, A. K. *J. Phys. Chem. C* **2012**, *116*, 5681.

(355) (a) Arai, T.; Tajima, S.; Sato, S.; Uemura, K.; Morikawa, T.; Kajino, T. *Chem. Commun.* **2011**, *47*, 12664 (b) Arai, T.; Sato, S.; Uemura, K.; Morikawa, T.; Kajino, T.; Motohiro, T. *Chem. Commun.* **2010**, *46*, 6944.

(356) (a) Kumar, B.; Smieja, J. M.; Kubiak, C. P. *J. Phys. Chem. C* **2010**, *114*, 14220 (b) Kumar, B.; Smieja, J. M.; Sasayama, A. F.; Kubiak, C. P. *Chem. Commun.* **2012**, *48*, 272.

(357) (a) Smieja, J. M.; Benson, E. E.; Kumar, B.; Grice, K. A.; Seu, C. S.; Miller, A. J. M.; Mayer, J. M.; Kubiak, C. P. *Proc. Natl. Acad. Sci. USA* **2012**, *109*, 15560 (b) Benson, E. E.; Kubiak, C. P. *Chem. Commun.* **2012**, *48*, 7374.

(358) (a) Kumar, B.; Llorente, M.; Froehlich, J.; Dang, T.; Sathrum, A.; Kubiak, C. P. *Annu. Rev. Phys. Chem.* **2012**, *63*, 541 (b) Benson, E. E.; Kubiak, C. P.; Sathrum, A. J.; Smieja, J. M. *Chem. Soc. Rev.* **2009**, *38*, 89.

(359) Liu, R.; Yuan, G.; Joe, C. L.; Lightburn, T. E.; Tan, K. L.; Wang, D. *Angew. Chem. Int. Ed.* **2012**, *51*, 6709.

(360) Hernandez-Pagan, E. A.; Vargas-Barbosa, N. M.; Wang, T.; Zhao, Y.; Smotkin, E. S.; Mallouk, T. E. *Energy Environ. Sci.* **2012**, *5*, 7582.

(361) Trasatti, S. *J. Electroanal. Chem. Interfac. Electrochem.* **1972**, *39*, 163.

(362) Chen, G.; Delafuente, D. A.; Sarangapani, S.; Mallouk, T. E. *Catal. Today* **2001**, *67*, 341.

(363) Greeley, J.; Jaramillo, T. F.; Bonde, J.; Chorkendorff, I.; Norskov, J. K. *Nat. Mater.* **2006**, *5*, 909.

(364) Conway, B. E.; Bai, L. *Int. J. Hydrogen Energy* **1986**, *11*, 533.

(365) Brossard, L. *Int. J. Hydrogen Energy* **1991**, *16*, 13.

(366) Rasiyah, P.; Tseung, A. C. C. *J. Electrochem. Soc.* **1984**, *131*, 803.

(367) Gerken, J. B.; McAlpin, J. G.; Chen, J. Y. C.; Rigsby, M. L.; Casey, W. H.; Britt, R. D.; Stahl, S. S. *J. Am. Chem. Soc.* **2011**, *133*, 14431.

(368) Kelly, N. A.; Gibson, T. L.; Cai, M.; Spearot, J. A.; Ouwerkerk, D. B. *Int. J. Hydrogen Energy* **2010**, *35*, 892.

(369) Koinuma, H.; Takeuchi, I. *Nat. Mater.* **2004**, *3*, 429.

(370) Woodhouse, M.; Herman, G. S.; Parkinson, B. A. *Chem. Mater.* **2005**, *17*, 4318.

(371) Katz, J. E.; Gingrich, T. R.; Santori, E. A.; Lewis, N. S. *Energy Environ. Sci.* **2009**, *2*, 103.

(372) Liu, X.; Shen, Y.; Yang, R.; Zou, S.; Ji, X.; Shi, L.; Zhang, Y.; Liu, D.; Xiao, L.; Zheng, X.; Li, S.; Fan, J.; Stucky, G. D. *Nano Lett.* **2012**.

(373) Jaramillo, T. F.; Baeck, S.-H.; Kleiman-Shwarsctein, A.; Choi, K.-S.; Stucky, G. D.; McFarland, E. W. *J. Comb. Chem.* **2004**, *7*, 264.

(374) Jaramillo, T. F.; Ivanovskaya, A.; McFarland, E. W. *J. Comb. Chem.* **2001**, *4*, 17.

(375) Gerken, J. B.; Chen, J. Y. C.; Massé, R. C.; Powell, A. B.; Stahl, S. S. *Angew. Chem. Int. Ed.* **2012**, *51*, 6676.

(376) (a) Greeley, J.; Nørskov, J. K.; Mavrikakis, M. *Annu. Rev. Phys. Chem.* **2002**, *53*, 319 (b) Greeley, J.; Markovic, N. M. *Energy Environ. Sci.* **2012**.

(377) Norskov, J. K.; Bligaard, T.; Rossmeisl, J.; Christensen, C. H. *Nat. Chem.* **2009**, *1*, 37.

(378) Castelli, I. E.; Landis, D. D.; Thygesen, K. S.; Dahl, S.; Chorkendorff, I.; Jaramillo, T. F.; Jacobsen, K. W. *Energy Environ. Sci.* **2012**, *5*, 9034.

CHAPTER 2

2.1 Abstract

In this chapter, we will focus on p-type Si based photocathode integrated with nanoscale ZnO film or ZnO nanowire arrays. This chapter includes three published journal articles,

J|A|C|S
COMMUNICATIONS

Solution Synthesis of Large-Scale, High-Sensitivity ZnO/Si Hierarchical Nanoheterostructure Photodetectors

Ke Sun,[†] Yi Jing,[†] Namseok Park,[†] Chun Li,[‡] Yoshio Bando,[‡] and Deli Wang*,[†]

Department of Electrical and Computer Engineering, University of California—San Diego, La Jolla, California 92093, United States, and International Center for Materials Nanoarchitectonics (MANA), National Institute for Material Science, Namiki 1-1, Tsukuba, Ibaraki 305-0044, Japan

Received May 5, 2010; E-mail: dwang@ece.ucsd.edu

Abstract: This Communication reports a low-cost solution fabrication of wafer-scale ZnO/Si branched nanowire heterostructures and their high photodetection sensitivity, with an ON/OFF ratio larger than 250 and a peak photoresponsivity of 12.8 mA/W at 900 nm. This reported unique 3D branched nanowire structure offers a generic approach for the integration of new functional materials for photodetection and photovoltaic applications.

Branched nanowires (NWs) are 3D nanoscale tree-like structures that consist of a NW core ("trunk") and NW "branches".[1] The formation of branched NWs offers direct homo- or heteroepitaxal[2] integration of materials with very different properties at the nanometer scale, which often lead to function integration or novel materials/applications. Moreover, 3D branched NW heterostructures offer greatly enhanced surface area and function and thus promise very attractive potential applications in optoelectronics, photocatalysis, photovoltaics, and sensing.[3] ZnO and Si are the most investigated NW materials.[4] ZnO is a direct band gap semiconductor with a wide band gap (E_g = 3.4 eV). It has a large exciton binding energy of 60 meV and is piezoelectric,[5] and thus it has been broadly studied for use in light-emitting diodes[6] and lasers,[7] photodetectors,[8] electrical generators,[9] photovoltaics,[10] transparent electrodes,[11] chemical and biological sensors,[12] etc. On the other hand, Si NWs have an indirect band gap of 1.12 eV and are piezoresistive; they have been intensively researched for applications as transistors,[13] logic circuits,[14] photodetectors,[15] photovoltaics,[16] chemical and biological sensors,[17] thermoelectric devices,[18] etc. Herein we report a low-cost, wafer-scale synthesis of ZnO/Si branched NW heterostructures and their application as high-sensitivity photodetectors. The direct integration of ZnO and Si and the growth of 3D branched NW heterostructures enable new functional materials to be synthesized for applications in optoelectronics, catalysis, and photovoltaics.

The Si NW core and ZnO NW branches were synthesized using simple and cost-effective aqueous solution methods. Both methods are applicable for large-scale synthesis. The wafer-scale Si NW arrays were obtained using a previously reported metal-assisted chemical etching process.[19] Figure 1a shows a scanning electron microscopy (SEM) image of NW arrays that were etched for 5 min on a 2-in. p-type Si wafer. SiNWs were about 680 nm in length, showing single-crystalline structure (Supporting Information). An optical image (Figure 1b) shows a very dark brownish color in the NW region, in significant contrast to the surrounding area that was covered from etching electrolyte, indicating that the light absorption was due to the waveguide effect.[16b] Light absorption was then further improved by integration of ZnO NWs on Si NW surfaces, revealed by reflectance evaluations. This enhancement is due to smoothing of the refraction index on going from the environment to the Si substrate. Hydrothermal growth of ZnO NWs is attractive due to its low reaction temperature and large-scale synthesis capability. Compared to gas-phase approaches, this method does not require expensive equipment, metal−organic source materials, or high temperatures. Hydrothermal growth of ZnO NWs on the seeded Si NW arrays was conducted according to the technique reported elsewhere.[10a] To ensure a uniform coating over the Si NW surface, low-pressure sputtering was used for seeding. The as-grown ZnO NW/Si NW heterostructures are shown in Figure 1c−e. Hexagonal ZnO NWs with diameter around 30 nm and very high density grow nearly perpendicular to the surface of the Si NW core and form highly ordered 3D branched NW heterostructures, as can be seen in a low-resolution transmission electron microscopy (LR-TEM) image (Figure 1f). It also appeared that the ZnO NWs grown on Si NW tips have larger diameter, presumably because there is less spatial hindrance and higher reactant concentration from diffusion. Devices were then fabricated by embedding the heterostructure into an insulating polymer, followed by reactive ion etching (RIE) and top transparent contact deposition using indium tin oxide (ITO) and a Ti/Au probing pad (Figure 1g). Nanowire synthesis and fabrication procedures can be found in the Supporting Information.

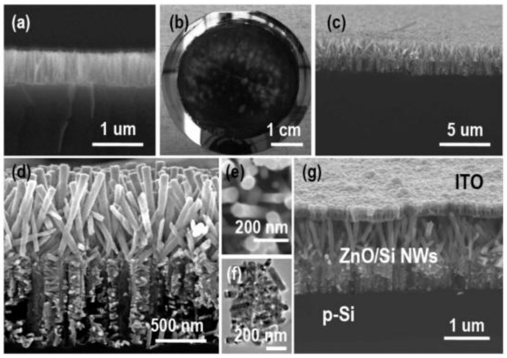

Figure 1. (a) Cross-sectional SEM image and (b) optical image of NW arrays on a 2 in. p-type Si wafer (etched for 5 min). (c) 45° view SEM micrographs of the ZnO/Si branched nanowire heterostructures at low magnification. (d) 89° view and (e) top view SEM micrographs of the ZnO/Si branched nanowire heterostructures at high magnification. (f) LR-TEM image on a single Si/ZnO branched NW. (g) 45° view SEM image of a photodetector device with top ITO contact.

[†] University of California−San Diego.
[‡] National Institute for Material Science, Japan.

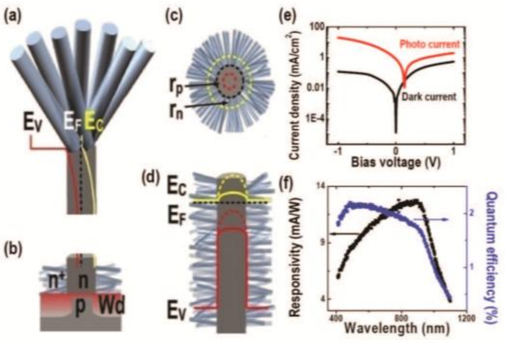

Figure 2. (a−d) Schematics of the ZnO/Si branched NW heterostructures: (a) top (NW tip) junction and energy band diagram; (b) bottom junctions and depletion layer in the silicon substrate; (c,d) cross-sectional view of the sidewall junctions and energy band diagram. (e) Current−voltage ($I-V$) characteristics measured in the dark and under xenon lamp illumination. (f) Spectral photoresponsivity and external quantum efficiency of ZnO/Si NW heterostructure photodetector from 400 to 1100 nm.

The current−voltage ($I-V$) characteristics of the Au/Ti/ITO/n-ZnO/p-Si/In device were tested in the dark and under illumination. Figure 2a−d illustrates the schematics of junctions along a single ZnO/Si NW heterostructure formed at different positions of the Si NW substrate, which are superimposed with the energy band diagrams. The carrier concentration was about 10^{18} cm^{-3} in ZnO NWs[10a] and about 10^{15} cm^{-3} in Si NWs. $\Delta E_C = 0$ eV and $\Delta E_V = 2.78$ eV were derived from the electron affinity and band gaps of ZnO and Si and confirmed by using a 1D Poisson solver[20] (Figure 2a,d). ZnO NWs had a carrier concentration 3 orders of magnitude higher than that of Si NWs. Therefore, the depletion width (r_p) was much larger in the Si NW core than in the ZnO branches (r_n) (Figure 2c), and the Si NWs were fully depleted and partially inverted to n-type (Figure 2d). p/n junctions were also formed between the ZnO NWs grown on Si substrate between the Si NWs, with larger depletion width (W_d) under the area between the Si NWs and smaller depletion width under the Si NWs, as shown in Figure 2b. Figure 2e shows the dark and photocurrent (under xenon lamp illumination) measurements at room temperature. Both dark and photocurrent voltage characteristics were rectifying, and the best ON/OFF ratio achieved at −1 V was about 250. Because of the clean interface between ZnO and Si NWs, the rectifying behavior was assigned to the ZnO/Si heterojunction and the Si substrate (Figure 2a−d). High-resolution TEM studies showed an oxide-free interface between ZnO and Si NWs (Figure S1, Supporting Information). A photovoltaic effect was observed, and the best solar cell device performance showed a power conversion efficiency under 1.5 a.m. solar simulator lumination of $\eta = 0.154\%$, with $J_{SC} = 4.1$ mA/cm^2, $V_{OC} = 0.15$ V, and FF = 0.25.

The spectral photoresponse of the ZnO/Si NW heterostructure device (400−1100 nm) was measured under a reserve bias of −1 V using a calibrated Si p-i-n photodiode (model 818-UV from Newport with OD3 attenuator) and monochromator (see Supporting Information for setup details). The photoresponsivity was calculated by calibrating the measured photocurrent density to that of the Si photodetector. Responsivity was calculated on the basis of eq 1,

$$R_\lambda = \frac{J_{\text{ph}}}{P_{\text{inc}}} = R_{\lambda\text{det}} \frac{J_{\text{ph}}}{J_{\text{det}}} \tag{1}$$

where R_λ and $R_{\lambda\text{det}}$ are the photoresponsivity of the ZnO/Si heterostructure device and calibration Si photodetector, respectively, J_{ph} and J_{det} are the measured current density from our device and the calibrated Si photodetector, and P_{inc} is the incident optical power. The external quantum efficiency (EQE) can be calculated by

$$\eta = R_\lambda \frac{q}{h\nu} = \frac{R_\lambda}{\lambda} \times 1240 \tag{2}$$

where η is the EQE, q, h, and ν are the electron charge, Planck's constant, and frequency of the incident photon, respectively, and λ is the wavelength. Figure 2f shows the photoresponsivity and EQE of the heterostructure device. The distinctive peak is the band edge absorption in the Si NW/substrate layer.[21] The maximum responsivity measured for this ZnO/Si heterostructure was as high as 12.8 mA/W at around 900 nm, and the maximum quantum efficiency was 2.20%.

In summary, ZnO/Si branched NW heterojunction photodiodes are fabricated using a cost-effective solution-phase process. This unique chemical integration of NW branches to vertical NW arrays promises enhanced light-trapping due to the aperiodically arranged nanowire array and high refractive index material filling, as well as advantages in broadband photon detection. Although ongoing research is addressing some of the challenging issues (such as uniform top contact and defects concentration) in order to further improve device performance, this unique branched NW heterostructure shows a peak responsivity of 12.8 mA/W at around 900 nm. These results indicate that the branched heterostructures, along with the wafer scale and low-cost solution processing, offer new functional materials for photodetection and photovoltaic cells.

Acknowledgment. D.W. acknowledges the U.S. DOE (DE-FG36-08G018016), NSF (ARRA ECCS0901113), the WCU program at Sunchon National University of South Korea, Abgent Inc., and AEM Inc. for financial support. The authors thank Dr. C. Soci of Nanyang Technology University of Singapore and W. Wei for useful discussions on the photoresponse measurement. K.S. thanks Dr. Y. Taur of UCSD for useful discussions.

Supporting Information Available: Nanowire synthesis and device fabrication procedures, TEM studies on the ZnO/Si interfaces, single SiNW device $I-V$ measurement, electrical contact properties, and photoresponse measurements. This material is available free of charge via the Internet at http://pubs.acs.org.

References

(1) (a) Dick, K. A.; Deppert, K.; Larsson, M. W.; Martensson, T.; Seifert, W.; Wallenberg, L. R.; Samuelson, L. *Nat. Mater.* **2004**, *3*, 380–384. (b) Wang, D.; Lieber, C. M. *Nat. Mater.* **2003**, *2*, 355–356. (c) Wang, D.; Qian, F.; Yang, C.; Zhong, Z.; Lieber, C. M. *Nano Lett.* **2004**, *4*, 871–874.
(2) (a) Jiang, Y.; Zhang, W. J.; Jie, J. S.; Meng, X. M.; Zapien, J. A.; Lee, S. T. *Adv. Mater.* **2006**, *18*, 1527–1532. (b) Jung, Y.; Ko, D.-K.; Agarwal, R. *Nano Lett.* **2006**, *7*, 264–268.
(3) (a) Bae, S. Y.; Seo, H. W.; Choi, H. C.; Park, J.; Park, *J. Phys. Chem. B* **2004**, *108*, 12318–12326. (b) Lao, J. Y.; Wen, J. G.; Ren, Z. F. *Nano Lett.* **2002**, *2*, 1287–1291. (c) Li, Y.; Gong, J.; Deng, Y. *Sensors Actuators A* **2010**, *158*, 176–182. (d) Mudusu, D.; Nandanapalli Koteeswara, R.; Alexander, P.; Fernando, P. *ChemPhysChem* **2010**, *11*, 809–814. (e) Wang, N.; Sun, C.; Zhao, Y.; Zhou, S.; Chen, P.; Jiang, L. *J. Mater. Chem.* **2008**, *18*, 3909–3911. (f) Xu, F.; Dai, M.; Lu, Y.; Sun, L. *J. Phys. Chem. C* **2010**, *114*, 2776–2782. (g) Bierman, M. J.; Jin, S. *Energy Environ. Sci.* **2009**, *2*, 1050–1059.
(4) Hochbaum, A. I.; Yang, P. *Chem. Rev.* **2009**, *110*, 527–546.
(5) Wang, Z. L.; Song, J. *Science* **2006**, *312*, 242–246.
(6) Bao, J.; Zimmler, M. A.; Capasso, F.; Wang, X.; Ren, Z. F. *Nano Lett.* **2006**, *6*, 1719–1722.
(7) Mariano, A. Z.; Jiming, B.; Federico, C.; Sven, M.; Carsten, R. *Appl. Phys. Lett.* **2008**, *93*, 051101.
(8) Soci, C.; Zhang, A.; Xiang, B.; Dayeh, S. A.; Aplin, D. P. R.; Park, J.; Bao, X. Y.; Lo, Y. H.; Wang, D. *Nano Lett.* **2007**, *7*, 1003–1009.
(9) Xu, S.; Qin, Y.; Xu, C.; Wei, Y.; Yang, R.; Wang, Z. L. *Nat. Nanotechnol.* **2010**, *5*, 366–373.
(10) (a) Law, M.; Greene, L. E.; Johnson, J. C.; Saykally, R.; Yang, P. *Nat. Mater.* **2005**, *4*, 455–459. (b) Yang, X.; Wolcott, A.; Wang, G.; Sobo, A.;

Fitzmorris, R. C.; Qian, F.; Zhang, J. Z.; Li, Y. *Nano Lett.* **2009**, *9*, 2331–2336.

(11) Lee, S.-H.; Han, S.-H.; Jung, H. S.; Shin, H.; Lee, J.; Noh, J.-H.; Lee, S.; Cho, I.-S.; Lee, J.-K.; Kim, J.; Shin, H. *J. Phys. Chem. C* **2010**, *114*, 7185–7189.

(12) Yang, K.; She, G.-W.; Wang, H.; Ou, X.-M.; Zhang, X.-H.; Lee, C.-S.; Lee, S.-T. *J. Phys. Chem. C* **2009**, *113*, 20169–20172.

(13) Cui, Y.; Zhong, Z.; Wang, D.; Wang, W. U.; Lieber, C. M. *Nano Lett.* **2003**, *3*, 149–152.

(14) Zhong, Z.; Wang, D.; Cui, Y.; Bockrath, M. W.; Lieber, C. M. *Science* **2003**, *302*, 1377–1379.

(15) Yang, C.; Barrelet, C. J.; Capasso, F.; Lieber, C. M. *Nano Lett.* **2006**, *6*, 2929–2934.

(16) (a) Kelzenberg, M. D.; Boettcher, S. W.; Petykiewicz, J. A.; Turner-Evans, D. B.; Putnam, M. C.; Warren, E. L.; Spurgeon, J. M.; Briggs, R. M.; Lewis, N. S.; Atwater, H. A. *Nat. Mater.* **2010**, *9*, 239–244. (b) Zhu, J.; Yu, Z.; Burkhard, G. F.; Hsu, C.-M.; Connor, S. T.; Xu, Y.; Wang, Q.; McGehee, M.; Fan, S.; Cui, Y. *Nano Lett.* **2008**, *9*, 279–282. (c) Hu, L.; Chen, G. *Nano Lett.* **2007**, *7*, 3249–3252. (d) Tian, B.; Zheng, X.; Kempa, T. J.; Fang, Y.; Yu, N.; Yu, G.; Huang, J.; Lieber, C. M. *Nature* **2007**, *449*, 885–889.

(17) Zheng, G.; Patolsky, F.; Cui, Y.; Wang, W. U.; Lieber, C. M. *Nat. Biotechnol.* **2005**, *23*, 1294–1301.

(18) Hochbaum, A. I.; Chen, R.; Delgado, R. D.; Liang, W.; Garnett, E. C.; Najarian, M.; Majumdar, A.; Yang, P. *Nature* **2008**, *451*, 163–167.

(19) Peng, K. Q.; Yan, Y. J.; Gao, S. P.; Zhu, *Adv. Mater.* **2002**, *14*, 1164–1167.

(20) Snider, G., 1D Poisson solver, http://www.nd.edu/~gsnider/.

(21) Chen, L. C.; Pan, C. N. *Eur. Phys. J. Appl. Phys.* **2008**, *44*, 43–46.

JA1038424

View Article Online / Journal Homepage / Table of Contents for this issue
Dynamic Article Links

Nanoscale

Cite this: *Nanoscale*, 2012, **4**, 1515

www.rsc.org/nanoscale

PAPER

3D branched nanowire heterojunction photoelectrodes for high-efficiency solar water splitting and H_2 generation†

Ke Sun,[a] Yi Jing,[a] Chun Li,‡[ab] Xiaofeng Zhang,[c] Ryan Aguinaldo,[a] Alireza Kargar,[a] Kristian Madsen,[a] Khaleda Banu,[a] Yuchun Zhou,[a] Yoshio Bando,[b] Zhaowei Liu[a] and Deli Wang*[ade]

Received 9th December 2011, Accepted 18th January 2012
DOI: 10.1039/c2nr11952h

We report the fabrication of a three dimensional branched ZnO/Si heterojunction nanowire array by a two-step, wafer-scale, low-cost, solution etching/growth method and its use as photoelectrode in a photoelectrochemical cell for high efficiency solar powered water splitting. Specifically, we demonstrate that the branched nanowire heterojunction photoelectrode offers improved light absorption, increased photocurrent generation due to the effective charge separation in Si nanowire backbones and ZnO nanowire branching, and enhanced gas evolution kinetics because of the dramatically increased surface area and decreased radius of curvature. The branching nanowire heterostructures offer direct functional integration of different materials for high efficiency water photoelectrolysis and scalable photoelectrodes for clean hydrogen fuel generation.

Introduction

Currently over 90% of electricity and over 95% of hydrogen are produced from fossil fuels and biomass.[1] Fossil fuels are believed to be the major cause of negative and irreversible environmental consequences,[2] which contribute the largest amount of greenhouse gas (carbon dioxide)[3,4] and air pollution (nitrous oxide and smog). Hydrogen is believed to be one of the sustainable and clean-energy alternatives to overcome the environmental challenges, which can work by itself as a source of energy or together with other carbon source to generate liquid hydrocarbons.[5] In order to be economically competitive and environmentally beneficial, it is essential to find a cost-effective and clean method for mass production of hydrogen.[6] Techniques for directly converting water to hydrogen using solar energy, known as photoelectrolysis, are receiving great attention recently, despite the fact that the electrolysis effect was discovered more than 200 years ago.[7] Mechanisms of water splitting driven by semiconductor photoelectrochemical (PEC) electrodes (photoelectrodes) are depicted in previous review works.[8–11] Continuous research effort and current challenges are to optimize photoelectrodes towards practical PEC applications with a broad spectrum of absorption, matching energy band to water reduction/oxidation energy levels, long-term stability in harsh conditions (like seawater or effluent, under both dark and illumination conditions), and most importantly high photocurrent density in order to reach high photo-to-hydrogen conversion efficiency.[12]

Materials that are currently attracting research interests include semiconductors (Si,[13–15] III–V,[16,17] II–VI,[18–21] *etc.*) and metal oxides (TiO_2,[22] ZnO,[23] Fe_2O_3,[24–26] WO_3[27–29]). Moreover, using heterojunction[30–33] or homojunction[34,35] and tandem cells enhances light absorption, charge separation and appropriate carrier energy, all of which could lead to a potentially viable device for spontaneous water splitting. Among all of the aforementioned materials, Si as one of the cheapest, most abundant, and most important semiconductor materials, has demonstrated broad application as solid-state solar cells and PEC cell devices. Recently, a one-dimensional nanowire (NW) array utilized in a Si solar cell provides conceptual advantages, such as improved light absorption and potentially improved charge separation.[13,36–40] On the other hand, Si nanostructure based photoelectrodes interfacing with liquid electrolyte as an alternative format of solar cells have shown great potential due to the advantages of high quality and conformal junction interface. Meanwhile, this structure improves the junction area, essentially eases the carrier separation and collection. Previously studies have demonstrated photoelectrodes with improved PEC properties using a p-type[14,41] or an n-type[31,42] doped Si NW array as

---

[a] *Department of Electrical and Computer Engineering, University of California, San Diego9500 Gilman Drive, La Jolla, CA, 92093, USA. E-mail: dwang@ece.ucsd.edu*
[b] *International Center for Materials Nanoarchitectonics (MANA), National Institute for Material Science, Namiki 1-1, Tsukuba, Ibaraki 305-0044, Japan*
[c] *Changchun Institute of Applied Chemistry, Chinese Academy of Sciences, 109 Remin Street, Changchun, Jilin, 130021, China*
[d] *Materials Science and Engineering, University of California, San Diego9500 Gilman Drive, La Jolla, CA, 92093, USA*
[e] *California Institute of Telecommunication and Information Technology, University of California, San Diego 9500Gilman Dr, La Jolla, CA, 92093, USA*

† This article was submitted as part of a collection highlighting papers on the 'Recent Advances in Semiconductor Nanowires Research' from ICMAT 2011.

‡ Current address: Materials Science and Engineering, North Carolina State University, 911 Partner's Way, Raleigh, NC, 27607, USA.

a photocathode or a photoanode, respectively. A large surface area provides significantly increased photoelectrochemical sites for water reduction/oxidation. However, problems with NW structures happen at the electrolyte interfaces where increased surface state recombination occurs. Moreover, poor interface kinetics further limits the performance of Si based photoelectrodes, resulting in low H_2 evolution.[43,44] In this article, we present a low-cost two-step solution phase integration of ZnO NW branches to Si NW backbones and the use of these p/n branched heterostructures for solar water splitting. The branched NW array structure is studied using scanning electron microscopy (SEM) and high-resolution transmission electron microscopy (HR-TEM). Structures with different lengths of Si NW backbones and ZnO NW branches are studied as a photocathode for H_2 production. Light absorption and transient current density at chopped light are studied.

Experimental

1. Device fabrication

p-Type boron doped (111) silicon wafers with a thickness of 250 μm (WaferWorld 1–10 Ω cm) were cleaned with solvent, rinsed with deionized (DI) water (>17.8 MΩ cm) and dried with N_2. The metal assisted chemical etching used to prepare the Si NW substrate is described in previous literatures[45–47] and as follows: a cleaned 2″ wafer, with both the edge and backside protected from exposure to the solution with polymer coating, was fixed on a homemade etching setup and immersed in the etching solution (a mixture of 0.02 M $AgNO_3$ and 4 M HF in DI water). The etching was performed at 50 °C with gentle agitation (100 rpm) for varying time periods, followed by immediate removal from the etching solution and thorough rinse with DI water for 5 min. The as-etched Si NWs were normally coated with a thick layer of chemically reduced Ag, the latter was etched in dilute nitric acid (1 : 10) for at least 1 h (depending on the length of NW). Finally, samples were rinsed well in DI water and dried gently with N_2.

For ZnO nanowire growth, a thin ZnO seeding layer was deposited on the Si NW substrates with low-pressure argon plasma RF sputtering using 99.99% ZnO target. Prior to the seeding process, Si NW samples were dipped in buffered oxide etching (1 : 6 BOE) solution for 10 s to remove the native oxide. Then, samples were carefully spray-cleaned using DI water, dried with N_2, and immediately transferred to a deposition chamber to minimize oxidation. During the sputtering, pressure in the chamber was maintained at 1.7 mTorr. The deposition rate was first characterized on a planar Si substrate. A thin layer of ZnO with 45 nm in thickness was achieved after 16 min, based on the deposition rate calculated from thin film deposition on the planar Si substrate. Hydrothermal growth of ZnO NWs[48,49] was carried out as follows: Si substrates were fixed on a supporting glass slide facing down and immersed in the reaction solution—25 mM solutions of zinc acetate and hexamethylenetetramine (HMTA, Sigma) in DI water at 85 °C with gentle agitation for varying time periods. The as-grown samples were ultrasonicated at low power (<30 W) to remove ZnO particles on the surface, thoroughly rinsed with DI water, and gently blow-dried with N_2 gas. Samples were stored under vacuum to minimize oxygen and water absorption before further measurement.

2. Morphological study

The NW morphology was examined using a field emission secondary electron microscope (FESEM, FEI-XL30) with an accelerating voltage of 5.0 kV. Energy dispersive X-ray (EDX) analysis was used to examine the efficiency of Ag etching. A cross-sectional transmission electron microscope (XTEM, JEOL JEM-3100FEF) equipped with an OMEGA-type energy filter in the microscope column with an accelerating voltage of 300 kV was used to study the crystalline structures and the ZnO/Si heterostructure interfaces. Images were collected using the Gatan image recording system with a resolution of 0.5 nm.

3. Reflectance measurement

Optical extinction spectra were measured using a halogen lamp and a CCD spectroscope coupled with an optical microscope.[50] Samples are in focus of microscope objectives. Specular and diffuse scattered light from the sample were collected using 50× objective lens (Carl Zeiss 422370-9960-000) with a numerical aperture of 0.8 and working distance of 0.6 mm. Reflected light was measured using a CCD spectrometer (Andor Shamrock). The diameter of the effective field of view collected by the CCD was around 50 μm.

4. PEC measurement

Prior to PEC measurement, indium paste was applied at the back of the sample and a copper wire was soldered to the sample providing ohmic electrical contacts. The backside and edges of samples were protected using epoxy and the copper wire was sealed in plastic tubes to prevent electrical shorts to the electrolyte such that only the sample front side was in contact with the electrolyte. Si NWs without ZnO NW branches were etched for 10 seconds in HF solution at room temperature and rinsed with DI water immediately prior to measurement, the ZnO/Si branched NW samples were tested directly without further treatment. The area of the samples exposed to the electrolyte varies and ranges about 0.5–1.2 cm^2. In electrochemical measurement using one-compartment cell setup, Pt wire was used as the counter electrode (CE) and was positioned as close as possible to the photocathode, while the Ag/AgCl (1 M KCl) reference electrode (RE) was placed as close as possible to the photocathode working electrode (WE). A xenon lamp from a solar simulator providing an output light intensity of 130 mW cm^{-2} was incident normal to the sample through a quartz window. Steady-state photocurrent density–voltage (*J*–*V*) curves under a slow scan rate (5 mV s^{-1}), and photocurrent density–time (*J*–*t*) curves were obtained by using a potentiostat (Digi-Ivy Inc). All data were recorded using software DY2300. The electrolyte solution was always 400 ml of 0.25 M Na_2SO_4 buffered with PBS with pH ≈ 7.2, which was measured using a pH meter (Acorn-Oakton pH5).

Results and discussions

Fig. 1 shows the cross-sectional and top views of Si/ZnO branched NW arrays with different backbone and branched lengths. Similar to the growth on the plain Si substrate, hexagonal ZnO NWs grown on the surface of Si NW backbones were

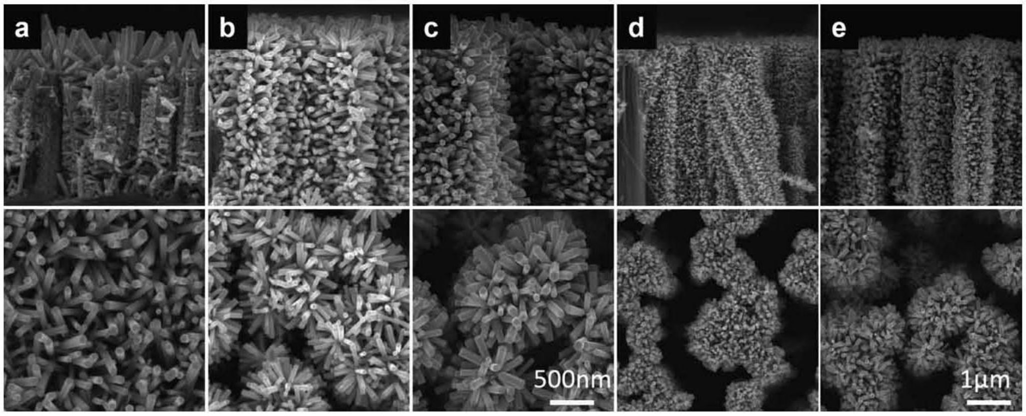

Fig. 1 Cross-sectional view (top row) and top view (bottom row) SEM images of Si/ZnO branched NW arrays with different backbone and branch lengths. ZnO NW branches from growth for 2.5 h on Si NWs with different lengths by chemical etching for (a) 5 min, (b) 10 min, and (c) 15 min, respectively (scale bar = 500 nm). ZnO NW branches grown for various times of (d) 30 min and (e) 2.5 h on Si NW arrays etched for 15 min (scale bar = 1 μm).

nearly perpendicular.[51] Geometries, distributions, and even optical properties of the ZnO branches strongly depend on the Si NW array. ZnO NW branches grown on short Si NWs (5 min etching) showed position-dependent sizes: ZnO NWs on the sidewall were smaller in both the diameter and length than those growing on top of the Si NW array (Fig. 1a). The position-dependent non-uniformity of ZnO NW growth is believed to be due to the limited diffusion of ZnO nanoparticles (NPs) during the hydrothermal growth from the reaction solution to nucleation sites on the sidewalls of the Si NWs. However, better uniformity was reached when ZnO NW branches grow on longer Si NWs (10 and 15 min etching), as shown in Fig. 1b and c. Longer Si NWs give smaller moments of inertia and spring constants; therefore they are more flexible, allowing van der Waals forces to deform adjacent NWs into clusters, which consequently affect the overall optical and electrical properties. This will be discussed in detail in later sections. Collapsed long NWs leave wider openings and thus ease the diffusion of ZnO NPs, which results in a uniform growth independent of the position. Moreover, ZnO NW branches grown on the same Si NW substrate for varying amounts of time are shown in Fig. 1d and e. Shorter and thinner branches were realized from 30 min growth (Fig. 1d), while branches were longer and wider in the case of 2.5 h growth (Fig. 1e). Estimation showed the extraordinary high density of ZnO NWs in the highly ordered 3D branched NW array. Techniques used for etching Si NW and growth of ZnO NW provided the advantages and potential applications in large-scale fabrications and cost-effective solution phase integration of nanoscale heterojunctions.

Fig. 2 shows TEM images of the branched NW sample fabricated on 5 min etched Si NW array. The cross-sectional TEM image at low magnification in Fig. 2a illustrated the non-uniform distribution of ZnO NWs on Si NWs, which may be due to the non-uniformity of Si NW diameters (20–200 nm) from the wet etching and the uneven coating of a ZnO seeding layer from RF magnetron sputtering. Secondly, samples could be slightly damaged during the TEM sample preparation process using the focus ion beam (FIB) milling. It can be seen from the high resolution TEM image (Fig. 2b) that there is no noticeable amorphous SiO_x at the ZnO/Si interface, even for samples that were stored in air for days prior to the TEM characterization. We believe that this is due to the HF etching, prior to sputtering of the ZnO seeding layer. H-terminated Si NW surfaces were effectively generated which made the Si NWs less prone to oxidation.[52] On the other hand, the interfacial native oxide layer as one kind of passivation layers could also benefit the device performance and its effect on optoelectrical properties was discussed before.[53–55] In our experiments, the rough surface of solution etched Si NWs provided high density of nucleation sites during the seeding layer deposition, which in turn promoted the growth of ZnO NW branches in the high aspect ratio Si NW arrays.

The wet-etched Si NW samples were dark and discoloration was observed after the growth of ZnO NW branches. Extinction spectra in the visible range (500–750 nm, which was limited by the optics of the measurement setup) were measured using a microscope with samples in focus and a CCD spectrometer (measurement setup details can be found in supporting document). Extinction spectra and optical images of different samples with the same Si NW length but different ZnO NW lengths are shown in Fig. 3. The Si NW sample etched for 5 min showed excellent and uniform light absorption around 95% (Fig. 3a-2 and red curve in Fig. 3b). This was due to the aperiodic and sharp-tip structure of the etched Si NW, which in turn smoothed the transition of refractive index of air to that of Si substrate[56] and also suppressed the angle of incident (AOI) effect.[41,57] Short time (30 min) growth of ZnO NW on Si NW (Fig. 3a-1 and blue curve in Fig. 3b) showed improved light absorption (up to 97.5%). This is believed to be due to the filling of ZnO (n_{ZnO} = 1.94–2.4)[58,59] in between Si NWs (n_{Si} = 3.54–6.8)[60] in the wavelength range 240–1100 nm further smoothening the refractive index transition from light incident media (n_{air} = 1) to the Si

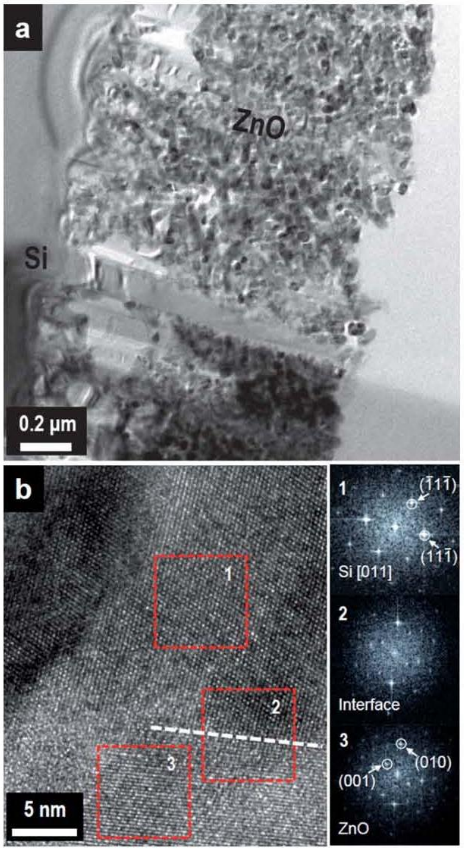

Fig. 2 TEM images of ZnO/Si branched NW arrays: (a) low resolution TEM showing the branched structure, (b) high-resolution TEM showing the interface of a typical single ZnO NW branch or a seeding particle on the surface of Si NWs. Insets are fast Fourier transform (FFT) patterns of the corresponding areas in (b).

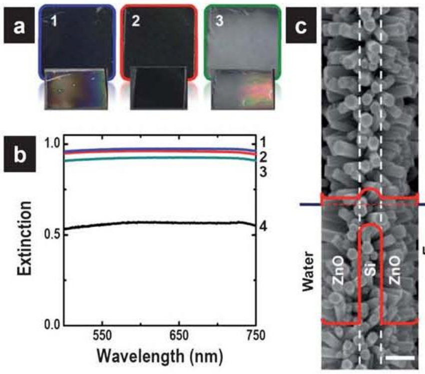

Fig. 3 (a) Optical images (first row: top view and second row: ~45 degree view) and (b) extinction spectra of different substrates: (1) 0.5 h ZnO NW growth on 5 min etched Si NW array (dark black, blue cure), (2) 5 min as-etched Si NW array (dark brownish, red curve), and (3) 2.5 h ZnO NW growth on 5 min etched Si NW array (light gray, green curve), and (4) polished Si reference sample (black curve). Sample size in this experiment is kept at 0.5 × 0.5 in^2. (c) Single Si/ZnO branched NW interfacing with the electrolyte superimposed with the energy band diagram at zero external bias with light illumination (scale bar = 200 nm).

substrate. However, the AOI effect became worse in ZnO NW branched samples (Fig. 3a). This can be seen in Fig. 3a where the optical image taken from a 45 degree viewing angle (second row) revealed the reflection patterns on this sample. Furthermore, the sample with longer ZnO NW branches (green curve in Fig. 3b) did not show further improvement in the light absorption. Careful investigation under SEM showed a more disordered structure of ZnO NWs from longer growth time, which scatters more light resulting in a light gray color (Fig. 3a-3). Therefore, we can conclude that the light absorption enhancement by vertical NW arrays minimizing light reflection/scattering is a combination effect of NW size, density, and shape.[61]

Fig. 3c shows the SEM image of ZnO NWs (branches grown on a single Si NW backbone) superimposed with the energy band diagram and water reduction level (at pH = 7). Si NWs with diameters larger than 20 nm were assumed to have the same electronic band gap as the bulk Si.[52] The conduction band of ZnO is lower than that of Si, which assists photo-generated electrons to transfer across the ZnO layer to the water reduction level, whereas holes flow to the back contact of Si. Band bending and an electron barrier at the ZnO/electrolyte interface due to the interaction with oxygen and water were also illustrated, which, we believe, is very important to the understanding of device performances. In addition, trapped O_2[62] on the ZnO NW surface results in a higher electron barrier at the electrolyte/ZnO interface, and thus a high onset potential. Branched NWs also offer other additional advantages as photoelectrodes in photoelectrochemical cells such as large surface area and large surface curvature leading to enhanced surface chemical reaction and more efficient H_2 evolution. Fig. 4a shows the *J–V* characteristics of the ZnO/Si branched NWs with different Si NW lengths. The longer Si NWs (from 15 min etching) give 50–100% higher photocurrent compared to that of the 5 min etched sample, which is believed to be due to the enhancement of light absorption and the larger overall surface area of the ZnO branches. Note that the dark current from the 15 min etched sample is much larger than the 5 min etched sample (Fig. 4a, inset), due to the much increased junction and surface area and thus recombination centers. Significant photocurrent was noticed starting at −1 V external potential and H_2 evolution was easily observed with the naked eyes in both samples (Fig. 4c). No photocurrent plateaus were observed indicating no light intensity limited photocurrent at the potential range measured.

Fig. 4b and the inset compare the current density from the branched NW photoelectrodes with different lengths of ZnO NW branches but the same Si NW length (etched for 5 min). The electrodes tested are 5 min etched Si NWs coated with the ZnO seeding layer, ZnO NWs grown for 30 min and 2.5 h, respectively. The photocathodic currents turn on at around −1 V and increase with the applied negative bias for the branched NW

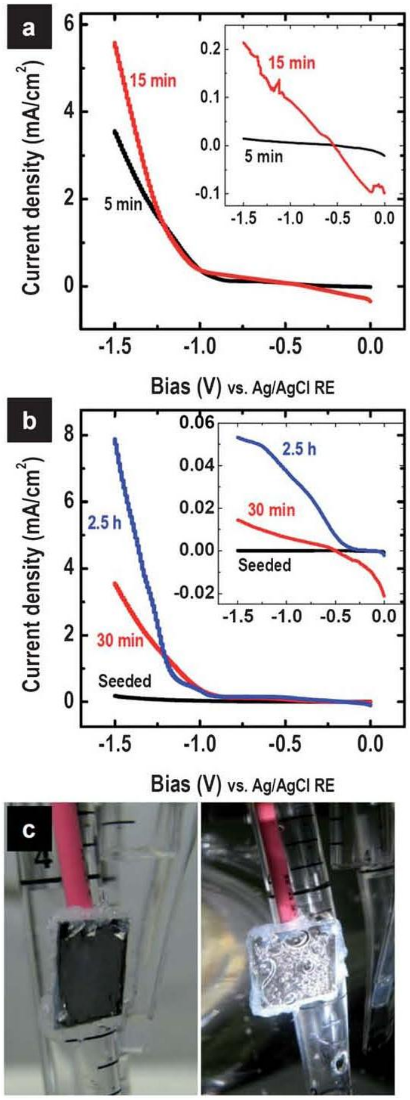

Fig. 4 Steady state current density *vs.* external bias (*J* *V*) on (a) 30 min growth of ZnO NW branches on Si NW arrays from various etching times (5 and 15 min) and (b) ZnO NW branches grown for varying times on 5 min etched Si NW arrays. Insets show the dark current of corresponding samples. (C) Optical image of a 3D branched NW photoelectrode: (left) in the dark and (right) H_2 gas evolution under illumination.

electrodes compared to the core–shell Si/ZnO NW sample (Si NWs are coated with the seeding ZnO layer). The photocurrent density increases with the length of ZnO NW branches, which reaches 8 mA cm^{-2} at -1.5 V for the electrode with ZnO NW branches grown for 2.5 h, which is about twice and 80 times compared to that for electrodes with ZnO NW branches of 30 min growth and ZnO coated Si NW electrodes, respectively. This enhancement in the photocurrent for photoelectrodes with longer and wider ZnO branches is probably due to the increase in the surface reaction area, which dominates the deficiency in reduced light absorption due to scattering (Fig. 3a and b). The superior current density levels achieved here are mainly due to the heterojunction that promotes the separation of photoinduced charge carriers, as well as the much enlarged surface area for efficient reaction. The inset compares the dark current of 5 min etched Si NWs coated with the ZnO seeding layer, ZnO NWs grown for 30 min and 2.5 h, which shows a clear trend of increase in current with the increase in ZnO NW growth time and the surface area. Note in Fig. 4, anodic current was observed both in the dark and under light illumination. The anodic currents in Fig. 4a and the inset (red curves) are most likely due to the band bending at the ZnO NW surface which leads to injection of thermal and photo-induced holes from ZnO to electrolytes, which increase as the Si NWs are longer and the surface area are larger. A similar increase of anodic dark and photo-currents in Fig. 4b and the inset (red curves) is due to the surface area increase for electrodes with 30 min ZnO NW branches compared to that with ZnO seeding layer alone. However, the anodic dark and photo-currents were suppressed for electrodes with longer ZnO NW branches (Fig. 4b blue curve), which is probably due to the increase of the ZnO NW diameter further leading to less charge separation to the surface.[62,63]

In addition, the transient photocurrent (*J*–*t*) test of the branched heterostructural samples was carried out under intermittent light illumination and constant external bias (-1.5 V *vs.* Ag/AgCl RE), as shown in Fig. 5a and b. The dark current of polished Si is almost zero, which is negligible and consistent with previously reported data. The photocurrent density at -1.5 V of the polished p-type Si photocathode was about 0.012 mA cm^{-2} under illumination. Si NW array and branched heterostructure array electrodes increased the photocurrent density by 250 and 400 times compared to the polished p-type Si photocathode, respectively, despite the small difference from sample to sample for the Si NW array and branched heterostructure array. Si and branched heterostructure NW arrays increased the surface area and thus the surface states, which result in increased dark currents of 7.5 and 25 times compared to that of the polished Si substrate, respectively.[14] The polished p-Si photoelectrode sample did not show significant photocurrent for H_2 evolution, because of the low kinetics for H_2 evolution.[43,64] It was pointed out that the H_2 generation rate is low at large values of photovoltage, due to the competing e^-/h^+ recombination at the surface. Conversion efficiency is limited by this competing process. Kinetics for reduction of H_2O is so poor that little or no current for H_2O reduction occurs until E_f is more negative than the H^+/H_2 potential.[12,43,64]

One can observe a large cathodic current jump responding to the illumination due to the photo-induced electron–hole pair separation. This photocurrent decayed quickly until reaching the steady state due to the recombination of electrons and holes *via* surface and interface states. Moreover, due to the limitation of the seeding process particularly non-uniformity on the longer Si NWs, this recombination may be partially caused by the

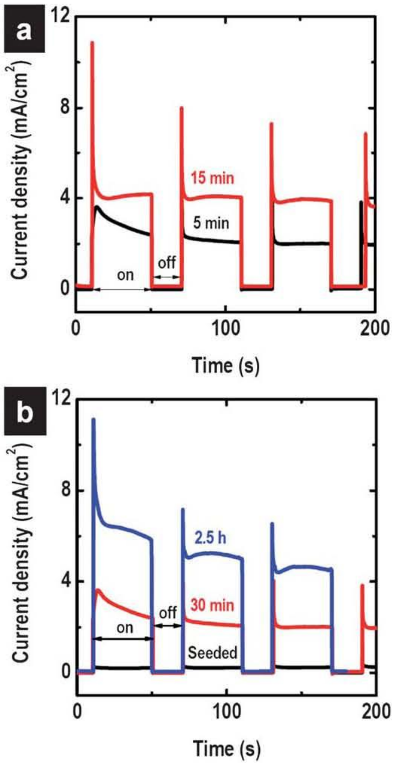

Fig. 5 Transient current density (*J t*) study on (a) 30 min growth of ZnO NW branches on Si NW arrays from various etching times (5 and 15 min) and (b) ZnO NW branches grown for varying times on 5 min etched Si NW arrays. These were measured at the external bias of −1.5 V (*vs.* Ag/AgCl RE).

exposure of Si NWs to the electrolytes and also accumulation at the ZnO/electrolyte interface due to surface band bending. Seeded Si NW array showed minimum dark and photocurrent response compared to the branched Si NW samples, which confirmed that the passivation of Si NW surface states using undoped ZnO seeding layer results in the ignorable recombination and consequently low dark current. Therefore, an increase in the dark current and cathodic current overshot were mainly due to the recombination at the ZnO NW/solution interface. Note that uniform seeding layer coating was obtained on 5 min etched Si NW array leaving minimum Si NW exposure to the solution. The photoelectrochemical stability of ZnO NW|planar Si photocathodes was studied and significant degradation and even complete removal were noticed in acidic and basic solutions after about 1 hour. Coating of metal thin films (for example ~5 nm Pt) as a co-catalyst on ZnO photoelectrodes showed improved stability and minimized the cathodic decomposition, in addition to the strongly improved electrochemical hydrogen reduction kinetics.[65]

Conclusions

In summary, we report the synthesis of 3D ZnO/Si branched NW arrays using the low-cost solution etching/synthesis method and the utilization as photoelectrodes in a PEC cell. The 3D nanowire heterostructures compared to ZnO NW/Si planar heterostructures, Si NW array, and Si planar structures demonstrated large enhancement in photocathodic current density (8 mA cm^{-2}) and overall hydrogen evolution kinetics. This solution-based technique for NW synthesis and heterojunction formation is inexpensive and most importantly can be scaled up to the level that would be required as a primary energy production method in the near future.

Notes and references

1 C. A. Grimes, O. K. Varghese and S. Ranjan, *Light, Water, Hydrogen-the Solar Generation of Hydrogen by Water Photoelectrolysis*, Springer, University Park, PA, 2008.
2 J. Hill, E. Nelson, D. Tilman, S. Polasky and D. Tiffany, *Proc. Natl. Acad. Sci. U. S. A.*, 2006, **103**, 11206 11210.
3 S. J. Davis, K. Caldeira and H. D. Matthews, *Science*, 2010, **329**, 1330 1333.
4 M. I. Hoffert, *Science*, 2010, **329**, 1292 1294.
5 R. Agrawal, N. R. Singh, F. H. Ribeiro and W. N. Delgass, *Proc. Natl. Acad. Sci. U. S. A.*, 2007, **104**, 4828 4833.
6 N. S. Lewis, *Science*, 2007, **315**, 798 801.
7 http://en.wikipedia.org/wiki/Electrolysis_of_water.
8 J. A. Turner, *Presented in Part at the DOE Hydrogen, Fuel Cells & Infrastructure Technologies Program Review, 2004*, 2004.
9 M. Grätzel, *Nature*, 2001, **414**, 338 344.
10 A. Heller, *Science*, 1984, **223**, 1141 1148.
11 Y. Li and J. Z. Zhang, *Laser Photonics Rev.*, 2010, **4**, 517.
12 D. C. Bookbinder, J. A. Bruce, R. N. Dominey, N. S. Lewis and M. S. Wrighton, *Proc. Natl. Acad. Sci. U. S. A.*, 1980, **77**, 6280 6284.
13 S. W. Boettcher, J. M. Spurgeon, M. C. Putnam, E. L. Warren, D. B. Turner-Evans, M. D. Kelzenberg, J. R. Maiolo, H. A. Atwater and N. S. Lewis, *Science*, 2010, **327**, 185 187.
14 A. P. Goodey, S. M. Eichfeld, K.-K. Lew, J. M. Redwing and T. E. Mallouk, *J. Am. Chem. Soc.*, 2007, **129**, 12344 12345.
15 Y. W. Chen, J. D. Prange, S. Dühnen, Y. Park, M. Gunji, C. E. D. Chidsey and P. C. McIntyre, *Nat. Mater.*, 2011, **10**, 539 544.
16 M. Szklarczyk and J. O. M. Bockris, *J. Phys. Chem.*, 1984, **88**, 5241 5245.
17 R. L. Woo, R. Xiao, Y. Kobayashi, L. Gao, N. Goel, M. K. Hudait, T. E. Mallouk and R. F. Hicks, *Nano Lett.*, 2008, **8**, 4664 4669.
18 J. Hensel, G. Wang, Y. Li and J. Z. Zhang, *Nano Lett.*, 2010, **10**, 478 483.
19 W. Zhu, X. Liu, H. Liu, D. Tong, J. Yang and J. Peng, *J. Am. Chem. Soc.*, 2010, **132**, 12619 12626.
20 W.-T. Sun, Y. Yu, H.-Y. Pan, X.-F. Gao, Q. Chen and L.-M. Peng, *J. Am. Chem. Soc.*, 2008, **130**, 1124 1125.
21 L. Liu, J. Hensel, R. C. Fitzmorris, Y. Li and J. Z. Zhang, *J. Phys. Chem. Lett.*, 2009, **1**, 155 160.
22 S. U. M. Khan, M. Al-Shahry and W. B. Ingler, Jr, *Science*, 2002, **297**, 2243 2245.
23 A. Wolcott, W. A. Smith, T. R. Kuykendall, Y. Zhao and J. Z. Zhang, *Adv. Funct. Mater.*, 2009, **19**, 1849 1856.
24 I. Cesar, A. Kay, J. A. Gonzalez Martinez and M. Grätzel, *J. Am. Chem. Soc.*, 2006, **128**, 4582 4583.
25 A. Kay, I. Cesar and M. Grätzel, *J. Am. Chem. Soc.*, 2006, **128**, 15714 15721.
26 D. K. Zhong, J. Sun, H. Inumaru and D. R. Gamelin, *J. Am. Chem. Soc.*, 2009, **131**, 6086 6087.
27 W. Smith and Y. P. Zhao, *Catal. Commun.*, 2009, **10**, 1117 1121.
28 K. Sivula, F. L. Formal and M. Grätzel, *Chem. Mater.*, 2009, **21**, 2862 2867.
29 W. Smith and Y. Zhao, *J. Phys. Chem. C*, 2008, **112**, 19635 19641.
30 Y. Lin, S. Zhou, X. Liu, S. Sheehan and D. Wang, *J. Am. Chem. Soc.*, 2009, **131**, 2772 2773.
31 Y. J. Hwang, A. Boukai and P. Yang, *Nano Lett.*, 2008, **9**, 410 415.

32 O. Khaselev and J. A. Turner, *Science*, 1998, **280**, 425 427.

33 J. Shi, Y. Hara, C. Sun, M. A. Anderson and X. Wang, *Nano Lett.*, 2011, **11**, 3413 3419.

34 A. Kampmann, P. Cowache, J. Vedel and D. Lincot, *J. Electroanal. Chem.*, 1995, **387**, 53 64.

35 D. Cahen, Y. W. Chen, R. Noufi, R. Ahrenkiel, R. Matson, M. Tomkiewicz and W.-M. Shen, *Sol. Cells*, 1986, **16**, 529 548.

36 E. Garnett and P. Yang, *Nano Lett.*, 2010, **10**, 1082 1087.

37 L. Hu and G. Chen, *Nano Lett.*, 2007, **7**, 3249 3252.

38 K.-Q. Peng, X. Wang, L. Li, X.-L. Wu and S.-T. Lee, *J. Am. Chem. Soc.*, 2010, **132**, 6872 6873.

39 B. Tian, X. Zheng, T. J. Kempa, Y. Fang, N. Yu, G. Yu, J. Huang and C. M. Lieber, *Nature*, 2007, **449**, 885 889.

40 J. Zhu, Z. Yu, G. F. Burkhard, C.-M. Hsu, S. T. Connor, Y. Xu, Q. Wang, M. McGehee, S. Fan and Y. Cui, *Nano Lett.*, 2008, **9**, 279 282.

41 M. D. Kelzenberg, S. W. Boettcher, J. A. Petykiewicz, D. B. Turner-Evans, M. C. Putnam, E. L. Warren, J. M. Spurgeon, R. M. Briggs, N. S. Lewis and H. A. Atwater, *Nat. Mater.*, 2010, **9**, 239 244.

42 G. Yuan, H. Zhao, X. Liu, Z. S. Hasanali, Z. Yan, A. Levine and D. Wang, *Angew. Chem., Int. Ed.*, 2009, **48**, 9680 9684.

43 A. B. Bocarsly, D. C. Bookbinder, R. N. Dominey, N. S. Lewis and M. S. Wrighton, *J. Am. Chem. Soc.*, 1980, **102**, 3683 3688.

44 R. N. Dominey, N. S. Lewis, J. A. Bruce, D. C. Bookbinder and M. S. Wrighton, *J. Am. Chem. Soc.*, 1982, **104**, 467 482.

45 K.-Q. Peng, Y. J. Yan, S. P. Gao and J. Zhu, *Adv. Mater.*, 2002, **14**, 1164 1167.

46 K. Peng, Y. Yan, S. Gao and J. Zhu, *Adv. Funct. Mater.*, 2003, **13**, 127 132.

47 K. Peng, Y. Wu, H. Fang, X. Zhong, Y. Xu and J. Zhu, *Angew. Chem., Int. Ed.*, 2005, **44**, 2737 2742.

48 L. E. Greene, M. Law, J. Goldberger, F. Kim, C. J. Justin, Y. Zhang, R. J. Saykally and P. Yang, *Angew. Chem., Int. Ed.*, 2003, **42**, 3031 3034.

49 L. Vayssieres, *Adv. Mater.*, 2003, **15**, 464 466.

50 A. Furube, Z.-S. Wang, K. Sunahara, K. Hara, R. Katoh and M. Tachiya, *J. Am. Chem. Soc.*, 2010, **132**, 6614 6615.

51 K. Sun, Y. Jing, N. Park, C. Li, Y. Bando and D. Wang, *J. Am. Chem. Soc.*, 2010, **132**, 15465 15467.

52 D. D. D. Ma, C. S. Lee, F. C. K. Au, S. Y. Tong and S. T. Lee, *Science*, 2003, **299**, 1874 1877.

53 S. Dengyuan and G. Baozeng, *J. Phys. D: Appl. Phys.*, 2009, **42**, 025103.

54 Y. S. Choi, J. Y. Lee, W. H. Choi, H. W. Yeom and S. Im, *Jpn. J. Appl. Phys.*, 2002, **41**, 7357.

55 Y. Cui, Z. Zhong, D. Wang, W. U. Wang and C. M. Lieber, *Nano Lett.*, 2003, **3**, 149 152.

56 L. Rayleigh, *Proc. London Math. Soc.*, 1879, **s1-11**, 51 56.

57 Y.-F. Huang, S. Chattopadhyay, Y.-J. Jen, C.-Y. Peng, T.-A. Liu, Y.-K. Hsu, C.-L. Pan, H.-C. Lo, C.-H. Hsu, Y.-H. Chang, C.-S. Lee, K.-H. Chen and L.-C. Chen, *Nat. Nanotechnol.*, 2007, **2**, 770 774.

58 X. W. Sun and H. S. Kwok, *J. Appl. Phys.*, 1999, **86**, 408 411.

59 A. Djurišić and Y. H. Leung, *Small*, 2006, **2**, 944 961.

60 M. A. Green and M. J. Keevers, *Progr. Photovolt.: Res. Appl.*, 1995, **3**, 189 192.

61 K. Sun, A. Kargar, N. Park, K. N. Madsen, P. W. Naughton, T. Bright, Y. Jing and D. Wang, *IEEE J. Sel. Top. Quantum Electron.*, 2011, **17**, 1033 1049.

62 C. Soci, A. Zhang, B. Xiang, S. A. Dayeh, D. P. R. Aplin, J. Park, X. Bao, Y.-H. Lo and D. Wang, *Nano Lett.*, 2007, **7**, 1003 1009.

63 C. Soci, A. Zhang, X. Bao, H. Kim, Y. Lo and D. Wang, *J. Nanosci. Nanotechnol.*, 2010, **10**, 1430.

64 D. C. Bookbinder, N. S. Lewis, M. G. Bradley, A. B. Bocarsly and M. S. Wrighton, *J. Am. Chem. Soc.*, 1979, **101**, 7721 7723.

65 K. Sun, K. Madsen, P. Andersen, W. Bao, Z. Sun and D. Wang, *J. Nanotechnol.*, 2012, submitted.

IOP PUBLISHING NANOTECHNOLOGY

Nanotechnology **23** (2012) 194013 (10pp) doi:10.1088/0957-4484/23/19/194013

Metal on metal oxide nanowire Co-catalyzed Si photocathode for solar water splitting

Ke Sun[1], Kristian Madsen[1,2], Pål Andersen[3], Weining Bao[4], Zhelin Sun[1] and Deli Wang[1,2]

[1] Department of Electrical and Computer Engineering, University of California, San Diego, 9500 Gilman Drive, La Jolla, CA 92093, USA
[2] California Institute of Telecommunication and Information Technology, University of California, San Diego, 9500 Gilman Drive, La Jolla, CA 92093, USA
[3] Department of Electronics and Telecommunications, Norwegian University of Science and Technology, NO-7491 Trondheim, Norway
[4] Department of Microelectronics, Fudan University, No. 220 Han Dan Road, Shanghai 200433, People's Republic of China

E-mail: dwang@ece.ucsd.edu

Received 10 January 2012, in final form 24 February 2012
Published 27 April 2012
Online at stacks.iop.org/Nano/23/194013

Abstract

We report a systematic study of Si|ZnO and Si|ZnO| metal photocathodes for effective photoelectrochemical cells and hydrogen generation. Both ZnO nanocrystalline thin films and vertical nanowire arrays were studied. Si|ZnO electrodes showed increased cathodic photocurrents due to improved charge separation by the formation of a p/n junction, and Si|ZnO:Al (n^+-ZnO) and Si|ZnO(N_2) (thin films prepared in N_2/Ar gas) lead to a further increase in cathodic photocurrents. Si|ZnONW (nanowire array) photocathodes dramatically increased the photocurrents and thus photoelectrochemical conversion efficiency due to the enhanced light absorption and enlarged surface area. The ZnO film thickness and ZnO nanowire length were important to the enhancements. A thin metal coating on ZnO showed increased photocurrent due to a catalyzed hydrogen evolution reaction and Ni metal showed comparable catalytic activities to those of Pt and Pd. Moreover, photoelectrochemical instability of Si|ZnO electrodes was minimized by metal co-catalysts. Our results indicate that the metal and ZnO on p-type Si serve as co-catalysts for photoelectrochemical water splitting, which can provide a possible low-cost and scalable method to fabricate high efficiency photocathodes for practical applications in clean solar energy harvesting.

(Some figures may appear in colour only in the online journal)

1. Introduction

After the idea of photoelectrolysis (solar-energy-assisted water splitting process) using a semiconductor electrode was introduced by Fujishima in 1972 [1], lots of research has been done, particularly in the past two decades, to search for a sustainable electrode material for photoelectrolysis (the device used for photoelectrolysis is well known as a photoelectrochemical cell or PEC cell), which is believed to be the essential approach to the clean H_2 economy. A photocathode is one of the electrodes for photoelectrolysis supplying photogenerated electrons to react with protons from the electrolyte and directly generate H_2 gas. An appropriate photocathode material should have band bending favorable for transfer of photogenerated electrons to the solid/solution interface, which requires the conduction band edge to be more negative than the H_2/H^+ redox potential, the Fermi level to be more positive than the H_2/H^+ redox potential, and for

0957-4484/12/194013+10$33.00

electrons to be the minority carriers. P-type Si meets these requirements and is one candidate photocathode material. Moreover, Si is abundant and cheap, and has a small bandgap (1.12 eV), which is good in terms of having a broad absorption coverage of the solar spectrum.

Surface kinetics is a very important parameter determining device performance, particularly for Si. Si shows extremely low surface kinetics leading to a competing process of recombination at an interface to an aqueous solution where band bending is minimal [2–6]. This is the result of a large number of surface states which cause 'Fermi level pinning' at the surface of the electrode, forcing band bending independent of the redox level of the solution.

However, studies of p-Si photoelectrodes also showed some problems, such as (i) the band alignment between Si and water redox levels does not allow spontaneous water splitting without an external bias and (ii) more seriously, Si is not chemically stable and photodecomposes (Si is particularly unstable under anodic bias). There is no single material that can meet all the criteria for photocathode selection and nature tends to be lacking in other choices of low-cost and stable p-type materials for photocathodes [7]. One possible approach is to integrate different materials to form a heterogeneous system with more desirable properties. Recent studies on coating an n^+-layer onto a p-type Si surface has shown to reduce the external bias due to the additional photovoltage generated at the n^+/p junction [8, 9]. Various metals in the form of particles or thin films deposited on the semiconductor photoelectrode surface are used to improve the catalytic activity. However, this metal|semiconductor structure is recognized to contribute to a large decrease in photovoltage because the metal coating promotes carrier recombination at the surface and decreases surface band bending [10].

In this paper, we report metal and metal oxide co-catalyzed p-type Si-based photocathodes, where an n-type wide bandgap metal oxide layer is sandwiched between the metal layer and p-Si. This structure allows enhanced charge separation and transport of photo-induced electrons from p-type Si to n-type metal oxide due to the internal p/n junction and band bending, as well as improved carrier travel across the metal oxide (electrons are majority carriers) to the electrolyte/electrode interface. Furthermore, a nanostructured metal oxide layer can improve the overall effective surface area for the chemical reaction, thus improving the cathodic photocurrent density. The metal thin film coating on metal oxide nanowire surfaces offer catalysis and protection to the heterostructure photocathodes.

2. Experimental procedures

2.1. Si wafer cleaning

Boron-doped prime grade p-type (100) Si wafers (1–10 Ω cm, University Wafer) were initially cleaned with a standard solvent cleaning process. Wafers were then dried with a stream of N_2 gas and immediately transferred to the sputtering deposition chamber avoiding further oxidation.

2.2. ZnO seeding layer coating and ZnO nanowire growth

A thin layer of different seeding materials was then deposited on the polished side of the wafer through magnetron RF sputtering. Normally argon gas was used to ignite the plasma. A mixed Ar with 10% N_2 was also used during ZnO sputtering. Deposition was conducted without substrate heating or RF bias. Different seeding materials used for investigation include 99.99% ZnO sputtered in Ar, labeled as ZnO(Ar), in mixed Ar/10% N_2, labeled as ZnO(N2), and 2% Al_2O_3-doped ZnO sputtered in Ar, labeled as ZnO:Al. The deposition rate was kept at a constant value of 3 nm min^{-1} and thickness of the seeding layer was varied from 25 to 170 nm. During deposition, sputtering power was fixed at 200 W with a constant gas flow rate of 30 sccm. Working pressure was kept at no higher than 1.9 mTorr at room temperature.

Seeded Si wafers were then diced into $6.35 \times 6.35\ \mathrm{cm}^2$ and stored under vacuum for further processing. To grow ZnO nanowires using a solution-based method, a solution of 0.25 M hexamethylenetetramine (HMTA, sigma) and the same concentration of zinc acetate ($Zn(AC)_2$, Sigma) was made in the reaction container (three-necked flask). Diced samples were then fixed on supporting glass slides face down and carefully transferred to the flask. The flask was purged with N_2 and immersed in the oil bath during growth. Growth was carried out at 90 °C. The growth timer was started once the solution temperature reached 60 °C. Samples were grown for various times from 10 min to 2 h. The samples were rinsed with DI water (17.6 M Ω cm) immediately after being taken out of the reaction solution. Gentle sonication was then used to remove surface particle residuals and the samples were then blown dry with a stream of N_2.

2.3. Metal catalyst deposition

Gas phase deposition of metal catalysts was realized using electron-beam evaporation at a base pressure of 8×10^{-7} Torr. The metal coating thickness was monitored by the quartz resonator. 5 nm of Pt, Pd and Ni was evaporated onto the various samples (plain Si, ZnO thin-film-coated Si and ZnO nanowire-coated Si).

2.4. Surface morphology analysis

A scanning electron microscope (SEM, Philips XL30 ESEM) equipped with a field emission gun and an energy dispersive spectroscopy (EDX) detector was used to investigate the surface morphology and chemical composition. A tapping-mode atomic force microscope (AFM, Veeco scanning probe microscope) equipped with a standard silicon probe (Umasch NSC15/no Al) was also used to evaluate the surface nanoscale topological differences between the thin film coatings. Raw data collected by AFM were processed using NanoScope software; surface roughness and grain size were obtained using NanoScope Analysis software.

2.5. Hall measurement

The resistivity and carrier concentration of the sputtered ZnO thin films were tested using a home-built Hall measurement set-up.

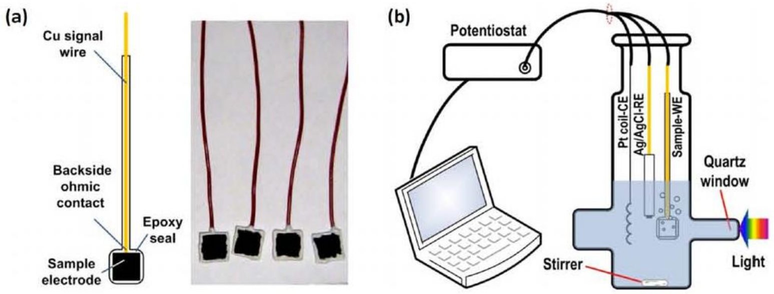

Figure 1. (a) Schematics (left) and optical image (right) of prepared sample electrodes and (b) schematics of PEC measurement set-up.

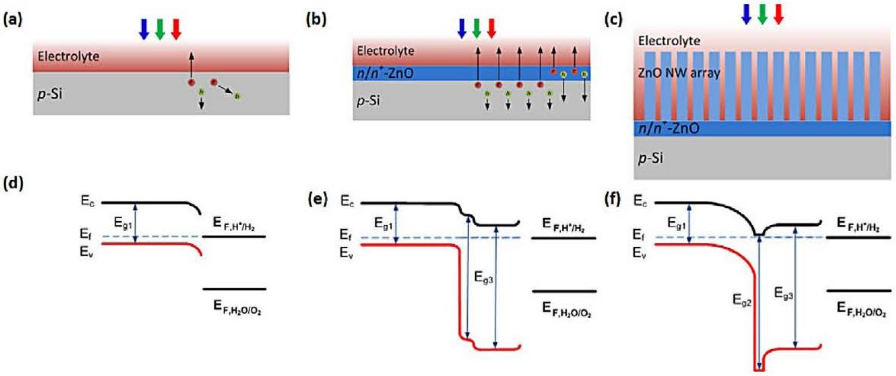

Figure 2. Schematics of photocathode structure: (a) bare planar p-Si, (b) p-Si|n/n$^+$-ZnO and (c) p-Si|n/n$^+$-ZnO|ZnO nanowires. Energy band diagram at equilibrium: (d) bare p-Si with Fermi level pinning, (e) p-Si|n-ZnO|ZnO nanowires and (f) p-Si|n$^+$-ZnO|ZnO nanowires.

2.6. Electrode and electrolyte solution preparation

The backsides of the Si samples were gently scratched and Ga/In eutectic alloy was applied to produce an ohmic contact between an insulated copper wire and the Si sample. The edges and backside of the samples were protected by epoxy to isolate them from contacting the electrolyte (figure 1(a)). Areas of epoxy-protected samples in contact with the electrolyte were calculated using image processing. All the electrochemical experiments were carried out in a PBS buffered 0.25 M sodium sulfate (Na_2SO_4 pH = 7.2) at room temperature. The pH was measured and monitored using a pH5 pH meter (Acorn, Oakton).

2.7. Photoelectrochemical measurement

In all the electrochemical measurements, a single cell and three-electrode set-up was used. The three electrodes consisted of a Pt mesh counter electrode (CE), Ag/AgCl reference electrode in 1 M KCl (RE) and the sample as a working electrode (WE). The measurement set-up is shown in figure 1(b). All of the electrodes were kept as close as possible and their position kept constant for every sample. A xenon lamp solar simulator (UV-enhanced, Newport) with 1.5AM filter was used as a light source. Distance from sample to the solar simulator was 22 cm which provided a constant power density of 100 mW cm^{-2} at the sample position. Power intensity and spectrum at this particular position was initially calibrated for a more accurate estimation of the efficiency and spectrum response. Irradiation was applied perpendicularly to the sample surface through a quartz window to minimize spectrum loss. A magnetic stir bar was employed to agitate the electrolyte, to remove bubbles at the sample surface and to further minimize the thickness of the diffusion layer on the electrode surface, which could introduce error into the measured current density. An inert gas purge using N_2 was applied prior to each measurement for at least 5 min to remove dissolved O_2 and mainly CO_2 in the electrolyte. This served to minimize the effect of these dissolved gases. Samples were stabilized in the electrolyte after each scan by monitoring the open circuit voltage for at least 10 min. During measurement the N_2 purge was kept running to maintain a N_2 saturation environment at the electrolyte/air interface. A potentiostat (DY2322, Digi-Ivy) was employed for the data collection.

3. Results and discussions

Figure 2 summarizes the structures of the photoelectrodes studied in this paper, where figures 2(a)–(c) show the schematic of the photoelectrodes of planar p-Si, n- or n$^+$-doped metal oxide thin-film-coated p-Si (n/p junction) and ZnO nanowire-coated n/n$^+$-ZnO/Si, respectively.

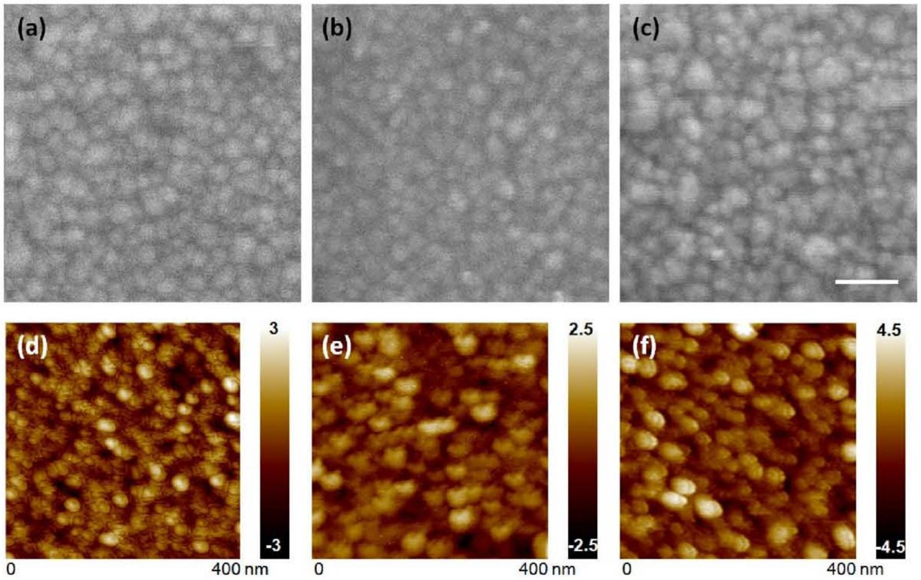

Figure 3. SEM and AFM images of different ZnO-coated Si photocathodes: (a) ZnO(Ar), (b) ZnO(N_2) and (c) ZnO:Al. Scale bar in SEM images is 50 nm and the scan range in AFM images was 400 nm.

Figures 2(d)–(f) show the energy band diagrams. Metal thin films were also coated on the three kinds of photoelectrodes, particularly as co-catalysts with the oxide or oxide nanowires, which were not shown in figure 2.

From the theoretical design point of view, a single-material electrode using Si alone offers limited photocurrent and low H_2 evolution kinetics, which is due to the competitive carrier recombination process (figure 2(a)) particularly when the band bending at the interface is small (figure 2(d)). Generally, this is true for Si where the Fermi level is pinned at the surface, without considering the energy distribution of the surface states or the large density of surface states [11, 12]. The pinned Fermi level results in the change of applied potential in the Helmholtz layer instead of the space charge region [3]. Unlike the single-material system, a binary system using n-type ZnO on p-type Si (figures 2(b) and (c)) forms a p/n junction between the materials, which can provide an effective electric field to separate the photogenerated carriers, minimizing carrier recombination in Si (figures 2(e) and (f)). In addition, the heterojunction between Si and ZnO maximizes the light absorption by allowing separate absorption in the UV and visible spectra and reduces the hot electron effect. Moreover, the growth of ZnO nanowires in figure 2(c) further increases light absorption due to light trapping effects and, more importantly, increases the surface area for photoelectrochemical reaction and photocurrent density. Note that figure 2(f) shows the extreme case that the seeding layer is heavily doped, which offers high electrical conductivity, but the double-sided barrier does not favor the carrier transport when compared to an unintentionally/intrinsically doped ZnO film.

Figure 3 shows SEM and AFM images of the deposited thin films on polished p-Si, which shows the effect of deposition conditions through the addition of nitrogen during sputter, with flow rate and deposition rate held constant. The SEM images of the ZnO film prepared using pure Ar gas in figure 3(a) show similar morphology compared to those prepared in Ar:N_2 = 9:1 in figure 3(b), although the latter shows larger variation in grain size. However, AFM studies reveal that ZnO(Ar) films have average grain sizes of about 14.34 nm and a surface roughness of Ra = 0.59 nm (figure 3(d)), while ZnO(N_2) films have an average grain size of 13.64 nm and a surface roughness of Ra = 0.48 nm (figure 3(e)). Under normal conditions, sputtered ZnO films showed primarily *c*-plane orientation [13]. Although we are not quite clear what effect N_2 has on sputtered ZnO, by comparing figures 3(a)/(d) and (b)/(e), it seems that ZnO(N_2) thin films have a larger portion of smaller size crystallites or amorphous phase that is below the AFM resolution using a 10 nm Si tip. Both films are too resistive for Hall measurements. Figure 3(c) shows an SEM image of ZnO doped with 2% Al sputtered using pure Ar gas, which shows an even larger particle size distribution compared to figure 3(a). AFM images show ZnO:Al films have rougher surfaces (Ra = 0.86 nm) but larger average grain size of 16.75 nm compared to that of the undoped ZnO films sputtered using Ar. Note that the ZnO:Al films sputtered at the identical conditions have a slightly higher deposition rate, which might contribute to the large variation in crystallinity and orientation. The ZnO:Al thin films are reported to have mixed orientation of crystallinity, because Al dopants could migrate to the grain boundaries and surfaces to form Al_2O_3

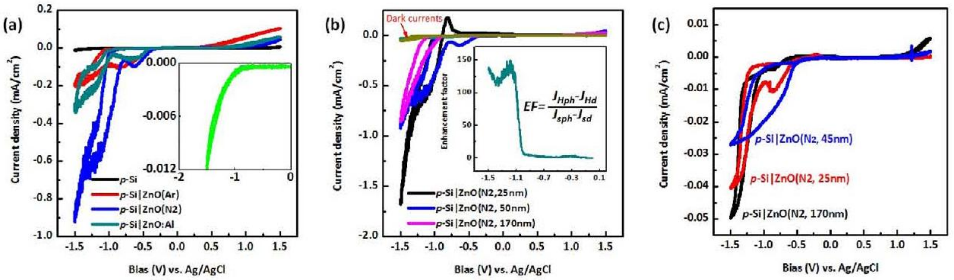

Figure 4. Cyclic voltammetry study of photocathodes with different structure: (a) seeded p-type Si substrate with three different ZnO seeding layers (50 nm). Inset shows planar p-Si photocurrent and dark current. (b) ZnO(N_2) seeded p-Si substrate with different seeding layer thickness, under 100 mW cm^{-2} light illumination. Inset shows the current enhancement factor as the ratio between the net photocurrent from heterostructure (25 nm ZnO(N_2) on Si) and bare Si. (c) Dark current of p-Si|ZnO(N_2) with different ZnO thickness.

via reaction with oxygen [14]. Hall measurements shows very conducting ZnO:Al films with 2% Al dopants before thermal annealing with average resistivity 0.1 Ω cm and average carrier concentration of 5.5×10^{19} cm^{-3} from three samples. Note that the AFM images show larger grain sizes compared to the corresponding SEM images, presumably due to the limitation of the Si AFM tip size (10 nm).

The *I–V* behavior of heterojunction photocathodes was tested (figure 4). For comparison, a single-material electrode using Si (figures 2(a)/(d)) alone was studied, which showed limited cathodic current at negative potential and an exponentially increasing anodic current density at positive potentials (figure 4(a) black curve and the inset). Under light illumination, a decrease in the exponentially behaving current density region was noticed under positive potential and a significant photoresponse was noticed in the limited current density region at negative bias. Photo-reduction of water directly at the p-Si electrode surface is slow and inefficient, due to the high overpotential (high kinetic loss) [3], which indicates a large external potential is needed to drive the water reduction reaction. Adding an n/n$^+$ layer on p-Si and formation of the heterojunction photocathode between ZnO and Si improves the interfacial charge transfer kinetics by minimizing electron–hole recombination and assisting in the injection of photogenerated electrons across the ZnO layer to the electrolyte. First of all, with a ZnO coating, the onset potential is effectively reduced, while the current density was enhanced about 20 times at biases above −1 V (versus Ag/AgCl 1 M KCl) (red curve). Second, ZnO:Al/Si electrodes (dark cyan) showed improved photocurrent level compared to ZnO(Ar) This can be attributed to the conductive nature of the ZnO:Al film (average resistivity 0.1 Ω cm with average carrier concentration of 5.5×10^{19} cm^{-3}, and even as high as 4×10^{20} cm^{-3} after thermal treatment). The highly doped n-ZnO can potentially increase light absorption due to the larger depletion range in p-Si and also provides a more efficient electron extraction from p-Si as well as transport in ZnO to the electrolyte. Finally, and interestingly, the ZnO(N_2) film on p-type Si (50 nm ZnO thickness after 10 min sputtering with a similar deposition rate and under the same sputtering conditions by adding 10% N_2 in Ar gas) showed dramatically enhanced photocathodic current, about 80 times at −1.5 V (versus Ag/AgCl 1 M KCl, blue curve) and a sharper current increase after onset potential, which is even higher than that of Si|ZnO:Al photoelectrodes. The mechanism behind this observation is unclear at this point and further investigation is needed to clarify the enhanced photocurrent effect in ZnO(N_2). Note that (i) ZnO films sputtered with and without adding N_2 were measured using a four-point Hall measurement, but reasonable readings on resistivity and doping type were not able to be obtained due to the limitation of the Hall measurement set-up, indicating the highly resistive nature of the ZnO film. (ii) Nitrogen's effect on the ZnO impurity energy band shallow/deep or donor/acceptor has been proposed [15–18], which might contribute to the visible light absorption, similar to that in TiO_2 [19]. (iii) The ZnO(N_2) films showed smaller grain sizes but rougher surfaces, which might lead to a larger effective surface area for catalytic reaction (figures 3(b)/(d)). (iv) ZnO|Si photoelectrodes show large hysteresis in the cathodic *I–V* scan and waves around −0.5 V (versus Ag/AgCl 1 M KCl), indicating photochemical instability under PEC operational conditions. Finally, also note in figure 4(a) the anodic photocurrents showed the opposite trend with photocurrent decreasing in the order of ZnO(Ar) > ZnO:Al > ZnO(N_2). This trend was fairly consistent with our study on the ITO|ZnO photoanode, where ZnO(Ar) gave the best photoanodic response.

The p-Si photocathode is effectively catalyzed by large bandgap n-type semiconductor material in this case, which can be actually quantified by introducing the definition of the current enhancement factor as the ratio between the net photocurrent from the heterostructure and bare Si (inset of figure 4(b)). Figure 4(b) shows the cathodic photocurrent dependence to oxide film thickness for p-Si|ZnO(N_2) samples, where photocurrent at a cathodic bias above −1 V (versus Ag/AgCl 1 M KCl) decreases with increasing thickness. ZnO has a smaller refractive index than Si over the same wavelength range and thus with ZnO coating it smooths out the refractive index transition from media (aqueous solution) to the Si substrate and minimizes light loss due to reflection. However, a thicker ZnO(N_2) film

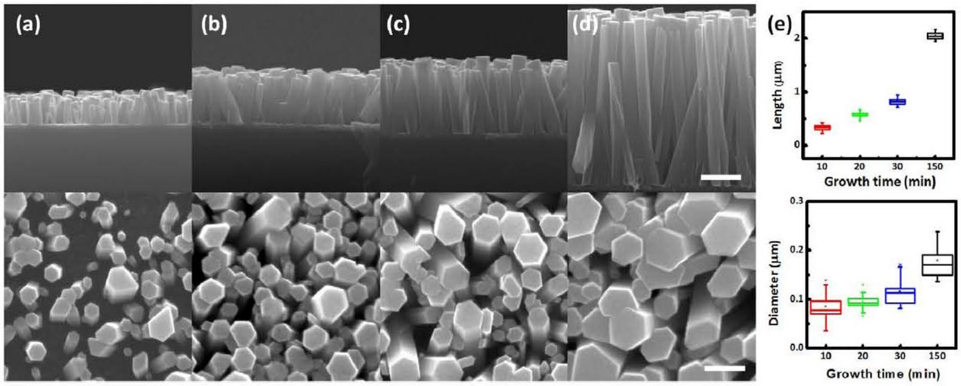

Figure 5. SEM images of ZnO nanowires on polished p-type Si from different growth times of (a) 10 min, (b) 20 min, (c) 30 min and (d) 2.5 h. First row (top): cross-sectional view (scale bar = 500 nm) and second row (bottom): top view (scale bar = 200 nm). Seeding layer here is 60 nm ZnO(Ar). (e) Statistics of nanowire length (top) and diameter (bottom) with sampling size of 20.

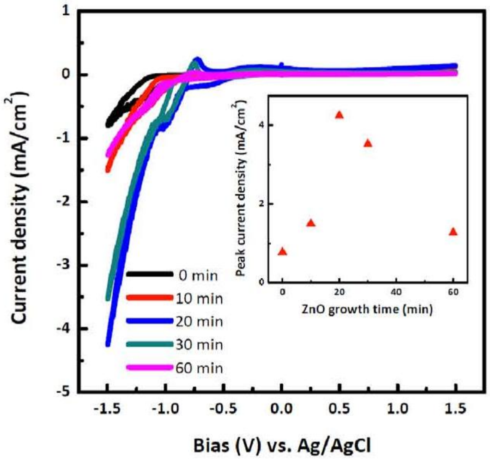

Figure 6. Cyclic voltammetry on p-Si|ZnO(N_2, 50 nm)|ZnO nanowire with various nanowire growth times.

results in a reduced transmittance and increased number of photogenerated holes from ZnO at the ZnO/electrolyte interface (figure 2(b)/(e)), which can significantly degrade the overall cathodic current. Also note that the diminished waves around −0.5 V (versus Ag/AgCl 1 M KCl) with the increased ZnO(N_2) film thickness is presumably due to the improved stability of thicker films. Figure 4(c) shows the dark currents of p-Si|ZnO(N_2) with different ZnO thickness. In general and within experimental fluctuation, thicker oxide films produce larger dark current and are more stable.

Figure 5 shows typical SEM images of samples with different lengths of ZnO nanowires from different times of hydrothermal growth (10, 20, 30 min and 2.5 h) on ZnO(Ar) seeded p-Si (figures 5(a)–(d)). The first ever reported ZnO crystal growth based on a hydrothermal method using seed crystals was documented by Laudise in 1960 [20]. Hydrothermal growth of compound materials is a low-cost and low-temperature technique which does not require high-profile equipment. This method has been extensively studied during the last few decades [21–24] and provides an approach to growing micro/nanocrystalline structures on various substrates for flexible and transparent optoelectronics devices. Significant progress on understanding the mechanism to achieve a controllable growth (e.g. crystal size [25], face of growth [26, 27], doping [28] and more) were developed. In our experiment, a thin seeding layer was used providing nucleation sites for nanowire growth, which can differentiate from seedless growth [29]. Preparation of ZnO nanowires on a polished bare Si substrate was done individually from separate processes due to the limited size of the reactor. However, it is confirmed that five samples fabricated separately showed a similar trend within acceptable errors. The cross section of a single ZnO nanowire is a hexagonal wurtzite structure with growth direction along the *c* axis (figures 5(a)–(d) bottom). As growth time increases, average size and length of ZnO nanowires generally become larger and longer [30], as shown in figure 5(e) (top and bottom). Growth in both length and diameter directions were saturated in the growth versus time curve (figure 5(e)) due to the limited reaction solution (100 ml). Growth rates in the linear fit region (10–30 min) were direction-dependent, with an average growth rate of 28 nm min^{-1} in the length (axial) direction and about 4 nm min^{-1} in the diameter (radial) direction. This statistical study showed high yield of device fabrication and repeatability from substrate cleaning, seeding layer sputtering and nanowire syntheses.

Figure 6 shows the *I*–*V* characteristics of the photocathodes of ZnO nanowires with different growth times on 50 nm ZnO(N_2) seeding layer on p-Si. All the data reported here were measured from at least three samples. With the increasing nanowire growth time, photocurrent density and catalytic effect initially increase from 0 min (seeding layer only, black curve) to 10 min (red curve) and 20 min (blue

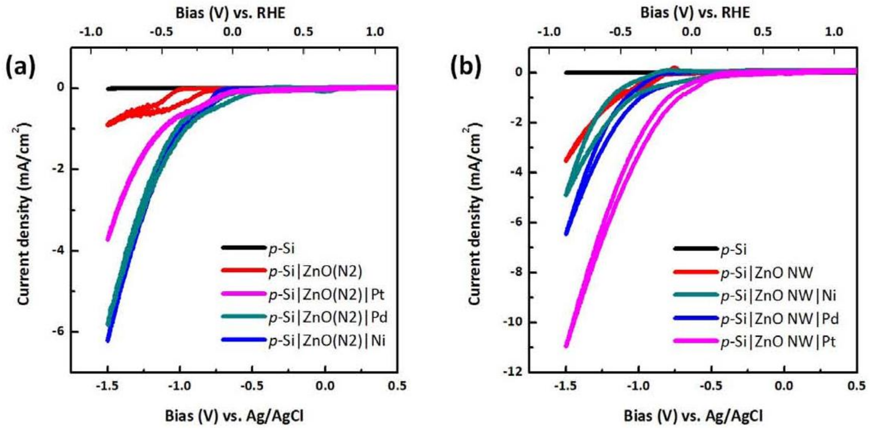

Figure 7. Cyclic voltammetry (CV) graphs of various metal co-catalyst-coated Si substrates without ZnO nanowires (a) and with ZnO nanowires (b). Seeding layer used was ZnO(N_2, 50 nm).

curve) growth, and decrease with growth time for longer nanowires, e.g. 30 and 60 min growth (dark cyan and magenta curves in figure 6, respectively). The peak photocurrent densities were summarized in figure 6, inset, with a peak photocurrent of 4.2 mA cm^{-2} for 20 min growth of ZnO nanowires at -1.5 V (versus Ag/AgCl 1 M KCl). These data suggest that the dependence of photocurrent to nanowire growth time is an overall effect of surface area (increase with nanowire length and thus growth time), ratio of accessible effective surface area (decrease with nanowire radius and thus growth time), light absorption (increase with nanowire length and thus growth time), charge separation and transport efficiency (decrease with nanowire length and thus growth time), surface trap states (decrease with nanowire radius and thus growth time), etc. Cathodic waves around -0.5 V (versus Ag/AgCl 1 M KCl) also showed length-dependent behavior, where longer nanowires showed minimum cathodic wave. This is believed to be due to the longer growth time which leads to an increase in nanowire array density and results in a reduced overall exposed area to the electrolyte.

The hydrogen evolution reaction (HER) catalyst remains an important part of the hydrogen economy for the conversion processes of H^+ to H_2 in artificial photosynthesis, as well as the reverse reaction of H_2 to H^+ in fuel cells. Platinum is the well-accepted and most-efficient HER catalyst. However, Pt metal is not able to meet large-scale production applications due to its limited availability and high cost. In order to address this problem, researchers are actively seeking non-noble alternatives. These alternatives containing metals from the transition metals in the form of heterogeneous metal alloy (Mo–Ni [31], Al–Ti [32]), metal oxides/sulfides (MoS_x [33]) or enzyme hydrogenases-like complexes (Pt-complex [34], Ni–Ru complex [35], Co-complex [36]) are the three major categories of catalysts attracting research interest. In this work, Ni, Pt and Pd metal were deposited on ZnO thin-film-coated p-Si, as well as ZnO nanowire-coated p-Si in order to reduce the overpotential. 5 nm of metal was coated on ZnO using e-beam evaporation. This thickness was chosen to produce a non-continuous film to minimize the loss of incident light. Compared to Pt, Ni and Pd showed higher activity on sputtered ZnO(N_2) film, as shown in figure 7(a). Direct metal coating on planar p-Si showed electrocatalysis in dark and minimized the photoresponse under cathodic bias. Metal catalyst deposited on the semiconductor surface dramatically decreases the photovoltage since it effectively lowers the energy barrier at the semiconductor/electrolyte interface, resulting in an enhancement in carrier recombination [10]. Using ZnO as an intermediate layer helps to maintain the photovoltage at ZnO/Si junction, which effectively separates the photogenerated carriers from Si and enhance the transport in ZnO and to the ZnO/electrolyte interface.

Figure 7(b) shows the photoelectrochemical activity increase of samples with metal coatings on ZnO nanowires in the order of Ni $<$ Pd $<$ Pt. The reason for this difference in catalytic activity of metals on ZnO thin film versus those on nanowires is not clear. One possibility is the difference in light scattering/absorption from the metal coating: light scattering from the metal coating on ZnO nanowires is minimal due to the vertical nanowire geometry and the light trapping effect. Pt showed higher activity on nanowire samples than on thin films, presumably due to improved catalytic behavior from the rough metal coating on nanowires. Moreover, it has been pointed out that electroless-deposited metals showed better performance than gas-phase-deposited metal film in terms of the catalytic effect due to the smaller particle sizes and larger surface area. However, we were not able to apply the metal nanoparticles to ZnO by electrochemical methods due to its fairly weak chemical stability in various pH environments. The bias scale versus Ag/AgCl 1 M KCl is converted to reversible hydrogen electrode values (top x axis in figure 7), which is independent of pH can be converted using the equation [37]

$$E_{\mathrm{RHE}} = E_{\mathrm{Ag/AgCl}} + 0.059\mathrm{pH} + E^{0}_{\mathrm{Ag/AgCl}} \qquad (1)$$

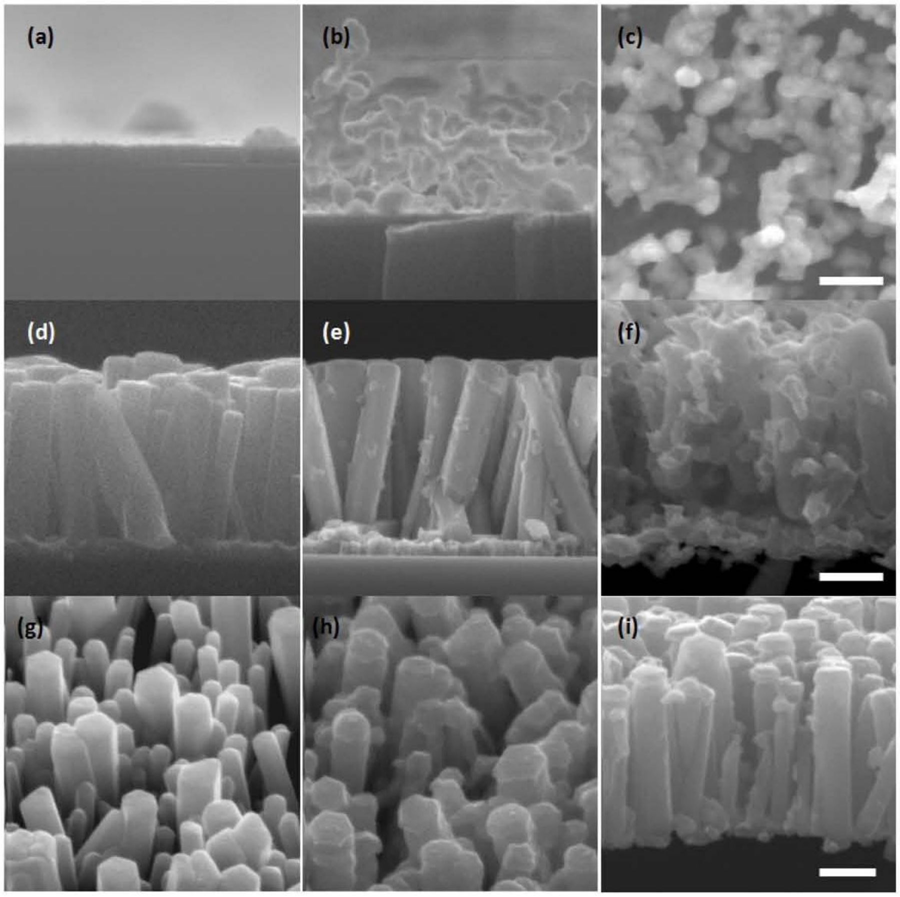

Figure 8. SEM images of photoelectrochemical stability: (a) cross-sectional view of p-Si|ZnO(N_2, 50 nm) photoelectrode at pristine condition, (b) cross-sectional view and (c) top view after one typical dark/photo *I–V* scan; cross-sectional view of p-Si|ZnO(N_2, 50 nm)|ZnO NW(20 min) photoelectrode at (d) pristine condition, (e) after one typical dark/photo CV scan and (f) tested under illumination and biased at −1.5 V (versus Ag/AgCl 1 M KCl) for 1 h; 45° view of p-Si|ZnO(Ar)|ZnO NW (30 min)|Pt photoelectrode at (g) pristine condition, (h) 45° view and (i) cross-sectional view of the tested sample under illumination and biased at −1.5 V (versus Ag/AgCl 1 M KCl) for 1 h.

where $E^0_{\mathrm{Ag/AgCl}}$ is the potential difference to the standard hydrogen potential, which is 0.236 V. One can see that metal coating effectively moves the onset potential, defined as when the photocurrent density exceeds 0.1 mA cm^{-2}, below the zero RHE level.

As mentioned earlier, the hysteresis of *I–V* scan indicated chemical instability of the photoelectrodes. Actually, ZnO is an amphoteric metal oxide which reacts with both acids and bases. An acidic environment has a much faster etching rate than a basic solution. Under bias, ZnO cathodic decomposition in acidic conditions and photodecomposition of ZnO is normally a concern when used as a photoanode.

Cathodic decomposition [38]:

$$\mathrm{ZnO} + 2\mathrm{e}^- + 2\mathrm{H}^+ = \mathrm{Zn} + \mathrm{H_2O}. \qquad (2)$$

Photoanodic decomposition [39]:

$$2\mathrm{ZnO} + 4\mathrm{h}^+ = 2\mathrm{Zn}^{2+} + \mathrm{O_2}. \qquad (3)$$

To better understand the photoelectrochemical stability of Si|ZnO photocathodes, samples after a typical *I–V* scan in dark and under illumination in an electrolyte with pH of 7.2 were investigated under SEM. As shown in figure 8, oxide particles (via SEM-EDX) were noticed on both ZnO thin-film and nanowire-coated p-Si after *I–V* scans. Figures 8(a) and (b) show the cross-sectional images of the ZnO thin films and changing into oxide particles, while figure 8(c) shows the top view of the re-deposited oxide particles. Figures 8(d)–(f) show the cross-sectional images of a p-Si|ZnO nanowire photoelectrode in pristine condition, after one typical *I–V* scan, and tested under illumination and biased at −1.5 V (versus Ag/AgCl 1 M KCl) for 1 h, respectively. Even more severe damage of ZnO and even complete removal was noticed in acidic and basic solutions. Metal co-catalyzed photoelectrodes showed improved stability and minimized the cathodic decomposition, in addition to the strong effect of improving the electrochemical hydrogen reduction kinetics. For example, figure 8(h), compared to (g), shows platinum-metal-coated p-Si|ZnO nanowires with minimized damage after *I*–*V* scans, which is also shown by the cross-sectional SEM of photoelectrodes tested under illumination and biased at −1.5 V (versus Ag/AgCl 1 M KCl) for 1 h in figure 8(i) compared to figure 8(f).

4. Conclusions

We report the systematic study of Si|ZnO and Si|ZnO|metal photocathodes for effective photoelectrochemical cells and hydrogen generation, where ZnO was in the form of nanocrystalline thin films and vertical nanowire arrays. ZnO thin films were deposited on p-Si under Ar or Ar/N_2 mixture atmosphere and 2% Al_2O_3-doped ZnO thin films were studied. ZnO coatings increase the photocathodic current due to the formation of a p/n junction, thus improving charge separation. The doped ZnO:Al (n^+-ZnO) thin films further increase the cathodic photocurrent because of higher conductivity. Interestingly ZnO thin films prepared in N_2/Ar gas demonstrated the highest enhancement in photocurrent, which is probably due to increased light absorption in the visible range (due to N levels in ZnO) and to increased surface area due to smaller nanocrystal sizes. An optimal oxide thickness of around 25 nm was found for the best photocurrent enhancement. Growth of vertical ZnO nanowires, with optimal growth time on Si|ZnO was found to dramatically increase the photoelectrochemical efficiency due to the enhanced light absorption and enlarged surface area. Metal co-catalysts on ZnO to further catalyze the hydrogen evolution reaction were studied and Ni was demonstrated to have comparable catalytic activities to that of expensive Pt and Pd. Finally, the photoelectrochemical instability of Si|ZnO photoelectrodes was demonstrated in pH neutral electrolytes, which can be minimized by metal co-catalysts. Co-catalysts using metal and metal oxides on p-type Si provide a low-cost and scalable solution for improved performance of photocathodes for practical applications in clean solar energy harvesting and conversion to clean H_2 fuel.

Acknowledgments

DW would like to thank the Department of Energy (DOE DE-FG36-08G018016) and the National Science Foundation (NSF ARRA ECCS0901113) for financial support. KS would like to thank Professor S Jin for stimulating discussion. KM would like to thank the UCSD Cal-IT^2 undergraduate student summer research program. WB would like to thank the UCSD international summer program. The authors would like to thank W Chen and Professor P Yu for help in Hall measurement.

References

[1] Fujishima A and Honda K 1972 Electrochemical photolysis of water at a semiconductor electrode *Nature* **238** 37–8

[2] Bookbinder D C *et al* 1979 Photoelectrochemical reduction of *N*,*N*′-dimethyl-4,4′-bipyridinium in aqueous media at p-type silicon: sustained photogeneration of a species capable of evolving hydrogen *J. Am. Chem. Soc.* **101** 7721–3

[3] Bocarsly A B *et al* 1980 Photoreduction at illuminated p-type semiconducting silicon photoelectrodes. Evidence for Fermi level pinning *J. Am. Chem. Soc.* **102** 3683–8

[4] Bookbinder D C *et al* 1980 Synthesis and characterization of a photosensitive interface for hydrogen generation: chemically modified p-type semiconducting silicon photocathodes *Proc. Natl Acad. Sci. USA* **77** 6280–4

[5] Fan F-R F, Reichman B and Bard A J 1980 Semiconductor electrodes: the p- and n-gallium arsenide-*N*,*N*′-dimethyl-4,4′-bipyridinium system. Enhancement of hydrogen evolution on p-gallium arsenide and stabilization of n-gallium arsenide electrodes *J. Am. Chem. Soc.* **102** 1488–92

[6] Memming R 1978 The role of energy levels in semiconductor-electrolyte solar cells *J. Electrochem. Soc.* **125** 117–23

[7] Paracchino A *et al* 2011 Highly active oxide photocathode for photoelectrochemical water reduction *Nature Mater.* **10** 456–61

[8] Boettcher S W *et al* 2011 Photoelectrochemical hydrogen evolution using Si microwire arrays *J. Am. Chem. Soc.* **133** 1216–9

[9] Pijpers J J H *et al* 2011 Light-induced water oxidation at silicon electrodes functionalized with a cobalt oxygen-evolving catalyst *Proc. Natl Acad. Sci.* **108** 10056–61

[10] Kaneko M and Okura I 2002 *Photocatalysis: Science and Technology* (New York: Springer and Kodansha Ltd)

[11] Bardeen J 1947 Surface states and rectification at a metal semi-conductor contact *Phys. Rev.* **71** 717

[12] Meyerhof W E 1947 Contact potential difference in silicon crystal rectifiers *Phys. Rev.* **71** 727

[13] Lee Y E *et al* 1996 Microstructural evolution and preferred orientation change of radio-frequency-magnetron sputtered ZnO thin films *J. Vac. Sci. Technol.* A **14** 1943

[14] Haug F-J *et al* 2001 Influence of deposition conditions on the thermal stability of ZnO:Al films grown by rf magnetron sputtering *J. Vac. Sci. Technol.* A **19** 171–4

[15] Look D C *et al* 2005 Evidence for native-defect donors in n-type ZnO *Phys. Rev. Lett.* **95** 225502

[16] Lee E-C *et al* 2001 Compensation mechanism for N acceptors in ZnO *Phys. Rev.* B **64** 085120

[17] Lany S and Zunger A 2010 Generalized Koopmans density functional calculations reveal the deep acceptor state of N–O in ZnO *Phys. Rev.* B **81** 205209

[18] Lautenschlaeger S *et al* 2011 A model for acceptor doping in ZnO based on nitrogen pair formation *Phys. Status Solidi* b **248** 1217–21

[19] Varley J B, Janotti A and Van de Walle C G 2011 Mechanism of visible-light photocatalysis in nitrogen-doped TiO_2 *Adv. Mater.* **23** 2343–7

[20] Laudise R A and Ballman A A 1960 Hydrothermal synthesis of zinc oxide and zinc sulfide *J. Phys. Chem.* **64** 688–91

[21] Sun L *et al* 2002 Control of ZnO morphology via a simple solution route *Chem. Mater.* **14** 4172–7

[22] Yu H *et al* 2005 A general low-temperature route for large-scale fabrication of highly oriented ZnO nanorod/nanotube arrays *J. Am. Chem. Soc.* **127** 2378–9

[23] Greene L E *et al* 2003 Low-temperature wafer-scale production of ZnO nanowire arrays *Angew. Chem. Int. Edn* **42** 3031–4

[24] Lange F F 1996 Chemical solution routes to single-crystal thin films *Science* **273** 903–9

[25] Liu B and Zeng H C 2003 Hydrothermal synthesis of ZnO nanorods in the diameter regime of 50 nm *J. Am. Chem. Soc.* **125** 4430–1

[26] Joo J *et al* 2011 Face-selective electrostatic control of hydrothermal zinc oxide nanowire synthesis *Nature Mater.* **10** 596–601

[27] Kim J H, Andeen D and Lange F F 2006 Hydrothermal growth of periodic, single-crystal ZnO microrods and microtunnels *Adv. Mater.* **18** 2453–7

[28] Yuhas B D *et al* 2006 Transition-metal doped zinc oxide nanowires *Angw. Chem. Int. Edn* **45** 420–3

[29] Hsu J W P *et al* 2004 Directed spatial organization of zinc oxide nanorods *Nano Lett.* **5** 83–6

[30] Sun K *et al* 2011 Crystalline ZnO thin film by hydrothermal growth *Chem. Commun.* **47** 7776–8

[31] McKone J R *et al* 2011 Evaluation of Pt, Ni, and Ni–Mo electrocatalysts for hydrogen evolution on crystalline Si electrodes *Energy Environ. Sci.* **4** 3573–83

[32] Chopra I S *et al* 2011 Turning aluminium into a noble-metal-like catalyst for low-temperature activation of molecular hydrogen *Nature Mater.* **10** 884–9

[33] Hou Y *et al* 2011 Bioinspired molecular co-catalysts bonded to a silicon photocathode for solar hydrogen evolution *Nature Mater.* **10** 434–8

[34] Varpness Z *et al* 2005 Biomimetic synthesis of a H_2 catalyst using a protein cage architecture *Nano Lett.* **5** 2306–9

[35] Ogo S *et al* 2007 A dinuclear Ni(μ-H)Ru complex derived from H_2 *Science* **316** 585–7

[36] Hu X *et al* 2005 Electrocatalytic hydrogen evolution by cobalt difluoroboryl–diglyoximate complexes *Chem. Commun.* 4723–5

[37] Bard A J and Faulkner L R 2000 *Electrochemical Method: Fundamentals and Applications* 2nd edn (New York: Wiley)

[38] Bard A J, Parsons R and Jordan J 1985 *Standard Potentials in Aqueous Solution* (New York: International Union of Pure and Applied Chemistry)

[39] Memming R 2001 *Semiconductor Electrochemistry* (Weinheim: Wiley–VCH)

Reproduced with permission from Journal of American Chemical Society, vol.132, pp.15465 (2010) Copyright 2010 American Chemical Society.

Nanoscale, vol. 4, pp. 1515 (2012) - Reproduced by permission of The Royal Society of Chemistry.

Nanotechnology, vol.23, no.19, pp.194013 (2012) - Reproduced by permission of Institute of Physics Publishing.

CHAPTER 3

3.1 Abstract

To maximize the photocurrent from Si, a coating which functions as a protection layer, a hole conducting layer, and a catalyst layer is needed. In this chapter, I will introduce three strategies that have been explored based on p-type nickel oxide (NiO). The first work published on the Journal of Energy and Environmental Science is based on a sol-gel NiO directly coated on polished n-type Si. Highly transparent non-stoichiometric NiO (NiO_x) was able to allow maximized light absorption at Si. p-type nature of the NiOx was able to provide a Schottky junction to effectively separate the charges up on illumination. Meanwhile, this coating effectively catalyzed the oxygen evolution reaction (OER). Finally, this coating successfully protected the Si from photooxidation. The second work published on the Nano Letters presents some improvement to the previous one, where a $NiRuO_x$ nanocomposite was synthesized using co-sputtering technique. This composite effectively reduced the ohmic loss in the NiO_x layer and further improved its OER catalytic activity. We also introduced a nanotextured Si to improve the light absorption and enhance the chemical reaction sites. The OER current density under illumination has been greatly improved. Lastly, the work presented in the last attached manuscript is based on a study of solution-casted NiO_x from thermal-decomposition of a nickel containing precursor which resulted an ultrathin NiO_x catalyst. The effect from the addition of a non-ionic surfactant and the thermal treatment process is studied. This coating was then synthesized on a surface inverted n-type Si (np^+-Si) photoanode. A novel semitransparent conducting oxide coating was used to effectively protect the Si substrate, to isolate the photovoltaics cells from the electrocatalyst reaction, and also to provide activation contact for the NiO_x. We finally demonstrated a further improved photoanodic performance.

View Article Online / Journal Homepage / Table of Contents for this issue
Dynamic Article Links

Energy &
Environmental Science

Cite this: *Energy Environ. Sci.*, 2012, **5**, 7872

www.rsc.org/ees

COMMUNICATION

Nickel oxide functionalized silicon for efficient photo-oxidation of water†

Ke Sun,[a] Namseok Park,[a] Zhelin Sun,[a] Jigang Zhou,[b] Jian Wang,[b] Xiaolu Pang,[c] Shaohua Shen,[d] Sun Young Noh,[e] Yi Jing,[a] Sungho Jin,[e] Paul K. L. Yu[a] and Deli Wang*[aef]

Received 21st March 2012, Accepted 17th April 2012
DOI: 10.1039/c2ee21708b

We report a nickel oxide (NiO_x) thin film, from a cost-effective sol–gel process, coated n-type silicon (n-Si) as a photoanode for efficient photo-oxidation of water under neutral pH condition. The NiO_x thin film has three functions: (i) serves as a protection layer to improve the chemical stability of the Si photoelectrode, (ii) acts as an oxygen evolution catalyst, and (iii) provides junction photovoltage to further reduce overpotential. The oxygen evolution onset potential is reduced to below the thermodynamic water oxidation level and oxygen evolution was observed at low overpotentials. Our results demonstrate the fabrication of robust photoelectrodes from low-cost NiO_x and Si, which enable a practical solar water oxidation with high efficiency.

Traditional hydrocarbon-based energy sources emit large amount of green-house gases to the atmosphere and have caused serious environmental issues. Converting and storing solar energy has great potential to address these problems.[1] Artificial photosynthesis (AP) mimics photosynthesis by using solar energy to drive a water oxidation reaction and to produce free electrons which consequently generate hydrogen[2] or carbohydrate with CO_2 participation.[3] One viable approach to AP is *via* inorganic semiconductor photo-electrochemistry, where semiconductor photoelectrodes harvest solar energy, generate photocarriers (electrons and holes), and then conduct electrochemical reactions at semiconductor–electrolyte interfaces. This creates a huge potential to produce sustainable energy and to reduce CO_2 emission[4] with a minimum number of energy conversion steps and thus offers a theoretically higher efficiency.[5] A major challenge with this particular approach for AP is to engineer and manufacture efficient photoelectrodes and catalysts from stable, non-toxic, and low cost materials to meet the global energy demand.

Silicon is an attractive candidate for photovoltaic applications in terms of moderate energy band-gap and great abundance on earth.[6] However, one of the problems with Si for photoelectrochemical (PEC) cell applications is that an insulating oxide film rapidly forms on the surface in aqueous solutions under either working or idle condition and thus the Si photoelectrode becomes immediately disabled from the oxide passivation. Approaches for this purpose include coating the Si surface with organic polymers,[7,8] derivatives,[9–11] metals or silicides,[12–14] wide band-gap semiconductors,[15,16] and/or selecting proper electrolytes.[17–20]

Besides the unfavourable thermodynamics discussed above, the other critical problem with the n-Si photoanode is associated with the kinetics of the competing carrier recombination. This results in the high overpotential loss; thus a high anodic bias is needed to drive the water oxidation process/oxygen evolution reaction (OER). In general, research focused on using the n-Si photoanode by means of altering charge transfer kinetics at the semiconductor–liquid interface to improve the current efficiency for the net water oxidation while

Broader context

Silicon is a very attractive photovoltaic material for efficient solar energy harvesting and has been broadly used for solar cells. However, it is not chemically robust enough for practical photolysis or solar water splitting applications. Herein, we report nickel oxide coated silicon as a highly efficient photoelectrode for water oxidation. The reported electrode offers improved oxidation overpotential from p/n junction formation, catalyzed oxygen evolution, and prolonged operation lifetime. Moreover, the heterogeneous photoelectrode uses cheap and earth abundant materials, employs low cost and scalable processes, and is potentially practical for solar hydrogen production.

---

[a] *Department of Electrical and Computer Engineering, University of California, San Diego, 9500 Gilman Dr., La Jolla, California 92093, USA. E-mail: deliwang@eng.ucsd.edu; Tel: +1 858-822-4629*
[b] *Canadian Light Source Inc., Saskatoon, Saskatchewan S7N0X4, Canada*
[c] *Department of Materials Physics and Chemistry, University of Science and Technology Beijing, Beijing 100083, China*
[d] *State Key Lab of Multiphase Flow in Power Engineering, Xi'an Jiaotong University, Xi'an, Shaanxi 710049, China*
[e] *Material Science Program, University of California, San Diego, 9500 Gilman Dr., La Jolla, California 92093, USA*
[f] *California Institute of Telecommunication and Information Technology, University of California, San Diego, 9500 Gilman Dr., La Jolla, California 92093, USA*

† Electronic supplementary information (ESI) available: Film deposition conditions, device fabrication, optical transmittance measurement, compositional measurement, setup attenuation coefficient measurement, PEC measurement setup, TiO_2 degradation, additional cyclic voltammetric data and two electrode linear scan data, and long term stability data. See DOI: 10.1039/c2ee21708b

limiting the anodic decomposition current. To make OER as well as the hydrogen evolution reaction (HER) as facile as possible, electrocatalysts have been broadly studied theoretically and experimentally.[21,22] Widely reported OER catalysts in the form of organic molecular, metal particles, or inorganic oxides normally contain transition metals of high electrochemical activity such as Mn,[23] Co[24] and Ru/Ir.[25] On the other hand, non-stoichiometric nickel oxide (NiO_x) is considered as one of the best OER electrocatalysts.[26] Although with higher overpotential than RuO_2 and IrO_2,[27] an NiO_x based electrocatalyst is more abundant and thus cost-effective (Ni is the 9th most abundant element in the earth's crust). Moreover, NiO_x has a wide band-gap and is one of the very few stable and p-type transition metal oxides.[28]

In this communication, we report the use of an inexpensive sol–gel NiO_x thin film coated n-Si photoanode for photo-oxidation of water operated under neutral pH condition. The NiO_x thin film has three functions – it protects Si from direct contact with aqueous solution and thus prevents severe anodic decomposition of Si during PEC operation. It serves as an OER electrocatalyst and provides junction photovoltage, both of which assist in the improvement of surface kinetics, reduction of the oxygen evolution onset potential, and therefore improvement of the overall water oxidation efficiency.

The NiO_x film was prepared using a previously reported sol–gel method[29,30] and subsequently dried in air at 300 °C afterwards (see ESI†). Further annealing at 400 °C in an inert environment was conducted to improve the crystallinity. Fig. 1a shows the typical scanning electron microscope (SEM) images with the cross-sectional view and 75° angle view of an annealed NiO_x film on n-Si. Both the as-prepared and annealed films were very uniform and crack-free (Fig. S1†). An atomic force microscopy (AFM) study on the annealed film revealed a root mean square-RMS surface roughness of 1.07 nm, indicating a very smooth surface. The annealed NiO_x film with a thickness of 37.4 nm showed >90% transmittance at a wavelength of 600 nm, indicating a very transparent coating (Fig. S2†). In addition, the annealed NiO_x film also showed a decreased refractive index (1.74 measured at a wavelength of 632.8 nm). Therefore, the NiO_x film also served partially as an anti-reflection coating on planar Si allowing minimized optical loss in the NiO_x film as well as at the interfaces.

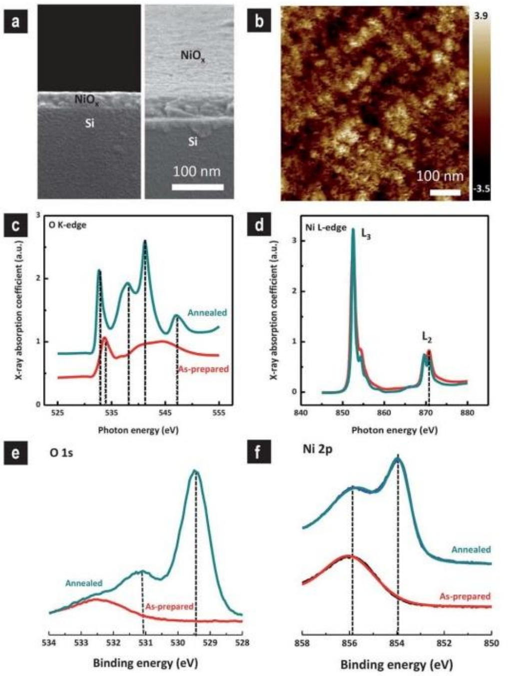

Fig. 1 (a) SEM images of the n-Si|NiO_x photoelectrode with a cross-sectional view (left) and 75 degree tilted view (right), (b) AFM image of the annealed NiO_x surface. XANES total electron yield spectra of O K-edge (c) and Ni L-edge (d) and XPS spectra of O 1s (e) and Ni 2p (f).

The energy-dispersive X-ray spectroscopy (EDXS) analysis showed an oxygen rich composition in the annealed NiO_x film. The films were further characterized using the X-ray absorption near edge spectroscopy (XANES) and X-ray photoelectron spectroscopy (XPS) (see ESI†). O K-edge absorption in the photon energy range of 535–550 eV in the XANES study corresponds to O 2p state hybridized with Ni 4sp state,[31] or the multiple scattering states.[32] The distinguished peaks resolved from the broad peak in the as-prepared film suggested a film with an improved crystallinity by thermal annealing (Fig. 1c). Moreover, the peak at ~532 eV to ~533 eV indicated a transition to O 2p state hybridized with Ni 3d state.[31] Relative peak intensity and peak shape of the transition to O 2p/Ni 3d states reflected the Ni–O covalence, *i.e.* an intensive peak could mean stronger Ni 3d/O 2p hybridization (stronger covalence). Therefore the relatively reduced peak intensity and sharpened peak profile in the annealed film hinted at a more ionic Ni–O bonding,[33] which also shifts the O K-edge threshold negatively. The Ni L-edge spectra (Fig. 1d) showed that the Ni^{2+} oxidation dominated in both samples and an increase of peak ratio of 852.5 eV over 854.4 eV at the L_3 edge of the annealed sample clearly indicated a reduced oxidation state by annealing in an inert environment.[34]

Fig. 1e shows the O 1s spectrum of the as-prepared and annealed NiO_x films. The broad peak at 532.5 eV was the only peak resolved from as-prepared sol–gel NiO_x film, probably due to C–O bonding of the residual organic species in the sol–gel film. This broad peak diminished during the annealing process. The peaks at 529.5 and 531.2 eV indicated the presence of Ni^{2+} and Ni^{3+} in the annealed film, respectively. The peak intensity ratio suggested a Ni^{2+} rich film. Analysis of the main peak of Ni $2p_{3/2}$ photoelectron spectra (854.0 eV) and satellite of the as-prepared and annealed NiO_x films provided semi-quantitative evidence of the degree of non-stoichiometry (Fig. 1f). Satellite intensity (855.9 eV) dropped while the main peak (854.0 eV) intensity increased from the annealed NiO_x film suggesting a reduction in Ni^{3+} concentration, which strongly supports the XANES and EDXS results. Further Ar^+ plasma depth profiling showed an increased intensity at a new peak (852.6 eV) due to the partial reduction of the film (not shown), which was also strongly dependant on the Ni^{3+} concentration.[35] In addition, an XPS depth profiling study revealed the reduced oxygen concentration from surface (Ni : O = 1 : 1.41) to bulk (Ni : O = 1 : 1.15), which was believed to originate from the adsorption of oxygen mainly at the surface.

Fig. 2 shows a cyclic voltammetry (CV) measurement (Fig. S3†) comparison of various well-accepted metal oxide protected n-Si photoanodes in a PBS buffered 0.25 M Na_2SO_4 electrolyte

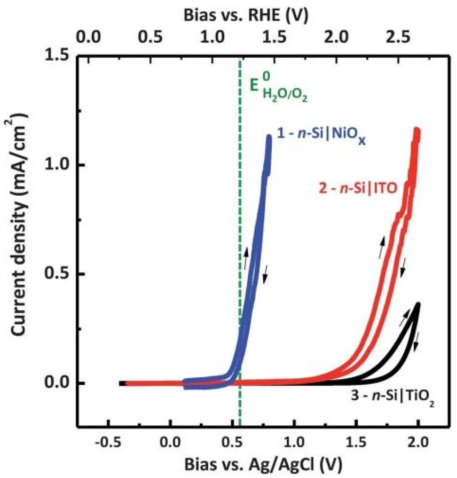

Fig. 2 CV characteristics of Si photoelectrodes with different coatings, including TiO_2, ITO, and NiO_x under 100 mW cm^{-2} illumination. All the voltammetrics were scanned at 10 mV s^{-1} at room temperature.

(pH = 7.2) including titanium dioxide (TiO_2) and tin-doped indium oxide (ITO), together with proposed NiO_x which represent three typical material selection strategies in n-Si based heterojunction photoanodes. Although all three are intrinsically wide band-gap, they show distinguished optoelectrical and electrochemical properties. TiO_2 is a well-known ultra-violet (UV) sensitive photocatalyst exhibiting n-type conduction, while ITO is non-photosensitive but highly conductive. NiO_x, on the other hand, is a non-photosensitive p-type electrocatalyst. Differences between these strategies are compared and discussed in detail below. n-Si|NiO_x (curve 1) showed the lowest onset potential ($V_{\text{ph-onset}}$) in the CV studies, which is defined as the potential where photocurrent density is higher than 0.1 mA cm^{-2} under 100 mW cm^{-2} illumination. This value of 0.52 V was lower than that of the photoelectrodes with ITO coatings by RF sputtering and ultrathin TiO_2 by atomic layer deposition (ALD, see ESI†). Moreover, the $V_{\text{ph-onset}}$ of n-Si|NiO_x was even below the thermodynamic oxidation level of water (E_{H_2O/O_2}, green dashed line). Indeed, oxygen bubbles were observed to form on the surface at a low overpotential (132 mV). Furthermore, the n-Si|NiO_x photoelectrode showed a much sharper turn-on of photocurrent compared to the samples coated by ITO and TiO_2 (curves 2 and 3) and a minimum difference between forward and backward scans suggesting a greater stability of the NiO_x protected Si. Curve 3 in Fig. 2 shows the CV scan of the n-Si photoanode protected by TiO_2 coating, which is a well-accepted passivation layer.[36] The n-Si|TiO_2 electrode showed the highest $V_{\text{ph-onset}}$ of 1.646 V and lowest current density. The TiO_2 layer was deposited using ALD for 50 cycles and was about 2.5 nm in thickness. The purpose of the ultrathin TiO_2 layer was to minimize the strong photocatalytic effect from TiO_2 while the photogenerated carriers from Si and Si–TiO_2 interface can tunnel through. A detailed study showed that an increase of TiO_2 thickness (from 2.5 to 75.5 nm) resulted in an increase of photoanodic current from TiO_2, which changed the tunnelling current to recombination-limited current.[37] Curve 3 also showed an irreversible reaction in the n-Si|TiO_2 system. This is presumably due to the non-optimized ALD growth condition in our system, caused by trapped Cl atoms in the film.[38] Consecutive multiple linear scans with a minimum stabilization time of 20 min between each scan and a long term stability scan at fixed external bias were collected (Fig. S4†). Current density at anodic bias (2 V) dropped from 0.3 to 0.07 mA cm^{-2}. This current degradation could be explained by the existence of pinholes providing pathways for Si oxidation in the presence of water. Most importantly, an ultrathin TiO_2 coating does not change the surface kinetics for charge transfer; therefore a large overpotential is still needed to drive a significant oxygen evolution current. In addition, as-grown TiO_2 showed high resistivity, which potentially causes the accumulation of holes at the interface and reduces current level.

Curve 2 (n-Si|ITO) in Fig. 2 shows overall higher photocurrent density in the same bias range and lower $V_{\text{ph-onset}}$ (1.454 V) compared to curve 3 (n-Si|TiO_2). Hall measurement revealed that the annealed ITO showed resistivity of as low as 5.9×10^{-4} Ω cm (carrier concentration 4.09×10^{20} cm^{-3} and Hall mobility 23.4 cm^2 V^{-1} s^{-1}). The high conductivity of ITO coating facilitated the hole transportation and removed photogenerated holes rapidly from the Si surface to the water,[16] which is one of the major reasons for the improved photocurrents. ITO protected n-/p-Si photoelectrodes were studied before,[39] and chemical stability of ITO is still a concern (Fig. S4†), which is related to the grained structure and chemical composition of ITO, as well as the bias polarity and pH environment.

Compared to ultrathin TiO_2 coating and conductive ITO coating, the coating of NiO_x to the n-Si photoanode has different electron transfer process at the interface. The mechanism of the NiO_x catalytic effect is summarized in a reversible process below:[40]

$$\mathrm{Si} \xrightarrow{h\nu} \mathrm{h}^+ + \mathrm{e}^- \tag{1}$$

$$\mathrm{Ni(II/III)} + \mathrm{H_2O} + \mathrm{h^+} \rightarrow \mathrm{Ni(II/III)(OH)} + \mathrm{H^+} \tag{2}$$

$$2\mathrm{Ni(II/III)(OH)} \rightarrow \mathrm{Ni(II/III)(O)} + \mathrm{Ni(II/III)} + \mathrm{H_2O} \tag{3}$$

$$2\mathrm{Ni(II/III)(O)} \rightarrow 2\mathrm{Ni(II/III)} + \mathrm{O_2}\uparrow \tag{4}$$

where Ni(II/III) in the equation above is the divalent or trivalent active site of Ni at the surface. Photogenerated free electrons in Si (eqn (1)) are blocked by a high conduction band barrier at the Si–NiO_x junction and flow to the back-contact. Holes, on the other hand, drift across the junction by the built-in field and participate in a series of surface reactions (eqn (2)) at potentials significantly lower than the water oxidation potential. Interstitial O and higher state Ni ions (Ni^{3+}) exist in NiO_x and Ni^{3+} ions act as acceptors leading to the p-type conductivity,[41] as well as OER catalytic centres.[42,43] The catalytic performance of the photoelectrodes was also investigated using a Tafel plot[44] extracted from the voltammetric scan (Fig. S5†), where one can see the greatly reduced overpotential as well as the reduced Tafel slope by switching ITO (n-Si|ITO blue ▲) to NiO_x (n-Si|NiO_x black ■). To further evaluate the catalytic effect of the NiO_x thin film, we performed a comparative study on NiO_x and Ir coatings. Ir is in the same transition metal group with Pt and is broadly used in catalysis, which is also the best corrosion-resistant metal. In our study, an ultrathin Ir layer (2–3 nm), with small grain sizes and a high transmittance, was sputtered on n-Si|ITO and n-Si|NiO_x photoelectrodes. Fig. 3a shows that n-Si|ITO|Ir (dark cyan ▼) had lower overpotential compared to that of n-Si|ITO|NiO_x

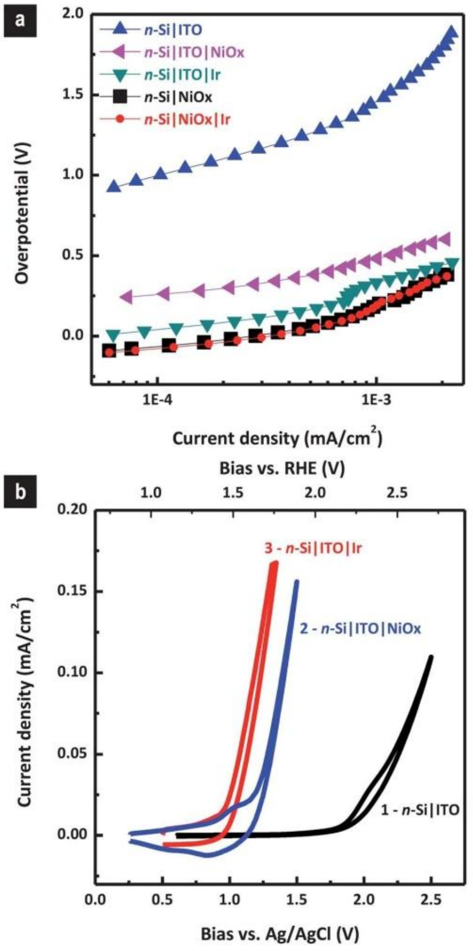

Fig. 3 (a) Comparison of the Tafel plot of n-Si|ITO, n-Si|NiO$_x$, n-Si|ITO|Ir, and n-Si|NiO$_x$|Ir under illumination at 100 mW cm^{-2}, and (b) comparison of voltammetric behavior of samples showing dark catalytic properties of NiO$_x$ and Ir coated n-Si|ITO sample.

(magenta ◄), which is consistent with previously reported results.[27] However, the n-Si|NiO$_x$|Ir (red ●) photoelectrode showed minuscule improvement with respect to n-Si|NiO$_x$. The lowest Tafel slope from the best of device was 129 mV per decade, which is close to the generally accepted 120 mV per decade on high surface area catalysts.[25] This value is considerably large compared to the previously reported best NiO$_x$ electrocatalysts,[45] presumably due to the limited mass transport,[46] the high resistivity of the NiO$_x$ film, as well as the low concentration of Ni^{3+} in annealed film.

The electrocatalytic effect of NiO$_x$ and Ir can be further identified by electrolysis in the dark (Fig. 3b). One can observe that due to the metallic nature of ITO and change of interface energetics by adding ITO between the electrolyte and Si, the dark electrolysis current of n-Si|ITO exponentially increased after an anodic bias of 2 V (curve 1) with an actual $V_{\text{ph-onset}}$ at 2.46 V. NiO$_x$ and Ir coating on n-Si|ITO showed clear dark catalysis (curve 2 and 3) with $V_{\text{ph-onset}}$ of 1.39 V and 1.18 V, respectively. This was due to the intrinsically higher catalytic activity of Ir compared to NiO$_x$. Anodic waves prior to the oxygen evolution current (curve 2) are due to oxidation and regeneration of Ni^{3+} ions.[47]

In order to isolate the catalytic effect from the photovoltage effect in the n-Si|p-NiO PEC electrode, we also characterized the NiO$_x$ coating on n-Si|ITO whose overpotential and Tafel slope, interestingly, fall between that of n-Si|ITO and n-Si|NiO$_x$. The n-Si|ITO|NiO$_x$ showed a reduced overpotential and Tafel slope compared to that of n-Si|ITO and demonstrated the catalytic effect of NiO$_x$, while increased values compared to that of n-Si|NiO$_x$ indicated an additional effect from the p-NiO$_x$–n-Si junction owing to the junction photovoltage. Rectifying *I–V* behaviour in the dark indicated a solid-state p–n junction between p-NiO$_x$ and n-Si (Fig. S6†). The solid state n-Si|p-NiO$_x$ heterojunction photovoltaic devices showed an open circuit voltage (V_{oc}) of 300 mV under 100 mW cm^{-2} solar irradiation, which could further reduce the overpotential needed. A similar idea using photovoltage to reduce overpotential was demonstrated earlier.[48] The p-NiO$_x$–n-Si junction facilitated the separation of photo-induced charge carriers under the built-in electric field and p-NiO$_x$ also served as a hole transporter and electron blocking layer[43,49] minimizing the leakage and dark current. However, we were not able to obtain the conductivity of NiO$_x$ film presumably due to the small hole mobility.[50] The non-optimized conductivity of the film was believed to be one of the limiting factors to the low photocurrent density.[51]

The applied bias solar conversion efficiency (ABCE) was calculated using eqn (3),

$$\eta(\%) = \frac{100J\left(E^0_{\mathrm{H_2O/O_2}} - V_{\mathrm{app}}\right)}{(1-\alpha)P} \tag{5}$$

where J is the current density (mA cm^{-2}), V_{app} is the applied electrode bias (V *vs.* Pt counter electrode), E is the Nernst potential for water oxidation (V *vs.* Ag/AgCl 1 M KCl at pH = 7.2), P is the incident optical power density (100 mW cm^{-2} in all the measurement), and α is the integrated optical attenuation coefficient introduced by the measurement setup (Fig. S7†). In order to take into account the ohmic losses and overpotential losses at the counter electrode, we used a two-electrode setup for this calculation[25] (Fig. S8†). Together with the aforementioned CV results, performances of various n-Si photoanode-based structures are summarized in Table 1. Power conversion efficiency was calculated at an additional overpotential of 432 mV to the water oxidation level (1 V of applied bias *vs.* Pt counter electrode). The n-Si|NiO$_x$ photoelectrodes showed 1.34% overall conversion efficiency, which is orders of magnitude higher than that of n-Si|ITO or n-Si|TiO$_2$ photoelectrodes. It is also much larger than the conversion efficiency of n-Si|ITO|NiO$_x$ (0.30%). Coating catalytic Ir thin film on n-Si|NiO$_x$ and n-Si|ITO photoelectrodes showed increase of conversion efficiency to 1.37% and 0.33%, respectively.

No noticeable changes or damages on the NiO$_x$ surface were observed after the CV study in PEC measurements, indicating the chemical and mechanical robustness. The ability of forming a uniform and robust thin film is one of the most critical merits for a photoanode protection layer. Although the photoelectrode was still able to provide efficient water oxidation current after 4 h of

Table 1 Summary of photoelectrode performance

Electrode (thickness in nm)	$V_{\text{ph-onset}} - E_{H_2O/O_2}$ (V)[a]	Tafel slope (mV per decade)	ABCE (% at 1 V)
n-Si|TiO_2(2.5)	1.078		$6.5 \times 10^{\ 4}$
n-Si|ITO(29.3)	0.886	385	$8.6 \times 10^{\ 3}$
n-Si|NiO_x(37.4)	−0.048	129	1.34
n-Si|ITO(29.3)|NiO_x(37.4)	0.316	129	0.30
n-Si|ITO(29.3)|Ir	0.067	129	0.33
n-Si|NiO_x(37.4)|Ir	−0.066	129	1.37
n-Si|TiO_2(2)|Ir[36]	−0.298		

[a] E_{H_2O/O_2} at pH = 7.2 is 0.568 V at room temperature, which was calculated based on E_{H_2O/O_2} (*vs.* SHE) = 1.229 − 0.059 × pH and also considering the potential difference using E (*vs.* SHE) = E (*vs.* Ag/AgCl 1 M KCl) + $E_{Ag/AgCl}$ (*vs.* SHE). In this equation, $E_{Ag/AgCl}$ (*vs.* SHE) = 0.236 V.[44] Tafel slopes were measured across the onset potential region (0.1 1 mA $cm^{\ 2}$).

intermittent operation over 3 days (Fig. S9†), the n-Si|NiO_x photoelectrode showed current degradation over time. Possible reasons included deactivation of NiO_x, limited diffusion of hydroxide, and deconstructive high current density. These possibilities are currently under investigation through various approaches.

Conclusions

Sol–gel NiO_x functionalized Si photoanodes were studied for high efficiency water photo-oxidation. n-Si|NiO_x shows a negative-shifted onset potential to about 1.18 V (*vs.* RHE), which is lower than that of other metal oxide coatings and is below the thermodynamic water oxidation level. Catalytic effects of the photoelectrodes are investigated and demonstrated using Tafel plots from comparisons of various systems under illumination and in the dark. The n-Si|NiO_x photoelectrode shows 1.34% overall conversion efficiency, which is more than 4.5 times larger than that of n-Si|ITO|NiO_x and orders of magnitude higher than that of the n-Si|ITO or n-Si|TiO_2 photoelectrode. A minimum difference between forward and backward scans is observed from the NiO_x coated electrode indicating a greater electrochemical stability. The sol–gel based approach is cost-effective and does not require any high-profile equipment for film deposition. The highly transparent NiO_x film from this technique also minimizes the light loss. These results enable a stable, low-cost and protective electrocatalyst made of an earth abundant element[52] and its coating to n-Si. This structure offers a potential solution to scalable and mass-producible low cost photoelectrochemical cells for practical clean hydrogen fuel production and artificial photosynthesis.

Acknowledgements

DW acknowledges the financial support from DOE (DE-FG36-08G018016) and NSF (ARRA ECCS0901113). DW also acknowledges the ONR-DURIP (N00014-08-1-0776) support for the ALD acquisition. The authors also acknowledge Drs B. Fruhberger and X. Lu (NANO3 facility, UCSD) for their support with ALD, X. Zhang (Changchun Inst. Appl. Chem., Chinese Academy of Sciences), K. Madsen (UCSD), P. Anderson (Norwegian Univ. of Sci. and Tech.), C. Riley (UCSD) and W. Bao (Fudan Univ. China) for their help in fabrication of PEC apparatus and modification of measurement setup, and W. Chen (UCSD) for her help with Hall measurement.

Notes and references

1 J. A. Turner, *Science*, 2004, **305**, 972 974.
2 A. J. Bard and M. A. Fox, *Acc. Chem. Res.*, 1995, **28**, 141 145.
3 E. E. Barton, D. M. Rampulla and A. B. Bocarsly, *J. Am. Chem. Soc.*, 2008, **130**, 6342 6344.
4 E. E. Benson, C. P. Kubiak, A. J. Sathrum and J. M. Smieja, *Chem. Soc. Rev.*, 2009, **38**, 89 99.
5 R. E. Blankenship, D. M. Tiede, J. Barber, G. W. Brudvig, G. Fleming, M. Ghirardi, M. R. Gunner, W. Junge, D. M. Kramer, A. Melis, T. A. Moore, C. C. Moser, D. G. Nocera, A. J. Nozik, D. R. Ort, W. W. Parson, R. C. Prince and R. T. Sayre, *Science*, 2011, **332**, 805 809.
6 K. Sun, Y. Jing, C. Li, X. Zhang, R. Aguinaldo, A. Kargar, K. Madsen, K. Banu, Y. Zhou, Y. Bando, Z. Liu and D. Wang, *Nanoscale*, 2012, **4**, 1515 1521.
7 M. D. Rosenblum and N. S. Lewis, *J. Phys. Chem.*, 1984, **88**, 3103 3107.
8 R. Noufi, A. J. Frank and A. J. Nozik, *J. Am. Chem. Soc.*, 1981, **103**, 1849 1850.
9 M. S. Wrighton, R. G. Austin, A. B. Bocarsly, J. M. Bolts, O. Haas, K. D. Legg, L. Nadjo and M. C. Palazzoto, *J. Am. Chem. Soc.*, 1978, **100**, 1602 1603.
10 J. M. Bolts, A. B. Bocarsly, M. C. Palazzotto, E. G. Walton, N. S. Lewis and M. S. Wrighton, *J. Am. Chem. Soc.*, 1979, **101**, 1378 1385.
11 P. Leempoel, M. Castro-Acuna, F.-R. F. Fan and A. J. Bard, *J. Phys. Chem.*, 1982, **86**, 1396 1400.
12 Y. Nakato, T. Ohnishi and H. Tsubomura, *Chem. Lett.*, 1975, **4**, 883 886.
13 F. R. F. Fan, G. A. Hope and A. J. Bard, *J. Electrochem. Soc.*, 1982, **129**, 1647 1649.
14 F. R. F. Fan, R. G. Keil and A. J. Bard, *J. Am. Chem. Soc.*, 1983, **105**, 220 224.
15 P. A. Kohl, S. N. Frank and A. J. Bard, *J. Electrochem. Soc.*, 1977, **124**, 225 229.
16 L. Thompson, J. DuBow and K. Rajeshwar, *J. Electrochem. Soc.*, 1982, **129**, 1934 1935.
17 D. R. Turner, *J. Electrochem. Soc.*, 1960, **107**, 810 816.
18 G. Yuan, K. Aruda, S. Zhou, A. Levine, J. Xie and D. Wang, *Angew. Chem., Int. Ed.*, 2011, **50**, 2334 2338.
19 M. Matsumura and S. R. Morrison, *J. Electroanal. Chem.*, 1983, **144**, 113 120.
20 E. A. Santori, J. R. Maiolo, M. J. Bierman, N. C. Strandwitz, M. D. Kelzenberg, B. S. Brunschwig, J. H. A. Atwater and N. Lewis, *Energy Environ. Sci.*, 2012, **5**, 6867 6871.
21 Y. Gorlin and T. F. Jaramillo, *J. Am. Chem. Soc.*, 2010, **132**, 13612 13614.
22 J. Greeley, T. F. Jaramillo, J. Bonde, I. Chorkendorff and J. K. Norskov, *Nat. Mater.*, 2006, **5**, 909 913.
23 I. Zaharieva and H. Dau, *Energy Environ. Sci.*, 2012, **5**, 7081 7089.
24 E. R. Young, R. Costi, S. Paydavosi, D. G. Nocera and V. Bulovic, *Energy Environ. Sci.*, 2011, **4**, 2058 2061.
25 M. G. Walter, E. L. Warren, J. R. McKone, S. W. Boettcher, Q. Mi, E. A. Santori and N. S. Lewis, *Chem. Rev.*, 2010, **110**, 6446 6473.
26 E. L. Miller and R. E. Rocheleau, *J. Electrochem. Soc.*, 1997, **144**, 1995 2003.
27 Y. Matsumoto and E. Sato, *Mater. Chem. Phys.*, 1986, **14**, 397 426.
28 D. Adler and J. Feinleib, *Phys. Rev. B: Solid State*, 1970, **2**, 3112 3134.
29 J. L. Garcia-Miquel, Q. Zhang, S. J. Allen, A. Rougier, A. Blyr, H. O. Davies, A. C. Jones, T. J. Leedham, P. A. Williams and S. A. Impey, *Thin Solid Films*, 2003, **424**, 165 170.
30 P. A. Williams, A. C. Jones, J. F. Bickley, A. Steiner, H. O. Davies, T. J. Leedham, S. A. Impey, J. Garcia, S. Allen, A. Rougier and A. Blyr, *J. Mater. Chem.*, 2001, **11**, 2329 2334.
31 W.-S. Yoon, K. Y. Chung, J. McBreen, D. A. Fischer and X.-Q. Yang, *J. Power Sources*, 2006, **163**, 234 237.
32 Z. Y. Wu, C. M. Liu, L. Guo, R. Hu, M. I. Abbas, T. D. Hu and H. B. Xu, *J. Phys. Chem. B*, 2005, **109**, 2512 2515.
33 F. M. F. de Groot, M. Grioni, J. C. Fuggle, J. Ghijsen, G. A. Sawatzky and H. Petersen, *Phys. Rev. B*, 1989, **40**, 5715 5723.
34 H. Wang, P. Ge, C. G. Riordan, S. Brooker, C. G. Woomer, T. Collins, C. A. Melendres, O. Graudejus, N. Bartlett and S. P. Cramer, *J. Phys. Chem. B*, 1998, **102**, 8343 8346.

35 A. R. Gonzalez-Elipe, J. P. Holgado, R. Alvarez and G. Munuera, *J. Phys. Chem.*, 1992, **96**, 3080 3086.

36 Y. W. Chen, J. D. Prange, S. Dühnen, Y. Park, M. Gunji, C. E. D. Chidsey and P. C. McIntyre, *Nat. Mater.*, 2011, **10**, 539 544.

37 J. Shi, Y. Hara, C. Sun, M. A. Anderson and X. Wang, *Nano Lett.*, 2011, **11**, 3413 3419.

38 C. B. Musgrave and R. G. Gordon, *Future Fab Intl.*, 2005, **18**, 126 128.

39 G. Hodes, L. Thompson, J. DuBow and K. Rajeshwar, *J. Am. Chem. Soc.*, 1983, **105**, 324 330.

40 J. O. M. Bockris, *J. Chem. Phys.*, 1956, **24**, 817 827.

41 P. Lunkenheimer, A. Loidl, C. R. Ottermann and K. Bange, *Phys. Rev. B: Condens. Matter*, 1991, **44**, 5927 5930.

42 K. Schultze and H. Bartelt, *Int. J. Hydrogen Energy*, 1992, **17**, 711 718.

43 E. L. Ratcliff, J. Meyer, K. X. Steirer, A. Garcia, J. J. Berry, D. S. Ginley, D. C. Olson, A. Kahn and N. R. Armstrong, *Chem. Mater.*, 2011, **23**, 4988 5000.

44 A. J. Bard and L. R. Faulkner, *Electrochemical Method: Fundamentals and Applications*, Wiley, 2000.

45 M. H. Miles, Y. H. Huang and S. Srinivasan, *J. Electrochem. Soc.*, 1978, **125**, 1931 1934.

46 D. W. Banham, J. N. Soderberg and V. I. Birss, *J. Phys. Chem. C*, 2009, **113**, 10103 10111.

47 D. Yohe, A. Riga, R. Greef and E. Yeager, *Electrochim. Acta*, 1968, **13**, 1351 1358.

48 J. J. H. Pijpers, M. T. Winkler, Y. Surendranath, T. Buonassisi and D. G. Nocera, *Proc. Natl. Acad. Sci. U. S. A.*, 2011, **108**, 10056 10061.

49 M. D. Irwin, D. B. Buchholz, A. W. Hains, R. P. H. Chang and T. J. Marks, *Proc. Natl. Acad. Sci. U. S. A.*, 2008, **105**, 2783 2787.

50 F. J. Morin, *Phys. Rev.*, 1954, **93**, 1199 1204.

51 K. Jun, Y. S. Lee, T. Buonassisi and J. M. Jacobson, *Angew. Chem., Int. Ed.*, 2012, **51**, 423 427.

52 P. Du and R. Eisenberg, *Energy Environ. Sci.*, 2012, **5**, 6012 6021.

NANO LETTERS
Letter
pubs.acs.org/NanoLett

Metal Oxide Composite Enabled Nanotextured Si Photoanode for Efficient Solar Driven Water Oxidation

Ke Sun,[†] Xiaolu Pang,[‡] Shaohua Shen,[§] Xueqiang Qian,[‡] Justin S. Cheung,[†] and Deli Wang*,[†,‖,⊥]

[†]Department of Electrical and Computer Engineering, University of California, San Diego, La Jolla, California 92093, United States
[‡]Department of Materials Physics and Chemistry, University of Science and Technology Beijing, Beijing 100083, China
[§]State Key Laboratory of Multiphase Flow in Power Engineering, Xi'an Jiaotong University, Xi'an, Shaanxi 710049, China
[‖]Material Science Program and [⊥]California Institute of Telecommunication and Information Technology, University of California, San Diego, 9500 Gilman Drive, La Jolla, California 92093, United States

Supporting Information

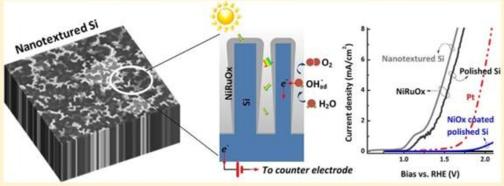

ABSTRACT: We present a study of a transition metal oxide composite modified n-Si photoanode for efficient and stable water oxidation. This sputter-coated composite functions as a protective coating to prevent Si from photodecomposition, a Schottky heterojunction, a hole conducting layer for efficient charge separation and transportation, and an electrocatalyst to reduce the reaction overpotential. The formation of mixed-valence oxides composed of Ni and Ru effectively modifies the optical, electrical, and catalytic properties of the coating material, as well as the interfaces with Si. The successful application of this oxide composite on nanotextured Si demonstrates improved conversion efficiency due to enhanced catalytic activity, minimized reflection, and increased surface reaction sites. Although the coated nanotextured Si shows a noticeable degradation from 500 cycles of operation, the oxide composite provides a simple method to enable unstable photoanode materials for solar fuel conversion.

KEYWORDS: *Solar water oxidation, electrocatalyst, nanotextured Si*

An optical band gap of 1.12 eV makes Si, the second most earth abundant material, a very attractive candidate for solar fuel conversion. However, the fundamental photoelectrochemistry properties of Si, when in contact with aqueous solution, do not favor Si for solar water splitting, in which solar energy is typically converted and stored in chemical bonds. Thermodynamic oxidation potential of Si is above the water oxidation level, which introduces a competition reaction when operating with energetic holes.[1] This oxidation effectively passivates the Si, which also becomes a concern when p-Si photocathode is in idle condition[2] or has to go through a destructive subsequent coating process.[3] Moreover, having a significantly higher conduction band edge of Si to the proton reduction level results in a slow charge transfer kinetics. This fact limits the conversion efficiency of Si-based photoelectrode when directly interfacing with electrolyte. To replace this troublesome interface at the Si/electrolyte junction, a new conformal and rectifying junction is essential to suppress the self-oxidation and improve the kinetics.[4] Structures using homogeneous junctions through surface inversion have been utilized to solve aforementioned problems and have been demonstrated on both n and p-type Si photoelectrode.[5] On the other hand, strategies using heterogeneous coatings on Si photoelectrode have also been developed using molecule surface functionalization, metals, alloys, or other semiconductors.[6]

Theoretically, a rectifying junction relies on the work function difference between the coating material and Si. For n-Si, a coating with a high work function is essential to form a rectifying junction to separate the free charges. However, high work function metals such as Pt or Pd have inferior oxygen evolution reaction (OER) catalytic activity compared to Ir or Ru. Meanwhile, they are typically of high cost and limited resources, which are the main obstacles for large scale applications of noble metals in catalysis. In addition, noble metals are not stable in alkaline environment.[7] On the other hand, earth abundant transition metal oxides (such as Mn, Fe, Co, and Ni) show typically lower activity[8] but reasonable stability in alkaline environment. Furthermore, metal oxide outperforms metal because metal oxide can achieve a much higher work function than metals due to oxygen vacancies and cation oxidation states.[9] The work function of a transition metal oxide can be tuned through the incorporation of other metal or metal oxides. In addition, metal oxide can minimize the optical loss due to a typically larger optical band gap. Moreover, metal oxides with technically unlimited combinations are typically stable and nontoxic. Therefore, this stable metal oxide coating with a high work function and high transmittance is desired for

Received: January 27, 2013
Revised: March 15, 2013
Published: April 10, 2013

unstable n-type photoanode materials to form a Schottky barrier to assist the transportation of photoexcited holes to the reductant in the electrolyte and to maximize the amount of photons arriving at the underneath photoactive material.

From a design point of view for an optimized junction, a p-type coating with a higher hole-conductivity is essential. Ni oxide is intrinsically p-type and Ni-based oxides showed great potential. Doped or mixed nickel oxide is recognized as one of the promising OER catalyst that showed great stability in an alkaline environment.[10] Other applications of mixed-valence Ni oxide, such as supercapacitors,[11] batteries, fuel cells, and dye-sensitized solar cells,[12] were demonstrated because of its tunable functionalities. Ru oxide has been known as an excellent candidate for electrochemical capacitors due to its fast and reversible reduction/oxidation reactions from proton adsorption/desorption.[13] Meanwhile, Ru and its oxide are also known as the best OER catalysts. Applications of RuO$_x$ to improve the water oxidation reaction have been demonstrated before in some milestones solar driven water splitting devices.[14] Actually, the oxide composite (NiRuO$_x$) has also demonstrated applications as electrical contact,[15] pseudocapacitor electrode,[16] and OER catalyst.[7]

We hypothesize that (i) an oxide mixture of NiO$_x$ with a small amount of RuO$_x$ can maintain the stability of NiO$_x$ coated Si-based photoanode, and (ii) by controlling the synthesis condition this composite can improve the catalytic activity and thus improve the conversion efficiency of Si-based photoanode. In this work, we report a single-step protection and catalysis using a composite of Ru and Ni oxides on an n-type Si photoanode. This composite protects the Si photoanode from direct contact with the oxidizing water and thus prevents the photoanodic passivation of Si. The nanometer scale coating maintained its integrity and functionality during the long-term operation. Therefore, this composite coating eliminates the need for extra process of protection. The composite with a low resistivity significantly minimized the kinetic energy loss during the charge traveling across the coating to oxidize water. The rectifying junction between mixed oxides and Si improved charge transport and collection efficiency. The composite coated Si photoanode showed comparable activity to that of the Ru metal directly coated Si. Finally, we also demonstrated that a conformal coating of this composite on a nanotextured black Si photoanode can further improve the water oxidation efficiency.

Various strategies were developed to suppress the self-passivation of n-Si as well as other unstable photoanode materials under anodic bias and under illumination. Considerable success has been made using heterogeneous coating from various method, such as TiO$_2$,[17] ITO,[18] Fe$_2$O$_3$,[19] MnO$_2$,[6h,20] CoPi,[21] and NiO.[22] Nonstoichiometric NiO (NiO$_x$) coated Si photoanode with and without native oxides were tested and the native oxides effect was studied and the cyclic voltammograms (CV) are shown in Figure 1a. All electrochemical studies were measured using Ag/AgCl reference electrode at room temperature. However, all the biases discussed are converted to RHE (reversible hydrogen electrode) unless specified. NiO$_x$ coating from sputtering was very uniform and crack-free. Si photoanode without native oxides showed overall larger dark current density (not shown here) and slightly higher photocurrent at high bias as well. As a control and for comparison, polished bare n-type (100) Si was also tested (Figure 1a inset). Both studies in the dark and under illumination were conducted on n-Si with native oxides with dark scan first. In the dark, since majority carriers in n-type Si are electrons, anodic bias in this case was not able to drive significant anodic current. Slightly increased anodic current was noticed under a high bias of 1.25 V (black curve). On the other hand, significant anodic photocurrent was noticed at an anodic bias of 0.25 V due to the excess concentration of holes in n-type Si under illumination (blue curve). This current immediately saturated showing a diffusion limited behavior, indicating an irreversible reaction, which was primarily due to the anodic photopassivation of Si. The photocurrent dropped to dark current level after the first scan because of the thick SiO$_x$ developed at the Si surface. Actually, thermodynamic oxidation potential of Si, which is well below the water oxidation level (1.229 V), makes Si a strong reactant when interfacing with an aqueous electrolyte.[23]

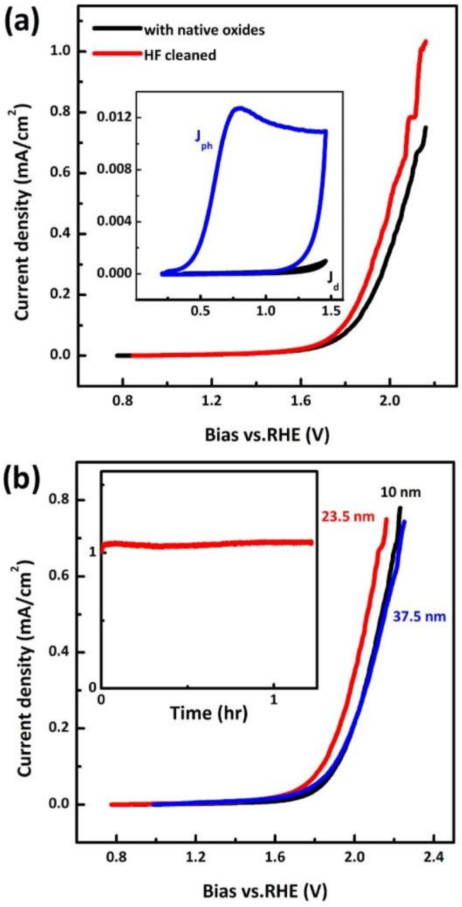

Figure 1. Electrochemical characterization: (a) NiO$_x$ coated n-Si with and without native oxides (inset: bare n-Si with native oxides), (b) thickness effect of NiO$_x$, (inset: stability of NiO$_x$ coated n-Si with a thickness of 23.5 nm biased at 2.25 V under AM 1.5G illumination).

The effect of NiO$_x$ thickness was also investigated. As shown in Figure 1b with the thickness increased from 10 to 37.5 nm, the photocurrent density increased and then dropped. Because of the trade-off between increased depletion of Si and series resistance loss on thick NiO$_x$ film, an optimum thickness configuration should be expected when one of the parameters is dominant over the other. In our case, we have found that NiO$_x$ film with a thickness of 23.5 nm was able to provide smaller on-set potential and better photocurrent density. The ampermetric study at a constant bias voltage of 2.25 V revealed a stable photoanode without noticeable signs of photocurrent degradation in the first 90 min of operation (Figure 1b inset). Compared to previous reported work, the sputtered film showed inferior activity but extended lifetime.[22] This is believed due to the compact protective film that did not develop pin-holes and thus pathways for oxidation of Si underneath during the operation. Apparently, improvement to further lower the external bias is needed to drive a considerable current density for consecutive chemical conversion.

The oxide composite (NiRuO$_x$) was synthesized using cosputtering technique and detailed deposition conditions can be found in the Supporting Information. Optical transmittance of the NiO$_x$ and NiRuO$_x$ on cleaned soda lime glass substrates was measured and shown in Figure 2. Morphology of the coating before and after annealing did not show significant changes (Figure 2a insets). On the NiO$_x$ sample, transmittance above 400 nm improved from 91 to 98% after annealing. This increase of transmittance at long wavelength maybe due to the enhancement of crystallinity with the thermal treatment, as well as out-diffusion of interstitial O atoms that acted as scattering centers to the incident light.[24] On the other hand, the as-prepared NiRuO$_x$ sample before annealing showed a less recognizable band edge transition. Moreover, the transmittance of NiRuO$_x$ at wavelength above 400 nm was reduced after annealing. The transition in the wavelength range of 300−400 nm appeared to be steeper after annealing due to the strong interband absorption of NiO$_x$. The direct band gap, owning to the unoccupied Ni 3d and mixed O 2p/Ni 3d, from extrapolating the linear portion of the Tauc relation ($\alpha h\upsilon^2$ vs $h\upsilon$) showed a blue shift for annealed samples from 3.33 to 3.66 eV for NiO$_x$ and 2.96 to 3.37 eV for NiRuO$_x$ (Figure 2b). This observation suggests a reduced density of structural defects and surface states under thermal treatment conditions that could contribute to the intraband absorption.[25] However, tails in the annealed NiRuO$_x$ film (Figure 2b black curves) suggest an existing multiple-interband transition besides the defects and surface states, presumably due to the smaller band gap of RuO$_x$.[26] Van der Pauw resistivity measurement on NiO$_x$ and NiRuO$_x$ samples revealed the reduced resistivity through the incorporation of Ru and thermal treatment processes. Ohmic contact with low resistivity was achieved using a sandwich layered ITO/Au/ITO structure deposited using gas phase sputtering. Detailed data on the ohmic contact and rectifying junction (Supporting Information Figure s1) and the resistivity of the composite before and after annealing (Supporting Information Table s1) can be found in Supporting Information.

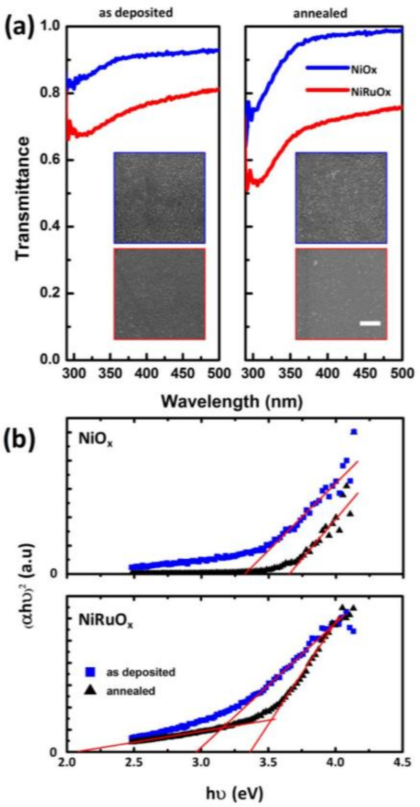

Figure 2. (a) Optical transmittance of oxide composite films before and after annealing. Inset: NiO$_x$ (first row) and NiRuO$_x$ (second row). Scale bar = 200 nm. (b) Tauc plots for NiO$_x$ and NiRuO$_x$ before and after annealing.

X-ray photoelectron spectroscopy (XPS) studies and deconvoluted peaks of the spectra of the annealed NiO$_x$ and NiRuO$_x$ film are shown in Figure 3. Interpretation of Ni 2p XPS spectrum can be difficult because of multiple splitting, shakeup, and plasmon loss.[27] It has been pointed out by Grosvenor et al. that it was difficult to assign single state to one peak.[28] However, since Ni(III) states dominated at higher energy level in the main peak,[27] we adopted a simple two peak fitting on the main Ni 2p3/2 peak to study the Ru effect on the NiO.[28] Ni 2p spectrum shown in Figure 3a suggests that the sputtered NiO$_x$ exhibited coexisting valence states of Ni(II) 2p3/2 (binding energy at 854.04 eV) and Ni(III) 2p3/2 (binding energy at 855.53 eV) (top curve in Figure 3a). On the other hand, composite NiRuO$_x$ (bottom curve in Figure 3a) showed significantly lower Ni(II)/Ni(III) ratio in the main Ni 2p3/2 peak compared to that of the pristine NiO$_x$ film, indicating an increase of valence state of Ni and an oxygen-rich composite film. Meanwhile, interstitial O atoms in the oxygen-rich NiRuO$_x$ composite could cause scattering or absorb the incident light, which also support the observation of reduced transmittance in the visible range and thus absorption tales into longer wavelength (Figure 2).

The Ru 3d5/2 peak with a binding energy at 281.12 eV and a spin−orbit splitting 3d3/2 of 285.11 eV revealed that Ru in the annealed NiRuO$_x$ composite was mainly composed of Ru(IV) in the oxidized state (Figure 3b). XPS spectra by peak fitting revealed the extra component at 282.16 eV with its splitting peak at 286.32 eV. Note that the XPS spectrum in the range showing in Figure 3b also includes superimposed C1s core-level (284.8 eV) besides Ru 3d level causing an intense Ru 3d3/2 peak. Deconvolution of the XPS spectrum is consistent with previous reported data.[29] This component was believed due to

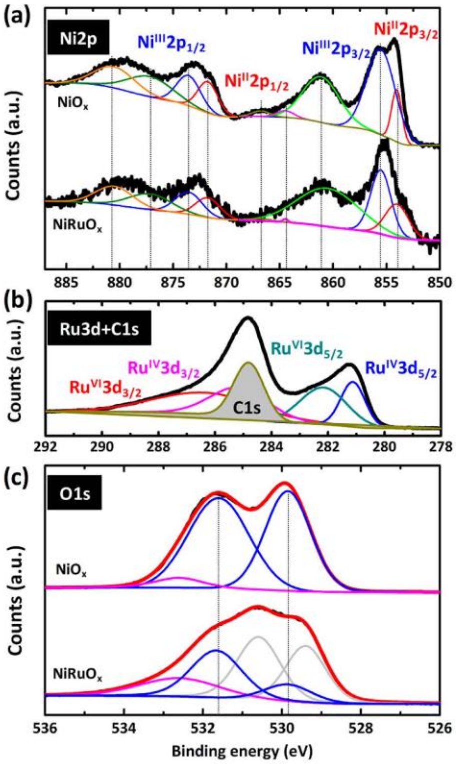

Figure 3. XPS spectrum of NiO$_x$ and NiRuO$_x$ composite: (a) Ni 2p, (b) Ru 3d and C1s, and (c) O 1s.

the unscreened Ru(IV) cations[30] or it could be also an indication of higher oxidation states of Ru coexisting such as Ru(VI) or Ru(VIII).[29] Note that the metal peak of Ru (~280.4 eV) was not noticed on annealed samples without experiencing Ar ion beam etching even with higher Ru concentration, confirming a complete Ru oxidation in the composite after annealing.

Further investigation on the O 1s XPS spectrum (Figure 3c) revealed three peaks corresponding to classical oxygen atoms in three different environment in the sputtered NiO$_x$ film including lattice oxygen (529.85 eV), hydroxyl group (531.66 eV), and surface-absorbed water (532.6 eV). These data are also in agreement with previous reported ones.[31] Additional features (gray curves) in the O 1s spectrum of NiRuO$_x$ in comparison to the one from the pristine NiO$_x$ were due to the oxygen binding in the RuO$_x$ corresponding to the lattice oxygen at 529.4 eV and hydroxyl group at 530.59 eV, as well as and surface-absorbed water overlapping with the one on NiO$_x$ at 532.6 eV. Similar to the NiO$_x$, NiRuO$_x$ sample also showed stronger hydroxyl component and weak surface absorbed water component. This observation suggested that oxyhydroxide may form resulting in a higher Ru oxidation state at the surface due to the exposure of ambient atmosphere. Importantly, areas of the deconvoluted curves can be used to semiquantitatively estimate the ratio of the Ni(II)/Ni(III), which decreases significantly from about 0.86 in NiO$_x$ to 0.35 in NiRuO$_x$. This indicated a Ni(III)-rich film was introduced by incorporation of RuO$_x$ consistent with the observation on Ni 2p peaks.

For electrochemical characterization, we directly deposited the NiO$_x$ and NiRuO$_x$ composite film on fluorine doped tin oxide (FTO) coated glasses (12−14 Ω/□, thickness <200 nm, TEC 15 Hartford Glass Co.). To avoid interactions between coating and the FTO film and to avoid high-temperature degradation of the FTO conductivity, the sintering temperature was kept at 400 °C in inert N$_2$ environment. The voltammograms without additional *iR* correction are shown in Figure 4. FTO glass electrode showed the highest onset potential to pass the double-layer current region. Application of NiO$_x$ with a thickness of 23.5 nm exhibited a catalyzed reaction by reducing the potential needed to drive the same level of current (Figure 4a). In the medium bias region of 1−10 mA/cm^2 when Faradaic process occurred, Tafel slopes were measured of 484 mV/dec for FTO glass and 290 mV/dec for FTO|NiO$_x$ (Figure 4a inset). Overpotentials at 10 mA/cm^2 for FTO glass and FTO|NiO$_x$ were 1829 mV and 1043 mV, respectively. Coating of NiO$_x$ on FTO reduced the overpotential needed to drive the anodic water decomposition current. Compared to NiO$_x$ OER

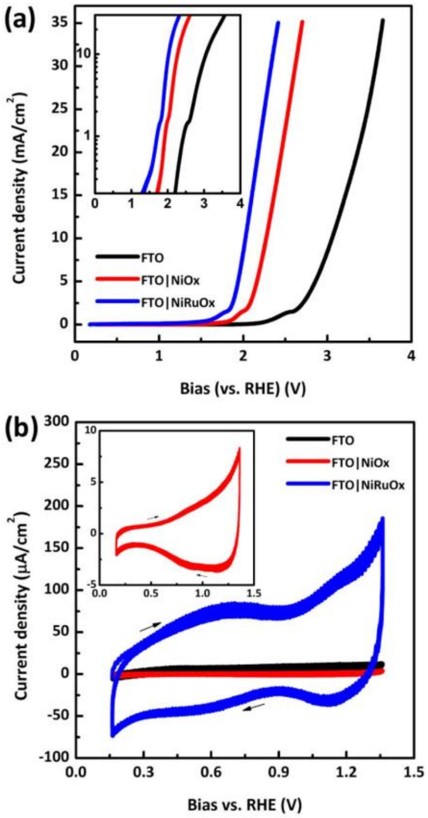

Figure 4. Electrochemical characterization of NiO$_x$ and NiRuO$_x$ composite coated FTO glass: (a) linear voltammograms; inset, Tafel plots. (b) Cyclic voltammograms of 5 consecutive scans; inset, magnified red curve.

electrocatalyst reported before, the sputtered film showed inferior catalytic activity. A dense and pinhole free film is needed to protect Si from contacting the oxidizing electrolyte and minimize the chances of penetration of electrolyte through grain boundaries. Often cases, a thicker film from sputtering can meet this specification and prevent the anodic passivation of Si. This dense and thick NiO_x film with limited surface reaction sites and high electronic ohmic loss (Supporting Information Figure s1 and Table s1) resulted in the poor catalytic performance. Addition of Ru lowered the onset potential, as well as the Tafel slope to 212 mV/dec Meanwhile, an overpotential needed to achieve 10 mA/cm^2 current was also reduced to 797 mV from the composite coating. The increase in Tafel slope at high current densities (>10 mA/cm^2) occurring at the electrode surface was due to the resistive controlled kinetics, such as series resistance loss from electrolyte and formed bubbles on the surface. None of the fresh prepared samples showed light response with a noticeable photocurrent. Cyclic voltammograms (CV) within a potential window of 0.2−1.4 V were obtained at a 100 mV/s scan rate. Redox response at 0.6−1.3 V due to the pseudocapacitve behavior of NiO_x was observed (Figure 3b inset). The cathodic current was believed due to the reduction of $NiOO_2$ to NiOOH and NiOOH to NiO of different phases. A more significant rectangular shape characteristic of the pseudocapacitance due to RuO_x was exhibited (Figure 3b). A much more pronounced amount of charges was stored and associated with the Ru redox process (blue curve) in the potential window compared to FTO|NiO_x (red curve) and bare FTO electrodes (black curve). The peaks corresponding to oxidation and reduction of the different Ru oxidation states in RuO_2 were noticed. The presence of these features was a strong indication that redox process also occurred on the RuO_2, which arises when the applied potential induces Faradaic current from the oxidation/reduction of electroactive materials via a coupled and reversible proton−electron transfer,[13] suggesting a catalytic active Ru in the composite film.

To demonstrate further the advantages of $NiRuO_x$ as a catalytic and protective coating on n-Si, we have compared this c-Si|$NiRuO_x$ structure to a Si photoanode directly coated with Ru (c-Si|Ru) and one with a high quality ultrathin TiO_2 protection layer in-between (c-Si|TiO_2|Ru). For example, Chen et al. used TiO_2 from atomic layer deposition (ALD) to protect n-Si photoanode from anodic photopassivation.[32] Pracchino et al. showed the extended lifetime of a unstable photocathode (p-Cu_2O) by effective passivation using TiO_2.[33] Recently, Lee et al. demonstrated this protective coating on III−V (p-InP) photocathode.[34] While providing excellent chemical stability, the ultrathin TiO_2 with a thickness of 2 nm maintained the effective charge transfer of excited carriers. In these works, electrocatalysts were then deposited on top of TiO_2 to lower the reaction overpotential and enhance current density. This so-called "two-step process" utilizes a protection layer (TiO_2) and an electrocatalyst layer (noble metal) separately. The thickness of TiO_2 is important particularly on n-type photoanode materials to maintain its light response (Supporting Information Figure s2), since TiO_2 prepared from various method is a well-known photoactive specifically to ultraviolet (UV) light. Without an outperforming catalyst, ultrathin TiO_2-coated crystalline n-Si (c-Si|TiO_2) photoanode still requires a large overpotential to drive the water oxidation reaction (Supporting Information Figure s3). Ru metal deposited on c-Si|TiO_2 photoanode effectively lowered the onset potential due to its superior OER catalytic activity. The photocurrent density from c-Si|TiO_2|Ru at 1.23 V was able to reach 0.24 mA/cm^2 (Supporting Information Figure s3). However, this value is around 4 times lower compared to the photocurrent density of 1.06 mA/cm^2 from the c-Si|Ru photoanode. This is believed due to the additional loss of tunneling carriers across the TiO_2 coating and low kinetics.[6f,g] The high dark current from c-Si|Ru was due to the metal-induced intermediate surface states, which resulted in a much lower on/off ratio of current (j_{ph}/j_d at overpotential of 230 mV). On the other hand, the c-Si|$NiRuO_x$ photoanode showed a similar photocurrent density to that of the c-Si|Ru sample at 1.23 V but much higher on/off ratio due to the suppressed dark current. Meanwhile, c-Si|Ru showed quicker degradation under operation conditions. As shown in Supporting Information Figure s4, photocurrent density dropped below half of the initial value in less than 20 min, despite its slightly higher initial photocurrent density than that of the c-Si|$NiRuO_x$. Note that to be comparable, Ru loading on all the samples were constant by controlling the deposition conditions (Supporting Information). Comparisons between aforementioned structures are summarized in Table 1.

Table 1. Comparisons between Different Photoanode Structures for Water Oxidation

	j_{ph}/j_d @ η = 230 mV	onset potential (V)	j_{ph} (mA/cm^2) @ 1.23 V	time for 50% drop of j_{ph}
c-Si|$NiRuO_x$	67.57	1.08	0.94	>1 h
c-Si|Ru	12.91	1.08	1.06	<20 min
c-Si|TiO_2|Ru	6.57	1.17	0.24	NA
c-Si|TiO_2	NA	2.46	4.31×10^4	NA

Surface textures effectively enhance the light utilization, increase the surface reaction sites, and minimize the bubble overpotential through a hydrophilic surface.[34,35] P-type Si with surface textures used as photocathodes for water reduction and H_2 generation was demonstrated before.[2,5c,36] Nanotextured Si (or black Si, b-Si) were generated through a facile chemical etching at room temperature, which is well documented[37] and details can be found in Supporting Information. The morphology as a function of the etching time is shown in Supporting Information Figure s5a-e. The depth of the nanotextured layer increased with the etching time. This etching process has a linear relationship with the etching time, before there is a significant chemical depletion and limited reactant diffusion due to the developed thick metal coating. Estimated etching rate at room temperature was about 1.55 nm/s (black ▲ curve in Supporting Information Figure s5f). Rough estimation on surface area showed a linear relationship with the etching time assuming no loss in the density of pores on the surface over time. However, this assumption may not be 100% true as seen in the SEM images in the second row in Figure s5a-e, due to the lateral overetching and increased filling factor of pores which led to a decrease in the surface area. Roughness factor estimated from SEM images are 2, 3.8, 8.6, 11.5, and 12.6 for samples with 1, 2, 5, 8, and 15 min etching, which is actually saturated with the increasing etching time (blue ■ curve in Supporting Information Figure s5f). This is one of the reasons that we did not use longer etching time to achieve deeper pores. The geometry of the b-Si is actually

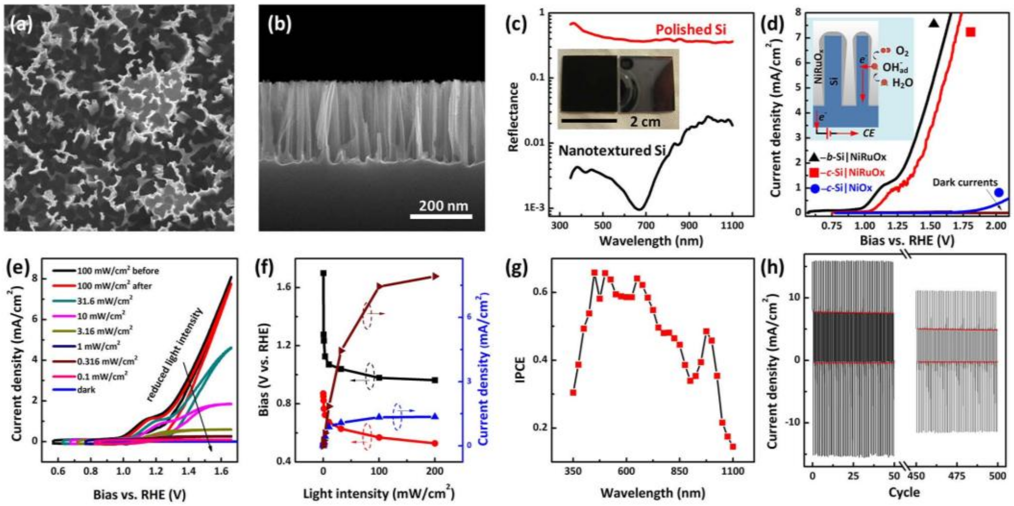

Figure 5. $NiRuO_x$ coated black Si: SEM image (a) top view and (b) cross-sectional view. Scale bar = 200 nm. (c) Specular reflectance on c-Si and b-Si. Insets: digital optical images of c-Si (right) and b-Si (left). (d) Comparison of linear voltammograms. (e) Cyclic voltammograms of b-Si|$NiRuO_x$ at varying light intensity. (f) V_{ocph}, V_{onset}, j@1.23 V, and j@432 mV overpotential versus light intensity. (g) IPCE spectrum and (h) chronoamperometric stability study in 500 cycles operation.

critical. Additional reasons for using an 8 min etched b-Si will be given in the later discussions.

Si photocathode for proton reduction is considerably stable under illumination and cathodic bias in an acidic environment.[36a] However, its stability does become a concern when in idle condition, under anodic bias, or alkaline electrolyte, where proper protection is needed.[3] Therefore, a high quality and conformal protection layer is particularly important to enable Si for water oxidation since the n-Si is typically anodically biased and excess carriers of holes. Gas phase deposition offers opportunities to reach a uniform coating on high-profile structures and offers minimum chances for exposure of substrates. Magnetron RF sputtering in this experiment was able to provide conformal coating on the b-Si with etching depth of 680 nm. However, with the increased depth in b-Si, a conformal coating became difficult and eventually failed where significant degradation of photoresponse was observed. This is another reason of using 8 min textured b-Si as the substrate for the demonstration of $NiRuO_x$ composite enabled Si photoanode.

The morphology of the b-Si substrate with a 680 nm thick porous layer on the surface is shown in Figure 5a,b. Specular reflection spectra of mirror-polished c-Si and nanotextured b-Si are shown in Figure 5c. The experimental verification of the specular reflectance discussed above was measured at a fixed incident angle of 30°. c-Si showed significant UV reflection with reflectance above 55% at wavelength below 400 nm. At wavelength between 400 and 700 nm, polished Si showed average reflectance of 41.8% and an average specular reflectance of 37.0% in the near-infrared (IR) and IR range (wavelength between 700 and 1100 nm), which is consistent with previous reported data.[38] For comparison, this b-Si showed a wide range suppression of reflection. The ultralow specular reflectivity was reached in the entire wavelength range of 350 to 1100 nm due to the effective coupling of incident light to the Si substrate. One of the primary physical effects behind this phenomenon is the change of the refractive index at the air and Si interface. The transition of the refractive index was effectively modulated and smoothed by the porous Si layer, resulting in the reduced specular reflectance, enhanced internal reflection, and thus enhanced absorption. A reflectance dip at wavelength around 640 nm indicated a strong resonance corresponding to physical geometry of the porous layer.[39] Although reflectance increased at wavelength above 700 nm, nanotexturing technique showed a broadband suppression of reflection due to the effective coupling of light offered by the porous layer. The optical image clearly showed the reflective nature of the polished Si where the reflection of the imaging camera can be seen (right image in Figure 5c inset) and the black appearance of the etched Si (left image in Figure 5c inset).

Linear voltammograms of $NiRuO_x$ composite coated c-Si and b-Si are shown in Figure 5d. Both photoanodes showed negligible dark currents. At 1.23 V, $NiRuO_x$ composite coated b-Si showed photocurrent density of 1.34 mA/cm^2, about 1.5 times greater than that of the c-Si|$NiRuO_x$ photoanode. The enhanced photocurrent density is due to the increased surface area under a fixed geometrical area (11.5 times larger) and improved light absorption. Catalytic reaction mechanism and oxygen evolution at both Ni and Ru sites can be generally described using equations below and illustrated in the Figure 5d inset

$$\mathrm{Si} \xrightarrow{h\nu} e^- + h^+ \tag{1}$$

$$\mathrm{M}^n + \mathrm{H_2O} + h^+ \rightarrow \mathrm{M}^{n+1}(\mathrm{OH}^-_{ad}) + \mathrm{H}^+ \tag{2}$$

$$2\mathrm{M}^{n+1}(\mathrm{OH}^-_{ad}) \rightarrow \mathrm{M}^{n+2}\mathrm{O} + \mathrm{M}^n + \mathrm{H_2O} \tag{3}$$

$$2\mathrm{M}^{n+2}\mathrm{O} \rightarrow 2\mathrm{M}^n + \mathrm{O_2} \tag{4}$$

where M^n is the metal active site (Ni and Ru with valence states of n^+).

Current fluctuation in the polarization study was reduced on the b-Si samples, which was believed due to the hydrophilic property of b-Si surface and reduced radius of curvature of nanowires. These facts eased the bubble release from electrode surfaces upon formation without contributing overpotential losses from large bubbles forming.[35] Importantly, significant improvement in light absorption and surface area did not improve the photocurrent dramatically. This is primarily because of the increased surface defects and thus recombination velocity.[40] In fact, nonoptimized electrodes displayed higher onset potential. These electrodes, for example, include samples with films deposited at higher O_2 partial pressure during the sputtering process, or annealed in O_2 environment during anneal process. Increased O_2 partial pressure improves the oxygen vacancy and also reduces the electrical resistivity, this could also cause of a loss of transmittance due to interstitial O as scattering centers.[24] As mentioned in the early discussion, electrodes coated with thicker NiO$_x$ film also showed inferior performance. In addition, poor ohmic contact or high contact resistance could also increase the onset potential. All of these nonoptimized fabrication conditions contributed to the increased O_2 evolution reaction overpotential resulting in a higher external driving bias and lower conversion efficiency.

The CV curves of b-Si|NiRuO$_x$ sample under different light intensities are shown in Figure 5e. With the reduced light intensity by applying a series of neutral density (ND) filters, we notice a continuous decrease of photocurrent density in the same bias range. At low light intensity, it was noticed that the intensity of the shoulder at 1 mA/cm^2 reduces and also it shifts to high bias value. This indicates a slow process presumably due to the limited OH$^-$ ion diffusion in the near neutral solution.[7] Current saturation was not noticed in the range of the measured bias at intensity of 100 mW/cm^2 and started to appear at incident light intensity below 10 mW/cm^2 due to the limited density of excess carriers. The saturation point shifts to lower bias values with the reduced light intensity. V_{oc} under illumination (V_{ocph}) shifted to more positive values with the reducing light intensity and eventually approached the V_{oc} value at dark (V_{ocd}) due to the reduced quasi-Fermi level separation. Note that the V_{oc} here is defined as the current shifts from cathodic to anodic direction. To confirm the stability of the sample, cyclic voltammograms were remeasured under normal incident at a light intensity of 100 mW/cm^2. Slight decrease (<5%) in current density over the scanned bias range was noticed indicating a minimal degradation.

The bias to maintain a certain current density (0.2 mA/cm^2) as a function of light intensity is primarily controlled by the interfacial property of b-Si|NiRuO$_x$ and catalytic activity of the composite, as shown in Figure 5f (black square curve). This onset potential for water oxidation shifts to lower values exponentially with the increased incident light intensities, which was expected as the V_{ocph} decreased (red ● curve). Therefore, the voltage difference ($|1.23\text{-}V_{oc}|$) increases exponentially with increasing incident light intensity, since the V_{oc} in a solar cell generally depends on the logarithm of the photogenerated current density. The V_{oc} versus light intensity in logarithm scale is shown in Supporting Information Figure s6. The sign of the slope indicating the photoanodic behavior of the Si|NiRuO$_x$ photoelectrode.[41] Meanwhile, photocurrent densities showed similar behavior as the V_{oc} (Figure 5f). For example, at the thermodynamic water oxidation potential (1.23 V), the photocurrent density increased exponentially with the increasing light intensity and finally approaching a saturated value of 1.36 mA/cm^2 at 100 mW/cm^2 (blue ▲ curve). Photocurrent density at 432 mV overpotential (brown ▶ curve) also exponentially increased with the increasing light intensity which followed the same trend as the photocurrent density at thermodynamic potential. The photocurrent density at this overpotential can be as high as 7.44 mA/cm^2 at an incident light intensity of 200 mW/cm^2.

The incident-photon-conversion efficiency (IPCE) as a function of wavelength for the b-Si|NiRuO$_x$ photoanode at 432 mV overpotential is shown in Figure 5g. The exposed area on the sample was fixed at 1 cm^2 controlled by the window size on the sample holder. The spot size (A_{ph} = 0.1 mm × 0.2 mm) of the monochromated light on the sample surface was much smaller than the sample size. This was considered in the IPCE calculation where the photocurrent was calculated using the equation below

$$j_{ph} = \frac{I_{ph} - I_d}{A_{ph}} \tag{5}$$

where I_{ph} and I_d is the current measured under chromated light illumination and in dark, respectively, and A_{ph} is the light spot size. The light intensity of the monochromated light from the monochromator equipped with an IR filter on the sample surface was calibrated using a Si photodetector at zero bias. IPCE was calculated using the equation below

$$\begin{aligned} \text{IPCE} &= \frac{1240[\text{nm}\cdot\text{mW}\cdot\text{mA}^{-1}] \times j_{ph}[\text{mA}\cdot\text{cm}^{-2}]}{\lambda[\text{nm}] \times \frac{j_{phD}[\text{mA}\cdot\text{cm}^{-2}]}{R_\lambda[\text{mA}\cdot\text{mW}^{-1}]}} \\ &= \eta_{ext} \times \frac{j_{ph}[\text{mA}\cdot\text{cm}^{-2}]}{j_{phD}[\text{mA}\cdot\text{cm}^{-2}]} \end{aligned} \tag{6}$$

where λ is the wavelength of incident light in nm, j_{phD} is the photocurrent from the Si photodetector in mA/cm^2, R_λ is the responsitivity of the Si photodetector provided by the supplier in mA/mW, and η_{ext} is the external quantum efficiency of the Si photodetector. The shape of the IPCE curve matched well with the typical Si solar cell showing response between 350 and 1100 nm with effective photocurrent generated in the wavelength range of 475–725 nm. With the increased surface area in the b-Si samples, the surface recombination velocity increases leading to an additional loss of current at surface recombination sites, meaning a loss of water oxidation efficiency on b-Si from a long etching time. It was reported that photoresponse at short and long wavelength regions is effectively affected by the surface recombination from surface textures[42] and Auger recombination from doping,[40a] which is another reason of using 8 min etched b-Si instead of ones from longer etching time.

Stability study of the photoanode was conducted using chronoamperometric measurement at 432 mV overpotential (Figure 5h). Photocurrent density degraded from 7 to 5.95 mA/cm^2 after 500 cycles of pulsing of an external bias (low, V_{ocph}, and high, 432 mV overpotential) in 1.5 h, suggesting a fairly stable photoelectrode. Stabilized photocurrent is highlighted using red lines in Figure 5h. Significant overshoot followed by a relaxation to its equilibrium state was observed corresponding to external potential changes. This photocurrent transient response to potential pulses was believed to be caused by possible recombination processes at the b-Si|NiRuO$_x$ and

NiRuO$_x$|electrolyte interfaces, as well as limited ionic diffusion and second order capacitance effect at both interfaces.

In conclusion, we have reported a Ni and Ru oxide composite enabled n-Si as an efficient device for photo-oxidation of water that showed the best on/off ratio, lowest onset potential, and the most elongated long-term stability compared to other structures. NiRuO$_x$ composites offered a manipulation of the interfaces properties between catalysts and photoactive materials, such as band bending and charge transfer, as well as the OER catalytic activity. Furthermore, the oxide composite coated nanotextured Si demonstrated improved current density and thus conversion efficiency due to the improved light harvesting and increased surface reaction sites. Advances of transition metal oxides catalysts promise the development of low-cost, active, and stable electrocatalysts under neutral and alkaline conditions for practical water splitting and solar fuel production, as well as other various applications.

■ ASSOCIATED CONTENT

Ⓢ Supporting Information

Materials and method section describing all experimental procedures, including film deposition, Van der Pauw resistivity measurement, ITO ohmic contact measurement, junction IV measurement, optical transmittance measurement, XPS, photoelectrochemical characterization, nanotextured Si fabrication, along with the IPCE measurement details. This material is available free of charge via the Internet at http://pubs.acs.org.

■ AUTHOR INFORMATION

Corresponding Author

*E-mail: dwang@ece.ucsd.edu. Telephone: (+1-858) 822-4723.

Author Contributions

The manuscript was written by K.S. All authors have given approval to the final version of the manuscript.

Notes

The authors declare no competing financial interest.

■ ACKNOWLEDGMENTS

D.W. acknowledges the financial support from DOE (DE-FG36-08G018016), NSF (ARRA-ECCS0901113 and CBET1236155), and UCSD Academic Senate Research Award to this project and ONR-DURIP (N00014-08-1-0776) for the ALD acquisition. K.S. would like to thank Professor E. Miller (DOE) for his stimulus discussions and useful suggestions during the early development of this work. K.S. and D.W. also would like to thank Professor P. K. L. Yu (UCSD) for allowing us to use the Hall measurement setup. K.S. also would like to thank Dr. W. Chen (UCSD) for her generous assistance on the Van der Pauw measurement and stimulus discussions and X. Lu and S. Park from UCSD CalIT2 for their assistance on the film deposition, ellipsometer, and four point probe measurements. D.W. also would like to thank Drs. R. Rao and B. Fruhberger of Cal-IT2 of UCSD for their unconditional support.

■ REFERENCES

(1) Leempoel, P.; Castro-Acuna, M.; Fan, F.-R. F.; Bard, A. J. Semiconductor electrodes: the Effect of Light Intensity and Iodine Doping on the Stabilization of n-Silicon by Phthalocyanine Films. *J. Phys. Chem.* **1982**, *86* (8), 1396−1400.

(2) Hou, Y.; Abrams, B. L.; Vesborg, P. C. K.; Björketun, M. E.; Herbst, K.; Bech, L.; Setti, A. M.; Damsgaard, C. D.; Pedersen, T.; Hansen, O.; Rossmeisl, J.; Dahl, S.; Nørskov, J. K.; Chorkendorff, I. Bioinspired molecular co-catalysts bonded to a silicon photocathode for solar hydrogen evolution. *Nat. Mater.* **2011**, *10* (6), 434−438.

(3) Seger, B.; Laursen, A. B.; Vesborg, P. C. K.; Pedersen, T.; Hansen, O.; Dahl, S.; Chorkendorff, I. Hydrogen Production Using a Molybdenum Sulfide Catalyst on a Titanium-Protected n+p-Silicon Photocathod. *Angew. Chem., Int. Ed.* **2012**, *51* (36), 9128−9131.

(4) Zhang, Z.; Yates, J. T. Band Bending in Semiconductors: Chemical and Physical Consequences at Surfaces and Interfaces. *Chem. Rev.* **2012**, *112*, 5520−5551.

(5) (a) Nakato, Y.; Tsumura, A.; Tsubomura, H. Efficient photoelectrochemical conversion of solar energy with n-type semiconductor electrodes surface-doped with IIIA-group element. *Chem. Lett.* **1982**, *11* (7), 1071−1074. (b) Nakato, Y.; Hiramoto, M.; Iwakabe, Y.; Tsubomura, H. ESCA and Photoelectrochemical Studies of p-n Junction Silicon Electrodes Protected by Platinum Deposition for Use in Solar Energy Conversion. *J. Electrochem. Soc.* **1985**, *132* (2), 330−334. (c) Boettcher, S. W.; Warren, E. L.; Putnam, M. C.; Santori, E. A.; Turner-Evans, D.; Kelzenberg, M. D.; Walter, M. G.; McKone, J. R.; Brunschwig, B. S.; Atwater, H. A.; Lewis, N. S. Photoelectrochemical Hydrogen Evolution Using Si Microwire Arrays. *J. Am. Chem. Soc.* **2011**, *133* (5), 1216−1219. (d) Nakato, Y.; Egi, Y.; Hiramoto, M.; Tsubomura, H. Hydrogen Evolution and Iodine Reduction on an Illuminated n-p Junction Silicon Electrode and Its Application to Efficient Solar Photoelectrolysis of Hydrogen Iodide. *J. Phys. Chem.* **1984**, *88* (19), 4218−4222.

(6) (a) Sun, K.; Madsen, K.; Andersen, P.; Bao, W.; Sun, Z.; Wang, D. Metal on Metal Oxide Nanowire Co-catalyzed Si Photocathode for Solar Water Splitting. *Nanotechnol.* **2012**, *23* (19), 194013. (b) Dominey, R. N.; Lewis, N. S.; Bruce, J. A.; Bookbinder, D. C.; Wrighton, M. S. Improvement of photoelectrochemical hydrogen generation by surface modification of p-type silicon semiconductor photocathodes. *J. Am. Chem. Soc.* **1982**, *104* (2), 467−482. (c) Rosenblum, M. D.; Lewis, N. S. Stabilization of n-type silicon photoanodes in aqueous solution by electrostatic binding of redox ions into charged polymers. *J. Phys. Chem.* **1984**, *88* (14), 3103−3107. (d) Kohl, P. A.; Frank, S. N.; Bard, A. J. Semiconductor Electrodes: Behavior of n- and p-Type Single Crystal Semconductors Covered with Thin n-TiO_2 Films. *J. Electrochem. Soc.* **1977**, *124* (2), 225−229. (e) Morisaki, H.; Ono, H.; Dohkoshi, H.; Yazawa, K. Iron-Oxide Coated n-Si as a Heterostructure Photoanode for the Photoelectrolysis of Water. *Jpn. J. Appl. Phys.* **1980**, *19*, L148. (f) Warren, E. L.; McKone, J. R.; Atwater, H. A.; Gray, H. B.; Lewis, N. S. Hydrogen-evolution characteristics of Ni-Mo-coated, radial junction, n$^+$p-silicon microwire array photocathodes. *Energy Environ. Sci.* **2012**, *5*, 9653−9661. (g) McKone, J. R.; Warren, E. L.; Bierman, M. J.; Boettcher, S. W.; Brunschwig, B. S.; Lewis, N. S.; Gray, H. B. Evaluation of Pt, Ni, and Ni-Mo electrocatalysts for hydrogen evolution on crystalline Si electrodes. *Energy Environ. Sci.* **2011**, *4* (9), 3573−3583. (h) Strandwitz, N. C.; Comstock, D. J.; Grimm, R. L.; Nichols-Nielander, A. C.; Elam, J.; Lewis, N. S. Photoelectrochemical Behavior of n-type Si(100) Electrodes Coated with Thin Films of Manganese Oxide Grown by Atomic Layer Deposition. *J. Phys. Chem. C* **2013**, *1117* (10), 4931−4936.

(7) Juodkazis, K.; Juodkazytė, J.; Vilkauskaitė, R.; Šebeka, B.; Jasulaitienė, V. Oxygen evolution on composite ruthenium and nickel oxides electrode. *Chemija* **2008**, *19* (1), 1−6.

(8) Jaksic, M. M. Hypo−hyper-d-electronic interactive nature of interionic synergism in catalysis and electrocatalysis for hydrogen reactions. *Int. J. Hydrogen Energy* **2001**, *26* (6), 559−578.

(9) Greiner, M. T.; Chai, L.; Helander, M. G.; Tang, W.-M.; Lu, Z.-H. Transition Metal Oxide Work Functions: The Influence of Cation Oxidation State and Oxygen Vacancies. *Adv. Funct. Mater.* **2012**, *22* (21), 4557−4568.

(10) Trotochaud, L.; Ranney, J. K.; Williams, K. N.; Boettcher, S. W. Solution-Cast Metal Oxide Thin Film Electrocatalysts for Oxygen Evolution. *J. Am. Chem. Soc.* **2012**, *134* (41), 17253−17261.

(11) Wang, H.; Gao, Q.; Jiang, L. Facile Approach to Prepare Nickel Cobaltite Nanowire Materials for Supercapacitors. *Small* **2011**, *7* (17), 2454–2459.

(12) Ndione, P. F.; Garcia, A.; Widjonarko, N. E.; Sigdel, A. K.; Steirer, K. X.; Olson, D. C.; Parilla, P. A.; Ginley, D. S.; Armstong, N. R.; Richards, R. E.; Ratcliff, E. L.; Berry, J. J. Highly-Tunable Nickel Cobalt Oxide as a Low-Temperature P-Type Contact in Organic Photovoltaic Devices. *Adv. Energy Mater.* **2012**, *3* (4), 524–531.

(13) Simon, P.; Gogotsi, Y. Materials for electrochemical capacitors. *Nat. Mater.* **2008**, *7* (11), 845–854.

(14) (a) Fan, F. R. F.; Hope, G. A.; Bard, A. J. Semiconductor Electrodes: Stabilisation of n-Si electrodes in aqueous solution photoelectrochemical cells by formation of platinum silicide layers. *J. Electrochem. Soc.* **1982**, *129* (7), 1647–1649. (b) Sakai, Y.; Sugahara, S.; Matsumura, M.; Nakato, Y.; Tsubomura, H. Photoelectrochemical water splitting by tandem type and heterojunction amorphous silicon electrodes. *Can. J. Chem.* **1988**, *66* (8), 1853–1856. (c) Licht, S.; Wang, B.; Mukerji, S.; Soga, T.; Umeno, M.; Tributsch, H. Efficient Solar Water Splitting, Exemplified by RuO$_2$-Catalyzed AlGaAs/Si Photoelectrolysis. *J. Phys. Chem. B* **2000**, *104* (38), 8920–8924.

(15) Liu, Y.; Senturk, B. S.; Mantese, J. V.; Aindow, M.; Alpay, S. P. Electrical and tribological properties of a Ni-18%Ru alloy for contact applicatios. *J. Mater. Sci.* **2011**, *46*, 6563.

(16) Liu, X. M.; Zhang, X. G. NiO-based composite electrode with RuO$_2$ for electrochemical capacitors. *Electrochim. Acta* **2004**, *49* (2), 229–232.

(17) Tsubomura, H.; Nakato, Y.; Hiramoto, M.; Yano, H. Metal oxide coated p–n junction silicon electrodes for photoelectrochemical solar energy conversion. *Can. J. Chem.* **1985**, *63* (7), 1759–1762.

(18) (a) Thompson, L.; DuBow, J.; Rajeshwar, K. Photoelectrochemical Generation of Chlorine on Catalytically Modified n-Silicon/Indium Tin Oxide Anodes. *J. Electrochem. Soc.* **1982**, *129* (9), 1934–1935. (b) Cox, C. R.; Winkler, M. T.; Pijpers, J. J. H.; Buonassisi, T.; Nocera, D. G. Interfaces Between Water Splitting Catalysts and Buried Silicon Junctions. *Energy Environ. Sci.* **2012**, *6*, 532–538.

(19) Ono, H.; Morisaki, H.; Yazawa, K. Photoelectrochemical Properties of Iron-Oxide Films and the Coating Effects onto n-Si as an Efficient Photoanode. *Jpn. J. Appl. Phys.* **1982**, *21*, 1075.

(20) Kainthla, R. C.; Zelenay, B.; Bockris, J. O. M. Protection of n-Si Photoanode against Photocorrosion in Photoelectrochemical Cell for Water Electrolysis. *J. Electrochem. Soc.* **1986**, *133* (2), 248–253.

(21) Pijpers, J. J. H.; Winkler, M. T.; Surendranath, Y.; Buonassisi, T.; Nocera, D. G. Light-induced water oxidation at silicon electrodes functionalized with a cobalt oxygen-evolving catalyst. *Proc. Natl. Acad. Sci. U.S.A.* **2011**, *108* (25), 10056–10061.

(22) Sun, K.; Park, N.; Sun, Z.; Zhou, J.; Wang, J.; Pang, X.; Shen, S.; Noh, S. Y.; Jing, Y.; Jin, S.; Yu, P.; Wang, D. Nickel oxide functionalized silicon for efficient photo-oxidation of water. *Energy Environ. Sci.* **2012**, *5*, 7872–7877.

(23) Chen, S.; Wang, L.-W. Thermodynamic Oxidation and Reduction Potentials of Photocatalytic Semiconductors in Aqueous Solution. *Chem. Mater.* **2012**, *24* (18), 3659–3666.

(24) Yang, J.-L.; Lai, Y.-S.; Chen, J. S. Effect of heat treatment on the properties of non-stoichiometric p-type nickel oxide films deposited by reactive sputtering. *Thin Solid Films* **2005**, *488* (1–2), 242–246.

(25) Castillo, N. C.; Heel, A.; Graule, T.; Pulgarin, C. Flame-assisted synthesis of nanoscale, amorphous and crystalline, spherical BiVO$_4$ with visible-light photocatalytic activity. *Appl. Catal., B* **2010**, *95* (3–4), 335–347.

(26) Patake, V. D.; Lokhande, C. D. Chemical synthesis of nano-porous ruthenium oxide (RuO$_2$) thin films for supercapacitor application. *Appl. Surf. Sci.* **2008**, *254* (9), 2820–2824.

(27) Mansour, A. N. Characterization of NiO by XPS. *Surf. Sci. Spectra* **1994**, *3* (3), 231–238.

(28) Grosvenor, A. P.; Biesinger, M. C.; Smart, R. S. C.; McIntyre, N. S. New interpretations of XPS spectra of nickel metal and oxides. *Surf. Sci.* **2006**, *600* (9), 1771–1779.

(29) Kaga, Y.; Abe, Y.; Yanagisawa, H.; Kawamura, M.; Sasaki, K. Ru and RuO$_2$ Thin Films by XPS. *Surf. Sci. Spectra* **1999**, *6* (1), 68–74.

(30) Madhavaram, H.; Idriss, H.; Wendt, S.; Kim, Y. D.; Knapp, M.; Over, H.; Aßmann, J.; Löffler, E.; Muhler, M. Oxidation Reactions over RuO$_2$: A Comparative Study of the Reactivity of the (110) Single Crystal and Polycrystalline Surfaces. *J. Catal.* **2001**, *202* (2), 296–307.

(31) Mun, C.; Ehrhardt, J. J.; Lambert, J.; Madic, C. XPS investigations of ruthenium deposited onto representative inner surfaces of nuclear reactor containment buildings. *Appl. Surf. Sci.* **2007**, *253* (18), 7613–7621.

(32) Chen, Y. W.; Prange, J. D.; Dühnen, S.; Park, Y.; Gunji, M.; Chidsey, C. E. D.; McIntyre, P. C. Atomic layer-deposited tunnel oxide stabilizes silicon photoanodes for water oxidation. *Nat. Mater.* **2011**, *10* (7), 539–544.

(33) Paracchino, A.; Laporte, V.; Sivula, K.; Grätzel, M.; Thimsen, E. Highly active oxide photocathode for photoelectrochemical water reduction. *Nat. Mater.* **2011**, *10* (6), 456–461.

(34) Lee, M. H.; Takei, K.; Zhang, J.; Kapadia, R.; Zheng, M.; Chen, Y.-Z.; Nah, J.; Matthews, T. S.; Chueh, Y.-L.; Ager, J. W.; Javey, A. p-Type InP Nanopillar Photocathodes for Efficient Solar-Driven Hydrogen Production. *Angew. Chem., Int. Ed.* **2012**, *51*, 10760–10764.

(35) Kibsgaard, J.; Chen, Z.; Reinecke, B. N.; Jaramillo, T. F. Engineering the surface structure of MoS$_2$ to preferentially expose active edge sites for electrocatalysis. *Nat. Mater.* **2012**, *11*, 963–969.

(36) (a) Oh, I.; Kye, J.; Hwang, S. Enhanced Photoelectrochemical Hydrogen Production from Silicon Nanowire Array Photocathode. *Nano Lett.* **2011**, *12* (1), 298–302. (b) Oh, J.; Deutsch, T. G.; Yuan, H.-C.; Branz, H. M. Nanoporous black silicon photocathode for H$_2$ production by photoelectrochemical water splitting. *Energy Environ. Sci.* **2011**, *4* (5), 1690–1694.

(37) Peng, K.; Yan, Y.; Gao, S.; Zhu, J. Dendrite-Assisted Growth of Silicon Nanowires in Electroless Metal Deposition. *Adv. Funct. Mater.* **2003**, *13* (2), 127–132.

(38) Huang, Y.-F.; Chattopadhyay, S.; Jen, Y.-J.; Peng, C.-Y.; Liu, T.-A.; Hsu, Y.-K.; Pan, C.-L.; Lo, H.-C.; Hsu, C.-H.; Chang, Y.-H.; Lee, C.-S.; Chen, K.-H.; Chen, L.-C. Improved Broadband and Quasi-Omnidirectional Anti-Reflection Properties with Biomimetic Silicon Nanostructures. *Nat. Nanotechnol.* **2007**, *2* (12), 770–774.

(39) Spinelli, P.; Verschuuren, M. A.; Polman, A. Broadband omnidirectional antireflection coating based on subwavelength surface Mie resonators. *Nat. Commun.* **2012**, *3*, 692.

(40) (a) Oh, J.; Yuan, H.-C.; Branz, H. M., An 18.2%-efficient black-silicon solar cell achieved through control of carrier recombination in nanostructures. *Nat. Nanotechnol.* **2012**, *7*, 743–748. (b) Noh, S. Y.; Sun, K.; Choi, C.; Niu, M.; Xu, K.; Yang, M.; Jin, S.; Wang, D., Multi-branched TiO$_2$/Si Nanostructures for Enhanced Photoelectrochemical Water Splitting. *Nanoenergy* 2012, in press.

(41) Katz, J. E.; Gingrich, T. R.; Santori, E. A.; Lewis, N. S. Combinatorial synthesis and high-throughput photopotential and photocurrent screening of mixed-metal oxides for photoelectrochemical water splitting. *Energy Environ. Sci.* **2009**, *2* (1), 103–112.

(42) Koshida, N.; Nagasu, M.; Sakusabe, T.; Kiuchi, Y. The Current-Voltage Characteristics of a Photoelectrochemical Cell Using p-Type Porous Si. *J. Electrochem. Soc.* **1985**, *132* (2), 346–349.

Reproduced with permission from Nano Letters, DOI: 10.1021/nl400343a Copyright 2013 American Chemical Society.

Energy and Environmental Science, vol.5, pp.7872 (2012) - Reproduced by permission of The Royal Society of Chemistry.

3.2 Ultrathin NiO_x on Si np^+ junction photoanode for efficient solar water oxidation

3.2.1 Abstract

Targeting on realizing large-scale solar fuel conversion, photoelectrochemical (PEC) electrodes based on earth abundant elements are essential. In this work, we report our effort to synthesize an ultrathin (few nanometers) NiO_x oxygen evolution reaction (OER) catalyst from a cost-effective solution-based method and apply it on a Si np^+ junction photoanode for a durable and efficient solar driven water oxidation. Surfactant and thermal treatment are critical parameters which allow to fine-tune and to optimize the OER activity. Meanwhile, a stable semitransparent conducting oxide was used to isolate the Si from corrosion in alkaline environment, to decouple the Si photovoltaics and electrocatalysis process, and to provide a pre-activation to the OER catalyst. Successful demonstration of this ultrathin NiO_x enabled Si junction photoanode results in a photocurrent of 1.98 mA/cm^2 at the water oxidation potential (E_{OER}=0.415 V vs. NHE at pH=13.8) and a solar to oxygen conversion efficiency of 0.7% under 0.51-sun illumination.

3.2.2 Introduction

Photoelectrochemical (PEC) solar fuel conversion becomes a very important research route[1] to solve energy problems, which relies on a separate production process of electricity generation (free energetic carriers) and generation of chemical products (fuels) which can be separated, stored, and used to reproduce the stored energy. Recently, considerable success has been achieved to generating hydrogen from splitting water using solar energy based on structures such as single large band gap materials[2,3], plasmonic metals coupled with wide band gap semiconductors utilizing hot electrons[4,5], photochemical diodes[6], z-scheme tandem cells[7-10], and inorganic/organic/hybrid multi-junction cells[11-13]. However, the large-scale production of chemical fuels relies on the development of PEC electrode based on earth abundant materials[1].

Silicon as the second most abundant element on earth has been used for photovoltaic solar cells to generate electricity because of its low cost and small band gap for solar spectrum absorption. Application of Si for water splitting is challenging due to its slow kinetics and passivation/corrosion at the Si electrolyte interface. Enabling Si for water splitting involves replacement of this problematic interface by insertion of a heterogeneous/homogeneous coating, which allows efficient light absorption, and charge separation/transportation, as well as catalytic reaction sites at the coating electrolyte interface. In other words, this coating effectively introduces two interfaces which subsequently separate the process of electricity generation at one interface (photoelectrical junction) and chemical product formation at the other (electrochemical junction).

Photoanodic water oxidation half reaction for O_2 generation from water splitting using Si is even more challenging due to, 1) the higher conduction band position of Si with respect to the water oxidation reaction potential, 2) a four-electron reaction, and 3) the surface oxidation or corrosion instead of water oxidation. To overcome these challenges, an efficient oxygen evolution reaction (OER) catalyst and a stable protection are essential.

In this work, we report our effort on synthesis and characterization of an efficient NiO_x based OER catalyst, identification of the surfactant and thermal treatment effect on its OER activity. We then integrated this active OER catalyst on a stabilized Si junction photoanode using a layered semitransparent ITO to demonstrate a stable and efficient water oxidation device.

3.2.3 Results:

3.2.3.1 Ultrathin NiO_x OER catalysts - role of surfactant and annealing temperature:

The NiO_x OER catalyst (labeled as NiO_x-TX) was synthesized by spin-coating a precursor solution of a mixture of nickel acetate ($Ni(Ac)_2$) and a non-ionic surfactant triton X-100 (TX) in ethanol on a conducting substrate and subsequent thermal decomposition as reported in ref [14]. In our experiment for a comparison, a catalyst from a precursor solution without the surfactant (labeled as NiO_x) and a precursor with only the TX surfactant in ethanol (labeled as TX) were also prepared and investigated. Morphology study using atomic force microscope (AFM) and chemical composition study using x-ray photoelectron spectroscopy (XPS) were conducted on NiO_x coated atomic flat Si (100) substrates and Au coated Ti foils (Alfa Aesar, 10385), respectively, while electrochemical studies on the NiO_x were conducted on fluorine-doped tin oxide glasses (MTI, TEC 15), as well as Ti foils and Si photoanode. Time required to decompose/anneal the spin-casted precursors was different due to the different thermal conductivity of different substrates, which is also depend on the air flow or stationary air. We found that NiO_x-TX gave the best catalytic activity annealed for 30 sec on Ti foil, which is equivalent to the one annealed for 1 min on FTO glass (Figure 2a).

Morphologies of the Si surface coated with NiO_x-TX, NiO_x, and TX annealed for 30 s at 300 ℃ are shown in Figure 1a-c. AFM studies revealed bigger grains from NiO_x-TX OER catalyst compared to that of the NiO_x and TX only samples. The presence of foreign molecules in the precursor affects the physical and morphological properties of the thin film. TX surfactant possesses a polar head group attached to a long chain aliphatic non-polar tail. Similar to the work reported by Canfield et al.[15], a metal-surfactant complex is formed. Meanwhile, the long chain of nondecomposed Ni-TX complex could also act as a spacer[16]. Thus the presence of a non-ionic surfactant TX, which bears a chain of approximately 10 ether groups, plays a crucial role in organizing the structure of the material and in creating well-defined and reproducible nanophases[17].

We use XPS to study the chemical composition of the catalysts prepared from different precursors and annealed for different time. Ni 2p spectra of bare Au substrate, TX-30s, NiO_x-30s, and NiO_x-TX-30s are shown in Figure 1d. No Ni peak was noticed on bare substrate or the TX coated substrate. O 1s spectrum revealed that the peak at a bare substrate at binding energy of

532.8 eV is probably from carbon contamination in the form of C-O. Appearance of the peak at binding energy of 530.54 eV is possibly due to the formation of Au_2O_3 during the annealing in air. Deconvolution of O 1s peaks of NiO_x-30s and NiO_x-TX-30s using classical oxygen fitting revealed the lattice oxygen (529.46 eV), hydroxyl group (531.41 eV) and surface-absorbed water (532.67 eV). The appearance of the new peak at 529.46 eV with the increasing annealing time suggests the increased lattice oxygen and the formation of NiO_x. The increasing intensity ratio between 529.46 eV and 531.41 eV further suggested a decreasing valence state of Ni. Interestingly, high resolution C 1s spectra reveal not only the presence of carbon contamination in the form of carbon-carbon bonding at binding energy of 284.8 eV, but also a peak typically recognized from carbonxylate group at binding energy around 288 eV potentially from $Ni(Ac)_2$[18]. Note that this peak was not resolved from samples made from precursors containing only $Ni(Ac)_2$ and certainly not from TX in ethanol. This is a sign of formation of Ni-TX complexes in the precursor. Higher intensity at binding energy of 284.8 eV could be a sign or more carbon concentration on the surface due to C-C or C=C groups from unfully decomposed Ni-TX complexes. Therefore, annealing for 30 s may not lead to complete removal of organic compound. Actually quantitative studies from De Jesus et al. [19] showed a decomposition of dehydrated nickel acetate occurs at 270 C in air. However, carbon residuals could potential facile the charge transfer between catalytic active sites and substrate, ease the activation process, which is noticed in the electrochemical measurement. The carboxylate component also presents in the sample prepared with higher concentration of surfactant and this peak diminishes in the precursors with only either the TX or $Ni(Ac)_2$. This fact suggests a surfactant effect on the decomposition of the nickel precursor which is believed due to the formed Ni-TX complexes.

We also use XPS to exam the annealing effect on the chemical composition of NiO_x-TX (Figure 1g). High resolution Ni 2p spectra in Figure 1g showed a more standout peak at lower energy with increased annealing time indicating a reduced valence state, which is believed to have great effect on the catalytic activity. Ni 2p spectra showed observable change in their shapes suggesting an effective annealing time effect on its chemical changes. This result is consistent with the O 1s spectrum (Figure 1h) indicating an increased intensity of lattice oxygen at binding energy of 529.46 eV. Although Ni 2p3/2 peak could be originate from different source of Ni^{2+} species, including unfully decomposed nickel acetate-surfactant complex, $Ni(OH)_2$ and NiO, one can effectively control the crystalline process and tune the catalytic activity by controlling the annealing time at a fixed temperature on the NiO_x catalyst. High resolution C 1s spectrum (Figure 1i) further showed the peak at 288 eV reduces its intensity with the increasing annealing time suggesting a more complete decomposition of precursors.

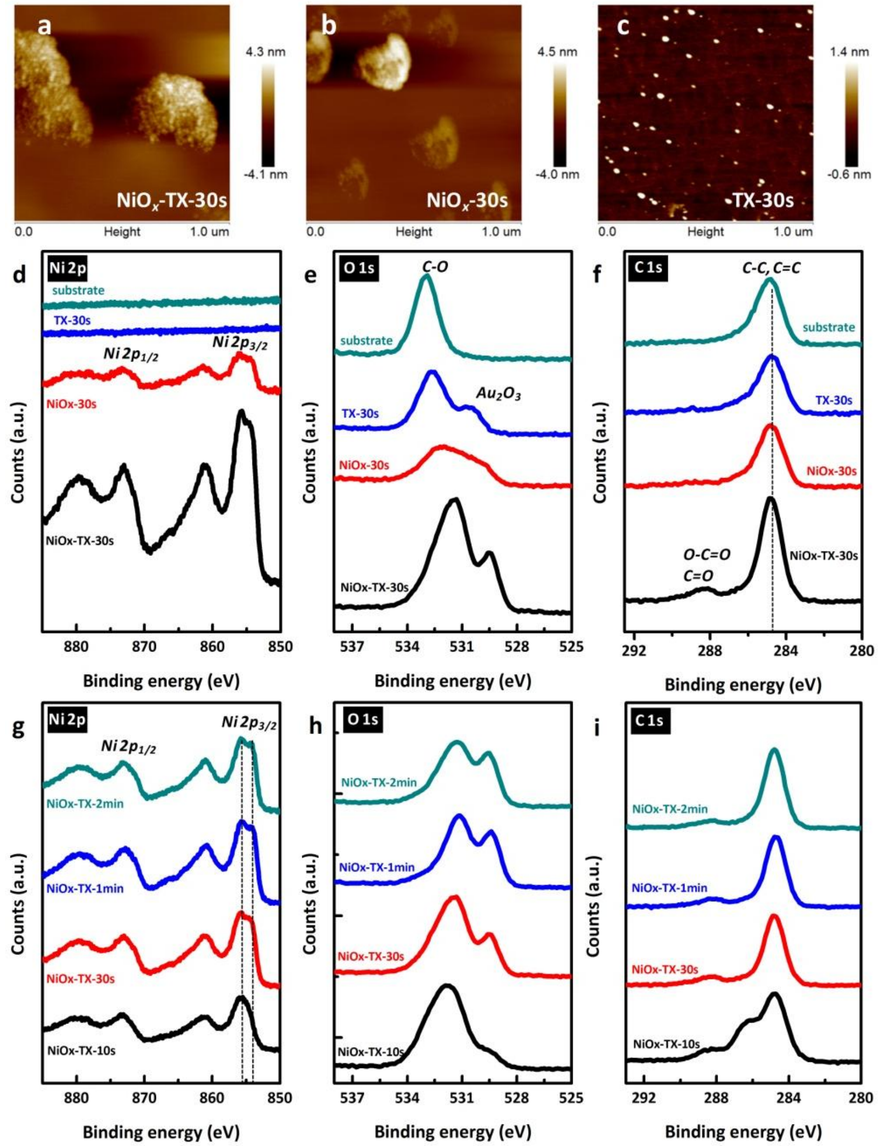

Figure 1. First row: AFM studies on catalyst (a) NiO$_x$-TX, (b) NiO$_x$, and (c) TX only. Second row: XPS spectra of (d) Ni 2p, (e) O 1s, (f) C 1s on samples studied in the first row. Third row: XPS spectra of Ni 2p (g), O 1s (h) and C 1s (i) on NiO$_x$-TX catalysts annealed for different time.

3.2.3.2 Catalyst activation, OER activity and stability:

Cyclic voltammograms (CV at a scan rate 10 mV/s) on the NiO$_x$ OER catalyst without TX in 1 M NaOH (pH=13.8) are shown in Figure 2a. Electrochemical measurement is done in 1 M NaOH electrolyte at room temperature and all the reported potential is converted to normal hydrogen electrode (NHE) unless specified. Current density and Tafel slope reported here are without iR correction on the uncompensated resistance loss. As-prepared NiO_x (black curve) shows a shoulder instead of oxidation/reduction peaks in the potential window of 0.4-0.7 V. Tafel slope of the as-prepared NiO_x is 87 mV/dec at 0.7 mA/cm^2, which resulted in an overpotential of 380 mV to drive an OER current density of 0.52 mA/cm^2. During the second scan, a more significant oxidation peak appeared at 0.58 V, as well as a slightly higher reduction peak at 0.5 V as shown in the red curve in Figure 2a. Tafel slope at 1 mA/cm^2 dropped to 57 mV/dec and current density at overpotential of 380 mV reached 3.34 mA/cm^2, shown in Figure 2b. A cyclic activation at a scan rate of 100 mV/s was then applied. After 500 cycles of activation, a slow CV scan at a scan rate of 10 mV/s was taken (magenta curve). Magnitude of the oxidation and reduction peaks was increased and the shape of the peaks became sharper with a noticeable asymmetry. Most importantly, the position of the peaks was shifted to higher potential (around 0.63 V). Improvement was also noticed on Tafel slope and overpotential (Figure 2b). Continuous activation for another 310 cycles did not further improve the catalytic activity at OER current, but a slightly shift of oxidation peak to higher potential. Note that the TX-30s sample showed a comparable current density level to that of the bare FTO within the potential window, which suggested no catalytic activity from the TX treated FTO glass. Previous results showed different phases of active NiO catalysts during water oxidation including α-$Ni(OH)_2$/γ-NiOOH and β-$Ni(OH)_2$/β-NiOOH. Importantly, α/γ transition is typically located at lower potential with a typically higher valence state of Ni (3.5-3.67) and β/β transition is typically located at higher potential with a lower valence state of Ni (2.7-3)[20]. We believe that the plateau in the CV of the as-prepared sample indicates a mixed phase of α/γ and β/β transition, which is because direct decomposition of nickle precursor did not yield a phase-pure NiO_x. The shoulder in the oxidation peak after the first scan suggests that the mixed phases still exist in the catalyst although the α/γ transition becomes stronger. Anodic shifted oxidation peak after cyclic activations suggests a phase transition from α/γ dominant to β/β dominant. Meanwhile, this result suggests that the OER activity is indefinitely maintained after 810 cycles of scan for over 5 hrs measurement. Note that anodic shifted redox peaks were noticed on sample that was re-scanned after stored in normal lab condition, which is observed on aged α-$Ni(OH)_2$ due to dehydration to β-$Ni(OH)_2$ in ambient. This aged catalyst can then transform back to α/γ due to the overcharging of the β-NiOOH[21].

On the other hand, the second CV scans on a NiO_x-TX catalyst annealed for varying time are shown in Figure 2c. Interestingly, oxidation peaks for NiO_x-TX annealed for 30 s and 1 min were located at potentials around 0.65 V and 0.63 V (Figure 2c) which was about 70 and 50 mV higher than the NiO_x case, respectively. Increasing the annealing time from 30 sec to 1 min reduced the overpotential of 357 to 341 mV and Tafel slope at 1 mA/cm^2 current density of 63 to 56 mV/dec (Figure 2d). For catalysts that were annealed for 2 and 5 mins, no significant peaks were noticed suggesting a diminished organized phase with the increased annealing time. Moreover, cyclic activation did not show improved OER activity over 1 hr cyclic scan on these two samples. Meanwhile the overpotential and Tafel slope increased to 378 mV and 64 mV/dec, respectively (Figure 2d). The position of the oxidation peaks of NiO_x-TX catalysts suggests an inherent β/β phase without cyclic activation. Presumably, this is because the surfactant has the effect of complexing the metal ions, so that the individual oxides do not form prematurely. Such complexing effect is well known in a sol-gel process. However, this sample with more than 500 cyclic scans showed a formation of a second peak at low potential, suggesting a developed phase of α/γ transition. Overheating the catalyst suppresses the magnitude of the oxidation/reduction peaks and most importantly degrades the OER activity. This overheating effect on the NiO_x activation was also noticed on gas-phase sputtered NiO_x film, where annealed films in inert gas at 400 ℃ showed significant lower OER activity and less chance to be activated within a fixed number of activation cycles than the as-sputtered ones. This data will be reported elsewhere. In summary, controlling the catalyst preparation conditions such as addition of surfactant and annealing temperature can result in an active material without going through a potentially destructive and energy-consuming activation process.

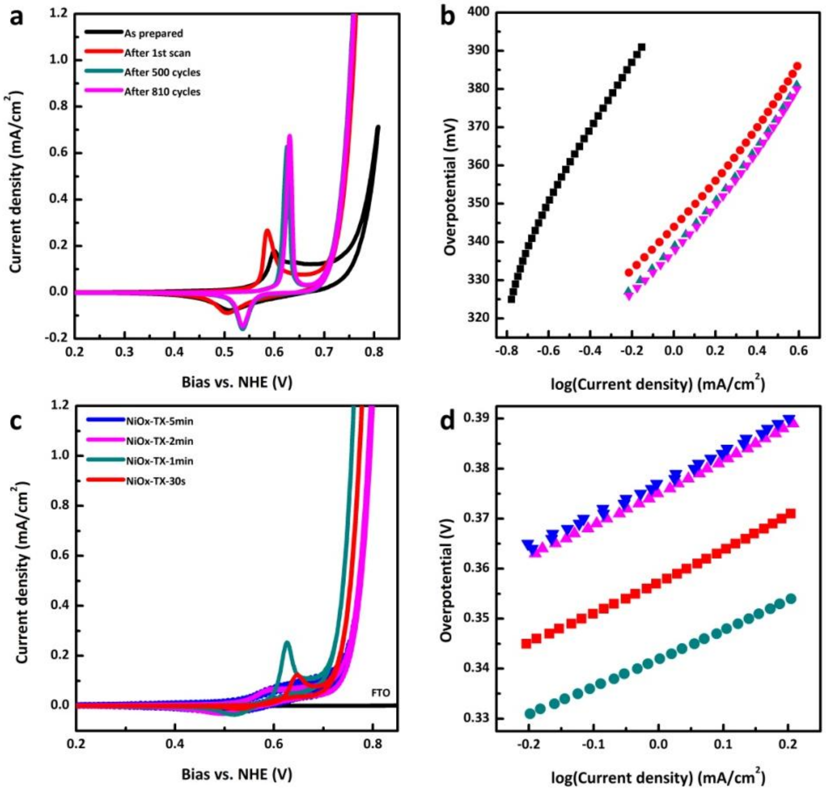

Figure 2. CV and Tafel plot on NiO$_x$ (a and b) annealed for 30 s, and NiO$_x$-TX catalyst annealed for varying time at 300 ℃ (c and d)

3.2.3.3 Si photoanode:

Strategies have been developed to enable Si-based photoanode including two-step and single-step approaches due to its intrinsic disadvantages when directly interfacing with water[22]. The two-step approach involves a protection coating using a wide-band gap semiconductor and an electrocatalyst coating. Examples include structures such as TiO_2|Ir[23], FTO|NiBi[24], and ITO|CoPi[25]. On the other hand, the single-step approach utilizes a coating that has multiple functions including conducting holes, protecting Si, and electrocatalyzing water oxidation. Coatings used before include α-Fe_2O_3[26], NiO$_x$[27], MnO_2[28], and organic compounds such as PEDOT:PSS[29]. However, the ultrathin NiO$_x$ studied in this case is not able to perform the passivation function due to the non-conformal nature on the Si surface (Figure 1a). Any exposure of Si to the extreme alkaline environment will result in etching of Si instead of forming an insulating SiO_x in near neutral environment, which is actually a well-known anisotropic texturing technique for Si microfabrication[30]. To prove this, p^+-Si directly coated with NiO_x catalysts without removing native oxides was tested. During the typical activation process, the redox peaks became more pronounced (Figure s1a). However, different from NiO_x coated FTO glass, the OER current dropped continuously (Figure s1b). Presumably, attacks on native oxides and then underneath Si may cause loss of catalysts, which is actually noticed during an in-situ x-ray absorption measurement, where Ni signal became undetectable with extended experiments (data not shown here). This resulted in a significant lower current density after the activation process (Figure s1c). To utilize the outstanding OER catalytic activity of the ultrathin alkaline catalyst, a stabilized n-Si photoanode that is chemically inert to the alkaline environment is required.

The schematic of Si based photoanode in our experiment is shown in Figure 3a. Detailed fabrication and electrode preparation can be found in the Method section. A semitransparent conducting oxide (s-TCO) based on a ITO (110 nm)|Au (5 nm)|ITO (110 nm) sandwich was used to protect the Si electrodes including n-Si, p^+-Si, and surface inverted n-Si (np^+-Si) prior to the NiO_x deposition. Average transmittance of this sandwich contact after experiencing the same annealing process of NiO_x precursor (30 s in air at 300 ℃) in the wavelength range of 360-1100 nm was 70% which is comparable to the as-deposited bare ITO (78%) (Figure 3b). Annealing on the hotplate improved the transmittance of ITO, but degraded its conductivity. On the other hand, annealed sandwich contact was able to reach a resistivity of 0.43 mΩ-cm, which was almost 6 times smaller than the annealed bare ITO (2.4 mΩ-cm). Most importantly, the bare ITO coated n-Si showed significant degradation during the measurement and this has been reported before[25]. The degradation of ITO and ITO|Si junction could become more significant in extreme alkaline environment. Despite the considerable light loss, lower ohmic loss and stabilized Si photoanode were able to be achieved using the sandwich semitransparent conducting oxide (Figure s2b). Besides passivation of Si from contacting the oxidative electrolyte, this s-TCO successfully decouples the photovoltaic cell and the overlaying electrocatalyst which allows in-situ characterization of photovoltaic performance and also the pre-activation of the OER electrocatalyst.

Photovoltaic measurement was first conducted in-situ in the measurement setup filled with the electrolyte with an IR filter under masked illumination. Schottky junction between ITO|Au|ITO and n-Si was able to provide a small V_{oc} due to the Fermi level pinning. Si np^+ junction exhibited a better photovoltaics performance with a larger V_{oc} and J_{sc} due to the improved junction configuration (Figure 3c).

Cyclic activation of the NiO_x catalyst was then conducted prior to the PEC measurement by connecting the working electrode to the activation contact (ITO|Au|ITO) in a three-electrode configuration in 1 M NaOH electrolyte with ambient light. A typical series of CV scans for varying activation cycles is shown in Figure 3d. CV scans at a fast scan rate (100 mV/s) were able to activate the NiO_x OER catalyst within the first 40 cycles for 7 mins. Positions of the oxidation peak initially dropped and then shifted to slightly higher potential (0.63 V, red curve in Figure 3e) indicating an inherent and enhanced β/β transition. This observation is consistent with the experiments conducted on FTO glasses. However, no significant shift in the reduction peak position (black curve in Figure 3e) was noticed indicating an enlarged difference between oxidation and reduction peaks with the increasing activation cycles. One can also see an increase of the magnitude of the oxidation peaks from 0.27 to 4.28 mA/cm^2 with the varying activation cycles and a saturation began to appear after 40 cycles of scan (red curve in Figure 3f). Most importantly, OER current densities at an overpotential of 493 mV first dropped during the first 3 cycles of scan and then immediately shoot up and saturation after 40 cycles of scan (red curve in Figure 3g). Also, the overpotential to reach 1 mA/cm^2 OER current density in the oxidation branch increased initially and dropped 75 mV eventually after 40 activation cycles (black curve in Figure 3g). Therefore, activation of the NiO_x OER catalyst within the potential window for 40 cycles was really effective to improve the catalytic activity, where water oxidation current density at an overpotential of 493 mV increased about 4 times from 3.2 to 12.1 mA/cm^2.

PEC performances of the activated electrodes were then measured by switching the working electrode from the activation contact to the back contact (Figure 3a) and CV scans under illumination and in dark are shown in Figure 3h. The reduced onset potential and the overpotential needed to drive certain current density compared to the one measured directly through the activation contact (dark cyan curve in Figure 3h) were due to the photovoltage generated from the ITO|n-Si Schottky junction (magenta curve in Figure 3h) and the np$^+$-Si junction (black curve in Figure 3h). Current saturation was observed within a low bias (< 500 mV) for the np$^+$-Si junction based photoanode. Tafel slope at the current density of 1 mA/cm^2 on ITO|Au|ITO|NiO_x is 63.2 mV/dec, n-Si|ITO|Au|ITO|NiO_x is 203.9 mV/dec, and np$^+$-Si|ITO|Au|ITO|NiO_x is 97.4 mV/dec (Figure 3i).

The mechanism is illustrated in Figure 3j using the energy band diagrams based on the actual measurement results shown in Figure 3h. To maintain a current density of 1 mA/cm^2 on NiO_x coated ITO|Au|ITO contact, an overpotential of at least 350 mV was typically required which includes the activation overpotential and uncompensated resistance loss. Note that calculation showed the OER reaction potential at pH=13.8 is located at 0.415 V. This results in an external bias of 0.76 V is needed to drive this amount of OER current density. When an n-Si was added to the backside of ITO, the Schottky junction and thus the V_{oc} (~270 mV) up on illumination was able to shift the external bias needed to drive 1 mA/cm^2 current density cathodically by 220 mV. On the other hand, when a np+-Si junction was added to the ITO, this structure was able to further shift the onset potential cathodically, as well as the bias needed to drive the OER current density by 380 mV under illumination. This resulted in a reduced external potential required to drive the OER current. Higher Tafel slope on Si photoanode was believed due to the serious resistance loss across the Si junction as well as the Si ITO interface (Rc_1, Rs_1, Rc_2 and Rs_2 in Figure 3j). This can be also noticed from the finite slope of IV curves crossing the x-axes in Figure 3c.

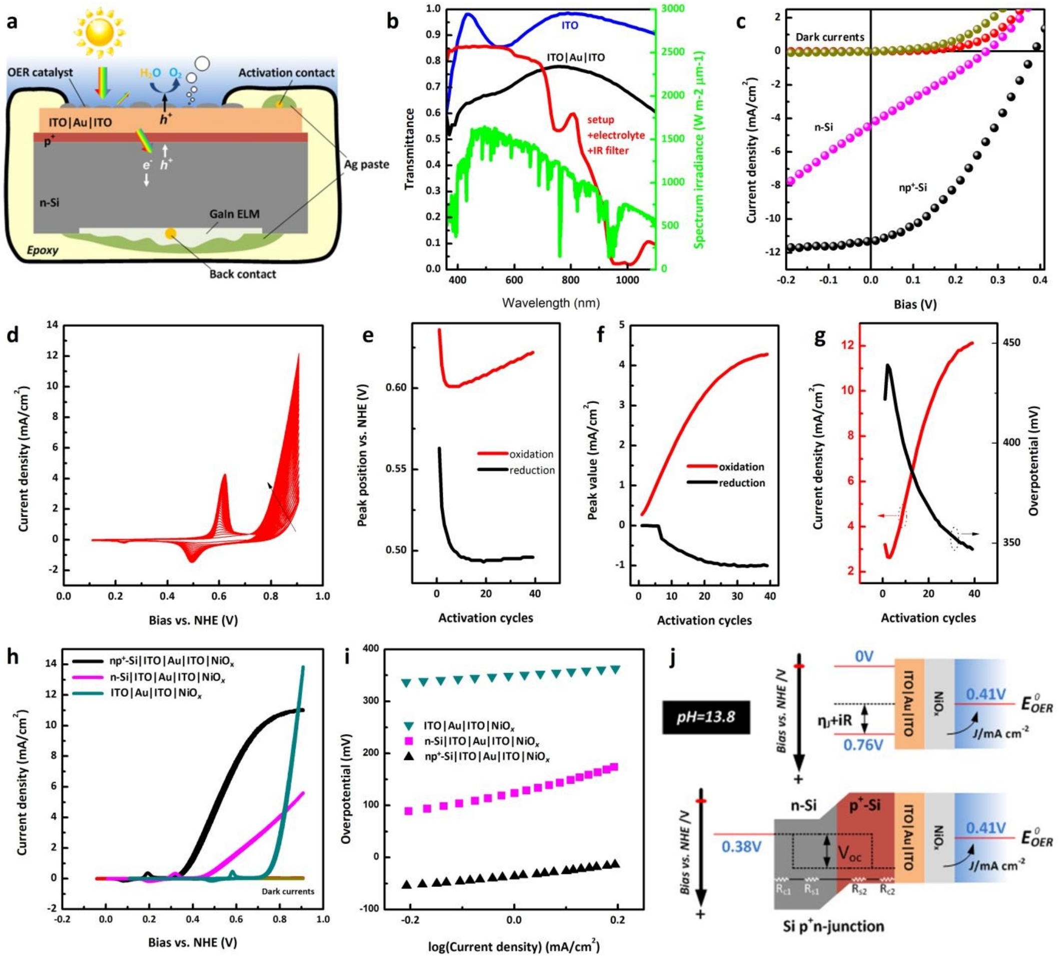

Figure 3. (a) Schematic of Si np$^+$-junction based photoanode. (b) transmittance of s-TCO, bare ITO, measurement setup, and AM 1.5G solar irradiance spectrum (green curve, data from NREL). (c) Comparison of photovoltaic performances of n-Si|ITO|Au|ITO Schottky junction and Si np$^+$-junction device measured under attenuated light. (d) Typical NiO_x OER catalyst activation process with a CV scan rate of 100 mV/dec for 40 cycles through the activation contact (shown in a), where one can see a shift of oxidation/reduction peak position (e), magnitude (f) as well as water oxidation current density at 493 mV overpotential (g) with respect to the activation cycles. Comparison of PEC photoanodes performance (h) and Tafel slope around 1mA/cm^2 current density (i). (j) Energy band diagram of NiO_x OER catalyst on conducting substrate (top) and on np$^+$-Si junction photoanode (bottom). Energy band diagram for n-Si is not shown.

3.2.3.4 np$^+$-Si|ITO|Au|ITO|NiO$_x$ photoanode:

Detailed studies on the np$^+$-Si based photoanode will be presented in this section including light intensity, stability and pH effects. Light intensity effect on the solar cell performance was studied by applying a series of neutral density (ND) filters with the sample in the measurement setup where light was attenuated. For comparison, samples were also measured in air where unmasked solar simulated light intensity at the sample position was measured 1 sun intensity (100 mW/cm^2, navy blue curve in Figure 4a). Under this standard condition, a V_{oc} of 424 mV, a J_{sc} of 22.43 mA/cm^2, a fill factor (FF) of 30.79% and a conversion efficiency of 2.92% were achieved using the np$^+$-Si photovoltaic cell. While under attenuated light in the measurement setup where intensity was measured 51.2% of the 1 sun intensity, a V_{oc} of 388 mV, a J_{sc} of 11.30 mA/cm^2, a FF of 36.97% and a conversion efficiency of 3.17% were achieved (black curve in Figure 4a). Note that the optical loss due to the s-TCO is not considered in the calculation. V_{oc} increased linearly, while J_{sc} increased exponentially with the inreasing light intensity in logarithm scale (Figure 4d).

PEC performance was also measured under different light intensities (Figure 4b). Saturation of photocurrent at a low overpotential was noticed due to the light limited carrier generation. The solar fuel conversion efficiency for O_2 generation under 0.51 sun illumination can be calculated by

$$SCE_{O_2} = \frac{J_{H_2O/O_2} \cdot |V_{onset}| \cdot FF}{I_{ph}}$$

where E^0 is the equilibrium water oxidation potential at 1 M NaOH solution, which is calculated 0.415 V, $J_{H2O/O2}$ is the current density at the E^0 , and V_{onset} is the overpotential when water oxidation current starts typically after the Ni oxidation peak. The data used for this efficiency calculation was based on a three-electrode configuration. Therefore half reaction on the photoanode was only considered. The efficiency is calculated 0.7% (inset Figure 4b).

Magnified Ni reduction/oxidation region in Figure 4b is shown in Figure 4c. Reduced V_{oc} with reduced light intensity effectively shifted the Ni reduction/oxidation peaks and onset water oxidation potential to higher potentials. Besides the reduction/oxidation peak position, the magnitude of the peaks was also effectively reduced and the shape of the peaks was also broadened with the decreasing light intensity. Similar to light intensity dependent J_{sc} (blue curve in Figure 4d), saturation current density measured at 0.908 V decreased exponentially with the decreasing light intensity (logarithm scale, Figure 4e).

The chemical stability of the np^+-Si|ITO|Au|ITO|NiO_x photoanode was studied to ensure the photoelectrode can be used in oxidative environment with reasonable lifetime. Figure 2f shows the comparison of CV scans (10 mV/sec) taken before and after 310 cycles of CV studies (100 mV/sec) under 0.51 sun illumination. The current density was normalized due to a slight variance in the position dependent light intensity. Ni reduction/oxidation peaks showed anodic shift while current density was reduced within the bias window. No saturation was noticed at 493 mV overpotential in the CV taken after 310 cycles of scans. Analysis showed increased Tafel slope from 97.4 mV/dec to 105.2 mV/dec and current density drop 5% at 493 mV overpotential. To further understand the degradation, solid state photovoltaic IV were measured under illumination and result revealed that no degradation on the Si np^+-junction photovoltaic unit after all the PEC measurement (red and blue curves in Figure 4g). This also suggested no significant conductivity change was noticed in the s-TCO film[25]. Therefore, the performance degradation of the photoanode (Figure 4f) could possibility have taken place at the ITO|NiO_x interface and/or NiO_x OER catalyst, indicating a well-protected Si substrate by the s-TCO.

Resistive (iR) losses from p^+-Si substrate and ITO|Au|ITO are negligible based on the geometry and resistivity. However, iR fitting on the CV curves measured after activation of the OER catalyst showed about 8-9 ohm loss in the p^+-Si|ITO|Au|ITO|NiO_x electrode (black curve) compared to ITO|Au|ITO|NiO_x electrode (red curve in Figure 4h). This number suggested an additional loss mechanism is involved in the electrode since no changes were made to the cell configuration during the switching of contact and thus no changes to the uncompensated solution resistance loss. This additional loss is recognized from the substrate including effect from the native oxide between ITO and Si, as well as between the GaIn eutectic liquid metal (ELM) and the Si.

As-prepared photoelectrodes were also measured in a neutral pH environment made of PBS buffered Na_2SO_4 electrolyte (pH=7.2). Activation of the catalyst was also conducted in this neutral electrolyte. Different from the activation behavior typically noticed in NaOH solution (Figure 3d), activation CV scans in neutral pH did not show improved catalytic activity. Photoanodic CV curves of n-Si|ITO|Au|ITO|NiO_x photoanodes, as one example, after activation in a different pH environment are shown in Figure 4i. Both electrodes showed significant increasing current density after the water oxidation potential. No Ni reduction/oxidation peaks were noticed on samples measured in the neutral pH environment. Overpotential needed to drive 1 mA/cm^2 current density for water oxidation is much larger (417 mV) than the sample measured in NaOH electrolyte (127 mV). This is presumably due to the lower activity of the alkaline metal oxide catalyst in lower pH electrolyte, lower concentration of available OH^- ions, and potentially poisoning of the catalyst in PBS buffered electrolyte.

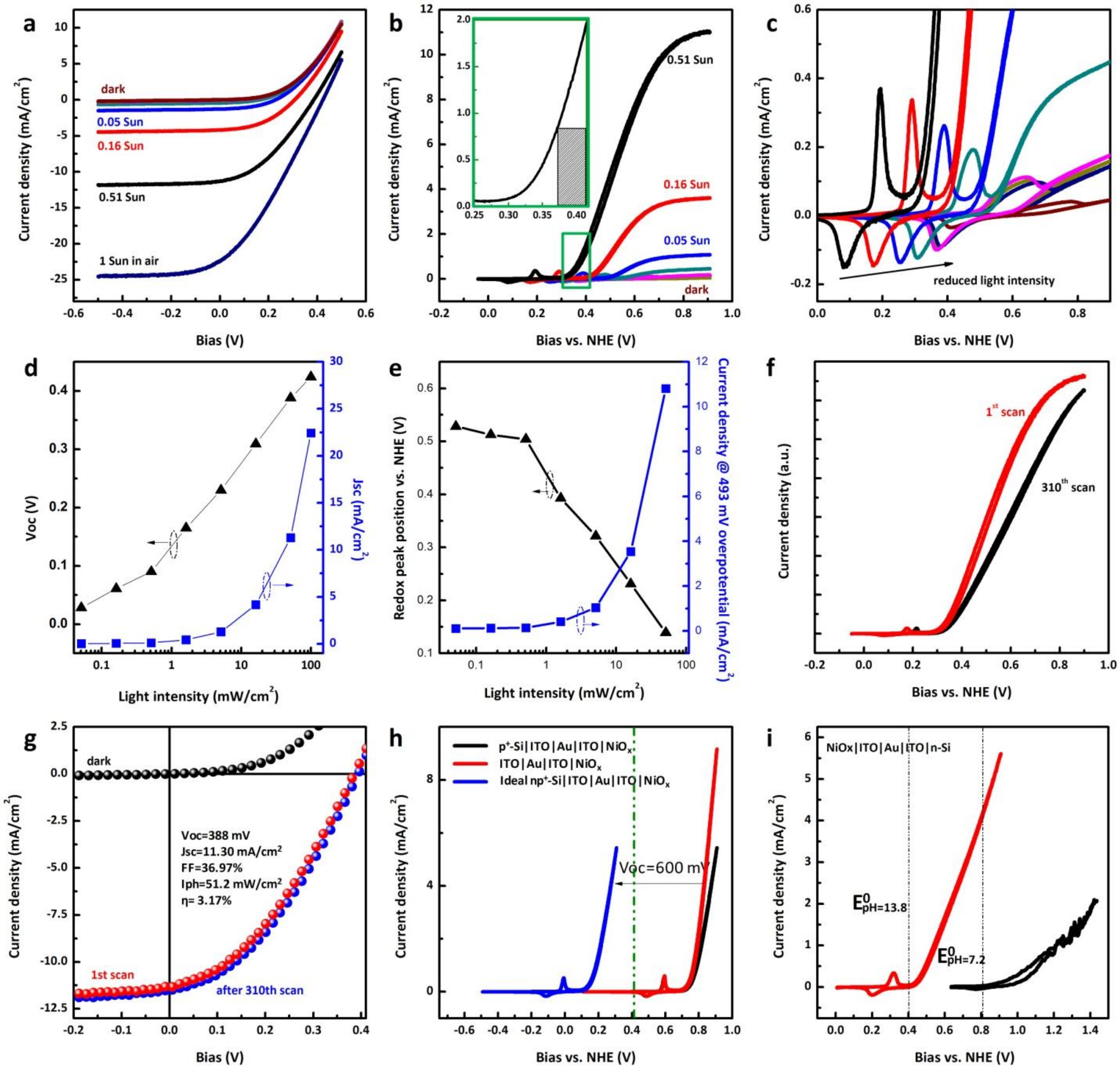

Figure 4. (a) IV of np$^+$-Si vs. light intensity measured in PEC measurement setup. (b) CV of np$^+$-Si|ITO|Au|ITO|NiO$_x$ photoanode vs. light intensity. (c) Magnification on the redox region before water oxidation current showing changes on the redox peaks and onset current with the change of light intensity. (d) Light intensity vs. V_{oc} and J_{sc} on solid state device. (e) Light intensity effect on the saturation current density at 493 mV overpotential and reduction/oxidation position of Ni. (f) Degradation of photoanode after 310 cycles CV scan under 0.51 sun illumination. (g) Stable solar cell performance indicates no degradation in the Si np$^+$-junction and ITO|Au|ITO coating. (h) CV comparison showing additional ohmic loss due to native oxides. Red curve measured through the activation contact and black curve measured through the back contact of p$^+$-Si on p$^+$-Si|ITO|Au|ITO|NiO$_x$ photoelectrode. (i) CV scans showing the pH effect on the photoanodic performance.

3.2.4 Discussion

In summary, we report our effort on the development of a Si based photoanode protected by a semi-transparent sandwiched ITO|Au|ITO layer and catalyzed by a solution-casted ultrathin NiO_x OER catalyst. This device shows a current density of 1.98 mA/cm^2 at the water oxidation potential and thus a SCE_{O2} efficiency of 0.7% (inset Figure 4b) under low light illumination. Comparative performances of previous Si based photoanodes for water oxidation is summarized with current-potential (vs. NHE) curves overlaid with each other in Figure 5. One may not directly compare the performance through the IV curve due to different measurement environment. However, as shown in the table, the device presented in this work shows comparable current density at water oxidation potential to others despite it is measured under 0.51 sun intensity due to the outstanding OER catalytic activity of the ultrathin NiO_x and stable s-TCO coating. Please note that the data summarized in the table are not the reported data from the original article, but directly calculated instead from the curve in the Figure.

Among the four elements in the first row transition metals (Mn, Fe, Co and Ni) which hold great promises to replace noble metal based OER catalysts such as Ir and Ru for large-scale solar fuel conversion, Ni based OER catalyst is believed to outperform others based on theoretical and experimental studies[31,32]. Activity of the NiO_x OER catalyst prepared from solution-casted precursors depends greatly on the annealing process. Overheating the precursors with the hope of improving crystallinity even at a considerably low temperature can degrade its catalytic activity. β-$Ni(OH)_2$/β-NiOOH is recognized as a more active species in the NiO catalyst. Activation process is typically used on amorphous catalysts either through a constant or a cycling current/bias[33-35]. Conditioning using a constant anodic current on a Ni-Borate OER catalyst can also induce a change of structure and valence state of Ni[34]. This conditioning on the catalyst enhanced the activity was greatly depend on the concentration of the conditioning solution. Yeo and Bell prepared β-$Ni(OH)_2$ by cycling the Ni metal electrode from the α-$Ni(OH)_2$ in concentrated KOH for up to 15 hrs[35]. The β-$Ni(OH)_2$ from their experiment also showed anodic shifted reduction/oxidation peaks. Activation process is also applied to other catalysts[36]. Addition of foreign molecules by forming metal-surfactant complexes and controlling thermal treatment process can effectively lower the energy input needed to achieve an activate catalyst. Ultimately, amorphous electrocatalysts without activation process is desired through an introduction of doping[37] or carbon-composites[38]. Alternatively, mesoporous catalyst[39,40] can be also applied. This can be realized by impregnation and calcinations of precursors on a mesoporous template, providing an enhanced surface reaction sites and potentially photon trapping.

Utilizing a best reported np^+-Si junction with a 600-mV Voc, 30-mA/cm^2 photocurrent density, and stabilized by a TCO coating with a minimum light loss, one can further shift the onset potential cathodically. A minimum 10 mA/cm^2 photocurrent at E_{OER} can be achieved based on rough estimation on the blue curve in Figure 4h. However, the maximum SCE_{O2} efficiency is limited by a single junction Si solar cell due to the large overpotential needed to drive efficient water oxidation current using earth abundant transition metal based catalysts, which typically need ~400 mV to drive 8.13 mA/cm^2 OER current[41]. This will result in a maximum SCE_{O2} efficiency of 3.2% using this ideal single Si junction photovoltaic cell and the reported ultrathin NiO_x OER catalyst in this work.

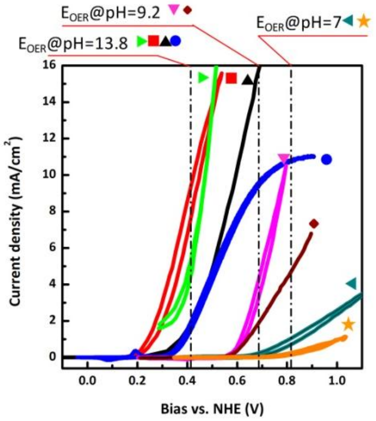

	Structure (ref.#)	Current density (mA/cm²)@ E_{OER}	Tafel slope‡ (mV/dec)@ 1 mA/cm²
▲	n-Si|α-Fe_2O_3 (ref.31)	1.86	132.2
■	n-Si|TiO_2|Ir (ref.26)	8.34	107.5
►	n-Si|MnO (ref.30)	5.3	-
★	n-Si|NiO_x (ref.20)	0.13	129
◄	npp^+-Si|ITO|CoPi (ref.28)	0.86	307.9
▼	npp^+-Si|FTO|NiBi (ref.27)	3.81	72.5
◆	npp^+-Si|FTO|NiFeO (ref.27)	1.9	
●	np^+-Si|ITO|Au|ITO|NiO_x (this work)	1.97 (0.51 sun)	97.4

‡ Tafel slope is measured based on extracted data in the figure on the left

Figure 5. Comparative performance of Si photoanode structures

3.2.5 Methods:

Ultrathin NiO_x **OER catalyst preparation.** All chemicals were used as it is without pre-purification. Aqueous chemical precursors were prepared by mixing nickel acetate (50 mM) in ethanol with a non-ionic surfactant Triton-X 100 (TX, 0.6 mM) with average molar weight of 624.82 followed by a through stirring of the mixture to obtain a clear solution[14]. The deposition of NiO_x on all different substrate was carried out by dropping 100 μL precursor, spin-casting at 3000 rpm for 90 sec, followed by heating on a hotplate at atmosphere for various time from 10 sec to 5 min to remove excessive solvent at 300 ℃ on Ti foil, Si and FTO glass.

Device fabrication. all Si substrates were diced into 0.5 × 0.5 inch^2 and cleaned using diluted HNO_3, acetone, and isopropyl alcohol with intermediate DI water rising and ultrasonication. Si substrates used for study included boron doped p^+-Si with a bulk resistivity of 0.05 Ω-cm and phosphors doped n-Si with a bulk resistivity of 0.3-0.5 Ω-cm (Universitywafers). Indium tin oxide and gold (Kurt J. Lesker) sandwich (ITO|Au|ITO) structure (100 nm/5 nm/100 nm) was deposited using RF magnetron sputtering (Denton). This contact was thermally annealed at 300 ℃ for 30 s to improve the transmittance and conductivity. To realize a p^+n-Si junction, we started with an n-Si wafer and diffusion process was performed using a boron-containing spin-on dopant (SOD, Filmtronics, Inc.). 400 μL SOD solution was first spin-coated on a 2" Si dummy wafer at 3000 rpm for 15 sec. Dummy wafer with SOD and samples were immediately transferred to a rapid thermal annealing (RTA) furnace. SOD coated dummy wafer and samples were facing each other separated by quartz spacers with a thickness of 1 mm. The diffusion was then conducted at 950 ℃ for 120 sec under a constant flow of N_2 at 0.85 L/min. After diffusion process, samples were unloaded from the furnace and immersed in buffered HF etchant to remove oxides and residuals. Finally, backside the diffused samples (100 nm) were then etched using a reactive ion plasma etching (Oxford 80 plus) with CF_4/O_2 gas at a rate of nm/sec for 5 min while the front side was protected using photoresist 1818. GaIn eutectic liquid metal (ELM) contact was then scratched into Si followed by attaching a metal wire through an Ag paste (Tedpella 16040-30). Activation contact was also made by attaching a metal wire using Ag paste. Samples made on Ti foil were fixed on a homemade sample holder with front side of exact 1 cm by 1 cm exposed to the electrolyte. Samples on FTO glass were fabricated by attaching a Cu wire to the sample surface using silver paste (Ted Pella), which could provide mechanical strength to hold wires to the substrate. Samples were then embedded in Epoxy (Hysol C1) with only the NiO_x exposed to the electrolyte. The Cu wire was enclosed in a high-grade polystyrene pipette tip instead of a glass tube to avoid etching and introduction of additional contamination to the measurement. Epoxy was dried for overnight before measurement. Sample areas were then measured through the digital images using Photoshop.

Solar cell and photoelectrode characterization. Current-voltage characteristics of the Si solar cells with ITO|Au|ITO semitransparent top contact and buried junction photoelectrodes with NiO_x OER catalysts were measured using a two-channel potentiostat (Digi-Ivy DY2300). AM 1.5 illumination was achieved with a 150-W xenon-lamp-based solar simulator (Newport Corporation) with an AM 1.5 filter. The light intensity on the masked light beam was calibrated using Si photoadiode. Effect from the measurement reactor, IR filter, and electrolyte on the light intensity was also measured. Transmittance of the three components was measured and shown in Figure 3b. Major loss is because of the water absorption, which can be seen in Figure s1. The calculated light intensity based on water absorption coefficient reported by Hale and Querry[42] and the measured light intensity showed great consistency. In addition, light intensity modulation also includes reflection at interfaces, scattering at particles, diffusion in random directions and absorption of other components. Calculations based on a calibration Si photodiode showed about 48.8% light loss under masked illumination, resulting in a light intensity of 51.2 mW/cm^2 at sample position in the measurement setup.

Electrochemical study was conducted using DY2100B potentiostat from Digi-Ivy in a three-electrode configuration. All the measurement were conducted in 1 M NaOH solution (with 17.6 Mohm-cm deionized water) at room temperature in a Taflon container to avoid excessive ions introduced from etching glassware at this extreme alkaline condition. A Hg/HgO with 1 M NaOH electrode (CH Instruments, CHI 152) and a Pt coil were used as a reference electrode and a counter electrode. The reference electrode was placed very close to the working electrode surface to minimize any uncompensated solution resistance loss and the distance between RE and WE was fixed between measurements. All the potential reported here is verses Hg/HgO 1M NaOH solution. The equilibrium oxygen electrode potential is E^0=0.415 V vs. NHE at this condition. The oxygen evolution overpotential is calculated $E-E^0$. Electrolyte was mechanically agitated and purged with N_2 gas before and during measurement. Data collection was conducted using DY2100B software from Digi-Ivy.

Surface characterization. The X-ray photoelectron spectroscopy measurements were conducted on a Kratos spectrometer (AXIS Ultra DLD) with monochromatic Al Kα radiation (hν=1486.69 eV) and a concentric hemispherical analyzer. Atomic force microscopic measurement: A tapping mode atomic force microscope (AFM, Veeco scanning probe microscope) equipped with standard silicon probe (Umasch NSC15/no Al) was also used to evaluate the surface nanoscale topological difference between the thin film coatings. Raw data collected by AFM were processed using NanoScope Software; surface roughness and grain size were obtained using NanoScope Analysis software.

Extracting data from reported IV curves: curves were extracted from corresponding published articles using MATLAB Grabit developed by Jiro Doke download link http://www.mathworks.us.

3.2.6 References:

(1) Gray, H. B. *Nat. Chem.* **2009**, *1*, 7.

(2) (a) Chen, X.; Liu, L.; Yu, P. Y.; Mao, S. S. *Science* **2011**, *331*, 746 (b) Yang, X.; Wolcott, A.; Wang, G.; Sobo, A.; Fitzmorris, R. C.; Qian, F.; Zhang, J. Z.; Li, Y. *Nano Lett.* **2009**, *9*, 2331.

(3) (a) Lee, J.; Mubeen, S.; Ji, X.; Stucky, G. D.; Moskovits, M. *Nano Lett.* **2012** (b) Mubeen, S.; Lee, J.; Singh, N.; Kramer, S.; Stucky, G. D.; Moskovits, M. *Nat. Nanotechnol.* **2013**, *advance online publication*.

(4) Haussener, S.; Xiang, C.; Spurgeon, J.; Ardo, S.; Lewis, N.; Weber, A. Z. *Energy Environ. Sci.* **2012**.

(5) (a) Sasaki, Y.; Kato, H.; Kudo, A. *J. Am. Chem. Soc.* **2013** (b) Mayer, M. T.; Du, C.; Wang, D. *J. Am. Chem. Soc.* **2012**, *134*, 12406 (c) Tada, H.; Mitsui, T.; Kiyonaga, T.; Akita, T.; Tanaka, K. *Nat. Mater.* **2006**, *5*, 782 (d) Khaselev, O.; Turner, J. A. *Science* **1998**, *280*, 425.

(6) (a) Rocheleau, R. E.; Miller, E. L.; Misra, A. *Energy & Fuels* **1998**, *12*, 3 (b) Esiner, S.; van Eersel, H.; Wienk, M. M.; Janssen, R. A. J. *Adv. Mater.* **2013**, n/a (c) Reece, S. Y.; Hamel, J. A.; Sung, K.; Jarvi, T. D.; Esswein, A. J.; Pijpers, J. J. H.; Nocera, D. G. *Science* **2011**, *334*, 645.

(7) Lewis, N. S. *Science* **2007**, *315*, 798.

(8) Trotochaud, L.; Ranney, J. K.; Williams, K. N.; Boettcher, S. W. *J. Am. Chem. Soc.* **2012**, *134*, 17253.

(9) Lyons, M. E. G.; Brandon, M. P. *Int. J. Electrochem. Sci.* **2008**, *3*, 1386.

(10) Bode, H.; Dehmelt, K.; Witte, J. *Electrochim. Acta* **1966**, *11*, 1079.

(11) Walter, M. G.; Warren, E. L.; McKone, J. R.; Boettcher, S. W.; Mi, Q.; Santori, E. A.; Lewis, N. S. *Chem. Rev.* **2010**, *110*, 6446.

(12) Canfield, G. M.; Bizimis, M.; Latturner, S. E. *Chem. Mater.* **2009**, *22*, 330.

(13) Matejka, P.; Vlckova, B.; Vohlidal, J.; Pancoska, P.; Baumruk, V. *J. Phys. Chem.* **1992**, *96*, 1361.

(14) Stathatos, E.; Lianos, P.; Tsakiroglou, C. *Microporous Mesoporous Mater.* **2004**, *75*, 255.

(15) Kim, I. T.; Nunnery, G. A.; Jacob, K.; Schwartz, J.; Liu, X.; Tannenbaum, R. *J. Phys. Chem. C* **2010**, *114*, 6944.

(16) De Jesus, J. C.; González, I.; Quevedo, A.; Puerta, T. *J. Mol. Catal. A: Chem.* **2005**, *228*, 283.

(17) Znaidi, L.; Soler Illia, G. J. A. A.; Benyahia, S.; Sanchez, C.; Kanaev, A. V. *Thin Solid Films* **2003**, *428*, 257.

(18) Sun, K.; Pang, X.; Shen, S.; Qian, X.; Cheung, J. S.; Wang, D. *Nano Lett.* **2013**, *5*, 2064.

(19) Chen, Y. W.; Prange, J. D.; Dühnen, S.; Park, Y.; Gunji, M.; Chidsey, C. E. D.; McIntyre, P. C. *Nat. Mater.* **2011**, *10*, 539.

(20) Cox, C. R.; Winkler, M. T.; Pijpers, J. J. H.; Buonassisi, T.; Nocera, D. G. *Energy Environ. Sci.* **2012**, *6*, 532.

(21) Pijpers, J. J. H.; Winkler, M. T.; Surendranath, Y.; Buonassisi, T.; Nocera, D. G. *Proc. Natl. Acad. Sci. USA* **2011**, *108*, 10056.

(22) Jun, K.; Lee, Y. S.; Buonassisi, T.; Jacobson, J. M. *Angew. Chem. Int. Ed.* **2012**, *51*, 423.

(23) Sun, K.; Park, N.; Sun, Z.; Zhou, J.; Wang, J.; Pang, X.; Shen, S.; Noh, S. Y.; Jing, Y.; Jin, S.; Yu, P. K. L.; Wang, D. *Energy Environ. Sci.* **2012**, *5*, 7872.

(24) Strandwitz, N. C.; Comstock, D. J.; Grimm, R. L.; Nichols-Nielander, A. C.; Elam, J.; Lewis, N. S. *J. Phys. Chem. C* **2013**, *117*, 4931.

(25) Mubeen, S.; Lee, J.; Singh, N.; Moskovits, M.; McFarland, E. W. *Energy Environ. Sci.* **2013**, *6*, 1633.

(26) Allongue, P.; Costa-Kieling, V.; Gerischer, H. *J. Electrochem. Soc.* **1993**, *140*, 1018.

(27) Sakaino, K.; Kawabata, Y.; Adachiz, S. *J. Electrochem. Soc.* **2000**, *147*, 1530.

(28) Provazi, K.; Giz, M. J.; Dall'Antonia, L. H.; Córdoba de Torresi, S. I. *J. Power Sources* **2001**, *102*, 224.

(29) (a) Bockris, J. O. M. *J. Chem. Phys.* **1956**, *24*, 817 (b) Subbaraman, R.; Tripkovic, D.; Chang, K.-C.; Strmcnik, D.; Paulikas, A. P.; Hirunsit, P.; Chan, M.; Greeley, J.; Stamenkovic, V.; Markovic, N. M. *Nat. Mater.* **2012**, *11*, 550.

(30) (a) Lu, P. W. T.; Srinivasan, S. *J. Electrochem. Soc.* **1978**, *125*, 1416 (b) Bediako, D. K.; Lassalle-Kaiser, B.; Surendranath, Y.; Yano, J.; Yachandra, V. K.; Nocera, D. G. *J. Am. Chem. Soc.* **2012**, *134*, 6801 (c) Yeo, B. S.; Bell, A. T. *J. Phys. Chem. C* **2012**, *116*, 8394.

(31) Vrubel, H.; Hu, X. *Angew. Chem. Int. Ed.* **2012**, n/a.

(32) Smith, R. D. L.; Prévot, M. S.; Fagan, R. D.; Zhang, Z.; Sedach, P. A.; Siu, M. K. J.; Trudel, S.; Berlinguette, C. P. *Science* **2013**, *340*, 60.

(33) Liang, Y.; Li, Y.; Wang, H.; Zhou, J.; Wang, J.; Regier, T.; Dai, H. *Nat. Mater.* **2011**, *10*, 780.

(34) (a) Kibsgaard, J.; Gorlin, Y.; Chen, Z.; Jaramillo, T. F. *J. Am. Chem. Soc.* **2012**, *134*, 7758 (b) Kibsgaard, J.; Chen, Z.; Reinecke, B. N.; Jaramillo, T. F. *Nat. Mater.* **2012**, *11*, 963.

(35) Bard, A. J.; Fox, M. A. *Acc. Chem. Res.* **1995**, *28*, 141.

(36) Hale, G. M.; Querry, M. R. *Appl. Opt.* **1973**, *12*, 555.

CHAPTER 4

4.1 Conclusions

To enable Si for solar fuel cell to realize artificial photosynthesis where solar energy is converted and stored in chemical bonds, technologies have to be developed to achieve an efficient, cost-effective, and durable devices. As a widely used material in the photovoltaic industry, Si has demonstrated great potential due to its abundance on earth and a small energy band gap. Interfaces, when Si is being placed in water to split water for H_2 fuel, need to be engineered. In this thesis, heterogeneous coating using nanostructured earth abundant metal oxides to replace the Si water interface is studied. An n-type ZnO on p-type Si photocathode and a p-type catalytic NiO on n-type Si photoanode are focused. The heterojunction is able to improve the slow charge transfer kinetics of Si and thus higher solar fuel conversion efficiency and to protect the Si from self-passivation/corrosion for elongated lifetime to operate in water. Further improvements are made through a nanotextured surface and a built-in Si junction. Four major contributions have been made through this thesis work.

Branched nanostructure: solution phase integration of nanowires on nanowires provides flexibility on integration of different functionalities. A photodetector and a photocathode based on this nanotree structure are successfully demonstrated.

Sol-gel NiO enabled Si: non-stoichiometric NiO film is directly coated on polished Si without removing native oxides. This structure demonstrates an activated n-Si photoanode with a reduced on-set potential below the water oxidation potential without an anodic activation in a neutral environment. Highly transparent uniform NiO coating maximized the light arrives at the Si. The Schottky junction between NiO and Si can effectively separate the charges effectively. This structure is one of the first demonstrations of transition metal oxides protected/catalyzed n-Si photoanode.

NiRuO composite from co-sputtering: Ru or RuO_2 directly coated n-Si does not allow an efficient and stable photoanode, even they are considered as the best OER catalyst. Mixing RuO_2 with NiO using co-sputtering technique allows the integration of the high activity of RuO_2 to the stable NiO. Gas-phase deposition also allows a uniform coating on a high-profile nanotextured surface which has better light absorption and surface reaction sites. Photocurrent density measured in a neutral environment showed nearly more than 10 times enhancement than the sol-gel NiO coated polished crystal n-Si photoanode.

Ultrathin solution casted NiO on a layered ITO protected build-in Si junction for efficient solar water oxidation: the activity of an ultrathin NiO from solution-casted method can be effectively tuned by addition of the surfactant and the thermal treatment process. This effect is successfully identified in this thesis work. An ITO based semi-transparent and stable coating is used to protect a surface inverted n-Si photoanode in an extreme alkaline environment. The activated NiO catalyzes the water oxidation reaction which is also facilitated by the photovoltage generated in the Si junction under illumination. This photoanode shows great stability over hundreds of cyclic scans. The photocurrent density at the water oxidation potential is about 2 mA/cm^2 under 0.5-sun illumination.

4.2 Suggested future work

There are several possible directions to improve the Si based photoelectrode. In this session, I will briefly discuss on these possibilities.

4.2.1 Earth abundant HER catalyst

Pt used on photocathode can be replaced by outstanding HER catalyst made of earth abundant materials. Molybdenum sulfide is a good candidate, which can be synthesized at low temperature from solution based method. References can be found in session 1.4.3.2.1. Careful characterization is needed due to the potential light loss at this coating.

4.2.2 Amorphous catalyst without activation

In the last session of Chapter 4, NiO_x OER catalyst has to be activated to give better activity. This energy input for this process has been minimized by controlling the thermal treatment process and surfactant in the precursor. However, a catalyst with intrinsically high activity without going through an activation process is desired. This goal can be potentially achieved through active doping of foreign metal ions, addition of carbon nanotubes/graphene, controlling surfactant, or mesoporous structure with high surface area.

4.2.3 Improved Si junction

Si photovoltaic cell isolated by the s-TCO presented in the last session of Chapter 4 is an important component to achieve high efficiency photoanodes. We have noticed significant series resistance loss and low Voc. This is primarily due to the non-optimized surface inversion processes. Optimization can be done to achieve better solar oxygen conversion efficiency.

4.2.4 In-situ Raman and X-ray absorption on catalyst

In-situ Raman and X-ray absorption will allow us to gain insights on the catalytic reaction when an external bias is applied and gas evolution is involved on the sample surface due to the fact that these techniques do not require high vacuum. The in-situ cell designed needs a few modifications in order to fit better for these studies.